2014

PRECIPITATION, ORIENTATION AND COMPOSITION EFFECTS ON THE SHAPE MEMORY PROPERTIES OF HIGH STRENGTH NiTiHfPd ALLOYS

Emre Acar
University of Kentucky, mailtoemre@yahoo.com

STUDENT AGREEMENT:

I represent that my thesis or dissertation and abstract are my original work. Proper attribution has been given to all outside sources. I understand that I am solely responsible for obtaining any needed copyright permissions. I have obtained needed written permission statement(s) from the owner(s) of each third-party copyrighted matter to be included in my work, allowing electronic distribution (if such use is not permitted by the fair use doctrine) which will be submitted to UKnowledge as Additional File.

I hereby grant to The University of Kentucky and its agents the irrevocable, non-exclusive, and royalty-free license to archive and make accessible my work in whole or in part in all forms of media, now or hereafter known. I agree that the document mentioned above may be made available immediately for worldwide access unless an embargo applies.

I retain all other ownership rights to the copyright of my work. I also retain the right to use in future works (such as articles or books) all or part of my work. I understand that I am free to register the copyright to my work.

REVIEW, APPROVAL AND ACCEPTANCE

The document mentioned above has been reviewed and accepted by the student's advisor, on behalf of the advisory committee, and by the Director of Graduate Studies (DGS), on behalf of the program; we verify that this is the final, approved version of the student's thesis including all changes required by the advisory committee. The undersigned agree to abide by the statements above.

Emre Acar, Student

Dr. Haluk E. Karaca, Major Professor

Dr. James McDonough, Director of Graduate Studies

PRECIPITATION, ORIENTATION AND COMPOSITION EFFECTS ON THE SHAPE MEMORY PROPERTIES OF HIGH STRENGTH NiTiHfPd ALLOYS

DISSERTATION

A dissertation submitted in partial fulfillment of the requirements for the degree of Doctor of Philosophy in the College of Engineering at the University of Kentucky

By

Emre Acar

Lexington, KY

Director: Dr. Haluk E. Karaca, Professor of Mechanical Engineering

Lexington, KY

2014

ABSTRACT OF DISSERTATION

PRECIPITATION, ORIENTATION AND COMPOSITION EFFECTS ON THE SHAPE MEMORY PROPERTIES OF HIGH STRENGTH NiTiHfPd ALLOYS

NiTiHf high temperature shape memory alloys are attractive due to their high operating temperatures (>100 ^{o}C) and acceptable transformation strain compared to NiTi. However, NiTiHf has limitations due to their lack of ductility and low strength, resulting in poor shape memory properties. In this study, Pd has been added to NiTiHf alloys in an attempt to improve their shape memory behavior. A combined approach of quaternary alloying and precipitation strengthening was used.

The characterization of a $Ni_{45.3}Ti_{29.7}Hf_{20}Pd_5$ (at. %) polycrystalline alloy was performed in compression after selected aging treatments. Transmission electron microscopy was used to reveal the precipitation characteristics. Differential scanning calorimetry, load-biased (constant stress) thermal cycling experiments and isothermal stress cycling (superelasticity) tests were utilized to investigate the effects of aging temperature and time. The crystal structure and lattice parameters were determined from X-ray diffraction analysis. Significant improvement in the shape memory properties of $Ni_{45.3}Ti_{29.7}Hf_{20}Pd_5$ was obtained through precipitation strengthening. The effects of chemical composition (effects of Hf content replacing with Ti) on the shape memory properties of NiTiHfPd alloys were also revealed.

Orientation dependence of the shape memory properties in aged $Ni_{45.3}Ti_{29.7}Hf_{20}Pd_5$ single crystals were investigated along the [111], [011] and [-117] orientations. The shape memory properties were determined to be strong functions of orientation and aging condition. A perfect superelastic behavior (with no irrecoverable strain) with 4.2 % recoverable compressive strain was obtained in the solutionized condition at stress levels as high as 2.5 GPa while 2 % shape memory strain under a bias stress of 1500 MPa was possible in an aged [111] oriented single crystal. A mechanical hysteresis of 1270 MPa at -30 ^{o}C, which is the largest mechanical hysteresis that the authors are aware of in the SMA literature, was observed along the [111] orientation.

Finally, thermodynamic analyses were conducted to reveal the relationships between microstructure (e.g. precipitate size and interparticle distances) and martensitic transformations in $Ni_{45.3}Ti_{29.7}Hf_{20}Pd_5$ SMAs. Precipitate characteristics were found to be effective on the elastic energies for nucleation, propagation with dissipation energy and these energies influenced the TTs and the constant stress shape memory properties in $Ni_{45.3}Ti_{29.7}Hf_{20}Pd_5$ alloys.

KEYWORDS: NiTiHfPd, Shape Memory Alloys, Mechanical Characterization, High Strength Shape Memory Alloys, High Hysteresis

Emre Acar

Student's Signature

04/28/2014

PRECIPITATION, ORIENTATION AND COMPOSITION EFFECTS ON THE SHAPE MEMORY PROPERTIES OF HIGH STRENGTH NiTiHfPd ALLOYS

By

Emre Acar

Haluk E. Karaca
Director of Dissertation

James McDonough
Director of Graduate Studies

04/28/2014

ACKNOWLEDGEMENTS

Firstly, I would like to thank my research advisor Prof. Haluk E. Karaca for his constant guidance and encouragement throughout my PhD study. He has kept encouraging me to do research and patiently taught me what I have learned so far. I have learned how to conduct systematic scientific research and to write articles under his mentoring.

I would like to thank my co-advisor Prof. Yang-Tse Cheng for his advices and time for this dissertation. I am also thankful to Prof. Keith Rouch and Prof. Charles Lu for their time and being in my advisory committee. I also would like to thank Dr. Ronald D. Noebe from NASA Glenn Research Center for his invaluable comments and suggestions during the research and writing process of most of my articles.

I would like to express my gratuities to Prof. Yuriy Chumlyakov for his insightful discussions and suggestions. Prof. Burak Basaran was a patient teacher for me at the beginning of my research and I would like to thank him for his time. I also would like to thank my office and laboratory mates; Ali Sadi Turabi, Irfan Kaya, Sayed Saghaian, Dr. Hirobumi Tobe, Mohannad Souri, Peizhen Li, Sesha Spandana Pulla. They have made the research and life easier during my study at the University of Kentucky.

I would like to acknowledge the Turkish Ministry of Education for the financial support during my graduate education in the United States and partially supporting research projects by the NASA Fundamental Aeronautics Program, Aeronautical Sciences Project and the NASA EPSCOR program under grant No: NNX11AQ31A, KY EPSCoR RID program under grant No: 3049024332.

TABLE OF CONTENTS

LIST OF TABLES

LIST OF FIGURES

1. INTRODUCTION

1.1. Motivation and objectives

Diffusionless solid to solid phase transformation is called martensitic transformation [1]. If a martensitic transformation is reversible, it is called thermoelastic martensitic transformation [1].

Owing to the thermoelastic martensitic phase transformations, shape memory alloys (SMAs) have the unique ability to recover large deformations upon heating or by removal of stress [2] in contrast to regular materials. Due to this atypical behavior, there are countless of potential and current applications for SMAs including use as actuators, sealing elements, sensors, couplers, stents, valves and surgical appliances in the biomedical, aerospace, oil-gas, automotive, robotics, and telecommunication industries [3]. Among the SMAs, NiTi is the most commonly used and well-known alloy since it has good physical and functional properties such as high ductility, low density, high corrosion resistance, and good fatigue life [2, 4]. However, it is also known that transformation temperatures (TTs) of NiTi alloys are usually below 100 ^{o}C, and they tend to exhibit low strength and poor cyclic stability [5] without thermo-mechanical treatments such as cold working. Consequently, changes in stoichiometry leading to precipitation strengthening, alloying and thermo-mechanical treatments have been utilized as the primary methods to tailor the shape memory behavior of NiTi [2, 6-8].

Ni-rich precipitates (e.g. Ni_4Ti_3) formed through aging can also increase the strength of Ni-rich NiTi alloys [9, 10]. Even without the precipitation hardening, NiTi

alloys with high Ni content are stronger than equiatomic or Ti-rich NiTi alloys [11]. Thus, Ni-rich alloys have been extensively studied by many researchers [2]

Beside precipitation strengthening, an alternative way to significantly increase the strength of NiTi alloys is thermo-mechanical treatments (e.g. cold working and post annealing) [2]. In equiatomic NiTi alloys, even though the matrix is not strong enough to observe perfect superelasticity (SE) in solutionized condition, it is possible to obtain full recovery in superelasticity after proper thermo-mechanical processing [2]. Furthermore, by combining Ni-rich compositions with thermo-mechanical processing, it is possible to get a high yield strength of 2800 MPa and superelastic behavior with negligible plastic deformation in $Ni_{55.9}Ti_{44.1}$ (wt.%) alloys after 42 % cold work followed by annealing [12].

One of the advantages that high strength SMAs can offer is high work output, which is crucial for solid state actuator applications. SMA based actuators have additional advantages over commercial pneumatic/hydraulic or motor driven systems such as higher energy density, compactness, lightweight and silent operation [13]. Commercial NiTi alloys have work output densities of about 10 $J.cm^{-3}$ [14], while NiTiPd and NiTiPt alloys have work output capabilities on the order of 6-9 $J.cm^{-3}$ and 13 $J.cm^{-3}$, respectively [15]. In a recent study, the work output of a Ni-rich NiTiHf polycrystalline alloys was found to be 18-20 $J.cm^{-3}$[16]. It is clear that alloying significantly affects work output, but further investigation is needed to improve the understanding the relationship between composition, microstructure and work output of NiTi based alloys.

On the other hand, shape memory alloys could be employed as dampers in many industries such as aerospace (in aircraft engines to dampen the acoustic energy) and construction (in impact damping devices to counter seismic movements) due to energy absorbing capabilities. Damping capacity is defined as the amount of energy that can be dissipated out of a system resulting in relief. Hence, good damping materials should have large mechanical hysteresis at high stress levels. In general, the stress hysteresis of NiTi alloys is around 200-400 MPa [2] while it can be increased to 500-600 MPa with the addition of Nb [17]. It was reported that damping capacities are 16 $J.cm^{-3}$ and 38 $J.cm^{-3}$ for NiTi and NiTiNb alloys, respectively [18] while it can reach up to 54 $J.cm^{-3}$ in NbTi/NiTi nanocomposite wires [19]. An alloy that has a similar damping capacity to NiTiNb and NbTi/NiTi systems but also with the ability to operate under higher stress levels would be very appealing for aerospace and biomedical applications [20, 21] as well as applications in civil and seismic structures [18, 20, 22]. They can provide several advantages such as high force accommodation, weight saving, portability and reduction in cost over existing systems [20] since less material will be used in a device due to high strength capability.

Tailoring shape memory properties can also be obtained through alloying process [2]. Among the many elements investigated as potential ternary alloying additions to NiTi, only Hf, Zr, Pd, Au and Pt are known to increase the TTs [3]. Due to the high cost of Pt, Pd, and Au, Zr and Hf are the most practical alloying additions for developing high temperature shape memory alloys (HTSMA) [3]. It is also known that Hf is more effective in increasing TTs compared to Zr at similar chemical compositions [3]. However, Ni-lean NiTiHf alloys suffer from large thermal hysteresis (results in additional

energy requirements and cycle time in actuator applications), poor thermal stability, brittleness and low strength impeding their superelastic behavior [23]. Furthermore, the use of quaternary alloying additions to overcome these limitations has not been generally pursued.

The objectives of current study are to;

1. Determine the effects of Pd addition on the strength and shape memory properties of NiTiHf shape memory alloys by conducting detailed experiments including shape memory effect under constant stress, stress-free transformation temperatures in differential scanning calorimetry (DSC) and superelasticity.

2. Reveal the effects of aging temperature and time on the microstructure, TTs, transformation strain, temperature and mechanical (stress) hysteresis of polycrystalline and single crystal NiTiHfPd alloys.

3. Investigate the effects of chemical composition on the shape memory properties of NiTiHfPd high strength shape memory alloys.

4. Investigate the orientation dependence of shape memory properties of single crystal NiTiHfPd alloys.

5. Determine the effects of aging on work output, and damping capacities of NiTiHfPd in polycrystalline and single crystal NiTiHfPd alloys.

6. Investigate on the microstructural dependence of the shape memory behavior and elastic energy storage in NiTiHfPd shape memory alloys

7. Establish microstructure-property-thermodynamics relationships in NiTiHfPd shape memory alloys

1.2. Thermodynamics of martensitic transformations in SMAs

Free-energy curves for austenite and martensite (forward) phase transformation are schematized in Figure 1.1 where G_{ch}^{p} and G_{ch}^{M} are free energies for austenite and martensite, respectively. T_o is the equilibrium temperature while M_s is martensite start temperature and A_s is austenite start temperature.

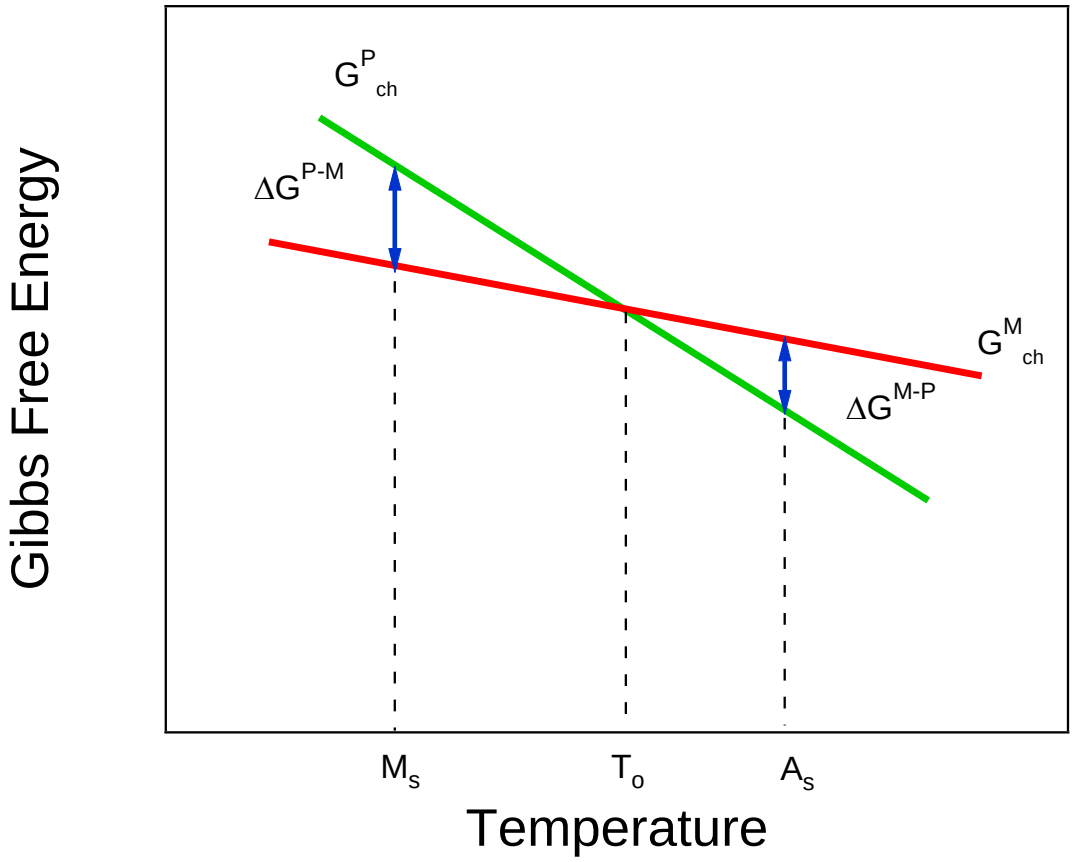

Figure 1.1: Schematics of free-energy curves of martensite and austenite during phase transformation

ΔG_{ch}^{p-m} is the chemical driving force for phase transformation from parent phase (austenite) to martensite and ΔG_{ch}^{m-p} is vice versa. Parent phase transforms to martensite and martensite transforms to parent phase when there is a sufficient driving force in the system. When the G_{ch}^{M} and G_{ch}^{A} are equal to each other, no transformation is expected since there is no difference (driving force) between the chemical energies of transforming

phases. The general thermodynamical equilibrium equiations for the forward transformation can be written of the forms [24] ;

$$\Delta G_{total}^{p-m} = \Delta G_{ch}^{p-m} + \Delta G_{nc}^{p-m} = \Delta G_{ch}^{p-m} + \Delta G_{el}^{p-m} + \Delta G_{irr}^{p-m} \quad (1)$$

where ΔG_{total}^{p-m} is the total Gibbs free energy difference to initiate the martensitic transformation, ΔG_{ch}^{p-m} is the change in chemical energy, ΔG_{nc}^{p-m} is the change in non-chemical energy. ΔG_{nc}^{p-m} energy can be expressed as a combination of ΔG_{el}^{p-m}, the change in elastic energy and ΔG_{irr}^{p-m} ,the irreversible energy during the phase transformation from austenite to martensite [25]. ΔG_{total}^{p-m} term should be smaller than zero in order to initiate the martensitic transformation.

The temperature at which the ΔG_{ch}^{p-m} is zero was defined to be T_o, equilibrium temperature [24]. At T_o, since there is no driving force to trigger the martensitic transformation, an additional energy should be supplied (by cooling or heating) to initiate the transformation.

Super-cooling (T_o-M_s) below T_o is necessary for parent phase to martensite transformation and super-heating (A_s-T_o) beyond T_o is required for martensite to parent phase transformation assuming negligible elastic energy storage.

ΔG_{el}^{p-m} is the stored elastic energy during the forward transformation and it is released completely upon back transformation from martensite to austenite. Hence, the elastic energy storage is a mechanically reversible process [24]. The amount of the stored elastic energy should be equal to the released energy upon back transformation if there is

no plastic relaxation due to dislocation generation/plastic deformation after a full transformation cycle [26, 27].

The irreversible energy ΔG_{irr}^{p-m} can be assumed as a combination of mainly frictional energy that is required to move phase front (between transforming phases), friction between martensite variants and internal twins in variants in addition to plastic relaxation energy due to dislocation generation. Both of the abovementioned mechanisms result in dissipation of energy and consequently, hysteresis in SMAs [11]

1.3. Mechanism of martensitic transformations in SMAs

1.3.1. Shape memory effect

Thermo-elastic martensitic transformation is a reversible solid to solid phase transformation that can be triggered by various parameters (e.g. temperature, stress, magnetic field) in SMAs. Martensitic transformation is a shape change between high temperature or parent phase and low-temperature phase (martensite) with small volume change [2]. Basic or the most common shape memory properties (e.g. shape memory effect and superelasticity) are directly related to this first order type martensitic transformation.

Variant re-orientation and stress induced martensite (SIM) formation are the two main mechanisms that result in strain in shape memory alloys. If a material is cooled down in the absence of stress, parent phase transforms to martensite by self-accommodating mechanism to minimize the energy of the system. If there is an external

stress applied, the stress distorts self accommodating structure and selects favored martensite variants along its application direction. In both cases, if the material is heated above A_f (austenite finish) temperature, the material transforms back to austenite. This mechanism is called one-way shape memory effect. Figure 1.2 shows schematics for the shape memory effect behavior in SMAs.

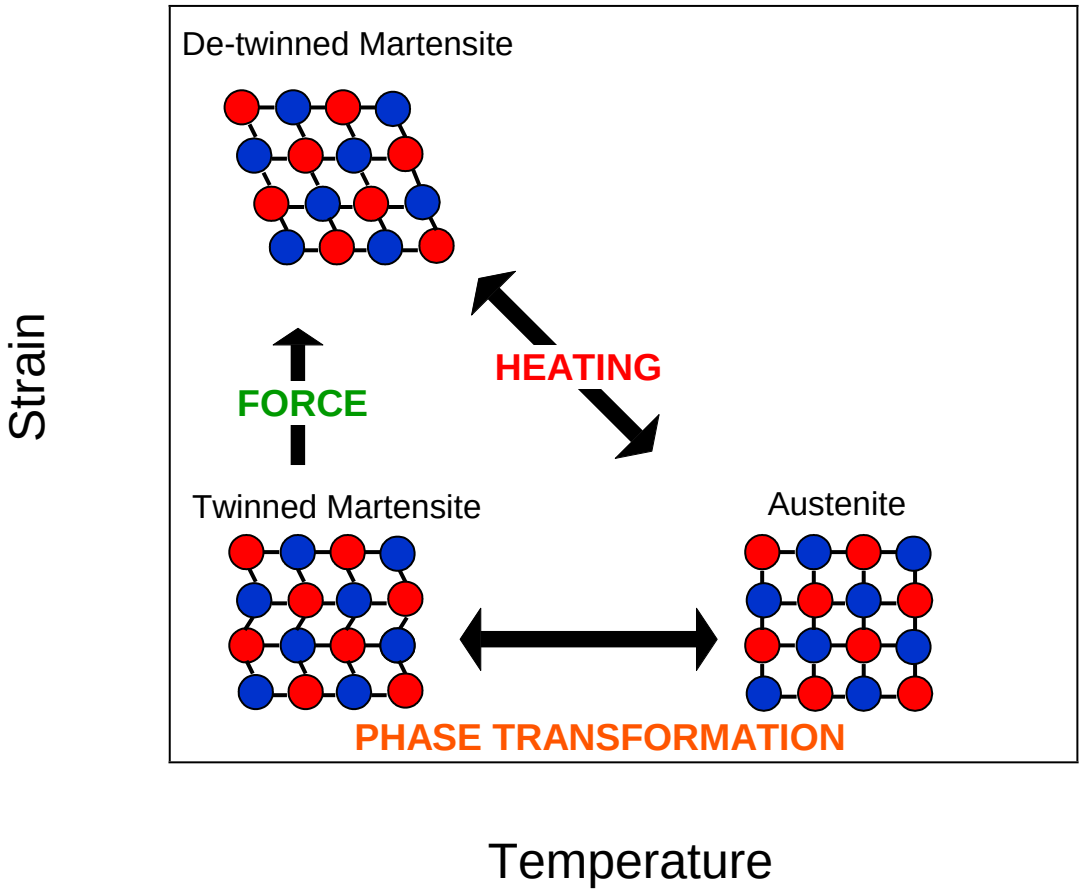

Figure 1.2: Representative schematics of shape memory effect in SMAs

If there is already internal stress in the microstructure, it is possible to obtain shape memory strain without applying an external stress and this process is called two-

way shape memory effect (TWSME) [28, 29]. The two-way shape memory effect, as an intrinsic property of SMAs, is closely related to the internal stress around precipitates, oriented dislocation arrangements and retained martensite [30, 31], that can be provided by training (e.g. thermal cycling, stress cycling) or martensite deformation. These procedures promote oriented dislocations in the microstructure and consequently, anisotropic stress fields are generated. Some martensite variants are favored by these stress fields acting like external stress and TWSME is observed.

1.3.2. Psuedoelasticity

Figure 1.3 shows a typical superelastic behavior and related transforming phases in SMAs. At temperatures above A_f, deformation of the parent phase results in stress induced martensite transformation. The initial linear part of the stress-strain plot represents the elastic deformation of the austenite phase. Subsequent to this elastic deformation, a deviation from linearity to a plateau is observed, which marks the initiation of the stress-induced austenite-to-martensite phase transformation. With further loading, where the plateau ends and work hardening increases steeply, deformation is probably due to some detwinning and elastic deformation of the martensite phase, which is expected to be fully de-twinned at the end of the stage.

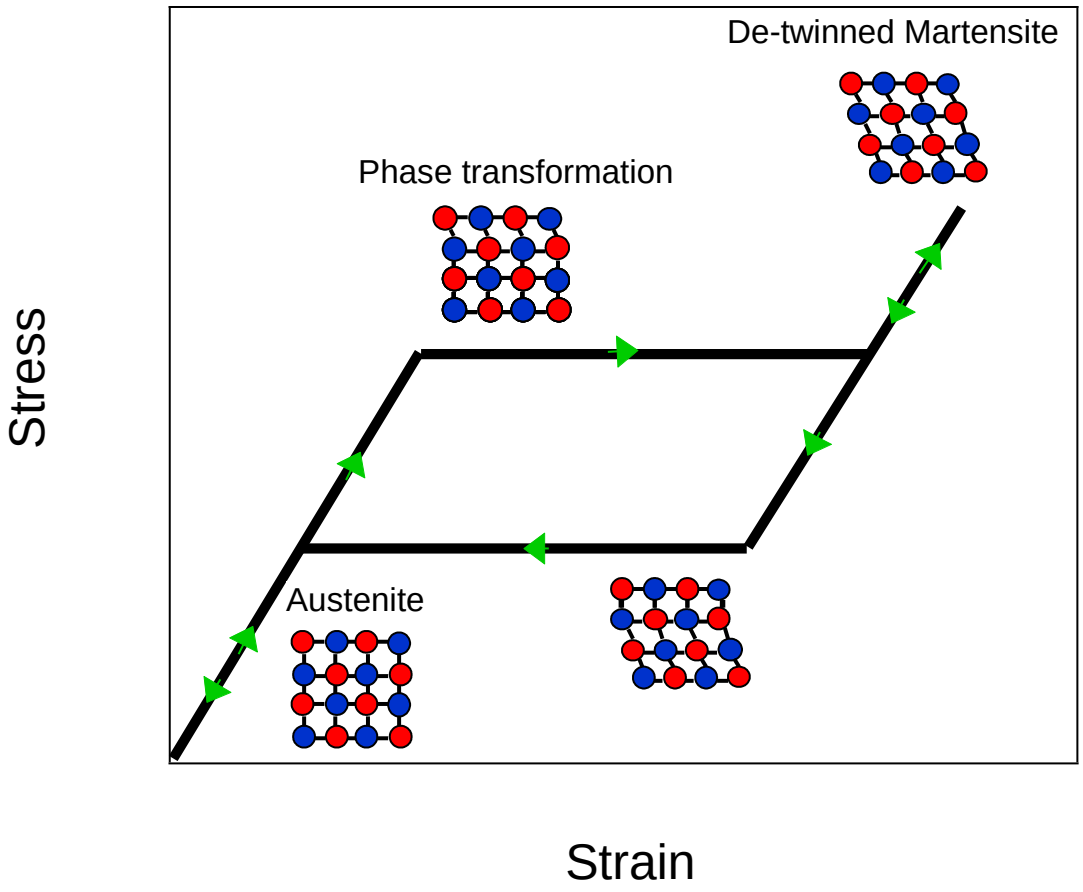

Figure 1.3: A typical superelastic behavior in SMAs.

Upon unloading, elastic recovery of the martensite takes place and then it is followed by the martensite-to-austenite back transformation. The superelasticity behavior can be observed up to a certain temperature of M_d (depending on material, composition etc.) where plastic deformation becomes the main deformation mechanism.

1.4. Brief background on NiTi and NiTi-based shape memory alloys

1.4.1. NiTi alloys

It was stated that NiTi alloys are the most common SMAs that have current and potential applications in many industries including medical [32, 33], automobile, aerospace [34] and construction [32, 35] due to superior physical and mechanical properties.

Annealed near equiatomic NiTi alloys undergo B2 (cubic) to B19’ (monoclinic) phase transformation [2]. If there is internal stress in the microstructure due to thermal treatments, cycling etc., NiTi shows two-step martensitic transformation. They undergo B2 to R-phase followed by R to B19’ phase transformation. R-phase is a transition structure that has commonly rhombohedral structure [2].

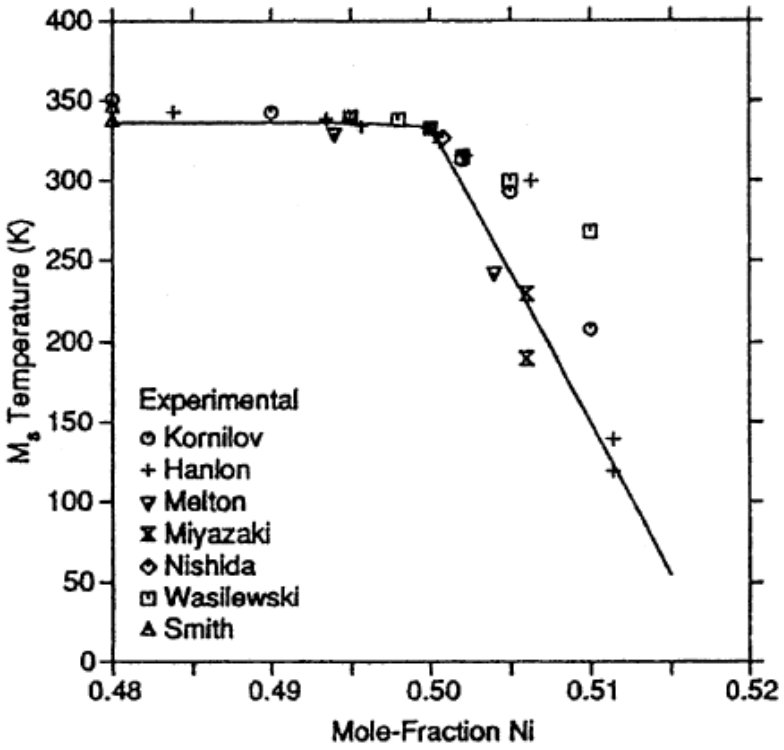

Figure 1.4: The change in TTs as a function of Ni concentration in NiTi alloys [2]

Figure 1.4 shows the effect of Ni mole fraction on the TTs in NiTi alloys. TTs are insensitive to aging in near-equiatomic NiTi since no precipitation is achievable in these materials through aging [2]. On the other hand, as the Ni content increases on the Ni-rich side (> 50.6 %) of the phase diagram, the TTs decrease rapidly. Aging of a Ni-rich NiTi alloy causes formation of Ni-rich precipitates resulting in Ni depletion in the matrix and consequently increase in TTs. In addition to TTs, Ni-rich precipitates can increase the strength of NiTi alloys and thus, Ni-rich NiTi alloys have been studied widely [9, 10] as compared to Ni-lean NiTi.

Despite of superior properties, it is also a fact that equiatomic NiTi alloys have low TTs and low strength beside poor cyclic stability [5]. It is possible to get

irrecoverable strain upon thermal cycling even under 50 MPa as shown in Figure 1.5. Consequently, changes in stoichiometry leading to precipitation strengthening, alloying, and thermo-mechanical treatments have been utilized as the primary methods to tailor (e.g. increase strength) the overall behavior of NiTi [2, 6-8].

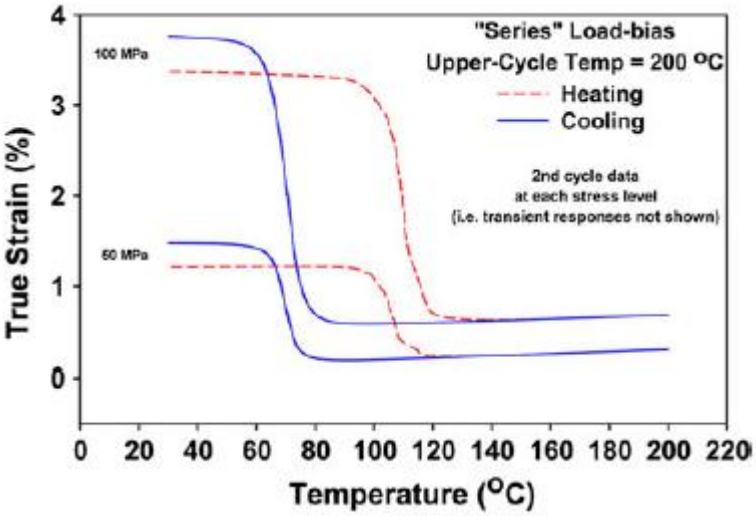

Figure 1.5: Constant stress thermal cycling response of $Ni_{49.9}Ti_{50.1}$ (at %) at 50 and 100 MPa [5]

Ni-rich NiTi alloys are stronger compared to Ni-lean alloys even without precipitation hardening [11]. In addition to precipitation hardening, thermo-mechanical treatments (e.g., cold working and post annealing) also can significantly increase the strength of NiTi [2]. In solutionized condition, fully recoverable superelasticity is not possible in equiatomic NiTi alloys due to their soft matrix. However, it is possible to obtain a superelastic behavior without significant plastic deformation under high stress (e.g. >1500 MPa) by utilizing Ni-rich compositions with thermo-mechanical treatments (e.g., $Ni_{50.83}Ti_{49.17}$ (at.%) after 42 % cold work followed by annealing [12]). It should be

noted that pre-treatments such as thermo-mechanical treatment and post annealing are required to obtain fully recoverable SE in near-equiatomic NiTi alloys.

A thermo-mechanical treatment is also effective in the change of active twinning modes during phase transformation in NiTi alloys. The most common twinning type observed in NiTi alloys is <011> type II [36]. Latterly, it has been observed that the twinning type can be a mixture of type I and type II while a combination of type I and compound twins were also observed after proper cold rolling [37].

Another important research area of NiTi alloys is the orientation dependence of their shape memory properties. Figure 1.6 shows the stress-strain responses of $Ni_{50.8}Ti_{49.2}$ shape memory alloys in various orientations in compression.

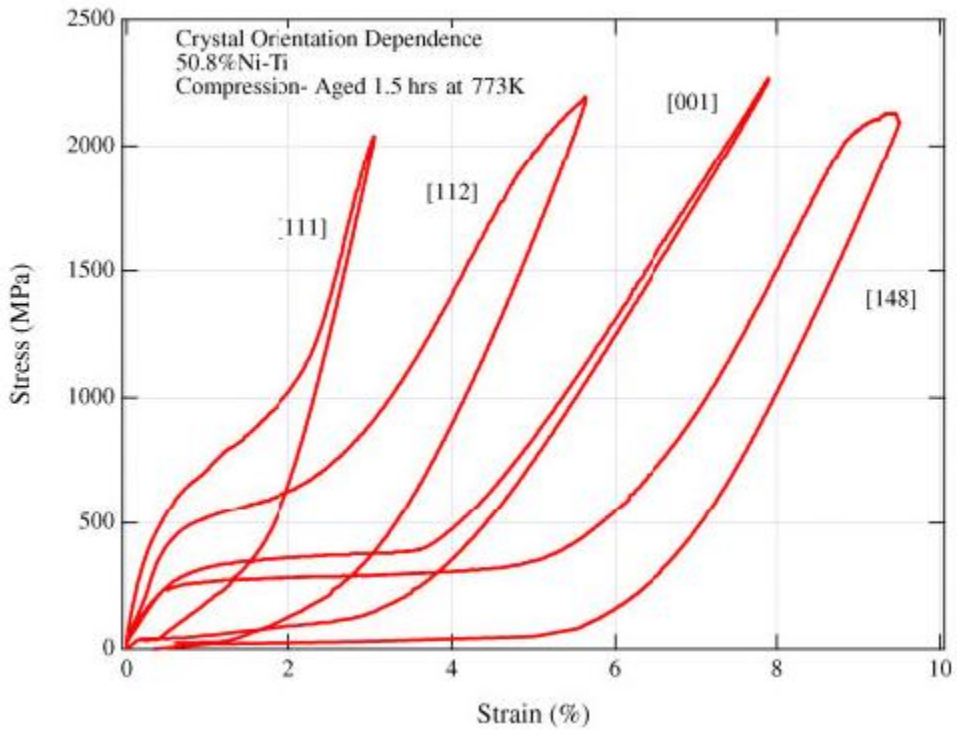

Figure 1.6: Orientation dependence of stress-strain behavior of $Ni_{50.8}Ti_{49.2}$ alloys [3]

It is known that texture formation is most likely during processing of SMAs and this may alter the mechanical and shape memory responses of the material. Thus, investigation of the shape memory properties of SMA single crystals is crucial due to the fact that shape memory properties could be optimized by texturing in a polycrystalline material [38-41].

It was revealed that multiple correspondant variant pairs (CVPs) were activated during stress induced martensite transformation along the [111] and [112] orientations in compression and this resulted in high hardening in the transformation region [41] of the $Ni_{50.8}Ti_{49.2}$ (at. %) single crystals. Because of this high hardening, they quickly reached the critical stress for plastic deformation. Thus, their transformation strain and

superelastic temperature window were limited [41, 42]. However, [148] orientation had only one active CVP and this yield a plateau-like transformation (low hardening transformation region) and a transformation strain close to theoretical values in $Ni_{50.8}Ti_{49.2}$.

1.4.2. NiTiHf alloys

In practical applications, TTs are important parameters in designing SMA related parts due to the fact that active control mechanisms are closely linked to them. Some applications in aerospace, energy conversion and automobile engines require higher TTs (above 100 ^{o}C), which is not possible for the NiTi alloys [3, 43]. High temperature shape memory alloys are good candidates for lightweight and compact actuators and sensors. HTSMAs must have good mechanical and functional properties (e.g. significant transformation strain, oxidation resistance, resistance to plastic deformation and creep etc.) at the high operation temperatures since these properties usually deteriorate as operation temperature increases [3].

Thus, many studies have been conducted in order to understand the fundamental basis in the TTs change in SMAs [44]. One attempt has been to obtain HTSMAs by using NiTi with the idea of taking advantages of its exceptional properties at also elevated operation temperatures. In order to increase the TTs of NiTi shape memory alloys, chemical alloying has been used [2] as a method. Addition of Fe, V, Al, Co, Cu, Mn in the expense of Ni reduces the TTs whereas addition of Hf, Zr, Pd, Pt, Au and W in the expense of Ti increases the TTs in NiTi shape memory alloys [3]. NiTiX (X= Hf, Zr)

alloys have been demonstrated to have a higher potential for actual applications due to lower costs compared to the Pd, Pt and Au additions [45].

Figure 1.7 shows the change in M_p (calculated to be peak point of transformation curve during forward transformation in a transformation cycle) temperature as a function of Hf and Zr content in a and b, respectively. Up to 3 % of Hf, the TTs are insensitive to composition change and they start increasing after 5 % Hf addition in Figure 1.7.a. There is an increase by ≈ 5 ^{o}C/at % up to 10 % of Hf where the increase becomes ≈ 20 ^{o}C/at % beyond 10 % Hf addition. M_p temperatures reach up to 400 ^{o}C for 25 % Hf in NiTiHf alloys.

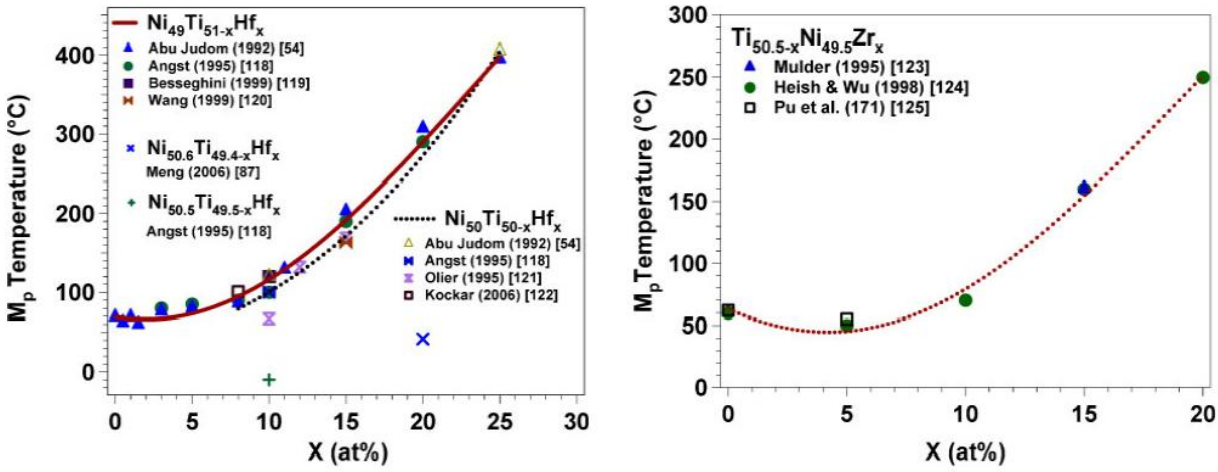

Figure 1.7: Mp temperatures as a function of a) Hf and b) Zr contents in NiTiX (X=Hf,Zr) alloys [3].

In Figure 1.7.b, Mp temperature is not a function of Zr addition up to 10 % beyond which there is almost ≈ 10 ^{o}C/at % increase with increasing Zr content. M_p temperatures reach up to 250 ^{o}C with addition of 25 % Zr. Thus, it can be concluded that Hf was more effective in increasing TTs compared to Zr for an equivalent additions in ternary NiTiHf

alloys [3]. Thus, among NiTiHf and NiTiZr systems, the earlier has been more pronounced due to its capability in elevating the TTs as mentioned previously [3].

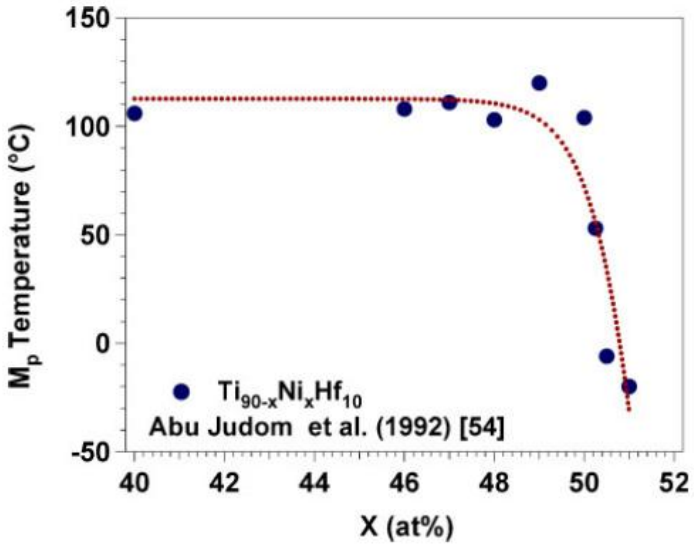

Figure 1.8: Mp temperature as a function of Ni content in NiTiHf alloys [3].

The change in M_p temperatures as a function of Ni content in NiTiHf alloys containing 10 % Hf is shown in Figure 1.8. It is obvious that M_p does not change up to 50 % and suddenly decreases to below 0 ^oC beyond equiatomic line with increasing Ni content.

1.4.3. NiTiHf-X (X= Cu, Nb, Zr) alloys

The TTs of NiTiHf alloys are promising for the high temperature applications. However, Ni-rich NiTiHf alloys have also limitations due to their high brittleness [16] for practical use and Ni-lean NiTiHf alloys have poor superelasticity response since the stress-induced martensite transformation and plastic deformation occur simultaneously

due to low critical stress for slip and high strain hardening in transformation region [16, 46].

Low ductility and strength of NiTiHf alloys are the main challenges that should be addressed before these alloys can be used in practical applications. Thus, quaternary elements have been added to NiTiHf alloys to improve their shape memory behavior.

Nb was added to $Ti_{35.5}Ni_{49.5}Hf_{15}$ (at %) alloys and it was found to increase the cold workability and shape recovery ratio of the $Ti_{35.5}Ni_{49.5}Hf_{15}$ shape memory alloys while decreasing the TTs and plastic strain in thermal cycling experiments under constant tensile stresses of 500 MPa [47]. It was revealed that Nb additions of greater than 20 % were also effective in decreasing plastic strain from 2.66 % to 0.24 % in constant stress thermal cycling experiments while decreasing the transformation temperatures [47] as shown in Figure 1.9.

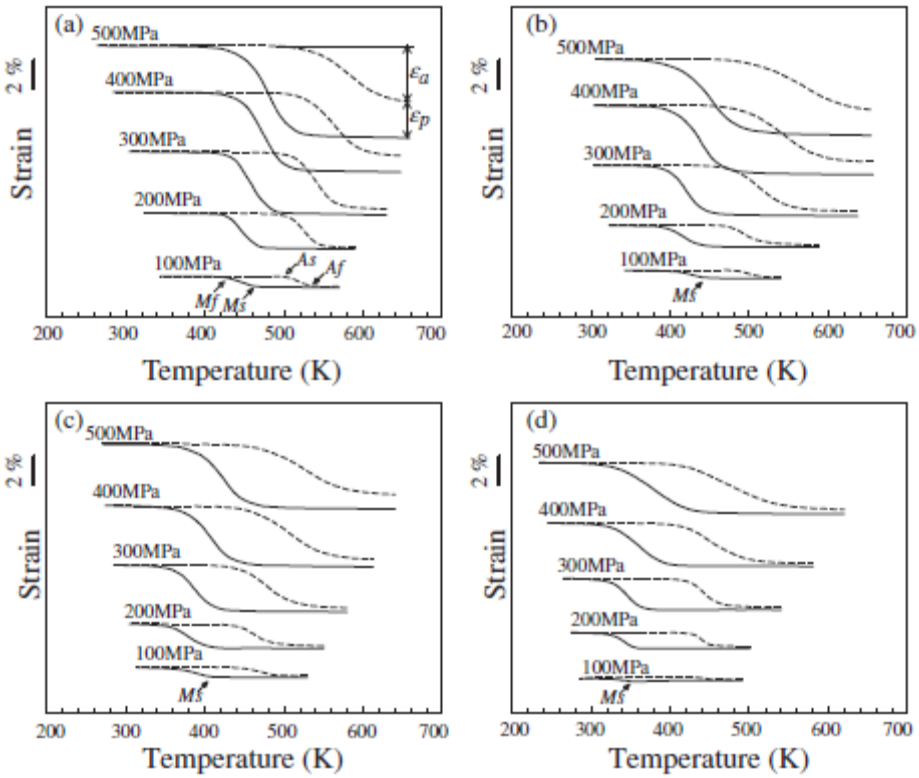

Figure 1.9: Constant stress thermal cycling experiments in a) $Ti_{35.5}Ni_{49.5}Hf_{15}$, b) $Ti_{30.5}Ni_{49.5}Hf_{15}Nb_5$, c) $Ti_{25.5}Ni_{49.5}Hf_{15}Nb_{10}$ and d) $Ti_{20.5}Ni_{49.5}Hf_{15}Nb_{15}$ alloys [28].

Cu has been another alloying addition to NiTiHf alloys. Cu addition generally improved the glass forming ability and thermal stability of NiTiHf alloys while decreasing their TTs [48, 49]. NiTiHfCu alloys have also good TWSME [50] due to anisotropic dislocation arrangements generated by so-called training procedures. Most of the studies on NiTiHfCu alloys were focused on the changes in TTs and microstructure through aging.

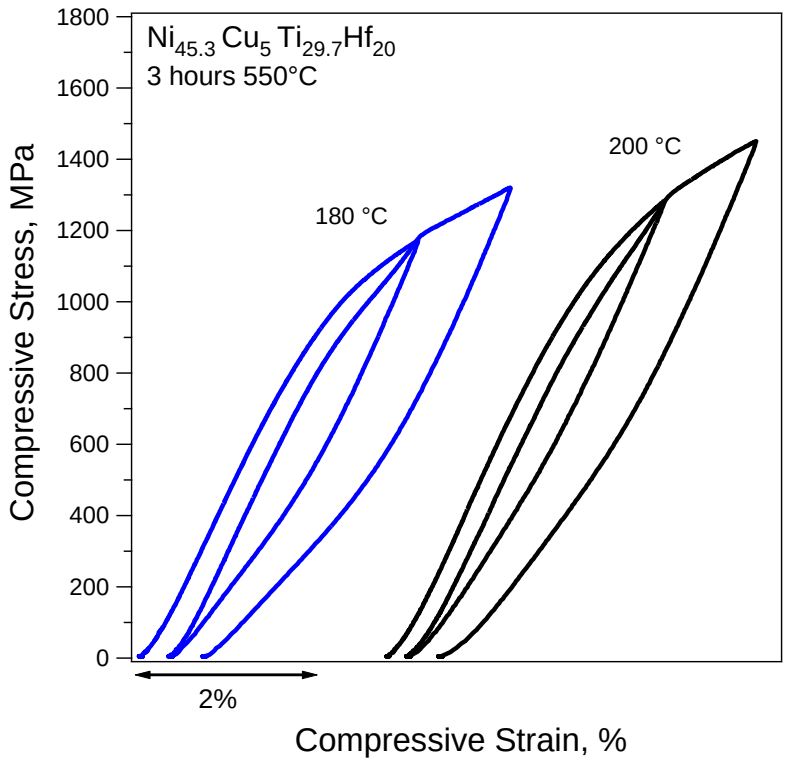

Figure 1.10: Stress-strain response of $Ni_{45.3}Ti_{29.7}Hf_{20}Cu_5$ alloys aged at 550 ^{o}C for 3 hours [51].

Karaca et.al. recently reported the crystal structures, TTs, microstructure, hardness, shape memory (including TWSME) and superelastic properties after addition of 5 % Cu to $Ni_{50.3}Ti_{29.7}Hf_{20}$ alloys replacing Ni [51]. In this study, $Ni_{45.3}Ti_{29.7}Hf_{20}Cu_5$ alloys were able to recover compressive strains of ≈ 2 % under 700 MPa above 100 ^{o}C, which is promising for potential high temperature applications and 0.8 % two-way shape memory strain was also possible above 80 ^{o}C. No fully recoverable superelasticity was reported due to high hardening, low strength and high hysteresis as shown in Figure 1.10.

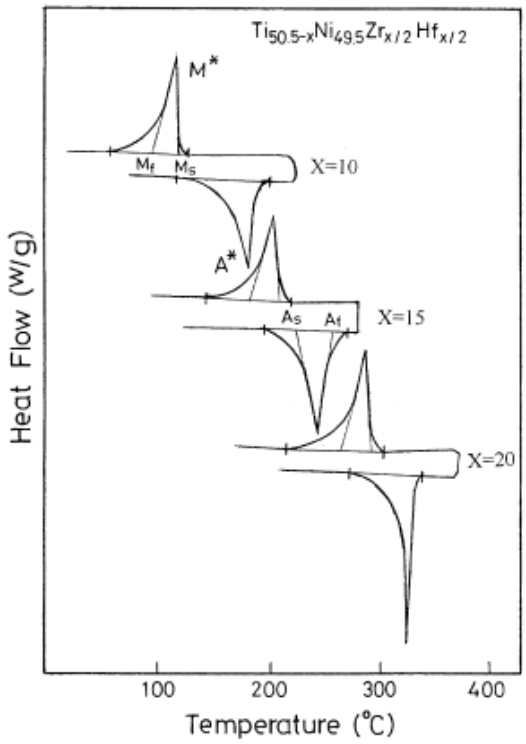

Figure 1.11: DSC heat flow curves for NiTiHfZr alloys in various chemical concentrations [29]

Martensitic transformations in $Ti_{50.5-x}Ni_{49.5}Zr_{x/2}Hf_{x/2}$ (X=0-20 at %) alloys were investigated by Hsieh et.al [52] and the related DSC curves are presented in Figure 1.11. TTs and hardness values increased as a function of Zr. M_p temperatures increased 50 to 323 ^oC with increasing Zr and Hf contents. No mechanical properties (e.g. constant stress thermal cycling, superelasticity) have been reported for the NiTiHfZr alloys.

2. EXPERIMENTAL PROCEDURE

This chapter describes the experimental methods used in characterization of NiTiHfPd polycrystalline and single crystal alloys in this study. The details of material fabrication, preparation (e.g. thermal treatments), crystal and micro structural analysis, calorimetric measurements and mechanical testing will be presented throughout the chapter.

2.1. Fabrication and thermal processing of materials

Induction melting method was used to process NiTiHfPd polycrystalline SMAs in various chemical compositions ($Ni_{45.3}Ti_{29.7}Hf_{20}Pd_5$, $Ni_{45.3}Ti_{34.7}Hf_{15}Pd_5$ and $Ni_{45.3}Ti_{39.7}Hf_{10}Pd_5$) as casting of a 1" diameter by 4" long rod. The melting was conducted with high purity elemental constituents (99.98 wt pct Ni; 99.995 wt pct Pd, 99.95 wt pct Ti and 99.7 wt pct Hf (excluding Zr, which is nominally 3%)). Some of the rods in chemical composition of $Ni_{45.3}Ti_{29.7}Hf_{20}Pd_5$ was homogenized at 1050 ^{o}C for 72 hours and then extruded at a 7:1 ratio in diameter at 900 ^{o}C. Other materials (including some of $Ni_{45.3}Ti_{29.7}Hf_{20}Pd_5$) were homogenized at 900 ^{o}C for 72 hours and were not extruded and left as-cast materials.

Bridgeman Technique was used to grow alloy single crystals in a He atmosphere. The aim composition of the starting alloy was $Ni_{45.3}Ti_{29.7}Hf_{20}Pd_5$ (at %) while the measured composition was $Ni_{45.3}Ti_{29.1}Hf_{20}Pd_{5.2}$ with 0.4 % Zr (at %), as determined by inductively coupled plasma atomic emission spectroscopy (ICP-AES). The single crystal ingots were oriented along [111], [011] and [-117] and cut into compression specimens (4mm x 4mm x 8mm) by electro discharge machining (EDM). The single crystals were

solutionized in vacuum quartz tubes (to avoid oxidation) followed by water quenching. Aging treatments were conducted in air using a Lindberg/Blue M BF5114841 box furnace. All specimens were water quenched after heat treatment unless a different method is stated in next chapters.

2.2. Crystal and micro structure analysis

X-ray diffraction measurements were carried to identify the crystal structures and lattice parameters of transforming phases by a Bruker-AXS D8 Discover diffractometer with CuK_{α} radiation. Both room temperature and elevated temperature scanning on mechanically polished specimens were conducted to reveal the diffraction patterns of transforming phases. Allen Bradley 900-TC8 temperature controller was used for maintaining desired temperatures in the XRD equipment.

Transmission electron microscope (TEM) observations were conducted at room temperature (RT) in a JEOL 2010F instrument operated at 200 kV. The specimens for TEM observation were prepared by a twin-jet polishing technique using a solution of 20% sulfuric acid and 80% methanol at around -15 ^{o}C (258 K).

2.3. Calorimetric measurements

The differential scanning calorimeter (The Perkin-Elmer DSC Pyris 1 as shown in Figure 2.1) method was used to capture TTs under stress-free conditions. Typical temperature range was from -150°C to 600°C and the heating and cooling rate used to run the experiments was fixed at 10°C/minute. Encapsulated samples in disposable Perkin Elmer or Thermal Support aluminum pans with 20-40 mg were used in calorimetric measurements.

Figure 2.1: Perkin-Elmer Pyris 1 DSC [53]

2.4. Mechanical experiments

The mechanical experiments were performed in an MTS Landmark servo hydraulic test platform shown in Figure 2.2 (100 kN) on 8x4x4 mm^3 compression specimens (Figure 2.3) cut by electro discharge machine (EDM) from the various chemical compositions NiTiHfPd ingots. Sides of the machined compression samples were mechanically polished to remove the EDM layers.

Figure 2.2: MTS Landmark servo hydraulic test platform

Strain was measured by an MTS high temperature extensometer with a gage length of 12 mm attached to compression grip faces as shown in Figure 2.4. A strain rate of 10^{-4} mm/sec was employed during loading of the specimens while unloading was performed at a rate of 100 N/sec.

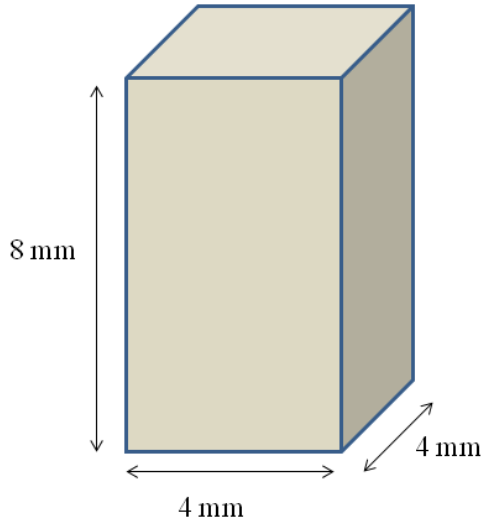

Figure 2.3: Schematic of a compression test specimen

Heating of the specimens occurred by means of mica band heaters retrofitted to the compression grips and cooling was achieved through internal liquid nitrogen flow in the compression grips. A heating-cooling rate of 10 ^{o}C/min was utilized during testing using an Omega CN8200 series PID temperature controller, which was capable of controlling temperature to ±2 ^{o}C. K-type thermocouples attached to the test specimens and the compression grips (total of three thermocouples) provided real-time temperature feedback.

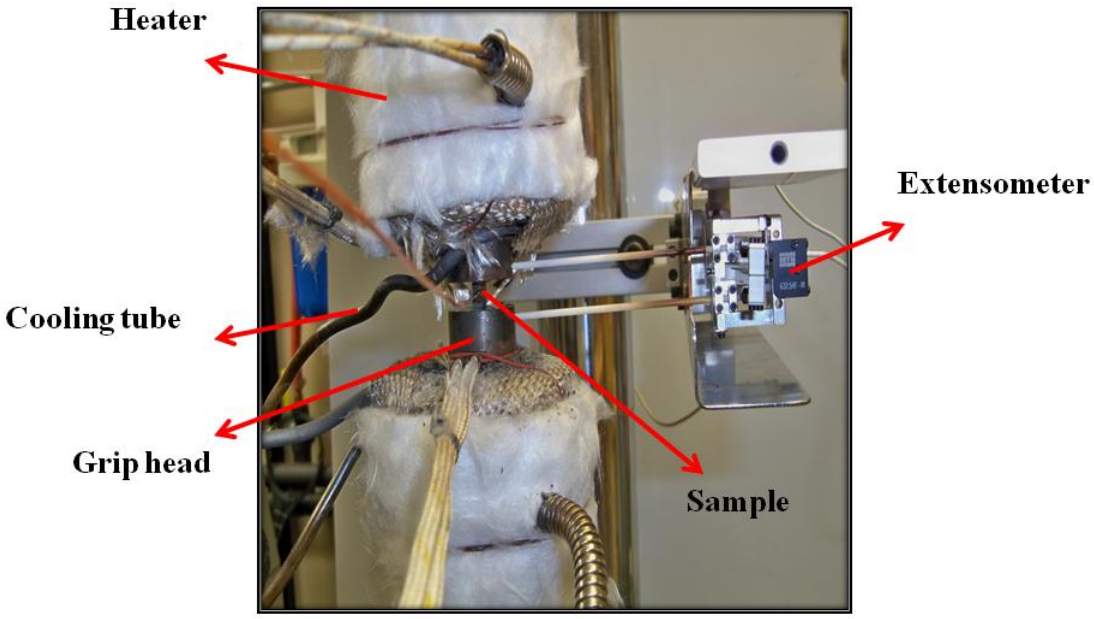

Figure 2.4: MTS high temperature extensometer with a gage length of 12 mm attached to compression grip faces of the test platform.

2.4.1. Thermal cycling under constant stress experiments

A schematic of a shape memory effect in a constant-stress thermal cycling experiment is shown in Figure 2.5. At an applied load, austenite starts transforming to martensite at M_s and the transformation finishes at M_f (martensite finish temperature) during cooling. Throughout heating, martensite phase starts transforming to austenite at A_s and transformation finishes at A_f. The induced strain upon cooling under load is fully recovered after heating above A_f (ignoring plastic deformation).

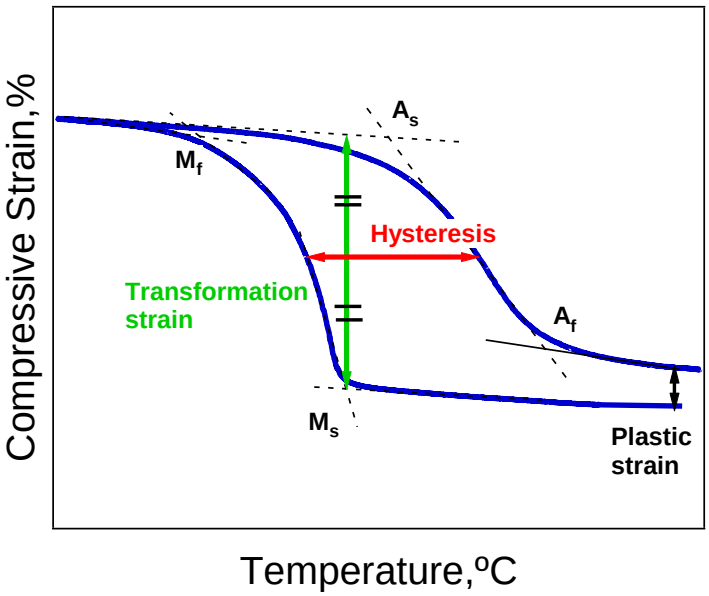

Figure 2.5: Schematic showing the methods of calculating shape memory parameters in the constant-stress thermal cycling experiments

Total strain was measured as the difference between cooling and heating curves at M_s, while the transformation strain was the difference between the total induced strain and plastic strain. The plastic strain (irrecoverable strain) was measured to be the difference between the cooling-heating curves at around A_f+20 ^oC. Thermal hysteresis was measured at the midpoint of the total induced strain as shown in Figure 2.5.

2.4.2. Psuedoelasticity/Superelasticity experiments

Figure 2.6 represents a typical psuedoelastic/superelastic response of an SMA at test temperatures above A_f. In superelasticity experiments that will be presented in the later chapters, samples were loaded under strain control and then unloaded under force control if anything else is not specified. The elastic deformation of the austenite phase

takes place in the initial linear part of the stress-strain plot. Following this elastic deformation, a deviation from linearity to a plateau is observed, which marks the initiation of the stress-induced austenite-to-martensite phase transformation. Further loading could result in detwinning and/or elastic deformation of martensite phase. During unloading, elastic recovery of the martensite is followed by the martensite to austenite back transformation.

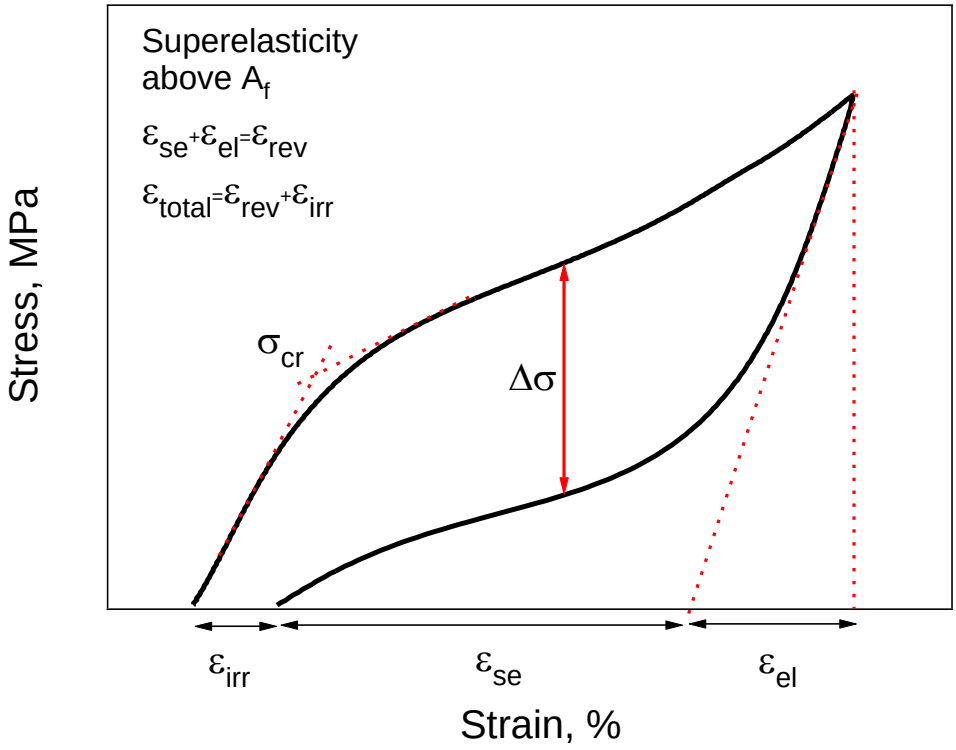

Figure 2.6: A typical superelastic response of an SMA with the calculation methods of relevant parameters

Critical stress for the stress induced martensite (σ_{cr}) is measured at the yielding point of the first linear part as shown in Figure 2.6. Calculation methods of elastic strain ε_{el} , superelastic/reversible strain ε_{se} and irreversible (e.g. irrecoverable) strain

ε_{irr} are also presented in Figure 2.6. The mathematical summation of ε_{se} and ε_{el} strains result in reversible strain ε_{rev} where the summation of ε_{rev} and ε_{irr} strains give the total applied strain.

3. $Ni_{45.3}Ti_{29.7}Hf2_{20}Pd_5$ POLYCRYSTALLINE SHAPE MEMORY ALLOYS

3.1. Introduction

The purpose of this chapter is to investigate the shape memory properties of a quaternary $Ni_{45.3}Ti_{29.7}Hf_{20}Pd_5$ (at. %) polycrystalline alloys in compression after selected heat treatments. The effects of aging temperature and time on the TTs, microstructure, work output, and damping capacities were determined by conducting a series of systematic experiments on an extruded $Ni_{45.3}Ti_{29.7}Hf_{20}Pd_5$ polycrystalline alloy. Additionally, the effects of superelastic cycling on the stress-strain and strain-temperature responses of the polycrystalline shape memory alloy were revealed.

3.2. Effects of aging on the microstructure of polycrystalline $Ni_{45.3}Ti_{29.7}Hf_{20}Pd_5$ shape memory alloys

In this section the microstructure characteristics of a quaternary $Ni_{45.3}Ti_{29.7}Hf_{20}Pd_5$ polycrystalline alloy were investigated after selected aging conditions. In order to investigate the effect of aging on the microstructure, TEM observation was conducted at RT in as-extruded and aged conditions. The as-extruded and 400 ^{o}C-3 hours aged specimens consist of a single B2 austenite phase without any detectable precipitates by conventional TEM, as shown in Figure 3.1. On the other hand, spindle-shaped precipitates were clearly observed in the 550 ^{o}C-3 hours and 650 ^{o}C-3 hours aged specimens.

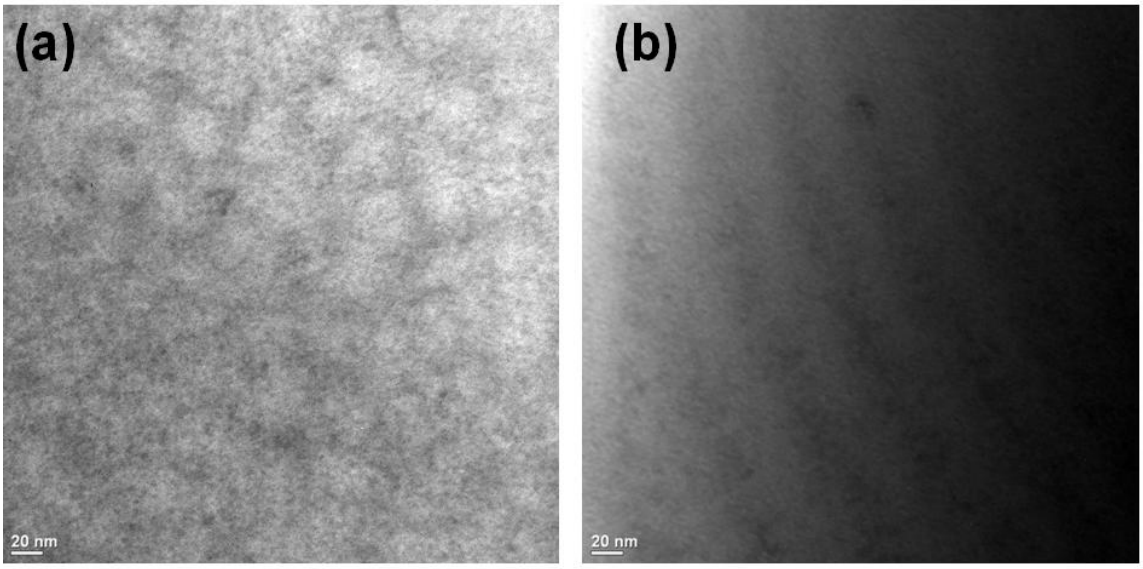

Figure 3.1: TEM images of a) as-extruded and b) 400 ^{o}C-3 hours aged $Ni_{45.3}Ti_{29.7}Hf_{20}Pd_5$ polycrystalline samples

Figure 3.2a shows the bright field image of the 550 ^{o}C-3 hours aged sample, where the inset is the magnified image of the area B. The selected area diffraction (SAD) pattern taken from the area B is shown in Figure 3.2b. Fine precipitates with the sizes of about 20-30 nm in length with the interparticle distance of about 10-30 nm were formed after 550 ^{o}C-3 hours aging. The B19′ martensite phase was observed between the precipitates. According to the SAD pattern, the fine striations which can be seen inside the martensite phase were determined as $(001)_{B19'}$ compound twins. The volume fraction of the precipitates increased with increasing the aging temperature from 550 ^{o}C to 650 ^{o}C.

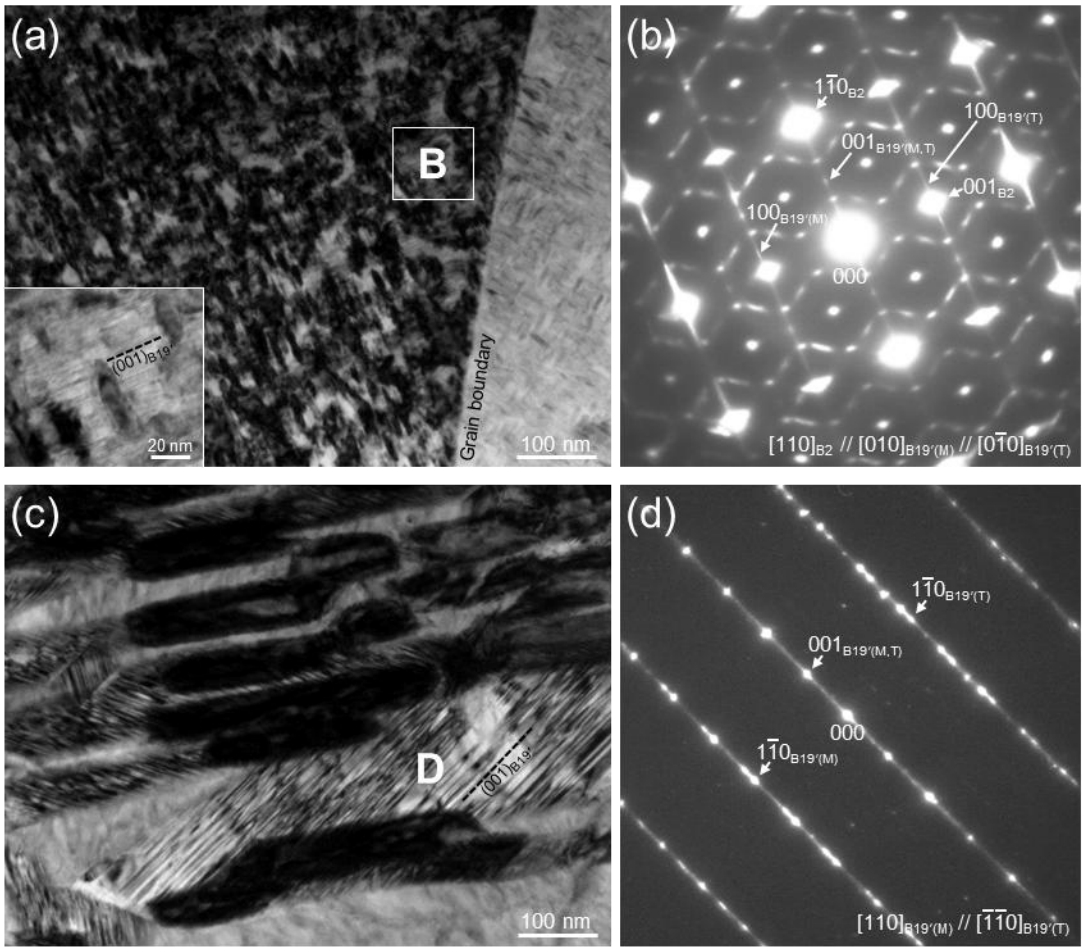

Figure 3.2: a) Bright field image and b) SAD pattern taken from area B of the 550 ^{o}C-3 hours aged specimen. Insert in (a) is the enlargement of area B. c) Bright field image and (d) SAD pattern taken from area D of the 650 ^{o}C-3 hours aged specimen. Subscripts M and T in the SAD patterns indicate matrix and twin, respectively.

Figure 3.2c shows the bright field image of the 650 ^{o}C-3 hours aged specimen. It is clear that the precipitates were quite large when compared with the 550 ^{o}C-3 hours aged specimen where their length varies from about 80 nm to 300 nm and their width is about 50 nm. Their interparticle distance varied from 15 nm to 150 nm. The $(001)_{B19'}$ compound twins were also observed in the 650 ^{o}C-3 hours aged specimen, which can be

confirmed by the SAD pattern shown in Figure 3.2d (taken from the area D in Figure 3.2c), indicating that the main twinning mode observed in the martensite phase was not affected by the aging temperature. The $(001)_{B19'}$ compound twins have been reported in NiTiHf alloys as the main substructure of martensite [48, 53, 54], although the $(001)_{B19'}$ compound twinning cannot be a lattice invariant shear alone according to the phenomenological crystallographic theory [2].

3.3. DSC heat flow curves of $Ni_{45.3}Ti_{29.7}Hf_{20}Pd_5$ alloys

To investigate the effects of aging on TTs at zero stress, DSC tests were conducted after 3 and 5 hours of aging at temperatures ranging from 400 to 900 °C by my previous colleague Gurdish S. Ded. The DSC curves are shown in Figure 3.3. For each DSC cycle, the endothermic peaks at higher temperatures represent the martensite to austenite transformation upon heating and the exothermic peaks at lower temperatures represent the austenite to martensite transformation upon cooling. For most of the aging conditions, three to five thermal cycles were completed to verify the stability of the TTs. Results from the as-extruded material are also included in Figure 3.3 as a baseline to compare the effect of aging time and temperature on TTs and stability of the samples.

Figure 3.3a shows the DSC response of the $Ni_{45.3}Ti_{29.7}Hf_{20}Pd_5$ after aging at selected temperatures between 400 ^{o}C and 900 ^{o}C for an aging period of 3 hours. It is evident that TTs change drastically with aging temperature. Initially, TTs decreased after aging at 400 and 450 ^{o}C, then, TTs monotonically increased with aging temperature between 500 and 600 ^{o}C. For aging temperatures above 600 ^{o}C, the TTs once again started to decrease.

Figure 3.3b shows the change in TTs for $Ni_{45.3}Ti_{29.7}Hf_{20}Pd_5$ polycrystalline specimens aged for 5 hours at temperatures between 400 ^{o}C and 600 ^{o}C. The trend in TTs with aging temperature was similar to that of the 3 hours aged conditions. For aging treatments at 400 ^{o}C and 450 ^{o}C, TTs were very low and remained beyond the cooling limit (-150 ^{o}C) of the DSC setup. Between 500 and 600 ^{o}C, TTs increased with increasing aging temperature. For a given aging temperature between 500 and 600 ^{o}C, the TTs were higher when the samples were aged for 5 hours compared to aging for 3 hours and the heat flow curves displayed better cyclic stability. The maximum A_f was 170 ^{o}C and M_s was 110 ^{o}C for material aged for 5 hours at 600 ^{o}C.

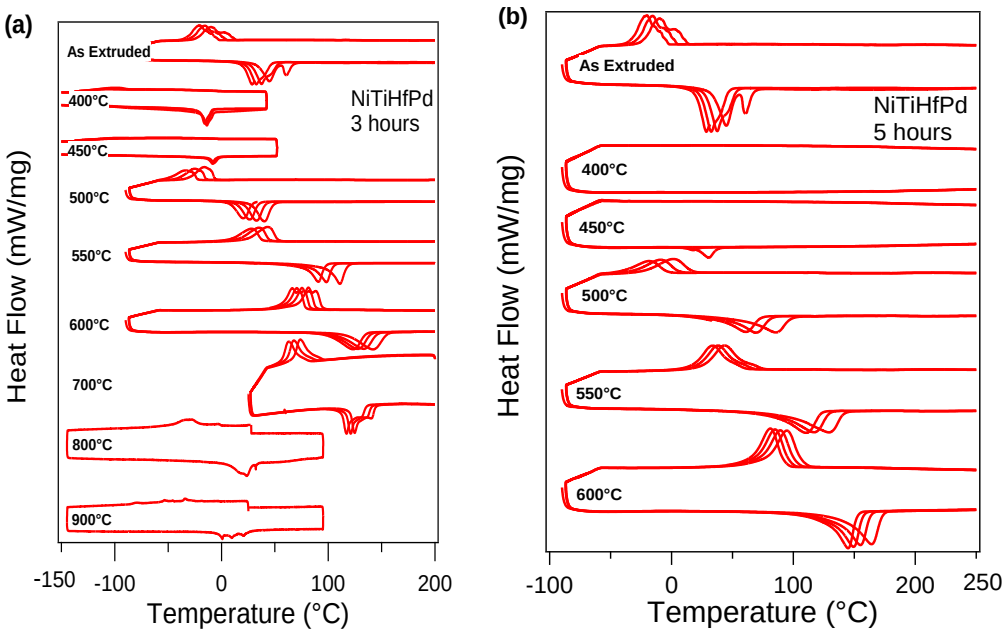

Figure 3.3: DSC responses for the $Ni_{45.3}Ti_{29.7}Hf_{20}Pd_5$ alloy after a) 3 hours and b) 5 hours aging as a function of aging temperature

Changes in the stress-free TTs with aging temperature and time have been determined from the DSC results presented in Figure 3.3 and the data is summarized in Figure 3.4. An initial decrease in TTs with aging temperature was observed for both 3 and 5 hour aging times reaching a minimum at aging temperature of about 400 °C. Between 400 to 600 °C the TTs increased with increasing aging temperature, reaching a maximum at about 600 °C, decreasing once again with any further increase in aging temperature. For 3 hours aging time, A_f reached a maximum of 150 ^oC following aging at 600 ^oC. Increasing the aging time from 3 to 5 hours at 600 ^oC resulted in an additional 20 ^oC increase in A_f to 170 ^oC. In contrast, aging at 400 ^oC and 450 ^oC for 5 hours, suppressed the TTs below the cooling limit of the DSC setup, resulting in over a 320 ^oC range in TTs due to aging.

The initial drop in TTs was attributed to the formation of precipitates with very small size and short interparticle distance. Thus, the resistance for martensite nucleation increased and formation of martensite required additional energy change, which in turn required further undercooling in the course of the forward transformation [55].

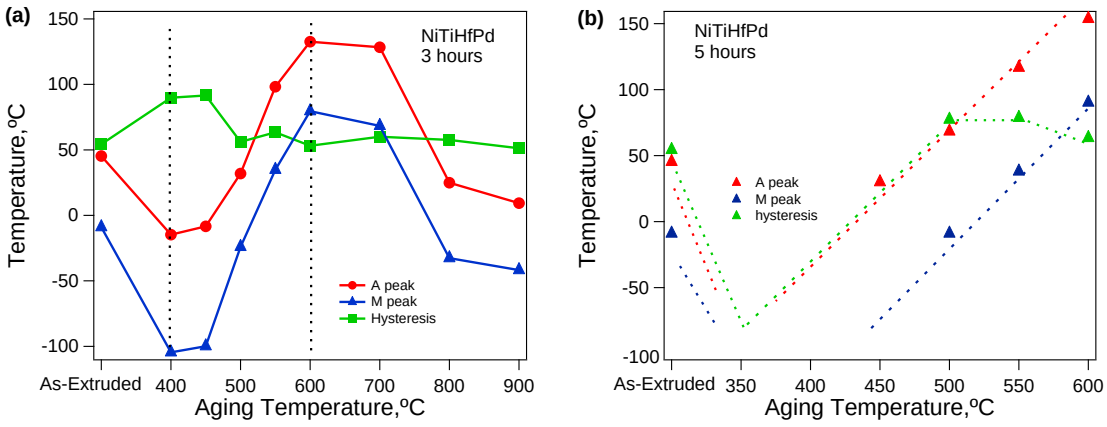

Figure 3.4: TTs change in the $Ni_{45.3}Ti_{29.7}Hf_{20}Pd_5$ alloy after a) 3 hours and b) 5 hours

The underlying reason for the increase in TTs after the initial decline could be an increase in the volume fraction of the precipitates, resulting in a change in composition of the remaining matrix material. It is well known that TTs are highly composition dependent in NiTi based SMAs [2]. In Ni-rich NiTi based alloys, TTs increase by formation of Ni-rich precipitates as in NiTi [6-9], NiTiPt [56], NiTiPd [57] and NiTiHf [58] alloys, while precipitation of Ti rich phases can potentially result in a decrease in TTs as has been reported in NiTiPd alloys [44]. Consequently, as the chemical composition of matrix changes during precipitate coarsening, the TTs are altered [2, 44]. The coherency of the formed precipitates in the microstructure is another factor that can affect the TTs. The mismatch between matrix and precipitate lattice parameters may cause internal stresses around precipitates that can also change (e.g. increase) the TTs [59].

The second drop in TTs was attributed both to a reduction in precipitate volume fraction and lose of coherency as the aging temperature increases and either approaches or surpasses the precipitate solvus temperature. Once again resulting in a Ni-rich matrix or decrease in the internal stress due to non-coherent precipitates and thus, decrease in TTs. It is important to note that TTs of the $Ni_{45.3}Ti_{29.7}Hf_{20}Pd_5$ alloy can be adjusted from -150 ^{o}C to 150 ^{o}C through simple heat treatments. Hence, the TTs of $Ni_{45.3}Ti_{29.7}Hf_{20}Pd_5$ alloys can easily be tailored by controlling aging time and temperature, which could be beneficial in designing of practical applications.

Figure 3.5 shows the thermal cycling experiments under zero stress of $Ni_{45.3}Ti_{29.7}Hf_{20}Pd_5$ shape memory alloys in the as-extruded and 650 ^{o}C for 3 hours aged conditions. For both specimens, 20 thermal cycles were conducted to see the variation of TTs upon repeated phase transformations in the absence of stress.

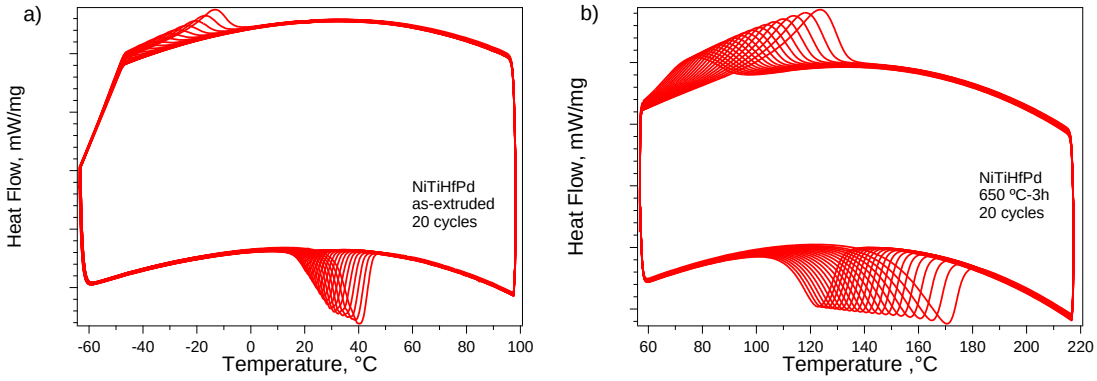

Figure 3.5: DSC thermal cycling responses of $Ni_{45.3}Ti_{29.7}Hf_{20}Pd_5$ in as-extruded and aged at 650 ^{o}C for 3 hours

It was observed that TTs were decreased upon thermal cycling in both the as-extruded specimen and the specimen aged at 650 ^{o}C for 3 hours. Another observation was that variations (e.g. decrease) of TTs were more visible in the aged specimen compared to the as-extruded specimen. M_s temperature was decreased by 20 ^{o}C in the as-extruded specimen while it was decreased by 50 ^{o}C in the aged specimen after 20 cycles.

The reason of the decrease in TTs upon thermal cycling in the both specimens was predicted to be dislocation generation at the interfaces of austenite and martensite upon reversible phase transformations. When the dislocations were generated, they acted as obstacles for phase transformation to martensite in the microstructure and lowered TTs as in NiTi alloys [60]. On the other hand, the better stability (e.g. less variation of TTs

upon cycling) of the as-extruded specimen can be a result of possibly smaller precipitates inherited from the manufacturing and slow cooling processes of the polycrystalline alloys. When the as-extruded material was aged at 650 ^{o}C for 3 hours, precipitates may get bigger and allow more spaces for dislocation generation and motion. Consequently, the higher density of dislocations may lower the TTs further upon cycling.

3.4. Work output and damping capacities of $Ni_{45.3}Ti_{29.7}Hf_{20}Pd_5$ polycrystalline shape memory alloys

One measure of the capacity of a solid-state actuator is its work output. As the work output of a material increases, the required weight or volume decreases, resulting in a more efficient system. There is an emerging need for actuators that produce high work output for applications in such industries as aerospace, biomedical, automotive, and down-hole energy exploration. For example, some actuation applications in civil or military aircrafts involve variable (area or geometry) inlets and nozzles that require up to 20 % shape change [61, 62]. Compared to existing hydraulic actuation systems in use, solid state actuators made out of SMAs may work more efficiently while occupying much less space, thus enabling certain aircraft designs. With suitable TTs, high work output SMAs may also be used in biomedical applications such as stronger stents for main arteries or certain implants.

In Figure 3.6, the maximum work output levels of various NiTi based SMAs are shown as a function of their typical operating temperature range. It was observed that $Ni_{45.3}Ti_{29.7}Hf_{20}Pd_5$ alloys can generate higher work outputs of 32-35 J/cm^3 (up to 120

^{o}C) compared to other NiTi based SMAs, though upper temperature capability was somewhat limited. NiTi alloys can generate work outputs more than 10-20 J/cm^3 [14], while Ni rich NiTiHf alloys can produce around 18-20 J/cm^3 [21]. $Ni_{45.3}Ti_{29.7}Hf_{20}Cu_5$ alloys can generate work outputs of around 14-15 J.cm^{-3} [51] while NiTiHfNb alloys [47] have work output levels of 17-18 J.cm^{-3} above 100 ^{o}C and 150 ^{o}C, respectively. Finally, NiTiPd and NiTiPt alloys can yield between 9-15 J/cm^3 at temperatures above 150 ^{o}C [15, 63].

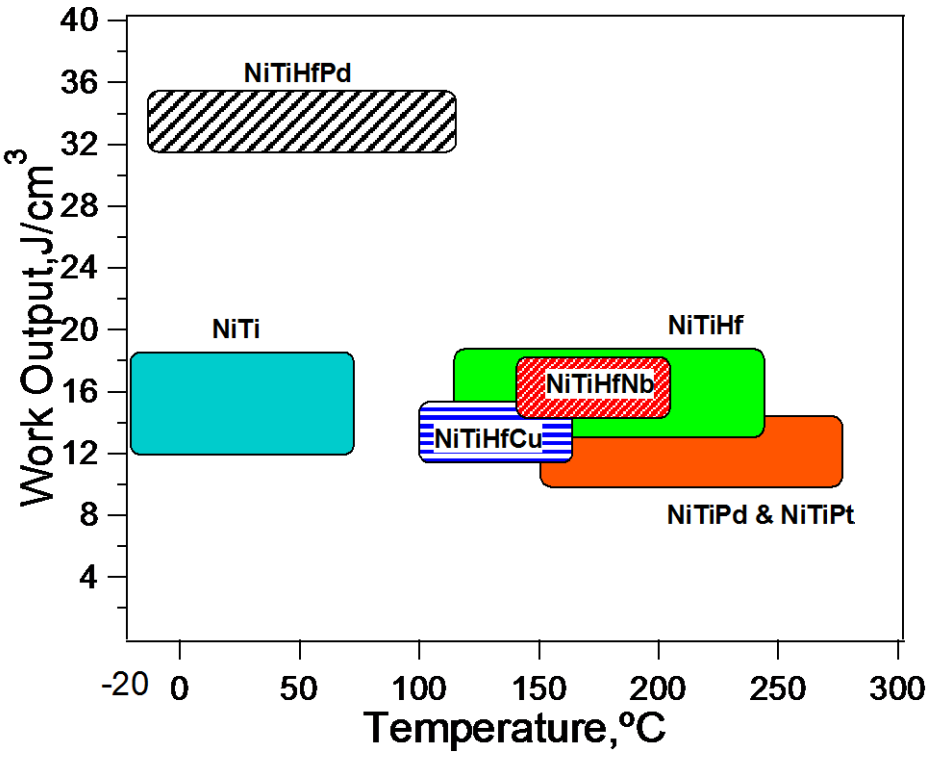

Figure 3.6: A comparison of work outputs for typical NiTi based SMAs.

Beside the high work output, $Ni_{45.3}Ti_{29.7}Hf_{20}Pd_5$ polycrystalline alloys have considerable damping/absorbed energy capacity, which in simple terms is the ability to repeatedly disperse unwanted energy from a system. Damping capacity is related to the

mechanical hysteresis and transformation strain and can be determined by calculating the area between the forward and reverse transformation curves in the superelastic stress-strain response, as depicted schematically in Figure 3.7a. High hysteresis and high transformation strain result in more energy dissipation from a system. Damping capacities of selected NiTi-based alloys are compared in Figure 3.7b as a function of operating stress levels (critical stress for forward transformation).

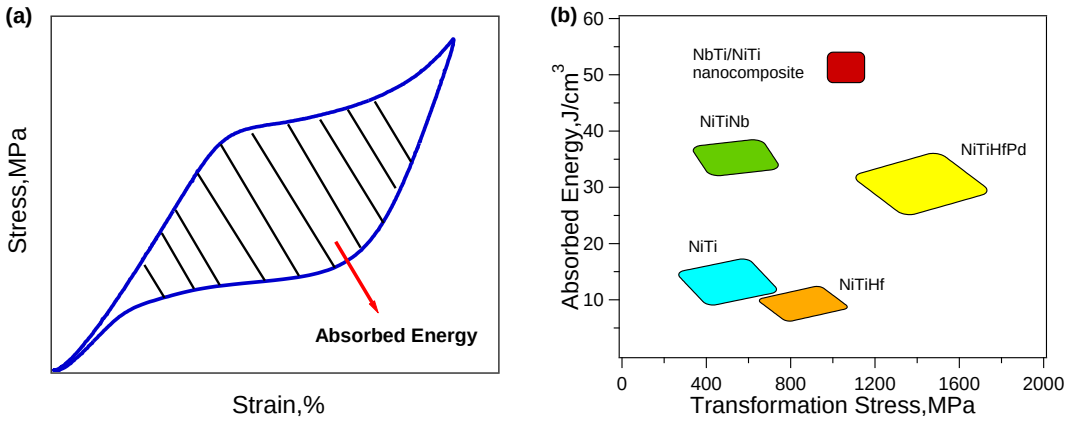

Figure 3.7: a) Calculation of the absorbed energy during a superelastic stress-strain cycle b) Damping capacity as a function transformation stress for various NiTi based SMAs.

The high damping capacity (30-34 $J.cm^{-3}$) of the present alloy stems from its outstanding mechanical hysteresis and good superelastic strain, approaching 4 %. In related systems, the damping capacity is 16 $J.cm^{-3}$, 18-20 $J.cm^{-3}$, 38 $J.cm^{-3}$, and 54 $J.cm^{-3}$ for NiTi, NiTiHf [21], polycrystalline NiTiNb alloys, and NbTi/NiTi nanocomposites, respectively [17-19]. The $Ni_{45.3}Ti_{29.7}Hf_{20}Pd_5$ alloy has similar capability to polycrystalline NiTiNb alloys that are often used in coupling applications, while both polycrystalline materials have damping capacity, which is less than new NbTi/NiTi nanocomposites.

However, it should be noted that $Ni_{45.3}Ti_{29.7}Hf_{20}Pd_5$ alloys have the ability to operate at much higher stresses (~2 GPa) than the NiTiNb and NbTi/NiTi systems.

In addition to damping applications, dissipation mechanisms due to the martensitic transformation allows SMAs to be used in applications that require wear resistance [64]. In particular, properties such as high strength, high hardness, corrosion resistance, and the ability to be used with conventional lubricants [65] combined with this superb damping capacity and wear resistance, open these types of materials to many tribological and wear resistant applications including bearings and gears [66].

3.5. High temperature mechanical cycling and thermal cycling under high stress responses of $Ni_{45.3}Ti_{29.7}Hf_{20}Pd_5$

For practical applications, the stability of shape memory behavior during thermal [60] and mechanical cycling [67] is crucial since SMAs are usually operated under cycling forces and temperatures [68]. It should be noted that, it is inevitable to avoid irreversible processes (e.g. defect generation, energy dissipation) during cyclic reversible martensitic phase transformations [60, 67, 69] that can result in degradation of the shape memory behaviors [67]. However, the extent of irreversible processes can be limited by increased resistance for slip using various techniques such as precipitation hardening, composition alteration and cold work [60, 70]. Hence, many studies have been conducted to understand the effects of thermal and mechanical cycling on the shape memory properties of NiTi to date [12, 40, 67, 69]. In general, it has been reported that transformation temperatures decrease with thermal cycling [50, 60, 71]. After SE cycling,

decrease in critical transformation stress levels and mechanical hysteresis and increase in hardening and residual strains were observed [67, 69].

In this study, the effects of superelastic cycling on both stress-strain responses and strain-temperature responses in polycrystalline $Ni_{45.3}Ti_{29.7}Hf_{20}Pd_5$ shape memory alloys aged at 550 ^oC for 5 hours are systematically investigated. The constant stress shape memory responses were recorded initially under stress levels ranging from 300 MPa to 1200 MPa followed by 5000 superelastic cycles at 160 ^oC. After the superelastic cycling tests, another set of constant stress thermal cycling experiments were conducted under same levels of stresses applied initially. Consequently, the effects of SE cycling on the stress-strain and strain-temperature responses were revealed in $Ni_{45.3}Ti_{29.7}Hf_{20}Pd_5$ polycrystalline shape memory alloys.

Figure 3.8 shows the shape memory responses of $Ni_{45.3}Ti_{29.7}Hf_{20}Pd_5$ alloy aged at 550 ^oC for 5 hours before and after the superelastic cycling experiments. Compressive stresses ranging 300 MPa and 1200 MPa were applied above A_f temperatures and specimens were cooled down below M_f temperature followed by heating back above A_f under the applied load. Before SE cycling, M_s was measured to be 98 ^oC and 154 ^oC under 300 MPa and 1200 MPa, respectively. Shape memory strains were 0.95 % and 1.9 % under 300 MPa and 1200 MPa, respectively. The irrecoverable strain was measured to be 0.25 % under 1200 MPa before the SE cycling. In the constant stress shape memory experiments conducted after the SE cycling, M_s was determined to be 58 ^oC and 125 ^oC under 300 MPa and 1200 MPa, respectively. Shape memory strains are 0.7 % and 1.6 % under 300 MPa and 1200 MPa, respectively. No irrecoverable strain was observed under 1200 MPa after the SE cycling as shown in Figure 3.8. The recovery in the plastic strain

after the SE cycling can be a result of work hardening upon SE cycling. Due to generated/re-arranged defects, further generation of dislocations can be impeded leading to diminish in the plastic strain after the SE cycling. It was truly remarkable that the $Ni_{45.3}Ti_{29.7}Hf_{20}Pd_5$ alloy can recover ~2 % strain against very high compressive stress level of 1200 MPa with no irrecoverable strain at high temperatures (>100 ^{o}C) after SE cycling. High strength at elevated temperatures has been always a desired feature in metallic materials due to the fact that the critical stress for plastic deformation tends to decrease with increasing temperature in general. Thus, this ability could give a unique potential to this alloy to be used in actuator applications that requires high strength at elevated temperatutes.

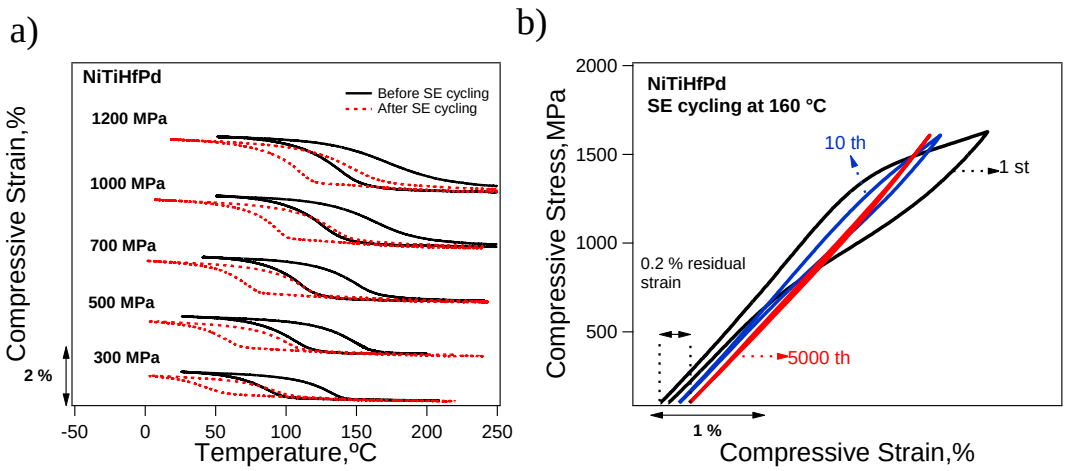

Figure 3.8: a) The compressive strain vs. temperature responses before and after the superelastic cycling and **b)** Superelastic cyclic responses of $Ni_{45.3}Ti_{29.7}Hf_{20}Pd_5$ alloy aged at 550 ^{o}C for 5 h at various cycle numbers

Superelastic cyclic responses of the $Ni_{45.3}Ti_{29.7}Hf_{20}Pd_5$ polycrystalline alloy after the initial thermal cycling experiments is presented in Figure 3.8b. The $Ni_{45.3}Ti_{29.7}Hf_{20}Pd_5$ polycrystalline alloy was mechanically cycled 5000 times at 160 ^{o}C under compressive

stresses ranging 50 MPa and 1600 MPa (nearly 3 % strain). Loading and unloading of the specimen was carried under force control in the mechanical test frame. The 1st, 10^{th} and 5000th cycles are shown in Figure 3.8b to observe the effect of 5000 cycles in the stress-strain responses. In Figure 3.8b, residual strain can be defined as the devitaion of the starting point of a SE cycle compared to the initial point of the first SE cyle. After 5000 SE cycles, 0.2 % residual strain was observed.

It was clear that the transformation stress levels, slopes of the transformation and stress hystereses were effected after the first cycle. It was also observed that the changes occured more rapidly at the initial SE cycles due to easier generation/re-arrangement of defects. With additional cycles, the changes in the superelastic cycles were not pronounced since the defect generation/re-arrangement became more difficult due to already existed defects. These observations were in good agreement with the superelastic cyclic results of NiTi polycrystalline alloys reported earlier in the literature [67, 69, 72].

In Figure 3.8b, transformation stress levels were tailored with increased superelastic cycles. It is known that defects are generated or re-arranged upon each superelatic cycling near precipitates in the microstructure and they are accumulated until reaching a saturation point [67]. Those defects may act as obstacles for the back transformation from martensite to austenite at some local areas in the microstructure and hence, some martensite plates may retain in the microstructure without transforming [73]. Furthermore, those defects may generate internal stress and provide easy nucleation sites for martensite formation in the next superelastic cycle. However, it was not always certainly answerable what type of defects were in charge for the change in the superelastic cycles.

A notable feature observed in the stress-strain responses upon SE cycling was the increased hardening during transformation. The increase in hardening can be connected to the residual stress and pinning effect of dislocations generated upon stress cycling. After each SE cycle, the growth of martensite was more difficult due to higher density of defects in the microstructure. These facts were displayed as the increased transformation slope/hardening of the stress-strain responses in the Figure 3.8b.

Stress hysteresis was also influenced after each SE cycle. Since the generated defects resisted the growth of martensite, they formed back stresses opposite to the applied external stress. When the applied stress was removed, the back stresses accumulated may effect the backward transformation and consequently the stress hysteresis. Also, energy dissiptaion is known to be strongly linked to martensite morphology in shape memory alloys [24]. Thermodynamically, wider and larger martensite plates will cause more energy dissipation compared to thin plates due to stored energy loss [24]. The generation and/or re-arrangement of defects upon SE cycling may change the martensite morphology by limiting the growth of martensite plates in the microstructure and consequently, the energy dissipation may be tailored after SE cycling resulting less stress hysteresis [74]. Moreover, it should be noted that the $Ni_{45.3}Ti_{29.7}Hf_{20}Pd_5$ alloy has very promising SE cyclic response at high temperatures (160 ^{o}C) even when very high stress of 1600 MPa was reached. This is a very unique property that can be very useful for high temperature and high strength SMA applications exposed to cycling forces.

In Figure 3.9a, linear dependence of the transformation temperatures (e.g. M_s) is shown as a function of applied stress in thermal cycling experiments before and after the SE cycling. It was clear that both M_s and A_s decreased after SE cycling.

The linear dependence can be explained by the Clausius-Clapeyron (C-C) relationship which is [75]

$$\frac{\Delta\sigma}{\Delta T} = -\frac{\Delta H}{T_o\,\varepsilon_{tr}} \qquad (2)$$

where $\Delta\sigma$ is the difference between critical stresses, ΔT is the temperature difference, ΔH is the change in transformation enthalpy, T_o is the equilibrium temperature and ε_{tr} is the transformation strain. The C-C slope was determined to be 17.6 MPa/^{o}C before the SE cycling while it decreased to 13.7 MPa/^{o}C after the SE cycling.

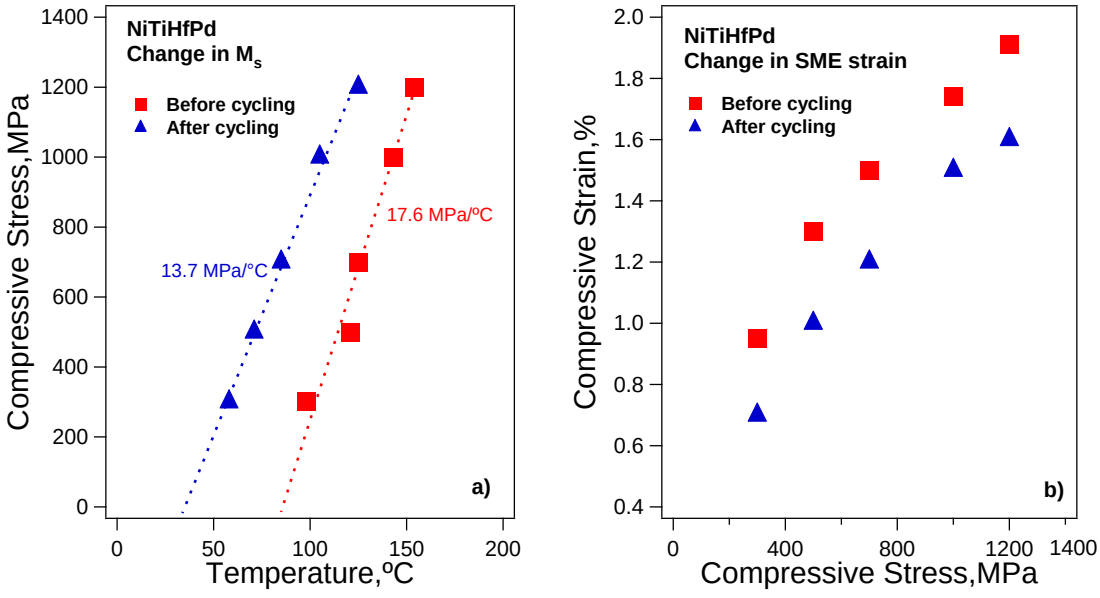

Figure 3.9: Effects of superelastic cycling on a) martensite start temperature and b) shape memory strain as a function of applied stress in $Ni_{45.3}Ti_{29.7}Hf_{20}Pd_5$ alloy

M_s was decreased by 40 ^oC under 300 MPa and 29 ^oC under 1200 MPa after the SE cyclic tests as shown in Figure 3.9a. The decrease of M_s can be attributed to hardening effect of generated dislocations upon SE cycling. The generated and/or re-arranged defects may hinder the martensitic transformation, thus futher undercooling, ΔT, was required. Thereby, M_s decreased further below the thermodynamic equilibrium temperature T_o [76],

$$M_s = T_o - \Delta T \tag{3}$$

The decrease in Ms has also been reported for NiTi based and Fe based shape memory alloys by many researchers after stress free thermal cycling experiments due to pinning effect of dislocations [50, 60, 71, 77].

Figure 3.9b presents the shape memory strains as a function of applied stress in the thermal cycling experiments before and after the SE cycling. Transformation strains also slightly decreased after the SE cyclic experiments in $Ni_{45.3}Ti_{29.7}Hf_{20}Pd_5$ polycrystalline alloys as shown in Figure 3.9b. It decreased by 0.25 % under 1200 MPa after the SE cyclic test. It was truly remarkable that up to 2 % shape memory strain with negligible irrecoverable strain was observed under high stress levels of 1200 MPa in polycrystalline $Ni_{45.3}Ti_{29.7}Hf_{20}Pd_5$ after SE cycling.

The decrease in transformation strain can be attributed to the suppression of martensite formation in some local regions with high defect density and retained martensite upon cycling. Due to interactions of growing martensite plates with precipitates and generated/re-arranged defect networks upon high number of SE cycles, some local regions may be slipped and transformation may not occur [78, 79]. Another

possible reason can be the limited detwinning process due to internal stress fields due to the defect pile-ups. Since the detwinning process may be blocked in some local regions, total transformation strain may decrease. It has been revealed that when there is strong internal stress in the microstructure due to constraints (e.g. precipitates), detwinning process is suppressed and less transformation strain is obtained as observed in $Ni_{50.375}Ti_{49.625}$ single crystals [80].

3.6. Summary and conclusions

Based on the results presented in this chapter, following conclusions can be deducted for the $Ni_{45.3}Ti_{29.7}Hf_{20}Pd_5$ (at %) polycrystalline shape memory alloys;

1. As-extruded and 400 ^{o}C-3h aged samples did not have any precipitates that were detectable with conventional TEM. Precipitates with sizes about 20-30 nm in length and interparticle distance of approximately 10-30 nm were formed after 550 ^{o}C-3 hours aging. The length of the precipitates varied from 80 nm to 300 nm with a width of about 50 nm and interparticle distances of 15 nm to 150 nm as the aging temperature was increased to 650 ^{o}C. $(001)_{B19'}$ compound twins were observed in all samples regardless of thermal treatment.

2. Shape memory properties (e.g. transformation temperatures) of the $Ni_{45.3}Ti_{29.7}Hf_{20}Pd_5$ alloys can easily be tailored by controlling aging temperature and time. TTs can be adjusted between –100 ^{o}C and 100 ^{o}C by simple heat treatments.

3. $Ni_{45.3}Ti_{29.7}Hf_{20}Pd_5$ alloy exhibits a fairly high, 30-34 J.cm^{-3}, damping capacity and a very high work output (30-35 J.cm^{-3}) capability at temperatures between 0 and 100 ^{o}C, especially in the as-extruded condition.

4. It was observed that $Ni_{45.3}Ti_{29.7}Hf_{20}Pd_5$ polycrystalline alloys can show very promising superelastic cyclic responses at high temperatures (160 ^oC) under high stress levels of 1600 MPa without any visible irrecoverable strains even after 5000 cycles.

5. Critical stress, slope and mechanical hysteresis were effected upon superelastic cycling.M_s was decreased by 30-40 ^oC in constant stress shape memory curves while shape memory strain and plastic strain were decreased by 0.25 % after SE cycling which can be both attributed to the defect generation/re-arrangement during the reversible thermo-elastic phase transformations.

4. EFFECTS OF CHEMICAL COMPOSITION ON THERMO-MECHANICAL RESPONSE OF NiTiHfPd ALLOYS

4.1. Introduction

The potential and current application areas of NiTi alloys include electronic devices, medical tools and home appliances [81]. However, NiTi alloys may have also restrictions to be utilized in specific areas since each application requires distinctive functional properties. For instance, low hysteresis can be very useful for actuator applications [82] while large hysteresis is desired for coupling [83] and damping applications [18]. Also, low TTs (near body temperature) might be suitable for biomedical applications [84] while high TTs (>100 ^{o}C) is essential for an SMA to be used in an aircraft or automobile engines [3]. Hence, NiTi based SMAs have been developed to meet the industrial needs besides benefiting from the excellent properties of NiTi. Alloying and composition alteration are known to be utmost effective for the controlling crucial shape memory properties (e.g. transformation strain, thermal and mechanical hysteresis, lattice parameters, TTs) [2].

The addition of Hf to NiTi can increase the TTs to several hundred degrees Celsius [3]. However, there are also several disadvantages to (Ti+Hf)-rich NiTiHf alloys such as a large thermal hysteresis, poor thermal stability, in addition to poor ductility and no evidence of superelasticity [23], which seriously limits their potential for practical applications. However, Bigelow et al. [85] has demonstrated that these limitations can be

overcome by working on the Ni-rich side of stoichiometry by developing a precipitation strengthened alloy.

As a ternary alloying addition, Cu (replacing Ni) was found to cause two step phase transformations (B2-B19-B19') in NiTiCu alloys with Cu contents from 5 at. % to 15 at. %. In the alloys of exceeding 15 % Cu content, single step phase transformation is observed from B2 to B19 phase [86]. Cu addition is also effective in shrinking hysteresis in NiTi alloys. In binary $Ni_{49.8}Ti_{50.2}$ (at %) alloys, hysteresis is more than 40 K [87] while it decreases to 11 K in NiTi-10Cu (at %) alloy [88]. In contrast to Cu, Nb addition can widen the thermal hysteresis in NiTi alloys to more than 130 K [89]. Chemical alloying is also effective on the mechanical hysteresis of NiTi alloys. The mechanical hysteresis is more than 200 MPa in $Ni_{50.2}Ti_{49.8}$ (at %) while it is less than 100 MPa and about 300 MPa in $Ti_{50}Ni_{40}Cu_{10}$ (at %) and $Ti_{48}Ni_{50}Nb_2$ (at %) alloys, respectively [90]. Lattice parameters are also functions of alloying additions such as in $Ni_{49.5}Ti_{50.5-x}Zr_x$ alloys. It was found that the lattice parameters a and c increased with the monoclinic angle β and lattice volume while the parameter of b decreased in martensite lattice with increased Zr content [91].

Previously, shape memory properties of $Ni_{45.3}Ti_{29.7}Hf_{20}Pd_5$ (at.%) were in investigated as functions of aging temperature and time in polycrystalline [92] conditions. The aged polycrystalline alloy was capable of recoverable shape memory strain up to ~4 % under 1000 MPa and had work output of 30-35 $J.cm^{-3}$ and damping capacity of 30-34 $J.cm^{-3}$ in the as-extruded condition. This chapter investigates the efffects of chemical composition change (replacing Ti with Hf) on the shape memory behavior (including two-way shape memory effect) and superelastic responses of as-grown $Ni_{45.3}$Ti-

$_{39.7}Hf_{20}Pd_5$, $Ni_{45.3}Ti_{34.7}Hf_{15}Pd_5$ and $Ni_{45.3}Ti_{29.7}Hf_{20}Pd_5$ polycrystalline shape memory alloys. The NiTiHfPd alloys used in this study were homogenized at 900 ^oC for 72 hours in vacuum followed by a furnace cooling process. Microstructure of the $Ni_{45.3}Ti_{34.7}Hf_{15}Pd_5$ alloy was revealed by transmission electron microscopy and effects of composition on the lattice parameters of the transforming phases and martensite morphology were discussed. For brevity, $Ni_{45.3}Ti_{39.7}Hf_{10}Pd_5$, $Ni_{45.3}Ti_{34.7}Hf_{15}Pd_5$ and $Ni_{45.3}Ti_{29.7}Hf_{20}Pd_5$ alloys will be called as NiTiPd-10Hf, NiTiPd-15Hf and NiTiPd-20Hf throughout the section.

Table 1 shows the TTs under stress-free conditions in NiTiPd-10Hf, NiTiPd-15Hf and NiTiPd-20Hf alloys, extracted from DSC measurements. M_s temperatures are -40, 35 and 75 ^oC for the NiTiPd-10Hf, NiTiPd-15Hf and NiTiPd-20Hf alloys. It is clear that TTs increased as a function of Hf content.

Table 1: TTs of NiTiPd-10Hf, NiTiPd-15Hf and NiTiPd-20Hf alloys obtained through DSC measurements

Material	**Martensite finish ,M_f (^oC)**	**Martensite start ,M_s (^oC)**	**Austenite start ,A_s (^oC)**	**Austenite finish ,A_f (^oC)**
NiTiPd-10Hf	-40	-4	1	45
NiTiPd-15Hf	35	50	63	106
NiTiPd-20Hf	75	110	102	150

4.2. Crystal and micro structure of NiTiPd-10Hf, NiTiPd-15Hf and NiTiPd-20Hf alloys

Figure 4.1 shows the X-ray diffraction patterns of NiTiPd-10Hf, NiTiPd-15Hf and NiTiPd-20Hf alloys at RT. All the alloys consist of two phases, B2 austenite and B19′ martensite at room temperature. The crystal structure of NiTiPd-10Hf austenite was B2 cubic with a= 0.3063 nm and the crystal structure of martensite is B19' monoclinic with lattice parameters of a=0.2985 nm, b= 0.4127 nm, c= 0.4732 nm and β= 99.3^{o}. For NiTiPd-15Hf, the crystal structure of the martensite was B19' with lattice parameters of a=0.3034 nm, b= 0.4109 nm, c=0.4805 nm and β= 100.9^{o} while the lattice parameter of B2 austenite phase was a=0.3085 nm. On the other hand, the NiTiPd-20Hf had a B19' martensite with lattice parameters of a= 0.3072 nm, b= 0.4128 nm, c= 0.4892 nm and β= 102.6° while the B2 austenite had a lattice parameter of a=0.3121 nm Thus, it can be concluded that as the Hf content increased, lattice parameters of the transforming phases also increased in the current alloys. The volume of the B2 cubic structure of the austenite was expanded by 2.09 % and 5.79 % as the Hf content was increased by from 10% to 15 % and to 20 %, respectively.

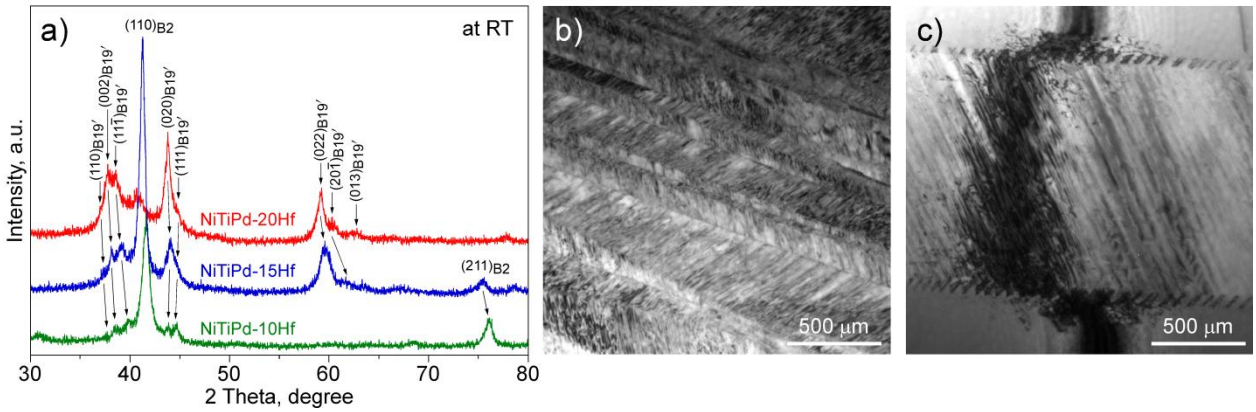

Figure 4.1: (a) X-ray diffraction patterns for the NiTiPd-10Hf, NiTiPd-15Hf and NiTiPd-20Hf alloys. Bright field TEM images of the (b) NiTiPd-15Hf alloy and (c) NiTiPd-10Hf alloy.

Figures 4.1b and c show the bright field TEM micrographs of the NiTiPd-15Hf and NiTiPd-10Hf alloys, respectively. The thickness of the martensite plates was lower in the NiTiPd-15Hf alloy than that in the NiTiPd-10Hf alloy. The internal twin of the NiTiPd-15Hf was found to be $(001)_{B19'}$ compound twin which has also been observed in the NiTiPd-20Hf [92]. On the other hand, the internal twin of the NiTiPd-10Hf alloy was confirmed to be $<011>_{B19'}$ type II twin. It is noted that the thickness of the $(001)_{B19'}$ compound twin was thinner than that of the $<011>_{B19'}$ type II twin and higher density of twins was observed in the NiTiPd-15Hf alloy.

4.3.The constant stress thermal cycling behavior of NiTiPd-10Hf

Figure 4.2 shows the constant stress shape memory response of the NiTiPd-10Hf alloy as a function of applied stress. Compressive stresses ranging from 25 MPa to 1000

MPa were applied above the austenite finish temperature and specimens were cooled down below the martensite finish temperature followed by heating back above A_f under the selected constant applied load. The martensite start temperature was approximately 2 ^oC and 104 ^oC under 25 MPa and 1000 MPa, respectively. No irrecoverable strain was observed up to stress level of 500 MPa while it was only 0.3 % at 600 MPa and 2.5% at 1000 MPa. The A_f temperature was approximately 80 ^oC and 180 ^oC under 25 MPa and 1000 MPa, respectively.

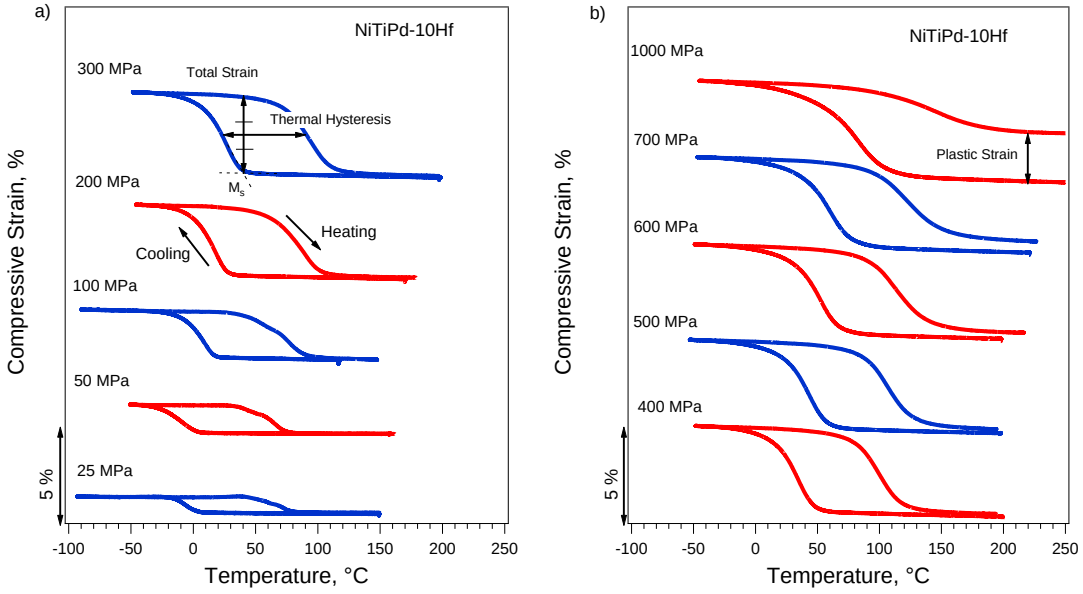

Figure 4.2: The constant stress thermal cycling response of the NiTiPd-10Hf alloy as a function of stress between a) 25 – 300 MPa and b) 400 – 1000 MPa.

4.4.The constant stress thermal cycling behavior of NiTiPd-15Hf

The constant stress shape memory responses of the NiTiPd-15Hf alloy as a function of stress are shown in Figure 4.3. Compressive stresses ranging from 25 MPa to 1000 MPa were applied in austenite and kept constant during the thermal cycling. No irrecoverable strain was observed up to a stress level of 400 MPa.

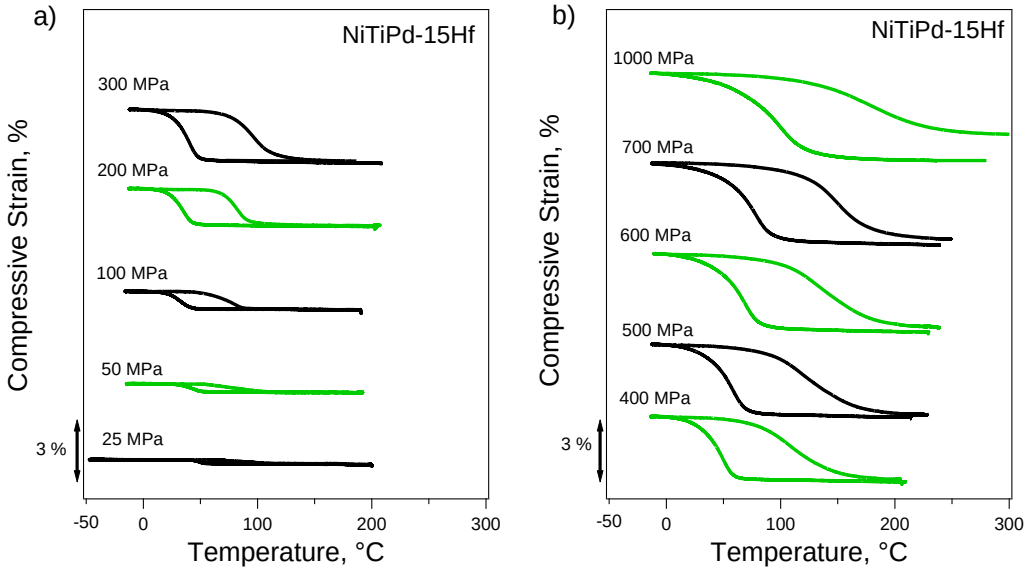

Figure 4.3: The constant stress thermal cycling response of the NiTiPd-15Hf alloy as a function of stress between 25 MPa – 1000 MPa.

4.5.The constant stress thermal cycling behavior of NiTiPd-20Hf

Figure 4.4 shows the shape memory responses of the NiTiPd-20Hf alloy as a function of compresive stress ranging from 25 MPa to 1000 MPa. It should be noted that irrecoverable strain was observed after 600 MPa.

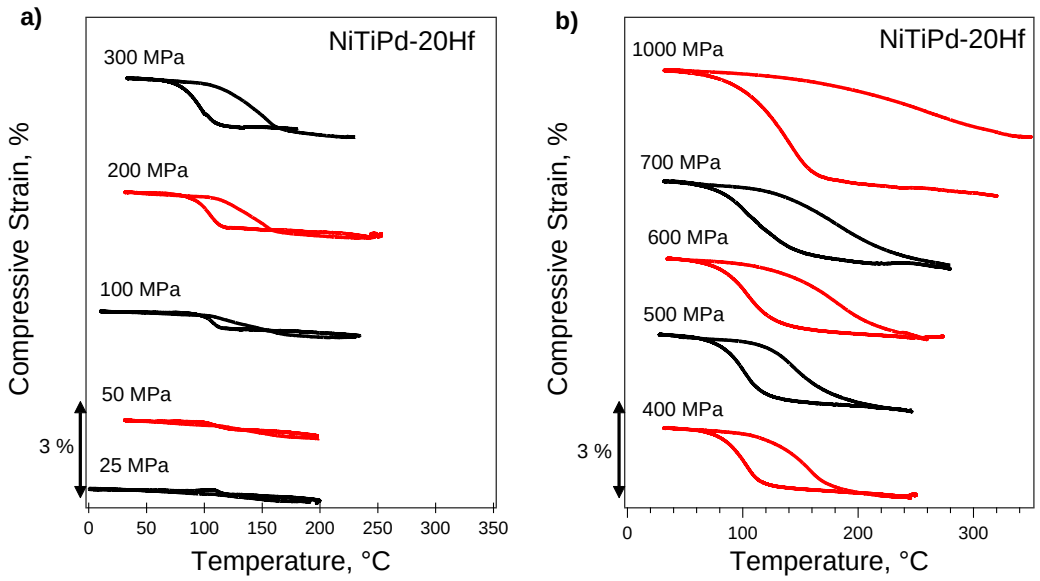

Figure 4.4: The constant stress thermal cycling response of the NiTiPd-20Hf alloy as a function of stress from 25 MPa – 1000 MPa.

4.6. Shape memory properties associated with the constant stress thermal cycling

Figure 4.5a shows the transformation strain values as functions of applied stress, extracted from the thermal cycling experiments shown in Figure 4.2, Figure 4.3 and Figure 4.4. Total strain was measured between the cooling and heating curves at M_s, as shown in Figure 4.2. As the applied stress increased, the total strain also increased and then saturated as the selection of preferred variants of martensite saturated at intermediate stress levels. Beyond the plateau, with further increase in stress, transformation strain started to decrease due to plastic deformation.

Transformation strain was calculated by subtracting the plastic strain from the total strain. For NiTiPd-10Hf, the transformation strains were 0.8 %, 4.6 %, and 5 % under 25 MPa, 500 MPa, and 1000 MPa, respectively. Transformation strains were 0.3

%, 3.5 %, and 3 % under 25 MPa, 500 MPa, and 1000 MPa, respectively, for NiTiPd-15Hf and 0 %, 2.2 %, and 2 % under 25 MPa, 500 MPa, and 1000 MPa, respectively, for NiTiPd-20Hf. It is clear that as the Hf content increased in the alloys, the transformation strains were decreased, which is in good aggrement with the previously reported data for NiTiHf alloys [93].

The change of transformation temperatures (e.g. M_s and A_f) with applied stress in the constant stress thermal cycling experiments (Figure 4.2, Figure 4.3 and Figure 4.4) are plotted in Figure 4.5b, 4.5c and 4.5d for the NiTiPd-10Hf, NiTiPd-15Hf and NiTiPd-20Hf, respectively. It was found that Classius-Clapeyron slopes were 8.5 MPa/^{o}C, 11.8 MPa/^{o}C and 15 MPa/^{o}C for M_s in the NiTiPd-10Hf , NiTiPd-15Hf and NiTiPd-20Hf alloys, respectively.The Clausius-Clapeyron relationship was formulated previously [75].

There is a good agreement with the C-C slopes and the transformation strain, ε_{tr} in the current alloys, based on the C-C equation. The C-C slopes were inversely proportional to the ε_{tr} values as expected.

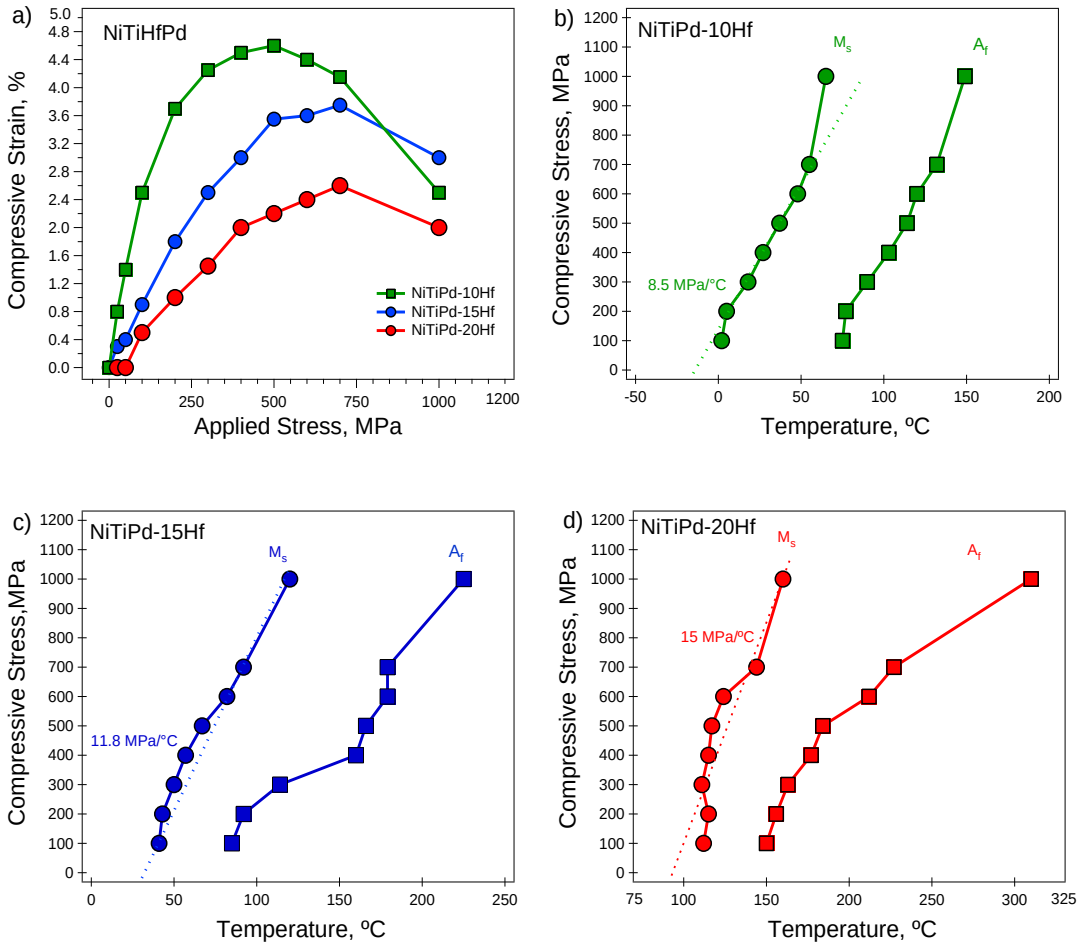

Figure 4.5: a) Transformation strain as a function of stress and b) C-C relationship in NiTiPd-10Hf, c) C-C relationship in NiTiPd-15Hf and d) C-C relationship in NiTiPd-20 alloys

Figure 4.6 shows the thermal hysteresis and irrecoverable strain values as a function of applied stress obtained from the constant stress thermal cycling tests. The irrecoverable strain was not observed up to 500 MPa, 400 MPa and 600 MPa in NiTiPd-10Hf, NiTiPd-15Hf and NiTiPd-20Hf alloys, respectively. As the stress was increased to 1000 MPa, irrecoverable strains of 2.5 % 1.3 % and 1.8 % were measured for NiTiPd-10Hf alloy, NiTiPd-15Hf and NiTiPd-20Hf alloys, respectively.

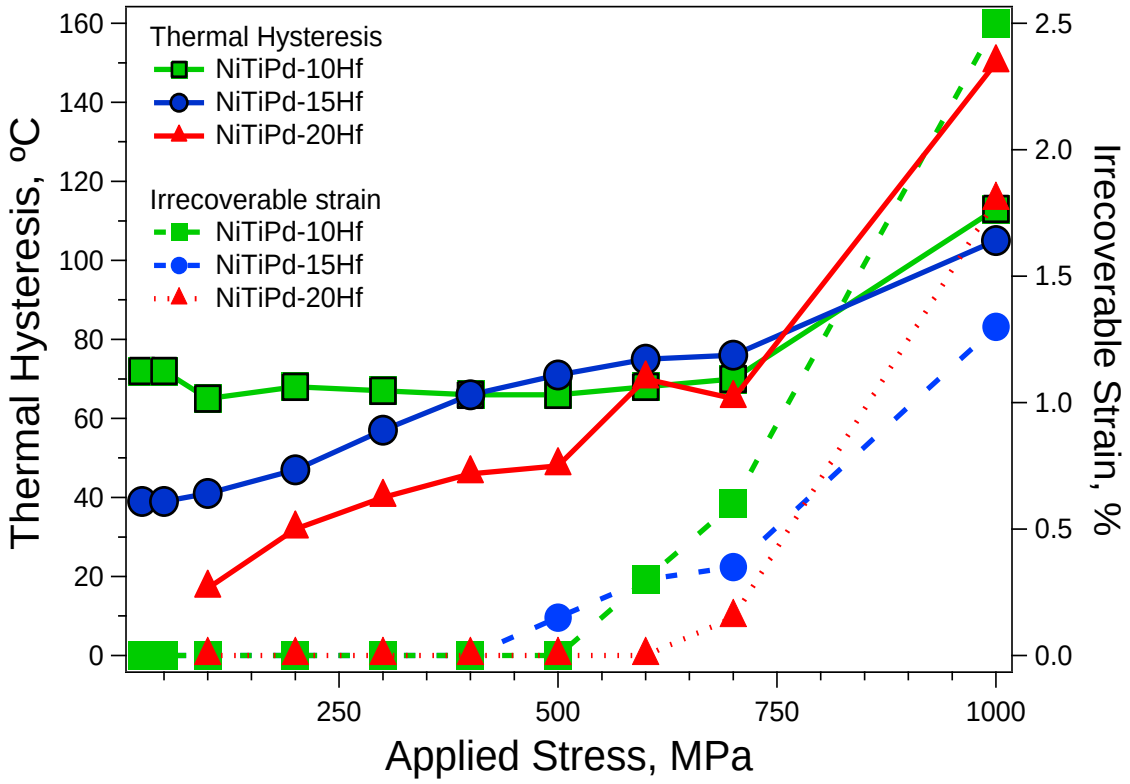

Figure 4.6: Thermal hysteresis and irrecoverable strain as functions of applied stress extracted from the load-biased thermal cycling tests of the NiTiPd-10Hf, NiTiPd-15Hf and NiTiPd-20Hf alloys

For the NiTiPd-10Hf, the temperature hysteresis was almost constant (66 ^{o}C) up to 500 MPa. This was followed by a slight (up to 700 MPa) followed by a dramatic increase in hysteresis to 113 ^{o}C as the applied stress was increased to 1000 MPa. The thermal hysteresis of the NiTiPd-15Hf was 39 ^{o}C under 25 MPa and increased to 105 ^{o}C under 1000 MPa. In the NiTiPd-20Hf, the hysteresis cannot be detected at 25 MPa while it was increased from 17 ^{o}C to above 150 ^{o}C as the applied stress increased from 100 MPa to 1000 MPa. Consequently, the increase of the Hf content resulted in lower initial

temperature hysteresis compared to NiTiPd-10Hf. It is also clear that the progress of the thermal hysteresis with stress was different for the selected alloys.

The evolution of the thermal hysteresis in the current alloys can be analyzed in two regions which are those before (pre-saturation region) and after (post-saturation region) saturation stress. The saturation stress could be defined as the stress at which transformation strain stops increasing and starts either saturating or decreasing in Figure 4.5a. For instance, the saturation stress was 500 MPa for the NiTiPd-10Hf alloy while it was 700 MPa for the NiTiPd-15Hf and NiTiPd-20Hf alloys. The thermal hysteresis in the NiTiPd-10Hf alloy was almost constant up to the saturation stress of 500 MPa where it increased progressively even before the saturation stress in the NiTiPd-15Hf and NiTiPd-20Hf alloys. After plastic deformation occurred (reflected by irrecoverable strain in Figure 4.6), the hysteresis increased almost abruptly in all alloys. It is known that the hysteresis is a result of dissipation mechanisms in shape memory alloys [1, 94]. In SMAs, the three main energy dissipation mechanisms can be expressed as *i)* friction between transforming phases or in-compatibility, *ii)* friction between martensite variants and *iii)* dislocation generation [11]. Addition to these main sources, friction between possible internal twins can also contribute to hysteresis.

When the stress is low, the difference between thermal hysteresis of the two alloys should be independent of possible effects associated with the applied stress. The thermal hysteresis was 72 ^{o}C, 41 ^{o}C and 17 ^{o}C at 100 MPa for NiTiPd-10Hf, NiTiHf-15Hf and NiTiPd-20Hf alloys, respectively.

This initial difference in the hysteresis could be related to the compatibility between the transforming phases of the alloys. It has been reported that there is a close

relationship between hysteresis and lattice compatibility that depends on the lattice parameters of the transforming phases in SMAs. When the interphase of the transforming phases is more compatible, a lower hysteresis is expected [95-97]. A sign of the compatibility between the transforming phases is the middle Eigen value λ_2 of a selected matrix of the phase transformation between crystal structures based on the Non-Linear Geometric Theory of Martensite (NLGTM) [95]. According to the theory, the closer the middle Eigen value is to 1, the less hysteresis is expected in shape memory alloys [96, 98-102]. The λ_2 values were calculated to be 0.9077, 0.8870 and 0.8747 for the NiTiHf-10Hf, NiTiPd-15Hf and NiTiPd-20Hf, respectively, using the parameters for B2 to B19' transformation [103]. It is clear that there is an inverse relation between the middle Eigen values and the initial temperature hysteresis in the alloys. Moreover, the λ_2 values are not even close to 1, which is the sign of incompatible microstructures, in the selected NiTiHfPd alloys. Thus, the compatibility between the transforming phases could not be the only reason alone in explaining the initial hysteresis differences in the current alloys.

The difference in the dissipation energy at low stress could be attributed to difference in internal twinning characteristics (Figure 4.1b and 4.1c) and/or formation of partial self accommodated martensite structures.

In the pre-saturation region, the gradual increase in the thermal hysteresis in the NiTiPd-15Hf and NiTiPd-20Hf alloys can be attributed to the increase in the friction between the martensite variants due to increased transformation strain by growing martensite plates. Since the strain was increased, the friction between martensite plates also increased resulting progressively increased hysteresis. On the other hand, the thermal hysteresis of the NiTiPd-10Hf alloy was almost constant in this region even though the

increasing transformation strain. The difference in the progress of thermal hysteresis in this pre-saturation region could stem from the observed difference in the twin types of the alloys. The $<011>_{B19'}$ type II twin was observed in NiTiPd-10Hf while $(001)_{B19'}$ compound twinning was observed in NiTiPd-15Hf and NiTiPd-20Hf alloys. The thickness of compound twins is smaller compared to those with the type II twins (as shown in Figure 4.1) and this may result in more interfaces and more friction due to increased interactions for the same volume of martensite during straining. Furthermore, it is more difficult to detwin the compound twins which increase the friction during propagation and selection of martensite variants. Previously, the mobility of the (001) type compound twins in a $Ni_{49.8}Ti_{42.2}Hf_8$ alloys were reported to be less than <011> type II twins in an equiatomic $Ni_{50}Ti_{50}$ [104]. Thus, the compound twins in NiTiPd-15Hf and NiTiPd-20Hf alloys may cause larger internal friction during the motion of the phase fronts in during generation of transformation strain due to the limited mobility, resulting an progressively increasing dissipation and hysteresis observed with increasing stress.

In all the alloys, an abrupt increase of the thermal hysteresis in the post-saturation region (>700 MPa) was observed. In this region, the increase in the hysteresis can be mainly attributed to the plastic deformation, which is manifested by the open loops (irrecoverable strain) at the end of the thermal cycles. As the dislocations were generated in the materials due to slip, the dissipation of energy was observed as the abruptly increased thermal hysteresis depending on the value of the generated dislocations.

4.7 Isothermal stress-strain behavior of NiTiPd-10Hf

Figure 4.7 shows the stress-strain responses of the NiTiPd-10Hf alloy at 15 ^{o}C and at 90 ^{o}C. It was clear from the thermal cycling response under 25 MPa shown in Figure 4.2a that the alloy was austenite at 15 ^{o}C when it was cooled down from a temperature above A_f. The specimen was incrementally loaded and unloaded at this temperature up to a strain of 11 % and stress of 2400 MPa. The initial linear part of the stress-strain curve (region I) shows predominantly elastic deformation of the existing phases (primarily austenite).

The onset of yielding and the plateau region (Region II in Figure 4.7a) is attributed to stress induced martensite formation (as opposed to general dislocation slip). However, in this case, it was not the only operative deformation mechanism, as there was significant residual strain after unloading the alloy in this region (in contrast to deformation at 90 ^{o}C, Figure 4.7b). Consequently, reorientation/dewtinning of any remnant martensite in the alloy was possibly occurring concurrently with the stress induced martensite formation.

At the end of Region II, the material is assumed to be fully transformed to martensite. This region was followed by what is primarily assumed to be elastic deformation of martensite (Region III.). In addition to elastic deformation of martensite in region III, further re-orientation and detwinning could also occur [105] with the possibility of some dislocation slip and deformation twinning activity [106].

After region III, plastic deformation became more dominant at the second yielding point, which was the onset of region IV. In this region, dislocation generation and/or deformation twinning were expected to dominate the deformation response [105].

Therefore, it was expected that bulk plastic deformation of martensite occurred at relatively high stresses, more than 2 GPa, which can be beneficial for high strength biomedical or industrial applications.

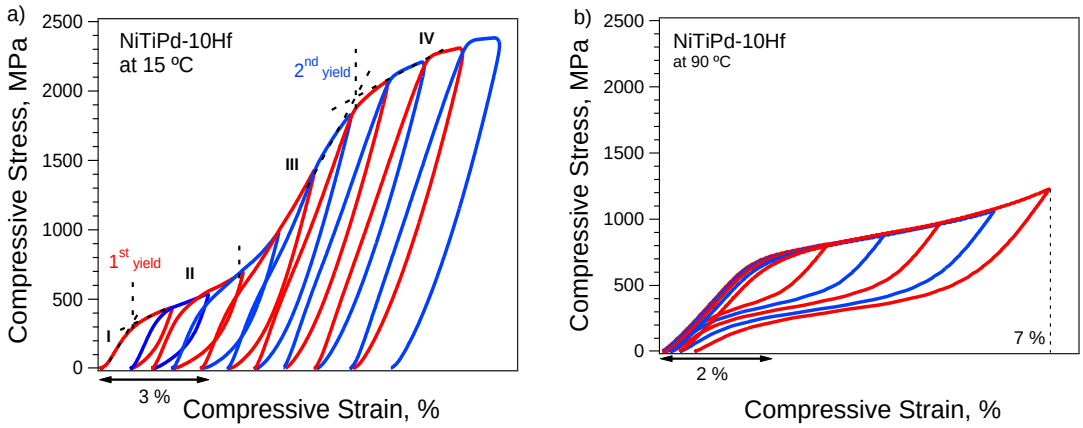

Figure 4.7: Stress-strain responses of NiTiPd-10Hf at a) 15 ^{o}C and b) 90 ^{o}C.

In Figure 4.7b, the specimen was incrementally loaded up to 7 % strain at 90 ^{o}C. This temperature was above the A_f temperature for the alloy and the deformation response was superelastic in nature. During loading at 90 ^{o}C, elastic deformation of austenite was observed up to the critical stress level for martensite transformation. Further loading resulted in austenite to martensite transformation accompanied with plateau-like behavior. Upon unloading, martensite was unloaded elastically and then the reverse transformation from martensite to austenite was observed, followed by elastic unloading of austenite. Almost fully recoverable strains were possible even when a stress level of nearly 1250 MPa was applied. When the sample was loaded to 7 % strain and unloaded, nearly all the strain was recovered between elastic recovery and transformation

strain with the transformation component of at least 4.3 %. Stress hysteresis, calculated between the loading and unloading curves at 3.5 % was determined to be 525 MPa.

It should be noted that plateau-like behavior was observed at 90 ^{o}C during superelastic deformation of this $Ni_{45.3}Ti_{39.7}Hf_{10}Pd_5$ alloy (Figure 4.7b), in contrast to a much steeper and shorter plateau region and high hardening observed previously in a $Ni_{45.3}Ti_{29.7}Hf_{20}Pd_5$ alloy [92]. The lack of hardening during transformation in NiTiPd-10Hf could be attributed to the formation of type II twins. It is known that the $(001)_{B19'}$ compound twins were observed in the $Ni_{45.3}Ti_{29.7}Hf_{20}Pd_5$ alloy, which is similar to Ni-rich NiTiHf alloys as the main substructure of martensite [48, 53, 54]. Thin compound twins in the $Ni_{45.3}Ti_{29.7}Hf_{20}Pd_5$ alloy can make the growth of martensite variants and detwinning more difficult due to pinning effects and/or increased elastic energy storage. Thus, during transformation or detwinning, the required energy to complete the stress induced martensite transformation increased, which would need to be supplied by an increasing external force during the transformation process. Also, in $Ni_{45.3}Ti_{29.7}Hf_{20}Pd_5$, the increased elastic energy storage was manifested as increased difference between the M_f and M_s during the cooling portion of the isobaric thermal cycling experiments [107].

4.8. Iso-thermal stress-strain response of NiiPd-15 Hf alloy

Figure 4.8 shows the stress-strain responses of the NiTiPd-15Hf alloy at 15 ^{o}C. The alloy was in martensite phase based on the TTs shown in Table 1 at 15 ^{o}C (due to M_f temperature of 35 ^{o}C) when it was cooled down from a temperature above A_f. The specimen was incrementally loaded and unloaded at this temperature up to strain of 8 %

and compressive stress of 2100 GPa. Therefore, it is expected that bulk plastic deformation of martensite occurs at relatively high stresses of more than 2 GPa, which is beneficial for high strength biomedical or other industrial applications

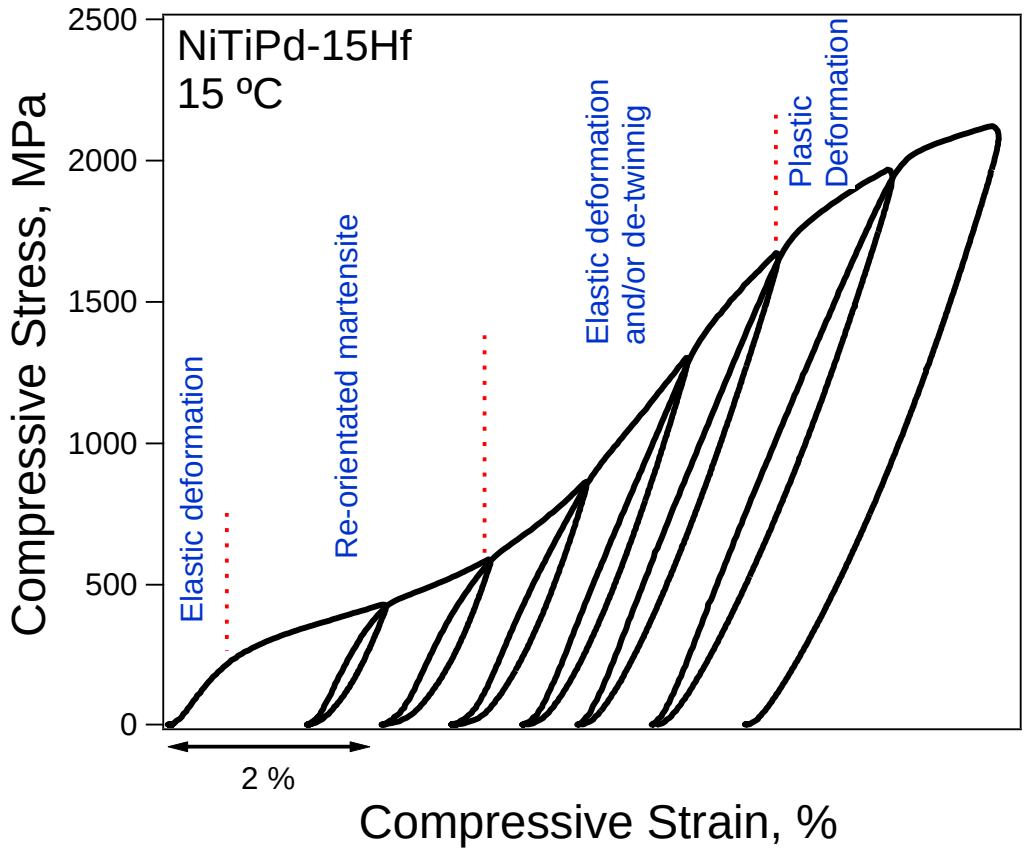

Figure 4.8: Stress-strain response of the NiTiPd-15Hf at 15 ^{o}C

In order to investigate the morphology of re-oriented martensite, TEM observation was conducted at room temperature for the NiTiPd-15Hf alloy after the compression tests shown in Figure 4.8. A bright field image of the re-oriented martensite is shown in Figure 4.9a. Thicker re-oriented martensite plates were frequently observed as compared to the thermally-induced martensite (Figure 4.1b). The thick martensite

variant is considered to be a favorable variant under stress. The selected area diffraction pattern obtained from the interface between the martensite plates A and B in Figure 4.9a is shown in Figure 4.9b. The twinning in the martensite plates was revealed as $(001)_{B19'}$ compound twin. The boundary between the plates A and B is determined to be $\{111\}_{B19'}$-type I boundary [48]. Although the plates A and B are $\{111\}_{B19'}$ type I twin related, the boundary of the plates is not completely parallel to the twinning plane, $\{111\}_{B19'}$, since the plates contain the $(001)_{B19'}$ compound twins. On the other hand, $\{011\}_{B19'}$ type I twin related martensite plates have been reported as SIM in a $Ni_{36}Ti_{49}Hf_{15}$ alloy deformed in tension [23]. It is considered that the twin relationship between re-oriented plates depends on the martensite variants.

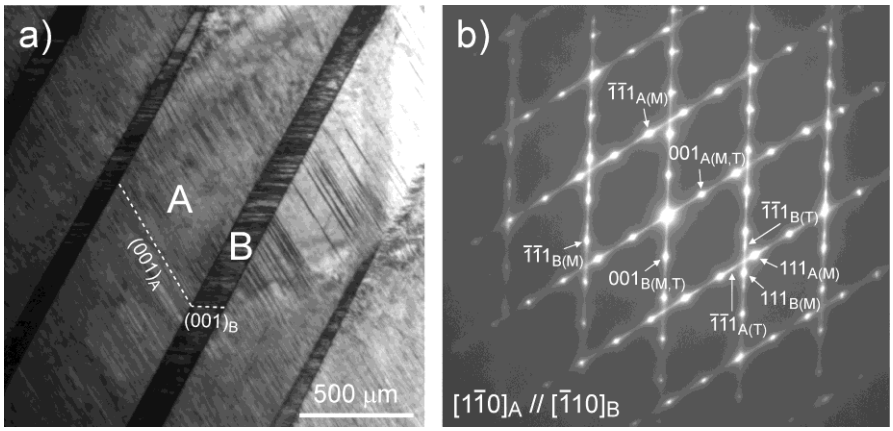

Figure 4.9: (a) Bright field image obtained at room temperature for the NiTiPd-15Hf alloy deformed at 15 ^{o}C and (b) selected area diffraction pattern taken from the interfaces between the martensite plates A and B in (a). Subscripts M and T indicate matrix and $(001)_{B19'}$ compound twin, respectively

In Figure 4.10, compressive stress-strain responses of NiTiPd-15Hf are shown at 60 ^{o}C and 90 ^{o}C. At 60 ^{o}C, full recovery was not observed since the test temperature was

below A_f. Upon heating above A_f, the retained strain was completely recovered as shown by the heating curve in Figure 4.10a.

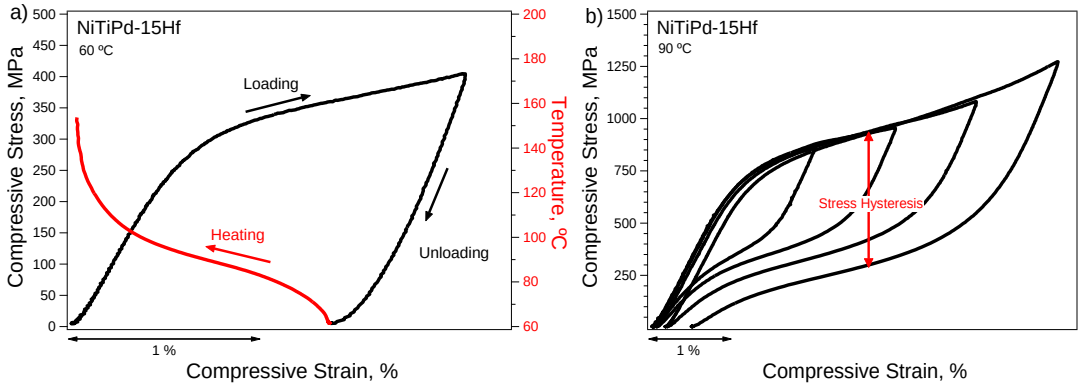

Figure 4.10: Stress-strain responses of NiTiPd-15Hf at temperatures of 60 ^{o}C and 90 ^{o}C

In Figure 4.10b, the sample was incrementally (by 1 %) loaded up to 5 % strain at 90 ^{o}C, above A_f. Almost fully reversible superelastic response was observed even when a stress level of nearly 1400 MPa was applied. When the sample was loaded to 5 % strain and unloaded, irrecoverable strain of 0.3 was observed. The transformation strain was determined to be 3.1 %. Stress hysteresis, calculated between the loading and unloading curves at 2.5 % (as shown in Figure 4.10b), was determined as 635 MPa at 90 ^{o}C.

4.9. Iso-thermal stress-strain behavior of NiTiPd-20Hf alloy

Figure 4.11 shows the stress-strain responses of the NiTiPd-20Hf alloy at 200 ^{o}C, which is above A_f. As the material was loaded to 1 %, a transformation strain of 0.7 % was obtained at 200 ^{o}C. The stress hysteresis calculated at 0.5 % was 260 MPa at 200 ^{o}C.

At the applied strain increased to 2 %, a full recovery was not realized due to high hardening and plastic deformation.

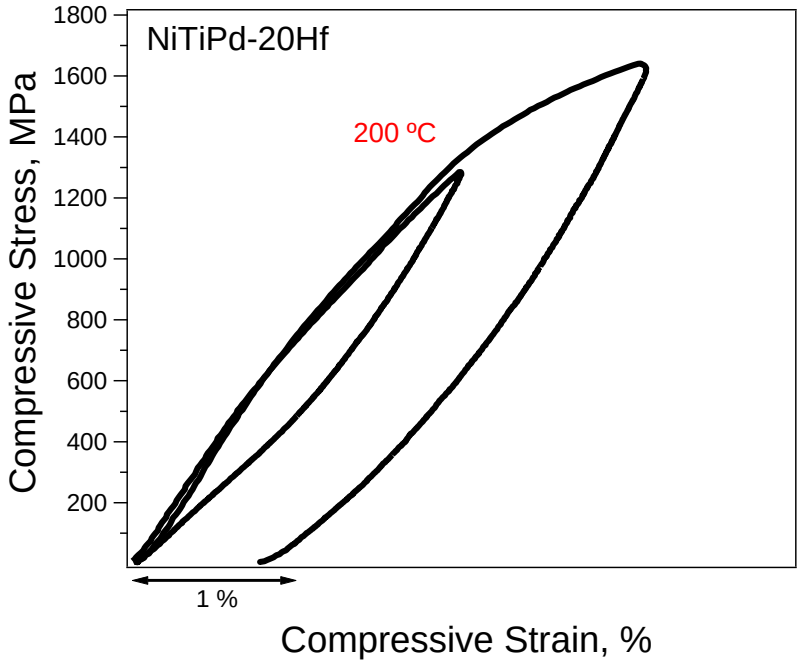

Figure 4.11: Stress-strain responses of NiTiPd-20Hf at 200 ^{o}C

4.10. Two-way shape memory effect in NiTiPd-10Hf

Figure 4.12 shows the strain-temperature responses of the NiTiPd-10Hf alloy under 5, 25 and 50 MPa before and after training. Training was consisted of thermal cycles under stress levels of up to 700 MPa as shown in Figure 4.2. The initial thermal cycling of the as-received material did not result in a significant strain since the applied stress of 5 MPa was not enough to favor any preferred martensite variants.

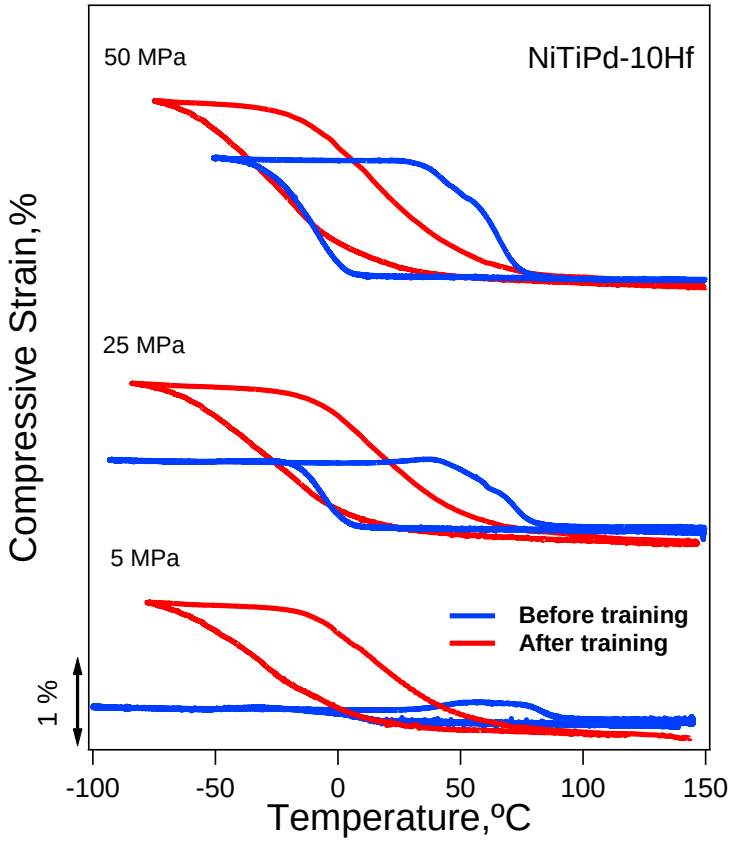

Figure 4.12: Strain-temperature responses of $Ni_{45.3}Ti_{39.7}Hf_{10}Pd_5$ under 5, 25 and 50 MPa before and after training

The thermal cycling response at 5 MPa after training essentially represents w a two-way shape memory effect, since the applied stress was very low and needed to keep to compression sample in place during thermal cycling. In this case, a transformation strain of 1.6 % was observed that can be attributed to the internal stresses generated during plastic deformation of the sample during training. It is known that TWSME behavior can be observed in SMAs upon generation of anisotropic internal stress by dislocation networks or nucleation sites for martensite by interfaces such as precipitates

or retained martensite after certain “training” procedures such as thermal cycling [31, 108], stress cycling [109], or plastic deformation during variant re-orientation [29, 110].

The constant stress thermal cycling experiments under 25 and 50 MPa before and after the training procedure are also included on Figure 4.12. The transformation strains before training were 0.8 % and 1.4 % under 25 and 50 MPa, respectively, while thermal hysteresis was 72 ^{o}C for both stress levels. After training, the transformation strains were 1.6 % and 2 % under 25 and 50 MPa, respectively, and the temperature hysteresis decreased to 47 ^{o}C at 25 MPa and 41 ^{o}C at 50 MPa.

The decrease in the thermal hysteresis after the training process can stem from the work hardening effect of the generated dislocations. As the material hardened, it became more difficult to form new defects and dislocations resulting in decreased energy dissipation. The dislocation networks may also obstruct the martensitic transformation resulting in extra elastic energy storage which helped the back transformation during heating and lowers the TTs for austenite formation [92, 111], as observed in Figure 4.12. Consequently, the hysteresis decreased in trained samples during the constant stress thermal cycling experiments.

4.11. Two-way shape memory effect in NiTiPd-15Hf and NiTiPd-20Hf alloys

Figure 4.13 shows the strain-temperature responses of the NiTiPd-15Hf under 5 MPa after various training conditions. The initial thermal cycling of the as-grown material (T-0) did not result in significant strain since the applied stress of 5 MPa was not enough to favor any preferred martensite variants. TWSME after thermal cycling under

700 MPa (T-1) and 1000 MPa (T-2), as shown in Figure 4.13, yielded in compressive strain.

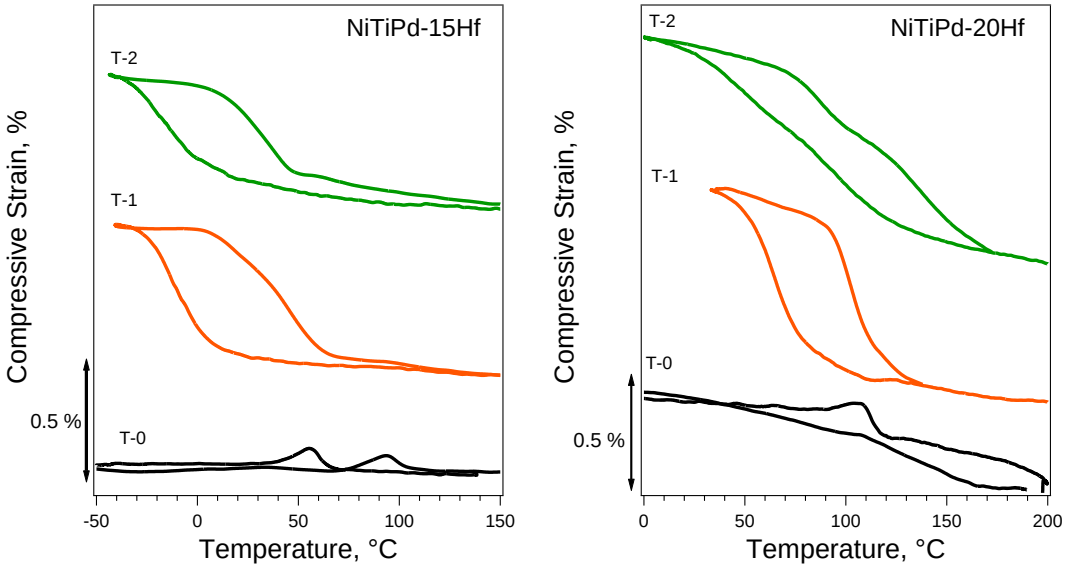

Figure 4.13: The constant stress strain-temperature responses of as-grown and trained $Ni_{45.3}Ti_{39.7}Hf_{15}Pd_5$ and NiTiPd-20Hf alloys at 5 MPa

The TWSME strain in T-1 was 0.6 % while thermal hysteresis was 45 ^{o}C. At T-2, the TWSME strain was 0.5 % and the temperature hysteresis was decreased to 40 ^{o}C. It is clear that the TWSME was decreased after the T-2 condition since significant dislocation generation was observed when the bias stress increased from 700 MPa to 1000 MPa as shown in Figure 4.3. The decrease in the thermal hysteresis in the T-2 condition can stem from the less volume of transformed material. Moreover, as the material hardens due to plastic deformation, it becomes more difficult to form new defects and dislocations resulting in decreased energy dissipation.

In NiTiPd-20Hf, TWSME strain in T-1 was 0.8 % with a thermal hysteresis of 35 ^{o}C. In T-2, TWSME strain was 0.85 % and the temperature hysteresis was decreased to

30 ^{o}C, similar to NiTiPd-15Hf alloy. It is clear that there is a huge elastic energy storage (monitored as a larger difference between M_s and M_f in Figure 4.13b) during the transformation in the T-2 case, which could be a result of hard propagation of phase fronts due to generated dislocations after the constant stress thermal cycling experiment at 1000 MPa (Figure 4.4b). In comparison, it should be recalled that the NiTiPd-10Hf alloy could develop two-way shape memory strain of 1.6 % without an intense training process, owing to larger internal stress and/or larger volume of favored martensite plates resulting in larger TWSME strain compared to the other alloys.

4.12. Work output

In Figure 4.14, work output levels for the NiTiPd-10Hf, NiTiPd-15Hf and NiTiPd-20Hf alloys are shown as a function of applied stress. The work output can be expressed as the mathematical product of reversible strain and the applied stress obtained from the load-biased thermal cycling experiments. As the applied stress increased, the work output also rose due to an increase in reversible strain and stress.

In the NiTiPd-10Hf alloy, work output was 0.2 J.cm^3 under 25 MPa and reached a maximum value of 29 J.cm^3 under 700 MPa. As for the current alloys, the work output was 0.075 J.cm^3 under 25 MPa and reached a maximum value of 30 J.cm^3 under 1000 MPa in the NiTiPd-15Hf alloy. The work output values were 5 J.cm^3 and 20 J.cm^3 at the compressive stress levels of 100 MPa and 1000 MPa, respectively in NiTiPd-20Hf. As the applied stress increased further to 1000 MPa, the work output decreased to 25 J.cm^3 due to a lower reversible strain of only 2.5 %.

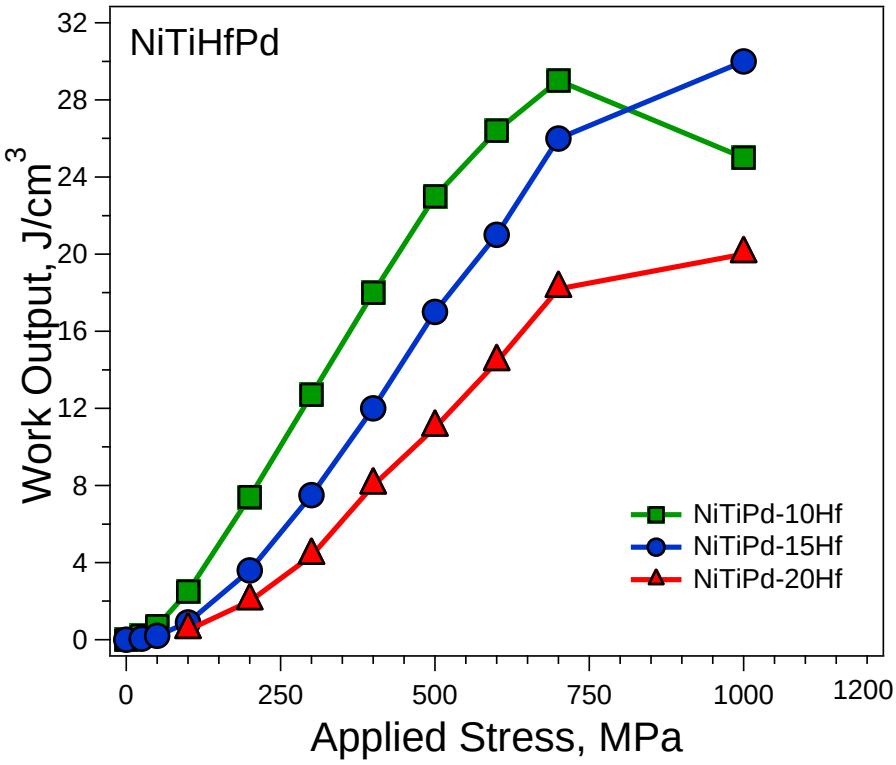

Figure 4.14: Work output and transformation strain values as a function of applied compressive stress for the NiTiPd-15Hf and NiTiPd-10Hf alloys.

In comparison, the NiTiPd-10Hf alloy has nearly comparable work output to a previously studied extruded $Ni_{45.3}Ti_{29.7}Hf_{20}Pd_5$ alloy, which is capable of 32-35 J/cm^3 [92]. Binary NiTi alloys can generally provide work outputs of 10-20 J/cm^3 [14], while Ni rich NiTiHf alloys can produce around 18-20 J/cm^3 [85, 112]. Finally, NiTiPd and NiTiPt alloys can yield work outputs of 9-15 J/cm^3 at temperatures above 150 ^{o}C [15, 63]. However, it should be noted that the upper temperature capability is limited in NiTiHfPd alloys compared to more conventional ternary NiTi-X (X=Hf, Pd, Pt) high temperature shape memory alloys. High work output levels were realized in the NiTiHfPd alloys owing to high stress capability and good transformation strain.

4.13. Summary and conclusions

Effects of chemical composition on the overall and shape memory properties were investigated in this chapter. Following conclusions were reached.

1. The internal twins formed in $Ni_{45.3}Ti_{39.7}Hf_{10}Pd_5$ under stress free transformation in the large martensite plates were <011> type II twins, which are commonly observed in NiTi binary alloys.

2. The $Ni_{45.3}Ti_{39.7}Hf_{10}Pd_5$ alloy exhibited near perfect shape memory response with 4.6 % transformation strain at 500 MPa. A near perfect superelastic response was observed at 90 ^{o}C with nearly complete recovery of 7 % applied strain, including ~4.3 % transformation strain at a stress level of 1250 MPa in $Ni_{45.3}Ti_{39.7}Hf_{10}Pd_{5.}$

3. It was found that Classius-Clapeyron slopes were 8.5 MPa/^{o}C, 11.8 MPa/^{o}C and 15 MPa/^{o}C for M_s in the NiTiPd-10Hf , NiTiPd-15Hf and NiTiPd-20Hf alloys, respectively.

4. The $Ni_{45.3}Ti_{39.7}Hf_{10}Pd_5$ alloy exhibited 1.6 % two-way shape memory strain after a simple training procedure consisting of thermomechanical cycling at up to 700 MPa. The $Ni_{45.3}Ti_{34.7}Hf_{15}Pd_5$ and $Ni_{45.3}Ti_{29.7}Hf_{20}Pd_5$ alloys exhibited two-way shape memory strains of 0.6 % and 0.8 %, respectively, after simple training.

5. The as-grown $Ni_{45.3}Ti_{39.7}Hf_{10}Pd_5$ alloy has a maximum work output energy density of 29 J.cm^{-3}, achieved at a stress level of 700 MPa. On the other hand, maximum work output were 30 J.cm^{-3} and 20 J.cm^{-3} for the as-grown $Ni_{45.3}Ti_{34.7}Hf_{15}Pd_5$ and $Ni_{45.3}Ti_{29.7}Hf_{20}Pd_5$ alloys, respectively.

6. A notable superelastic response was observed at 90 ^{o}C with nearly complete recovery of 5 % applied strain, including over 3 % transformation strain in $Ni_{45.3}Ti_{34.7}Hf_{15}Pd_5$ and $Ni_{45.3}Ti_{34.7}Hf_{15}Pd_5$ alloys while the high hardening limited the superelasticity in $Ni_{45.3}Ti_{29.7}Hf_{20}Pd_5$.
7. As the Hf content was increased, the transformation strain was decreased and the volume of crystal structures was expanded.
8. The evolution of the thermal hystereses with the applied stress was linked to the observed twinning types. A progressively increasing hysteresis with the applied stress in the load-biased thermal cycling tests was observed in the compound twinned NiTiPd-15Hfand NiTiPd-20Hf alloys in contrast to type-II twinned NiTiPd-10Hf alloy.

5. SHAPE MEMORY PROPERTIES OF [111]-ORIENTED $Ni_{45.3}Ti_{29.7}Hf_{20}Pd_5$ ALLOYS

5.1. Introduction

It has been well documented that shape memory properties of NiTi alloys are highly orientation dependent [9-14]. Originally, the stress induced martensitic phase transformation in NiTi single crystals was investigated by Takei et al. in 1983 [113], while Miyazaki et al. studied the shape memory and superelastic behaviors of $Ti_{49}Ni_{51}$ (at %) single crystals around the same time [114]. Since then, many aspects of NiTi single crystals such as cyclic deformation behavior [115], tension-compression asymmetry [39], orientation dependence of shape memory properties [59], and aging effects on shape memory behavior [42] have been investigated. In NiTi single crystals, yield strengths as high as 2000 MPa are possible in the martensite phase for $Ti_{48.5}Ni_{51.5}$ and $Ti_{49.2}$ $Ni_{50.8}$ with 3 % transformation strain along the [111] direction in compression [42, 59]. Moreover, the mechanical behavior of strongly textured polycrystalline materials can mimic the behavior of single crystals [3]. As an example, it is possible to get strongly <111> textured NiTi alloys by wire drawing that exhibit shape memory behavior similar to [111] oriented single crystals [116].

In this chapter, the shape memory properties of $Ni_{45.3}Ti_{29.7}Hf_{20}Pd_5$ single crystals were investigated along the [111] orientation. Effects of aging temperature and time on the functional properties of single crystals were also reported. Lastly, the effects of initial

microstructure and following aging treatments on the shape memory properties were reported.

5.2. Superelasticity of an ultra-high strength of [111] oriented $Ni_{45.3}Ti_{29.7}Hf_{20}Pd_5$ alloys

In this section, $Ni_{45.3}Ti_{29.7}Hf_{20}Pd_5$ single crystalline SMA was investigated in compression along the [111] direction. Its superelastic behavior as a function of temperature was revealed. Mechanical strength, damping capacity and mechanical hysteresis were also determined studying the potential of this ultra-high strength $Ni_{45.3}Ti_{29.7}Hf_{20}Pd_5$ single crystalline alloy for industrial applications that require high strength and high damping capacity.

High strength, high damping capacity and high work output are important parameters for consideration of SMAs in many practical applications. Work output is especially important in actuation applications where there are restrictions on weight and space such as adaptive engine components and morphing structures in aerial vehicles. As stated in Chapter 3, good damping materials should have large mechanical hysteresis and good strain. The stress hysteresis is about 200-300 MPa in polycrystalline NiTi [67], increasing to 400-500 MPa in [111] oriented $Ti_{48.5}Ni_{51.5}$ and $Ti_{49.2}Ni_{50.8}$ (at %) single crystals [42, 59], and is about 500 MPa in NiTiNb polycrystalline SMAs [17]. High strength and large hysteresis SMAs are very appealing for aerospace and biomedical applications [20, 21] as well as applications in civil and seismic structures [18, 20, 22]. Possible advantages that they can provide include high force accommodation, weight saving, portability and reduction in cost over existing systems [20].

In this study, the [111] oriented single crystal was solutionized (solution treated) at 1050 ^{o}C for 4 hours followed by water quenching. Figure 5.1 represents the superelastic response of the solution-treated [111] oriented $Ni_{45.3}Ti_{29.7}Hf_{20}Pd_5$ single crystal in compression at selected test temperatures above the austenite finish temperature, A_f. The sample was loaded under strain control and then unloaded under force control. In the first cycle, the material was loaded to a strain value of 3 % and then unloaded. In succeeding cycles, the applied strain was increased by 1 % (until a maximum applied strain of 6 % was reached

At all test temperatures, the transformation strain was fully reversible meaning that there was negligible amount of plastic deformation [59]. The superelastic window for the $Ni_{45.3}Ti_{29.7}Hf_{20}Pd_5$ single crystal alloy was at least 100 ^{o}C (with testing in this study conducted between – 30 ^{o}C and 70 ^{o}C). The maximum transformation strain was 4.2 % at -30 ^{o}C. The elastic moduli of the austenite and martensite phases were 65-75 GPa and 100-110 GPa, respectively.

Another remarkable feature observed in Figure 5.1 is the very high strength of the $Ni_{45.3}Ti_{29.7}Hf_{20}Pd_5$ single crystal that results in a perfect superelastic response with no permanent plastic deformation under compressive loads up to 2.5 GPa. Thus, it can be concluded that the stress required for dislocation slip or irreversible deformation twinning in the martensite phase is higher than 2.5 GPa for this material along [111] orientation.

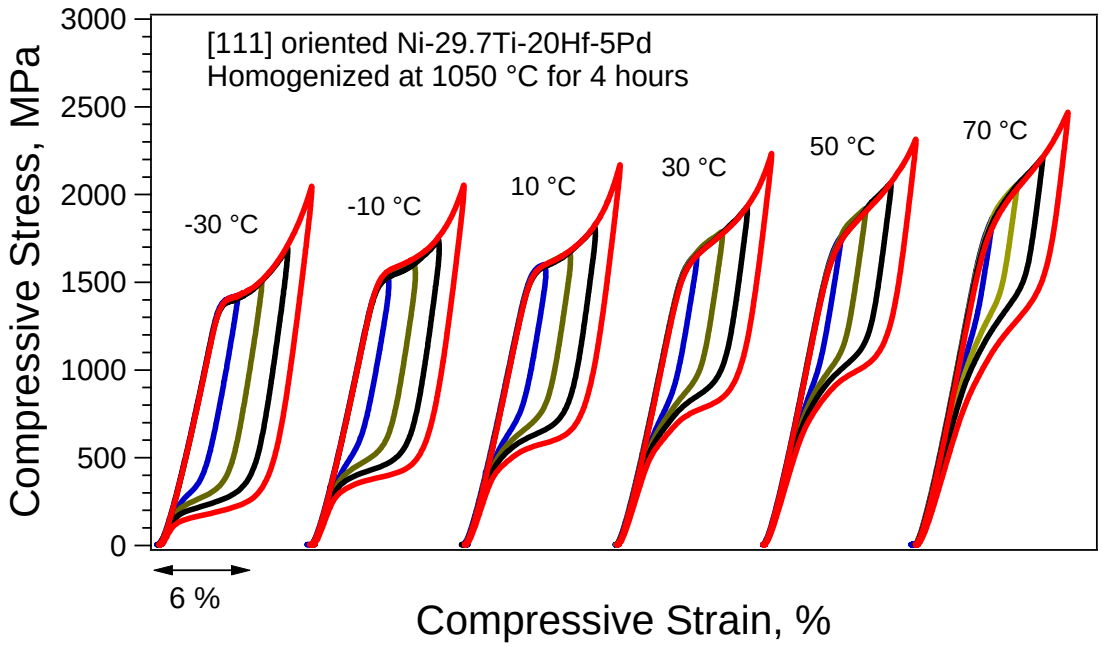

Figure 5.1: Superelastic response of solution-treated $Ni_{45.3}Ti_{29.7}Hf_{20}Pd_5$ single crystal along [111] orientation at constant test temperatures ranging from – 30 ^{o}C to 70 ^{o}C.

All of the superelastic loops in Figure 5.1 showed hardening even in the transformation plateau regions. Moreover, as evident by the increasing slopes of the transformation plateaus, hardening increased with increasing test temperature. The reason behind this tendency could be the operation of additional martensite variants activated by temperature as previously observed in NiTiHf and CoNiGa single crystals [117, 118]. Interactions among these variants may hinder the transformation or detwinning and more stress may be needed to propagate phase or twin boundaries [59, 119] as the test temperature was increased.

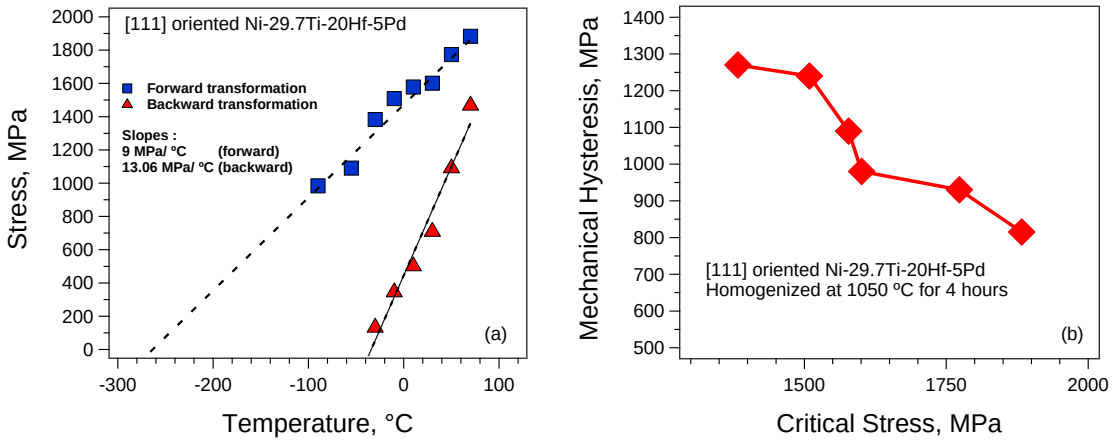

Figure 5.2: a) Clausius-Clapeyron and b) mechanical hysteresis vs. critical stress (for the forward transformation) relationships for $Ni_{45.3}Ti_{29.7}Hf_{20}Pd_5$ along [111] direction in compression.

Critical stresses for the forward and backward transformations were found graphically by intersecting line segments aligned with the plateau regions and the connected linear elastic regions of austenite and martensite, respectively, and the results are shown in Figure 5.2a. The critical stresses for both the forward and backward transformations increased with temperature and ranged between 1380 MPa and 1880 MPa for the forward transformation and 130 MPa to 1460 MPa for the back transformation within a pseudoelastic window of – 30 ^{o}C to 70 ^{o}C. The stress hysteresis as a function of temperature was also deduced from Figure 5.1 and these results are shown in Figure 5.2b. The stress hysteresis was calculated at the middle point of the plateau strain between the forward and reverse transformations when the sample is loaded up to 6 % applied strain. It was clear that the stress hysteresis tended to decrease with temperature and was almost independent of transformation strain.

The increase in stress induced martensite stress levels with temperature can be explained by the Clausius-Clapeyron relationship [75].The slope of the C-C line was 9 MPa/ ^{o}C for the forward transformation and 12.6 MPa/ ^{o}C for the backward transformation for the solution-treated $Ni_{45.3}Ti_{29.7}Hf_{20}Pd_5$ single crystal. The difference in C-C slopes also confirmed the decrease in hysteresis with temperature, which ranged from 1270 MPa at – 30 ^{o}C to 815 MPa at 70 ^{o}C. As a comparison, the C-C slope for the forward transformation was around 7 MPa/ ^{o}C in a peak aged $Ni_{50.8}Ti_{49.2}$ [111] single crystal and was on the average of 6.5 MPa/ ^{o}C for $Ni_{51.5}Ti_{48.5}$ single crystals in various orientations [42, 59].

Based on the stress-strain behavior shown in Fig 5.1, the yield stress of the martensite (and by inference the austenite phase) was greater than 2500 MPa for the solution treated $Ni_{45.3}Ti_{29.7}Hf_{20}Pd_5$ alloy along the [111] orientation. This level of yield stress was significantly higher than the yield strength of precipitation strengthened [111] oriented $Ni_{50.8}Ti_{49.2}$ single crystals, which had an austenite yield strength between 900 MPa and 1250 MPa in over-aged (aged at 550 ^{o}C for 1.5h) and peak-aged (aged at 450 ^{o}C for 1.5h) conditions, respectively, while the yield strength of the martensite phase was 1700 MPa for over-aged and 2100 MPa for the peak-aged conditions measured at temperatures above 100 ^{o}C [59]. In alloys that were even more Ni-rich, e.g., [111]-oriented $Ni_{51.5}Ti_{48.5}$ single crystals tested in compression, the martensite yield strength was reported to be around 2000 MPa for an over-aged (aged at 550 ^{o}C for 1.5h) state at 77 K [42].

The maximum recoverable strain for the $Ni_{50.8}Ti_{49.2}$ and $Ni_{51.5}Ti_{48.5}$ single crystals along the [111] direction was 3% in over-aged conditions in compression [42, 59]. The

maximum recoverable strain in the superelastic experiments for the $Ni_{45.3}Ti_{29.7}Hf_{20}Pd_5$ single crystalline alloy was around 4.2 %. Consequently, this alloy can recover more strain compared to the aforementioned [111]-oriented NiTi single crystals and it possesses a higher yield strength even in the solution treated condition. It should be noted that in the current study, no irrecoverable strain was observed when the $Ni_{45.3}Ti_{29.7}Hf_{20}Pd_5$ single crystalline specimens were deformed at 70 ^{o}C up to a stress level of 2500 MPa.

Hysteresis in SMAs is a decisive parameter in the design and operation of many SMA-based components. Hysteresis in these systems is defined as the non-reversible energy dissipation during the thermoelastic martensitic phase transformation. The mechanical (or stress) hysteresis was extracted from the superelastic curves in Figure 5.1 and is summarized in Figure 5.2b as a function of the critical stress for the forward transformation. The comparison between the results of the current study and other NiTi based alloys is depicted in Figure 5.3. The [111]-oriented $Ni_{45.3}Ti_{29.7}Hf_{20}Pd_5$ single crystalline alloy yields a mechanical hysteresis of 1270 MPa at -30 ^{o}C, which is the largest mechanical hysteresis observed in SMAs. In NiTi polycrystals, the mechanical hysteresis was around 200-300 MPa [67] while it is around 400-500 MPa in NiTiNb alloys [17]. It was clear that [111]-oriented $Ni_{45.3}Ti_{29.7}Hf_{20}Pd_5$ alloys had significantly higher stress hysteresis around room temperature than any other SMAs. Thus, $Ni_{45.3}Ti_{29.7}Hf_{20}Pd_5$ alloys could be a cost effective and promising candidate for biomedical and damping applications in a case of texturing.

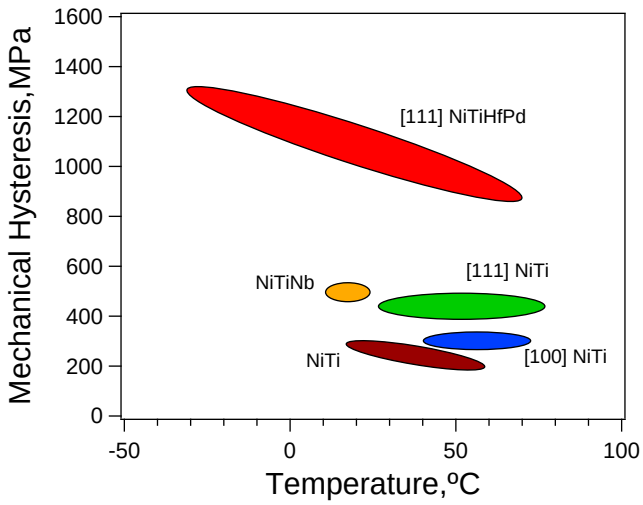

Figure 5.3: Comparisons of mechanical hysteresis for various NiTi based SMAs [2, 17, 46, 59].

It is well known that the lattice friction and dislocation generation increases both mechanical and thermal hysteresis in SMAs [11, 120, 121]. Since there was almost no irrecoverable strain in the superelastic behavior of the material and stress hysteresis was independent of transformation strain, dislocation generation can be ruled out as a prospective reason for the large hysteresis observed. Thus, this large hysteresis can mainly be attributed to the lattice incompatibility between the transforming phases, restricted mobility of phase front/twin boundaries due to high frictional resistance or relaxation of elastic energy.

In thermo-elastic phase transformations, elastic energy is stored during the forward transformation and in turn, promotes back transformation. Elastic strain energy does not directly affect thermal and mechanical hysteresis [11]. However, if the stored elastic energy is relaxed subsequent to phase transformation, the potential of the

remaining elastic energy to promote back transformation is lessened and thus the mechanical hysteresis is expected to be larger [11, 120, 122].

Lattice friction is another dissipative mechanism, which escalates the hysteresis. Friction can be described as the resistance for phase front or variant motion in the material [11]. Interactions between martensite variants or among variants and phase front imperfections (i.e., dislocations, other point or lineal lattice defects, second phase particles, precipitates, etc.) may increase this resistance and yield more friction. This means more energy dissipation and larger hysteresis.

Since the matrix was rather strong in this $Ni_{45.3}Ti_{29.7}Hf_{20}Pd_5$ single crystal and it was consisted of alloying elements with dissimilar atomic radii, the resistance for phase propagation might be responsible for the high dissipation of energy. A similar phenomenon was reported in $Ni_{51.5}Ti_{48.5}$ single crystals, which had a stronger matrix than the $Ni_{50.1}Ti_{49.9}$ single crystals [11]. However, it is hard to explain the considerable change in hysteresis with temperature in the $Ni_{45.3}Ti_{29.7}Hf_{20}Pd_5$ single crystal by only considering the lattice friction.

The close relationship between hysteresis and lattice compatibility of transforming phases is well known. Lattice compatibility is a function of lattice parameters of the transforming phases in SMAs. When the interphase of the transforming phases is more compatible, a lower hysteresis is expected [95-97]. The large hysteresis observed in our $Ni_{45.3}Ti_{29.7}Hf_{20}Pd_5$ single crystal alloy could be attributed to the incompatibility between austenite and martensite phases. It should be noted that the mechanical hysteresis observed is about 1270 MPa at – 30 ^{o}C and 900 MPa at 70 ^{o}C for an applied strain of 6 %. Such a change in hysteresis with temperature can be due to the

change in lattice parameters of the transforming phases, which leads to a more compatible crystal structure at the interphase.

Mechanical hysteresis is closely related to the damping capacity of SMAs, which may become a useful ability for various applications in defense, construction, and transportation industries [20]. For [111] oriented $Ni_{45.3}Ti_{29.7}Hf_{20}Pd_5$ single crystals, the damping capacity was approximately 44 $J.cm^{-3}$, which is larger than 38 $J.cm^{-3}$ for NiTiNb and 16 $J.cm^{-3}$ for $Ni_{50.6}Ti_{49.4}$ alloys [18].

The ultra-high strength, exceptional damping capacity, and practical ability to demonstrate superelastic behavior at room temperature without irrecoverable strain makes $Ni_{45.3}Ti_{29.7}Hf_{20}Pd_5$ SMAs an intriguing candidate for strategically important applications in biomedical, aerospace, oil-gas, and construction applications. It should be noted that for biomedical applications, the presence of Hf and Pd would also improve the visibility of $Ni_{45.3}Ti_{29.7}Hf_{20}Pd_5$ components such as stents, prosthetics, etc. during magnetic resonance imaging.

5.3. Effects of aging temperature on the shape memory properties of [111]-oriented $Ni_{45.3}Ti_{29.7}Hf_{20}Pd_5$ single crystals

In the previous section, superelastic properties of solutionized [111]-oriented $Ni_{45.3}Ti_{29.7}Hf_{20}Pd_5$ single crystals were determined in compression [123]. This material was capable of 4.2 % transformation strain, extremely high critical and yield stress levels (> 2000 MPa), and high damping capacity/absorbed energy (44 $J.cm^{-3}$) due to a high stress hysteresis (> 1200 MPa) at temperatures between -30 ^oC and 70 ^oC. In the present section, the effects of aging (550 ^oC and 600 ^oC for 3 hours) on the shape memory properties of $Ni_{45.3}Ti_{29.7}Hf_{20}Pd_5$ single crystals along the [111] orientation were investigated under compression. In addition to superelastic tests at selected temperatures, constant-stress thermal cycling tests were conducted and the transformation temperatures, transformation strain, thermal hysteresis, work output, and energy absorption as functions of stress and/or temperature were determined.

As an experimental method, the [111]-oriented $Ni_{45.3}Ti_{29.7}Hf_{20}Pd_5$ single crystals were solutionized at 1050 ^oC for 4 hours in sealed quartz tubes followed by a water quench. Subsequently, they were aged at 550 ^oC or 600 ^oC for 3 hours in air and again quenched in water. For brevity, the $Ni_{45.3}Ti_{29.7}Hf_{20}Pd_5$ specimen aged at 550 ^oC for 3 hours and the specimen aged at 600 ^oC for 3 hours will be referred as "550 ^oC-3h" and as "600 ^oC-3h" throughout the section, respectively.

Figure 5.4 shows TEM images of 550 ^oC-3h and 600 ^oC-3h aged samples. It was clear that precipitates with different sizes were formed after aging. The microstructure of the 550 ^oC-3h sample consisted of a high-density of very fine precipitate phase (< 20nm). The precipitate phase had the same face-centered orthorhombic lattice structure as those

found in a NiTiHf alloy by Han et al [124] based on electron diffraction patterns. The precipitates were spindle shaped; the size of the long axis increased from 10-20nm to 50-60nm when the aging temperature was increased from 550 ^{o}C to 600 ^{o}C.

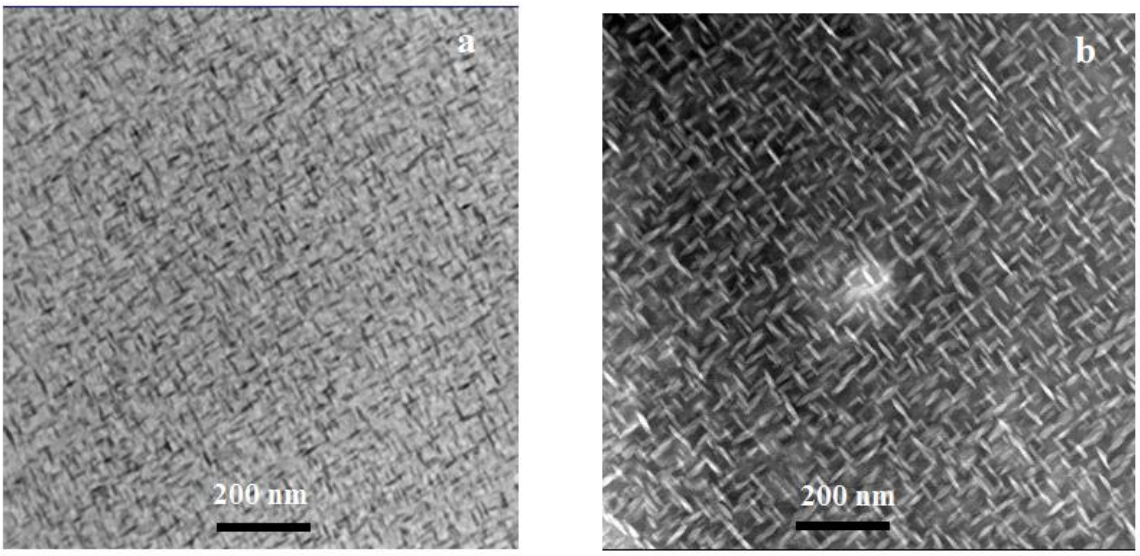

Figure 5.4: Microstructure of the $Ni_{45.3}Ti_{29.7}Hf_{20}Pd_5$ alloy aged at a) 550 ^{o}C for 3h and b) 600 ^{o}C for 3h.

Figure 5.5 shows the constant stress thermal cycling response of the [111] oriented $Ni_{45.3}Ti_{29.7}Hf_{20}Pd_5$ single crystals after aging. The transformation temperatures (M_s, M_f, A_s and A_f) as function of applied stress were determined using the tangent method. M_s and A_f were 20 ^{o}C and 61 ^{o}C under 100 MPa and 105 ^{o}C and 135 ^{o}C under 1000 MPa, respectively, for the 550 ^{o}C-3h aged condition. In the 600 ^{o}C-3h case, M_s and A_f temperatures were 61 ^{o}C and 142 ^{o}C under 100 MPa and 115 ^{o}C and 195 ^{o}C under 1000 MPa, respectively.

The transformation strains and thermal hystereses were extracted from Figure 5.5a and 5.5b and plotted as a function of applied stress in Figure 5.5c. With increasing stress, the transformation strains increased since stress drove the selection of more favored martensite variants. However, at some point this process would saturate and the transformation strains would become independent of stress or actually start to decrease if pastic deformation began to dominate. In the 550 ^{o}C-3h aged condition, transformation strain initially increased with stress up to 500 MPa and then saturated. It was 0.2 % at an applied stress level of 100 MPa and 2.2 % at 1500 MPa. The transformation strains for the 600 ^{o}C-3h aged sample behaved in a similar fashion, initially increased with stress up to 700 MPa and then saturated. The transformation strains for the 600 ^{o}C-3h aged sample were 0.3 % at100 MPa and 2 % at 1000 MPa.

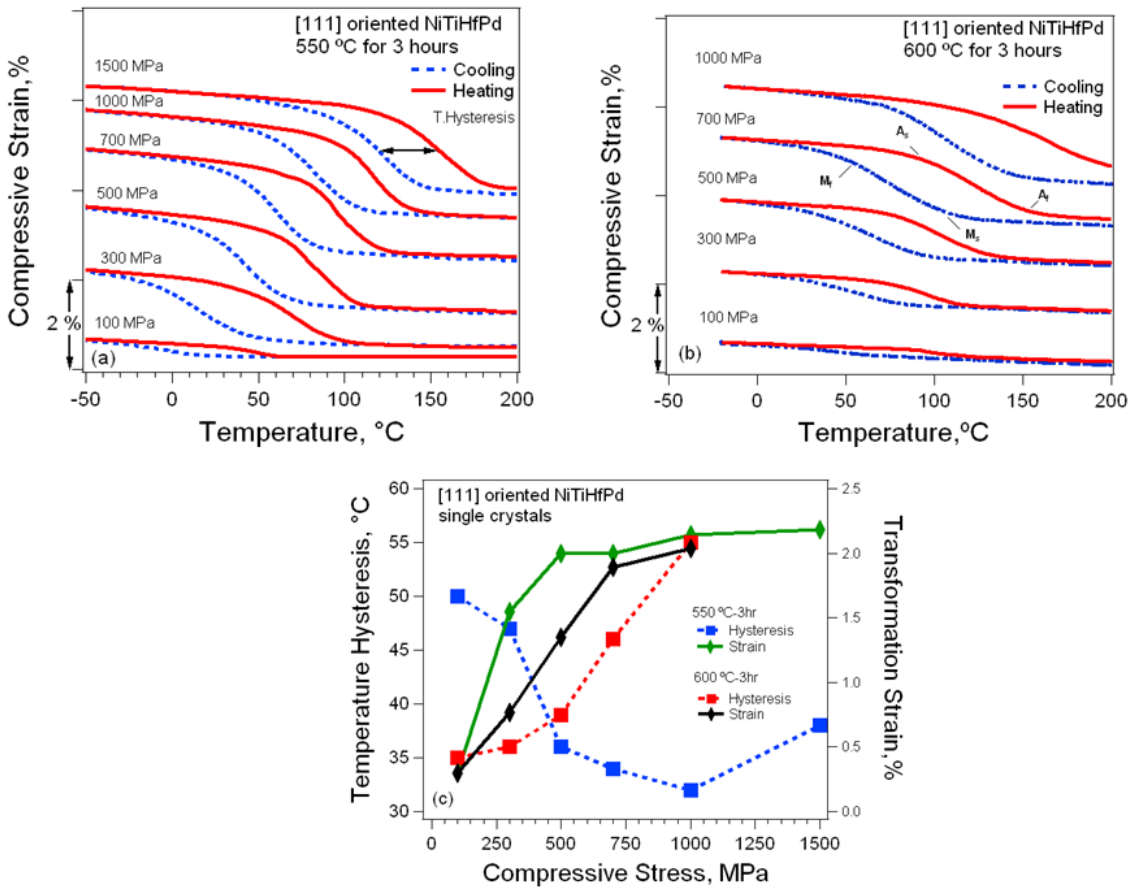

Figure 5.5: Shape memory behavior under stress for a) 550 °C-3h condition, b) 600 °C-3h condition, c) temperature hysteresis and transformation strain as functions of applied stress for [111] oriented $Ni_{45.3}Ti_{29.7}Hf_{20}Pd_5$ single crystals aged at 550 °C for 3h and 600 °C for 3h.

It should be noted that almost perfect shape memory behavior was observed even at stress levels as high as 1000 MPa in both aged materials. However, the shape memory behavior of the 550 °C-3h aged specimen at a stress level of 1500 MPa was truly remarkable. The alloy's ability to show shape memory behavior under such high stresses can be attributed to the high strength of the precipitation hardened single crystal due to a high density of relatively fine and coherent precipitates. This was the highest stress level

under which a fully reversible shape memory strain of any significance (e.g., >2%) has been obtained. This ability can afford a very unique opportunity for the current alloy to be utilized in applications where there is a need to recover strain under very high levels of compressive force.

Temperature hysteresis as a function of applied stress was determined graphically between the cooling and heating curves in Figures 5.5a and b at the mid-point of the transformation strain and is summarized in Figure 5.5c for both aging conditions. In the 550 ^{o}C-3h aged material, the temperature hysteresis decreased rapidly from 50 ^{o}C to 37 ^{o}C when stress was increased from 100 MPa to 500 MPa and continued to decrease more slowly resulting in a minimum hysteresis of 28 ^{o}C to 1000 MPa. Further increase in stress to 1500 MPa reversed this trend resulting in a slight increase in hysteresis but only to 38 ^{o}C.

The change in hysteresis with stress correlated well with the corresponding change in transformation strain. The initial decrease in hysteresis can be related to the decrease in the number of martensite variants formed with incerasing stress level. Since fewer martensite variants were formed, the interaction between the variants diminished resulting in a smaller hysteresis. The further change in hysteresis between 500 MPa to 1000 MPa can be attributed to the change in lattice compatibility of the tranforming phases with temperature and stress, and will be described in detail later. Under 1500 MPa, a small irrecoverable strain was observed indicating the occurrence of plastic deformation, which resulted in the subsequent increase in hysteresis.

In the 600 ^{o}C-3h aged condition, the temperature hysteresis increased only slightly up to 500 MPa and then increased rapidly with further increase in applied stress (Figure 5.5c). The temperature hysteresis was 35 ^{o}C, 46 ^{o}C and 55 ^{o}C at 100 MPa, 700 MPa and 1000 MPa, respectively. The rapid increase in temperature hysteresis at stresses greater then 500 MPa can be attributed to an increase in plastic deformation, which was exhibited as irrecoverable strain in the strain-temperature curves shown in Figure 5.5b. It is clear that the evolution in temperature hysteresis was different for the two aging conditions. This difference was attributed to the fact that in the 550 ^{o}C-3h condition, the material was stronger due to the finer coherent precipitates, which did not allow energy dissipation by defect generation. After 600 ^{o}C-3h aging, plastic deformation was easier due to formaton of larger and presumably semi-coherent or incoherent precipitates, which were not as effective in strengthening the material.

The superelastic responses of the aged single crystals along the [111] orientation were shown in Figure 5.6. Specimens were loaded to a total strain of 4 % for the 550 ^{o}C-3h and to 3% total strain for the 600 ^{o}C-3h aged conditions. It was clear that both aging treatments resulted in perfect superelasticity with no irrecoverable strain.

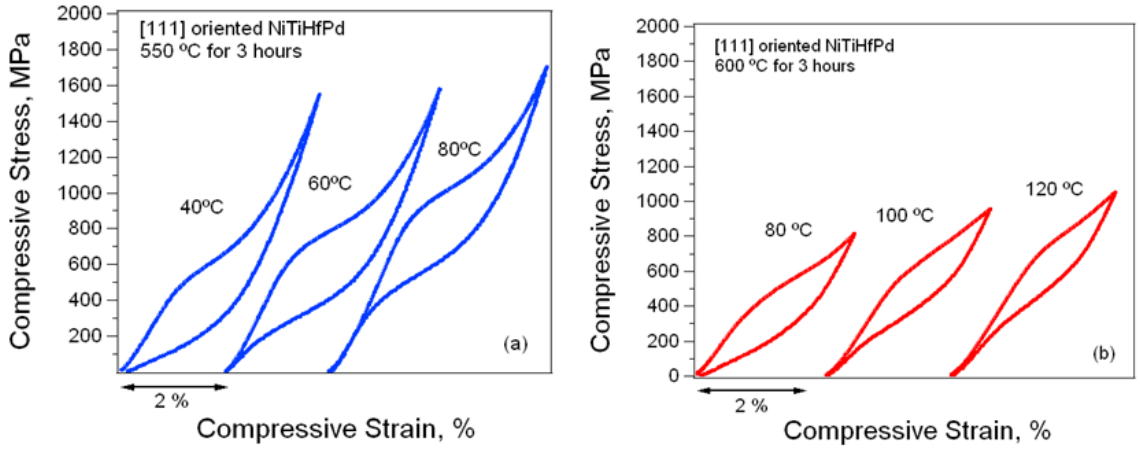

Figure 5.6: The stress vs. strain responses for the $Ni_{45.3}Ti_{29.7}Hf_{20}Pd_5$ alloys aged at a) 550 ^{o}C for 3h and b) 600 ^{o}C for 3h.

The C-C slopes were 11 MPa/ ^{o}C and 11.6 MPa/ ^{o}C for the 550 ^{o}C-3h and 600 ^{o}C-3h aged specimens, respectively. For the same material in the solution-treated condition, the C-C slope was 9 MPa/ ^{o}C [11]. Previous studies have reported C-C slopes of approximately 7 MPa/ ^{o}C in peak aged $Ti_{49.2}Ni_{50.8}$ and 6.5 MPa/ ^{o}C for $Ti_{48.5}Ni_{51.5}$ single crystals in the [111] direction [42, 59].

Pertinent shape memory and superelastic properties for this single crystal alloy are summarized in Table 2. These include M_s, maximum transfromation strains extracted from Figure 5.5 (SME strain) and Figure 5.6 (SE strain), Clausius-Clapeyron slopes (obtained from Figure 5.5), stress hystereses extracted from Figure 5.6, and temperature hystereses under 100 MPa and 1000 MPa isobaric stress conditions (extracted from Figure 5.5). It was clear that transformation temperatures increased with aging temperature for constant aging time. M_s was approximately 10 ^{o}C and 50 ^{o}C (at a stress level of 100 MPa) for the 550 ^{o}C-3h and the 600 ^{o}C-3h aged single crystals, respectively.

In the solution-treated condition, M_s was predicted to be less than -200 ^oC [11]. The increase in TTs can be attributed to the formation of (Ni+Pd)-rich precipitates upon aging at 550 ^oC (Figure 5.4) and their increase in volume fraction by elevating the aging temperature to 600 ^oC for the same aging time. It is well known that in NiTi based alloys, TTs increase by formation of Ni-rich precipitates since they deplete the matrix of Ni moving the matrix composition closer to stoichiometry and thus to higher transformation temperatures [2, 44].

Table 2: Comparison of shape memory parameters for solution-treated [15] and aged $Ni_{45.3}Ti_{29.7}Hf_{20}Pd_5$ single crystals along the [111] orientation in compression

Material	M_s (^oC)	SME strain (%)	SE strain (%)	C-C slope (MPa/ ^oC)	Stress Hysteresis (MPa)	Temperature Hysteresis (^oC)
Solutionized	<-200	-	4.2	9	1270-900	-
550 ^{o}C-3h	~10	2.2	2.2	11.1	400-365	50-38
600 ^{o}C-3h	~50	2	1.6	11.6	250-235	35-55

Mechanical hysteresis was graphically evaluated from Figure 5.6. For the 550 ^oC-3h aged sample, stress hysteresis was 400 MPa at 40 ^oC and 365 MPa at 80 ^oC. It was 250 MPa at 80 ^oC and 235 MPa at 120 ^oC for the 600 ^oC-3h aged sample. It should be noted that the stress hysteresis of the solution treated material was abut 1270 MPa at -30^oC and 900 MPa at 70^oC [11]. It was clear that as testing temperature increased, stress hysteresis decreased in all cases. Furthermore, stress hysteresis decreased with aging

temperature. The difference in stress hysteresis can be attributed to a change in martensite morphology and/or compatibility of the transforming phases with aging and testing temperature. When the compatibility between the transforming phases was better, less dissipation was expected [95]. It should be noted that compatibility depends on the lattice parameters of the transforming phases, which are subsequently depended on matrix composition and temperature. Therefore, it was possible that both aging and testing temperature could alter the lattice parameters in a manner that could result in improved compability. In the $Ni_{45.3}Ti_{29.7}Hf_{20}Pd_5$ alloy, aging had concurrent effects as it alters the matrix composition (increases the transformation temperatures) and decreased the stress hysteresis.

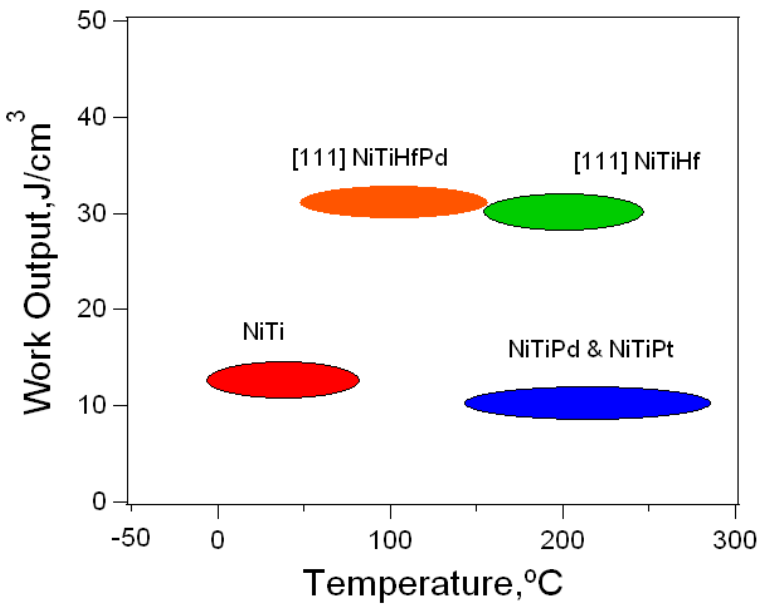

Figure 5.7: Comparison of the work output energy densities for NiTi-based shape memory alloys as a function of operation temperature.

A unique aspect of the [111]-oriented $Ni_{45.3}Ti_{29.7}Hf_{20}Pd_5$ single crystals was their high work output energy density, which was calculated by multiplying the recoverable strain and the applied stress from the constant stress thermal cycling experiments. Work output is a crucial criterion for solid-state actuators, especially for applications in the aerospace industry. A comparison of the work output for various NiTi-based SMAs is shown in Figure 5.7. It was reported that NiTi alloys can generate work output values exceeding 10 $J.cm^{-3}$ [14]. Above 100 ^{o}C, Ni-Ti-Pd and Ni-Ti-Pt SMAs have relatively high work outputs that are on the order of 9 $J.cm^{-3}$ to 13 $J.cm^{-3}$ [15][125]. For the [111]-oriented $Ni_{45.3}Ti_{29.7}Hf_{20}Pd_5$ single crystal, the work output was 33 $J.cm^{-3}$ after aging at 550 ^{o}C for 3 hours and 20 $J.cm^{-3}$ after 600 ^{o}C-3h aging. The former had similar work output to a [111] oriented ternary NiTiHf (30 $J.cm^{-3}$) alloy [118], and all the NiTiHfPd single crystals have higher work outputs than those of NiTiPd and NiTiPt alloys, but at lower temperatures. Finally, the energy absorption capacity was determined to be around 3-4 $J.cm^{-3}$ and 7-8 $J.cm^{-3}$ for 600 ^{o}C-3h and 550 ^{o}C-3h aged samples, respectively. This was much smaller than for the solution treated $Ni_{45.3}Ti_{29.7}Hf_{20}Pd_5$, which was 44 $J.cm^{-3}$ due to the very wide mechanical hysteresis [11].

Aging provided the ability to tailor the TTs and increase the strength of certain alloys such as $Ni_{45.3}Ti_{29.7}Hf_{20}Pd_5$ alloys. However, the intrinsic high strength of the $Ni_{45.3}Ti_{29.7}Hf_{20}Pd_5$ can be attributed to a combination of solid solution strengthening due to the dissimilar atomic size of the elements (as demonstrated in the solution treated alloy [11]) and to precipitate strengthening, especially in the case of a fine homogeneous distribution of coherent nanosize particles as in the material aged at 550 ^{o}C-3h. This type of ultra high strength SMA would be promising for many applications where weight is

critical. The high energy density of the $Ni_{45.3}Ti_{29.7}Hf_{20}Pd_5$ alloy would provide the ability to deliver high forces through small electrochemical devices. Moreover, $Ni_{45.3}Ti_{29.7}Hf_{20}Pd_5$ alloys may be used in biomedical applications (assuming they have good biocompatibility) where high force and MRI compatible stents or implants are needed.

5.4. Effects of aging time on shape memory and superelasticity behavior of [111]-oriented $Ni_{45.3}Ti_{29.7}Hf_{20}Pd_5$ alloys

This section presents a detailed characterization studies after aging at 600 ^{o}C for durations of 3, 48 and 72 hours, while monitoring changes in microstructure and its subsequent effects on shape memory properties of $Ni_{45.3}Ti_{29.7}Hf_{20}Pd_5$ single crystals along the [111] orientation in compression.

Figure 5.8 shows the constant stress thermal cycling behavior of [111] oriented $Ni_{45.3}Ti_{29.7}Hf_{20}Pd_5$ single crystals aged at 600 ^{o}C for 3, 48 and 72 hours. Transformation strain was graphically measured as the difference between the cooling and heating curves at the M_s temperature while the tangent line method was used to determine TTs, as conducted previously. Transformation strain and TTs at 100 MPa and 1000 MPa were derived from Figure 5.8 and summarized in Table 3. M_s of the 3, 48 and 72 hours aged samples were 61 ^{o}C, 103 ^{o}C and 125 ^{o}C at 100 MPa, respectively. It should be noted that the M_s under zero stress was extrapolated to be ~ -270 ^{o}C in solutionized (at 1050 ^{o}C for 4 hours) $Ni_{45.3}Ti_{29.7}Hf_{20}Pd_5$ single crystals [123]. The increase in TTs after aging the solutionized material can be attributed to compositional changes of the $Ni_{45.3}Ti_{29.7}Hf_{20}Pd_5$ matrix due to precipitation [2, 44].

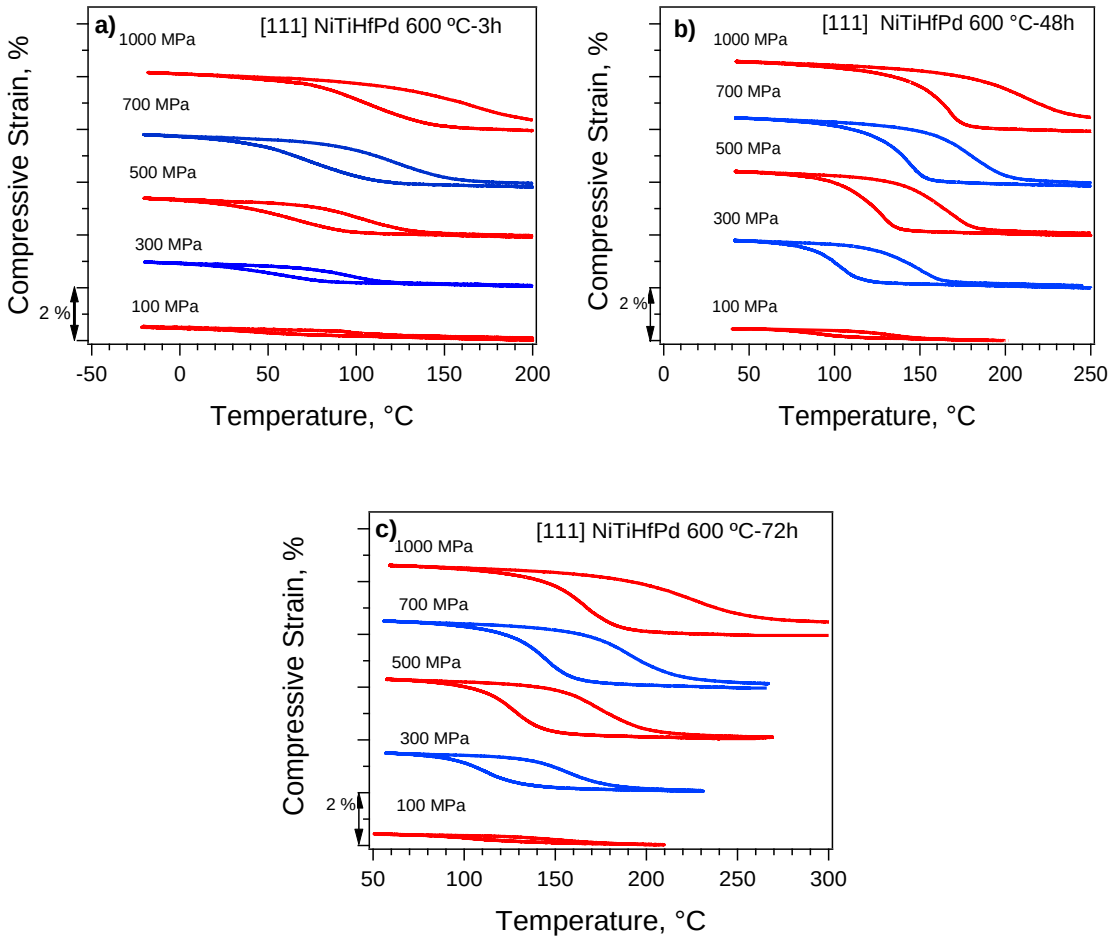

Figure 5.8: Shape memory effect of $Ni_{45.3}Ti_{29.7}Hf_{20}Pd_5$ single crystals aged at 600 ^{o}C for a) 3 hours, b) 48 hours and c) 72 hours as a function of applied compressive stress.

All the aged single crystals showed perfect shape memory effect at 500 MPa and limited residual strain even at 1000 MPa above temperatures of 100 ^{o}C which can be advantegeous for high temperature/high strength applications. Transformation strains of the samples aged at 600 ^{o}C for 3, 48 and 72 hours at 1000 MPa are 2.1 %, 2.5 % and 2.6 %, respectively. The shape memory strain of the 3 hours aged sample was lower than those of the ones aged for longer times. There are several possible explanations for this behavior. One of the reasons for less strain in the 3 hour aged specimen could be the

difficulty in selection and growth of favored martensite variants due to the stress fields around the fine, closely spaced, coherent precipitates. Another reason for the lower strain after 3 hours of aging could be attributed to the presence of untransformed local regions in the microstructure. Due to very small interparticle distances, some local regions of the microstructure might have already experienced plastic deformation before any transformation [78, 79]. Another reason could be the lack of detwinning in the martensite. Detwinning of the martensite could be restricted by the small, coherent particles, which could lower the total recoverable strain, as in the case for $Ti_{49.62}Ni_{50.38}$ (at %) single crystals [80].

Transformation strains for the samples aged for 48 and 72 hours were comparable. This can be attributed to the similar size, shape, and volume fraction of the precipitates for these two aging conditions. As clearly seen in Figure 5.8, the shape memory curves in the 3 hours aged material were more gradual, i.e., not as steep as in those of the 48 and 72 hours aged materials.

Temperature hysteresis was determined graphically at the midpoint of the transformation strain between the cooling and heating curves. Temperature hysteresis of the aged samples were very close initially (35-37 ^{o}C) at 100 MPa and was almost constant up to 700 MPa for all aged specimens. Then, it increased to 55 ^{o}C, 52 ^{o}C and 65 ^{o}C as applied stress was increased to 1000 MPa for 3, 48 and 72 hours of aging, respectively. The reason of the abrupt increase in hysteresis could be attributed to dislocation generation due to plastic deformations which are evident from the unclosed thermal cycling loops at stress levels above 700 MPa.

A linear relationship between M_s and applied stress was observed for the aged single crystals. The C-C slopes representing the aforementioned correlation are 11.9 MPa/^{o}C, 12.8 MPa/^{o}C and 15.7 MPa/^{o}C for the samples aged for 3, 48, and 72 hours, respectively. The C-C slopes for the current specimens were comparable to the values for [111]-oriented Ni-rich NiTiHf single crystals (i.e., 11.6 MPa/ ^{o}C [118] while they are higher than the C-C slopes of [111]-oriented NiTi single crystals, which are 6.5-7 MPa/ ^{o}C [42, 59].

The superelastic behavior of the single crystal specimens aged at 600 ^{o}C for 3, 48, 72 hours are shown in Figure 5.9. The specimens were first loaded to a total strain of 2 %, unloaded, and then loaded to 3 % strain at selected test temperatures.

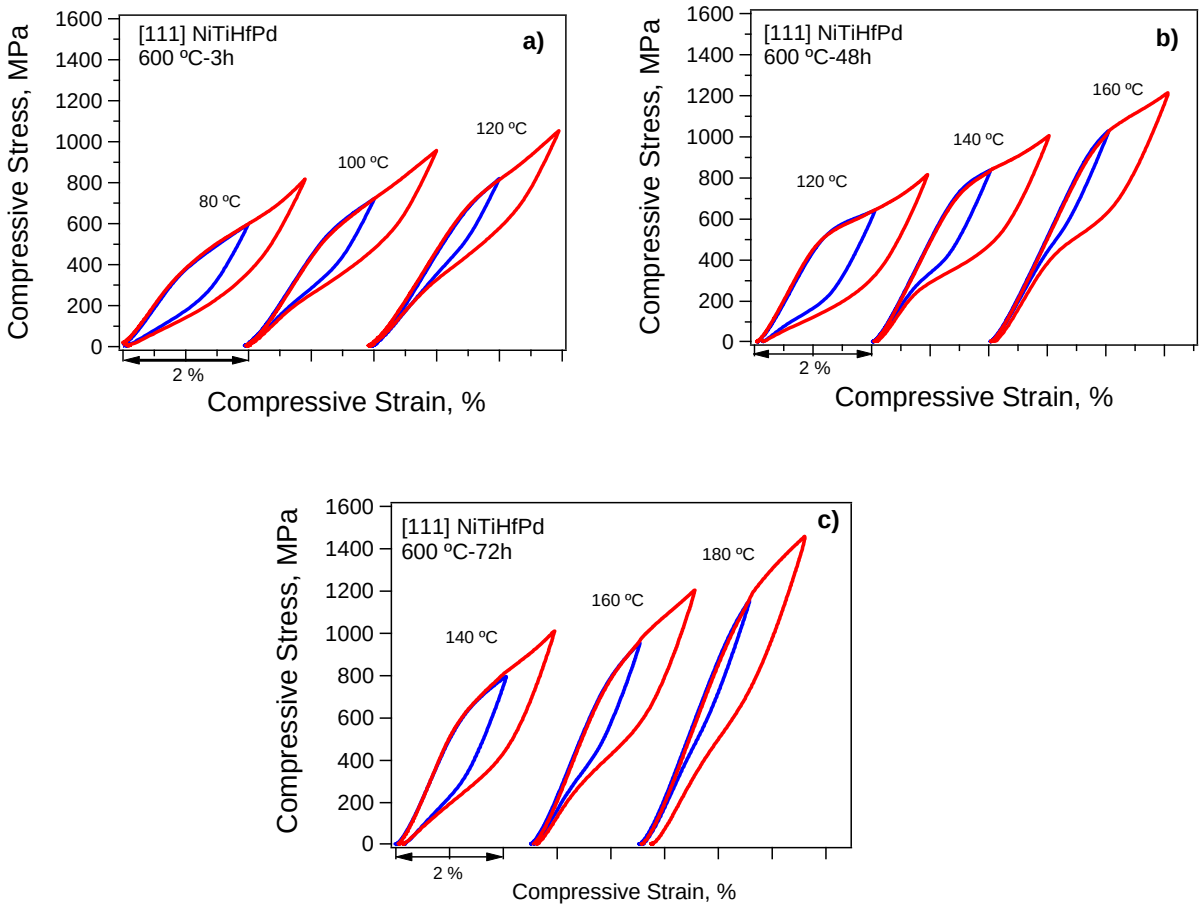

Figure 5.9: The stress vs. strain responses of $Ni_{45.3}Ti_{29.7}Hf_{20}Pd_5$ single crystals aged at 600 ^{o}C for a) 3 hours, b) 48 hours and c) 72 hours.

For each aging treatment, near perfect superelastic response was observed at test temperatures above 100 ^{o}C at compressive stress levels between 1000 and 1400 MPa. This respose can be utilized for industrial applications demanding elevated temperatures and greater material strength. In all the superelastic curves, high hardening was observed during stress induced martensitic transformations in contrast to NiTi alloys [2]. Similar behavior is commonly observed in NiTiHf alloys and responsible for the lack of

superelasticity [23]. Due to stronger matrix in $Ni_{45.3}Ti_{29.7}Hf_{20}Pd_5$ high hardening did not result in a loss of the superelasticity behavior.

The mechanical hysteresis (stress hysteresis) values were determined as the difference between the loading and unloading lines at the corresponding midpoint value of the applied strain in Figure 5.9. The stress hysteresis range was 235-249 MPa, 341-385 MPa and 376-423 MPa for 3, 48 and 72 hours aging, respectively. Mechanical hysteresis tended to decrease with testing temperature for the 3 hours aged specimen, while it increased with temperature for both 48 and 72 hours aged samples.

5.5. Microstructural dependence of the shape memory properties in [111]-oriented $Ni_{45.3}Ti_{29.7}Hf_{20}Pd_5$ alloys

In NiTi-based shape memory alloys, thermo-mechanical treatments have been one of the most powerful tools to improve/alter the mechanical properties of an alloy [2], hence many research efforts have been on this direction [4, 42, 58, 113, 114, 126-128]. It was mentioned that the precipitation formation is found to be an effective method to alter the crucial shape memory properties such as matrix strength [58], transformation strain [114], transformation temperatures [44] and transformation stress [4]. The microstructure characteristics (e.g. precipitate size & coherency, interparticle distance, grain size) have been found to be very effective in tailoring the detwinning [80] and the elastic energy storage processes [129, 130] in addition to the aforesaid shape memory properties.

In the current study, the effects of microstructure on shape memory properties of [111] oriented $Ni_{45.3}Ti_{29.7}Hf_{20}Pd_5$ single crystals were investigated. The constant-stress shape memory behavior of [111] single crystals was compared for as-grown plus aged

(550 °C-3h) samples versus crystals that were first solution-treated and then aged. In contrast, given the large and stable superelastic response observed previously for solution-treated crystals [22], the superelastic response of [111]-oriented $Ni_{45.3}Ti_{29.7}Hf_{20}Pd_5$ single crystals was analyzed in four conditions: the as-grown single crystal, solution-treated, as-grown+aged, and solution-treated+aged. Significant differences in superelastic response were observed in the various conditions and attributed to stark changes in the microstructure. Some specimens were aged at 550 ^{o}C for 3 hours in air and they are named as "as-grown+aged" in the text. Other compression specimens were solutionized at 1050 ^{o}C for 4 hours in sealed quartz tubes (to avoid oxidation) followed by water quenching. They were aged at 550 ^{o}C for 3 hours in air after the solution treatment and named as "solution-treated+aged" throughout the text for brevity.

Figures 5.10a and 5.10b are bright field TEM micrographs and corresponding selected area diffraction (SAD) patterns taken at RT for the $Ni_{45.3}Ti_{29.7}Hf_{20}Pd_5$ single crystals in the as-grown and solution-treated conditions, respectively. The as-grown and solution-treated materials were composed of austenite with B2 structure, and precipitates were not observed in the bright field micrographs of either material. However, in the SAD pattern obtained from the as-grown specimen, shown as an insert in Figure 5.10a, circular diffuse scattering could be seen in addition to the fundamental reflections of the B2 austenite phase. The diffuse scattering is most likely caused by tiny precipitates, which were too small to be observed by conventional TEM, inherited from the slow cooling during the growth of the single crystals. Sandu et al. [131] have reported the same diffuse scattering in an aged NiTiZr alloy (as can be seen in Figure 5.11 of Reference [131]). Little or no diffuse scattering was observed in the diffraction patterns

of the solution-treated specimen, shown in Figure 5.10b, indicating that the specimen has fewer/negligible precipitates, as expected.

In contrast to the as-grown and solution-treated specimens, precipitates were clearly observed in the aged materials. The bright field micrographs obtained from the as-grown+aged and solution-treated+aged specimens are presented in Figures 5.10c and 5.10d, respectively. For the as-grown+aged specimens, the estimated length of the long axis of the spindle shaped precipitates was $\approx$20-30 nm and the interparticle distance was $\approx$ 40-60 nm. On the other hand, the solution-treated+aged samples had thinner precipitates with a length of $\approx$15-20 nm along the long axis and a smaller interparticle distance of $\approx$15-20 nm.

The differences in the precipitate size and interparticle distance for the aged samples are attributed to the differences in the initial microstructures of the samples before aging. In the as-grown materials, very small precipitates (<5nm) are present, while after solution-treatment, the microstructure was expected to be essentially precipitate free, as evident from the respective SAD patterns. During aging of the as-grown material, the previously existing precipitates simply coarsen into larger precipitates with longer interparticle distances as shown in Figure 5.10c. On the other hand, in the solution-treated material, aging results in nucleation and growth of smaller precipitates with shorter interparticle distances as shown in Figure 5.10d. In the as-grown crystal, nucleation of the precipitates occurred as the material slow cooled during solidification so that nucleation occurred at higher temperatures with less excess solute and therefore fewer nucleation sites than if the material is aged directly from the quenched condition at 550 °C. Thus, while precipitation was homogeneous in both cases, it would be expected

that a much greater density of fine precipitates will form in the solution-treated and aged sample, as shown in Figure 5.10.

In the SAD pattern shown in Figure 5.10c, there were superlattice reflections at 1/2 positions along $<110>_{B2}^{*}$ in reciprocal space, which correspond to the B19′ martensite phase in the as-grown+aged material. Figure 5.10d shows that martensite in the solution-treated+aged samples consisted of large plates with many precipitates incorporated inside a single lathe. In this case, the formed precipitates were embedded in large martensite plates. The large martensite plates observed in Figure 1d were related to $\{011\}_{B19'}$ type I twinning, which was frequently observed in NiTiHf alloys [48, 54, 132]. It should be noted that the martensite phase observed in the solution-treated+aged specimen was probably formed during the electropolishing process, since the martensitic transformation start temperatures of the solution-treated+aged specimen was determined by extrapolation to be ≈-2 °C, as will be discussed later. Figure 5.10e shows the dark field image taken from the as-grown+aged specimen using the superlattice reflection circled in the SAD pattern. It was clear that the martensite plates were formed between the precipitates instead of bypassing the precipitates.

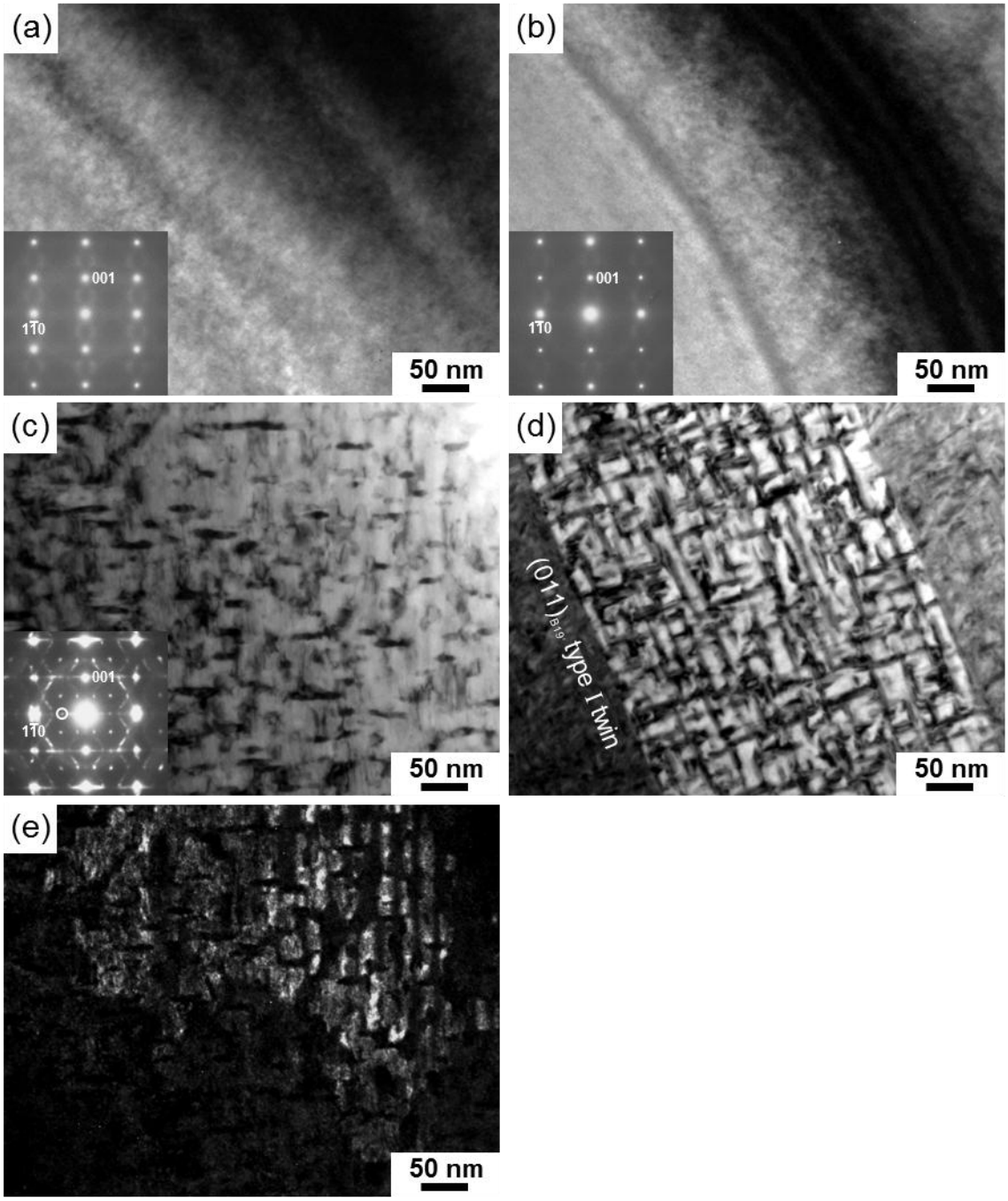

Figure 5.10: Bright field TEM micrographs of $Ni_{45.3}Ti_{29.7}Hf_{20}Pd_5$ in the (a) as-grown, (b) solution-treated, (c) as-grown + aged at 550 ^{o}C for 3 hours, and (d) solution-treated + aged at 550 ^{o}C for 3 hours conditions, (e) Dark field TEM micrograph of (c) showing the

martensite phase. The insets in (a), (b), and (c) are the corresponding $[110]_{B2}$ SAD patterns.

Figure 5.11 shows the shape memory responses of the as-grown+aged $Ni_{45.3}Ti_{29.7}Hf_{20}Pd_5$ single crystals as a function of applied stress along the [111] orientation with limited comparison to the solution-treated+aged condition. Thermal cycles were conducted between a temperature above the austenite finish temperature and below the martensite finish temperature under compressive stresses ranging from 300 MPa to 1000 MPa. The transformation temperatures were determined by the tangent method from the inflection points of the shape memory curves and the transformation strains were measured between the heating and cooling lines at the M_s temperature.

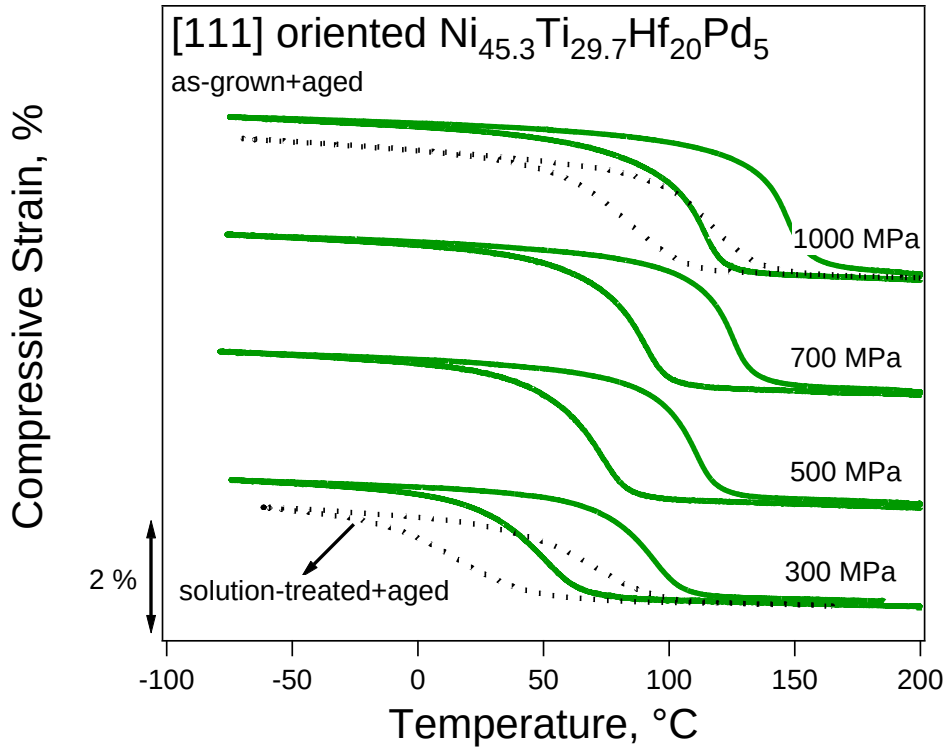

Figure 5.11: The strain-temperature responses of [111] oriented as-grown+aged and solution-treated+aged $Ni_{45.3}Ti_{29.7}Hf_{20}Pd_5$ single crystals.

M_s temperatures were 65 ^oC and 123 ^oC in the as-grown+aged specimen under 300 MPa and 1000 MPa, respectively. The transformation strains were 2 % and 2.5 % under 300 MPa and 1000 MPa, respectively. In comparison, the solution-treated+aged specimen had M_s of 38 ^oC and 106 ^oC and transformation strains of 1.55 % and 2.15 % under 300 MPa and 1000 MPa, respectively. As expected, the transformation temperatures and the transformation strains increased with stress in both aged materials.

It was clear that the form of the shape memory curves was different in the two aged materials. The transformation took place more rapidly (higher slope in the transformation region of the shape memory curves) in the as-grown+aged specimen while

it was more shallow (lower slope in the shape memory curve) in the solution-treated+aged specimen during cooling and heating. The reason for the shallow transformation with temperature in the solution-treated+aged $Ni_{45.3}Ti_{29.7}Hf_{20}Pd_5$ single crystal could be attributed to larger elastic energy storage compared to the as-grown+aged material [107, 129], which can be explained based on the differences in the martensite formation types.

The precipitate-martensite interaction could be the main reason in the different shape memory responses and elastic energy storage in the aged $Ni_{45.3}Ti_{29.7}Hf_{20}Pd_5$ single crystals [11, 129]. In the solution-treated+aged alloy, the precipitates were small and interparticle distance was short enough, thus the growing martensite plates tried to bypass and surround nearby precipitates resulting in larger martensite plates with embedded precipitates as it has been previously observed in CuAlMn SMAs [133]. The elastic energy storage could be observed as gradual increase/decrease in shape memory curve in thermal cycling experiments as mentioned earlier. In the solution-treated+aged alloy, the growth of martensite was slower and harder due to the process of trying to bypass and encapsulate precipitates in the microstructure. Thus, energy required to complete the transformation increased resulting in high elastic energy storage [11, 120, 129, 134] and lower slope strain-temperature curve in the solution-treated+aged alloy.

However, when the interparticle distances were large enough as in the as-grown+aged alloy, the martensite plates would not be able to bypass the precipitates but instead tended to form in the channels between the precipitates (as in Figure 5.10c) as also observed $Ni_{45.3}Ti_{29.7}Hf_{20}Pd_5$ single crystals aged at 600 ^{o}C for 48 and 72 hours [107]. In this case, the size of the martensite plates were determined by the interparticle

distances. The strain fields surrounding the precipitates might favor the nucleation of martensite plates between the precipitates due to the larger particle size and interparticle distance as shown in Figure 5.10c. This mechanism can make the transformation easier without large elastic energy storage and can be displayed as steeper strain-temperature curves as in Figure 5.11.

It should be noted that the observed results are similar to $Ni_{45.3}Ti_{29.7}Hf_{20}Pd_5$ polycrystalline alloys [92] while they are not to $Ni_{50.3}Ti_{29.7}Hf_{20}$ and $Ni_{50.3}Ti_{29.7}Zr_{20}$ polycrystalline shape memory alloys [16, 135]. In the extruded and aged quaternary $Ni_{45.3}Ti_{29.7}Hf_{20}Pd_5$ alloys, as the martensite was formed between precipitates, the slope of the shape memory curves in the thermal cycling experiments was either low (indicating hard transformation) or steep (indicating easier transformation) depending on aging condition. As the material was aged at 550 ^{o}C for 3 hours, the precipitates were formed in size of 20-30 nm with interparticle distance of 10-30 nm. In this case, the martensite was formed between precipitates resulting in lower strain-temperature curve slope due to hard transformation. However, as the material was aged at 650 ^{o}C for 3 hours, the precipitates were coarsened in size which were $\approx$ 80-300 nm in length and $\approx$50 nm in width while the interparticle distance was varied between 15-150 nm. In this case, the martensite formation was constrained between large precipitates that had larger interparticle distances and the transformation was easier compared to the 550 ^{o}C-3h case. Thus, the slope of the strain-temperature curves were steeper [92].

The slope of the shape memory curves in the thermal cycling experiments were lower when the precipitates were constrained between the formed precipitates while the slope was steeper as the small precipitates were embedded in big martensite plates.In the

$Ni_{50.3}Ti_{29.7}Hf_{20}/Zr_{20}$ alloys, effects of different aging conditions on the interpaticle distances and possible effects of these interparticle distances on the growth of martensite plates should be revealed. Another possible difference between the ternary and the quaternary $Ni_{45.3}Ti_{29.7}Hf_{20}Pd_5$ alloys could be a possible difference in the mobility of the martensite plates. There is a 5 % Pd addition in the quaternary alloy and that addition increased the lattice parameters of the transforming phases [92]. This could limit the mobility of the phase front and increase the energy for martensite propagation in the $Ni_{45.3}Ti_{29.7}Hf_{20}Pd_5$ alloys compared to the ternary alloys. Thus, a more detailed study should be conducted to understand the nature (internal twinning, compatibility, twinning density dependent interparticle distance etc.) of the differences in the shape memory responses (easy or hard transformation) between the ternary $Ni_{50.3}Ti_{29.7}Hf_{20}/Zr_{20}$ and the quaternary $Ni_{45.3}Ti_{29.7}Hf_{20}Pd_5$ alloys.

Another indication that the elastic energy storage in the solution treated+aged sample was higher compared to the as-grown+aged sample was the change in the transformation type observed in the thermal cycling curves under 1000 MPa. The as-grown+aged sample had an M_s of 123 ^oC and A_s of 135 ^oC while the solution treated+aged sample had an M_s of 106 ^oC and A_s of 98 ^oC under 1000 MPa as shown in Figure 5.11. The transformation type of the as-grown+aged material was “Class I” since its M_s was lower than A_s ($M_s<A_s$). In contrast, the transformation for the solution-treated+aged material was “Class II”, since its M_s was higher than A_s ($M_s>A_s$) [136]. The change in the transformation types from “Class I” to “Class II” is typically attributed to additional elastic energy storage [92, 111], which helps the back transformation and

consequently results in a lowering of A_s. Similar behavior was previously reported for $Ni_{45.3}Ti_{29.7}Hf_{20}Pd_5$ polycrystalline alloys [92].

The stress-strain responses of [111] oriented $Ni_{45.3}Ti_{29.7}Hf_{20}Pd_5$ single crystals in both the as-grown and the solution-treated plus quenched conditions are shown in Figure 5.12. The samples were initially loaded to a strain of 3 % and unloaded isothermally at various temperatures above A_f. Subsequently, the sample was reloaded with the strain value increased by 1 % for each additional strain cycle up to a total strain of 6 %. The final stress-strain curves to 6 % strain for the solution-treated plus quenched material at -30 and 10 °C are include in Figure 5.12 for a direct comparison of the stress hysteresis for the two conditions.

The initial linear portion of the stress-strain curves represents the elastic deformation of austenite. This is followed by a plateau like region due to the stress induced martensitic transformation, transitioning to a region of higher work hardening due to elastic deformation and detwinning/reorientation of the stress-induced martensite. During unloading, elastic unloading of the martensite is followed by the martensite-to-austenite back transformation and finally elastic unloading of austenite. It was clear that fully reversible superelasticity was observed in both materials with a large SE window for the as-grown crystals ranging from below -30 ^oC to 70 ^oC. The maximum transformation strain was 4.4 % at – 30 ^oC. The elastic moduli of the austenite and martensite phases were calculated to be 48-59 GPa and 87-97 GPa, respectively for the as-grown single crystal.

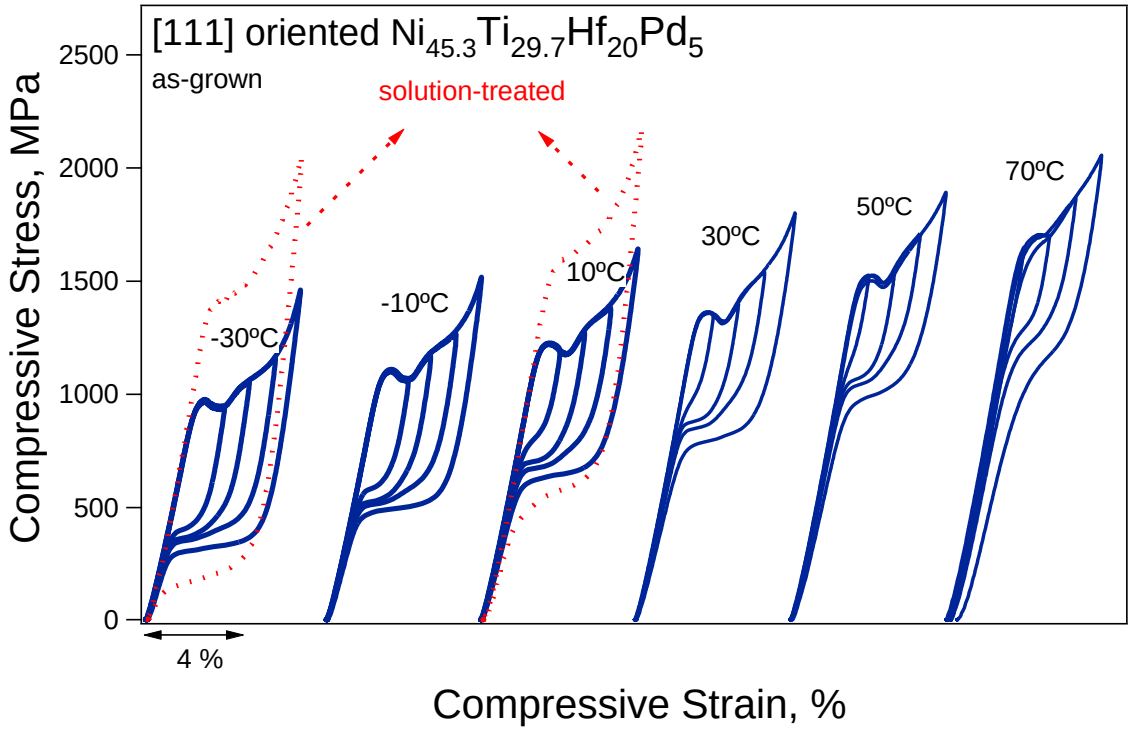

Figure 5.12: The superelastic responses of [111]-oriented $Ni_{45.3}Ti_{29.7}Hf_{20}Pd_5$ alloys in as-grown and the solution-treated conditions as a function of temperature.

In addition to a large transformation strain of 4.4 %, the as-grown $Ni_{45.3}Ti_{29.7}Hf_{20}Pd_5$ single crystals displayed perfectly closed superelastic loops, even when the applied stress levels reached 2 GPa with little or no plastic deformation along the [111] orientation. Beside the high strength, they had relatively large mechanical hysteresis ranging from 720 MPa at -30 ^{o}C to 560 MPa at 70 ^{o}C. But these values were roughly half that for the solution-treated+quenched single crystals, which nonetheless were anomalously large.

The superelastic behavior of the solution-treated and quenched [111] oriented $Ni_{45.3}Ti_{29.7}Hf_{20}Pd_5$ single crystals at test temperatures of -30 ^{o}C and 10 ^{o}C are also presented in Figure 5.12 for comparison. Its SE window was previously determined to be

between – 30 ^{o}C and 70 ^{o}C with a maximum transformation strain of 4.2 % at – 30 ^{o}C and elastic moduli of the austenite and martensite phases of 65-75 GPa and 100-110 GPa, respectively [137]. It should be noted that it was quite remarkable to get over 4 % strain under 2.5 GPa without any plastic deformation. Compared to the as-grown specimens, the solution-treated samples had larger mechanical hysteresis ranging from 1270 MPa and 830 MPa at – 30 ^{o}C and 70 ^{o}C, respectively, and a higher hardening rate was observed in the transformation regime [137].

Figure 5.13 shows the superelastic responses of the as-grown+aged single crystals along the [111] orientation in compression. The samples were simply loaded to a strain of 4 % and unloaded, at various temperatures above A_f ranging between 80 ^{o}C and 200 ^{o}C. Nearly complete superelastic responses were obtained at temperatures as high as 160 ^{o}C, with increasing levels of irrecoverable strain observed in the SE curves at temperatures above 160 ^{o}C.

The superelastic response of the solution-treated+aged single crystal at 80 ^{o}C [138] is included in Figure 5.13 for comparison. It is evident that the hardening rate in the transformation region is much higher in the solution-treated+aged specimen while there is almost “Luders type” transformation in the initial stress-strain curves of the as-grown+aged single crystal. Transformation strain was 2.6 % in the as-grown+aged condition while it is 2.1 % in the solution-treated+aged single crystal when deformed to a total strain of 4% at 80 ^{o}C.

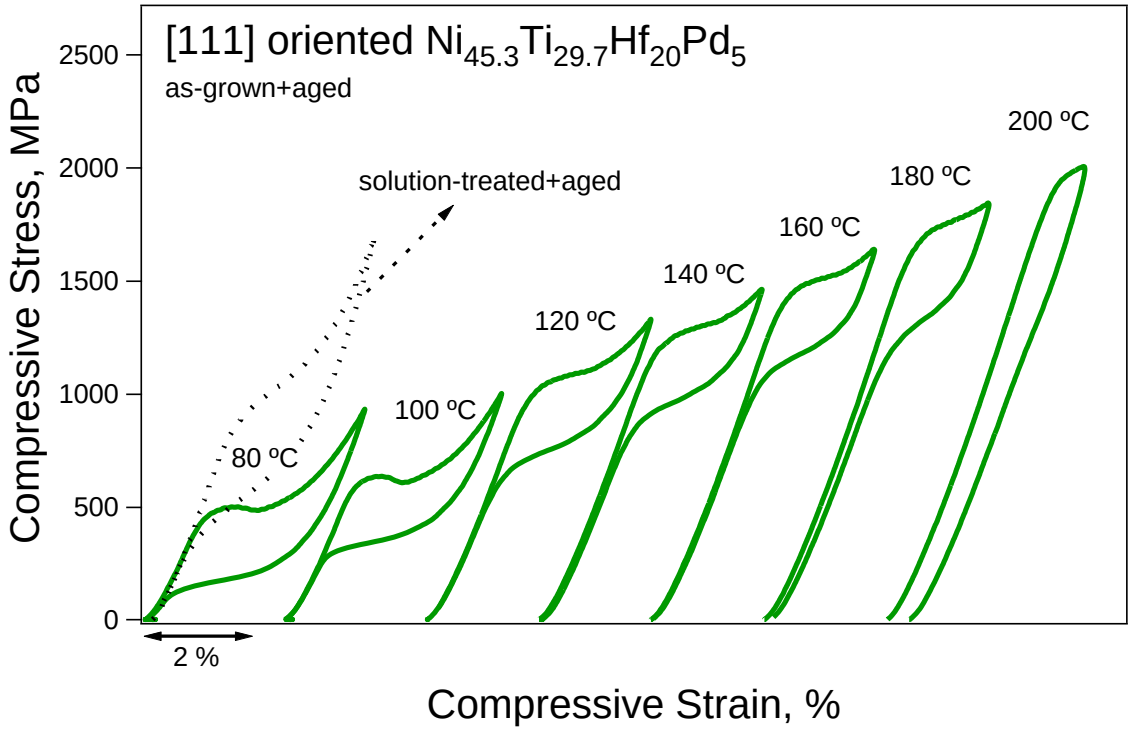

Figure 5.13: The stress-strain responses of [111]-oriented $Ni_{45.3}Ti_{29.7}Hf_{20}Pd_5$ single crystals in as-grown+aged and solution-treated+aged conditions.

Figure 5.14a summarizes the critical stresses for the onset of stress induced martensite formation as a function of test temperature as determined from the SE experiments. The C-C slopes were 6.8 MPa/^{o}C, 9 MPa/^{o}C, 12.2 MPa/^{o}C and 11.4 MPa/^{o}C for the as-grown, solution-treated, as-grown+aged and solution-treated+aged single crystals, respectively. The data in Figure 5.14a indicates that the solution-treated material had higher critical stresses than the as-grown material, while the solution-treated+aged single crystals had higher critical stress levels at equivalent test temperatures compared to the as-grown+aged single crystals. For instance, the critical stress was 1380 MPa and 950 MPa in the solution-treated and in the as-grown single crystals, respectively, at -30 ^{o}C,

while it was 900 MPa in the solution-treated+aged sample and 615 MPa in the as-grown+aged sample at 80 ^{o}C.

The slopes of the as-grown and solution-treated samples were similar in magnitude as were the as-grown+aged and solution-treated+aged single crystals, with the slopes of the former pair slightly smaller than the latter. Consequently, the differences in the transformation stress at a given temperature for each pair of samples (unaged and aged) could be attributed to the lower TTs of the solution treated and solution-treated+aged samples compared to their as-grown counterparts. Since the solution-treated materials had lower TTs, the austenite phase would be more stable at equivalent test temperatures and therefore in order to start SIM, additional stress would be needed.

The as-grown, solution-treated, as-grown+aged and solution-treated+aged single crystals had extrapolated (Figure 5.14a) M_s of $\approx$-170 ^{o}C, $\approx$-270 ^{o}C, $\approx$38 ^{o}C and $\approx$-2 ^{o}C, respectively, at 0 MPa. It was clear that the TTs were lower in the solution-treated and solution-treated+aged materials with respect to their as-grown and as-grown+aged counterparts. The higher transformation temperatures of the as-grown material, compared to the solution-treated condition, could be attributed to the small and randomly distributed precipitates that form during the slow-cooling process of the single crystal growth. In contrast to the as-grown material, there was little evidence of precipitation in the solution-treated condition. Due to chemical composition differences of the matrix due to precipitation, the TTs could be higher in the as-grown single crystal. Composition dependence of TTs is a well-known phenomenon in NiTi based SMAs [2]. As Ni-rich precipitates are formed in Ni-rich NiTi based alloys, TTs increase. The same ternd is observed with preciptate formation in NiTiPt [56], NiTiPd [57] and NiTiHf [58] alloys.

Similary, aging significantly increased the transformation temperatures of the $Ni_{45.3}Ti_{29.7}Hf_{20}Pd_5$ single crystals (Fig. 5.14a), with the as-grown+aged material, containing larger and presumably a greater volume fraction of the precipitate phase, having slightly higher trasnformation temperatures than the solution-treated+aged material.

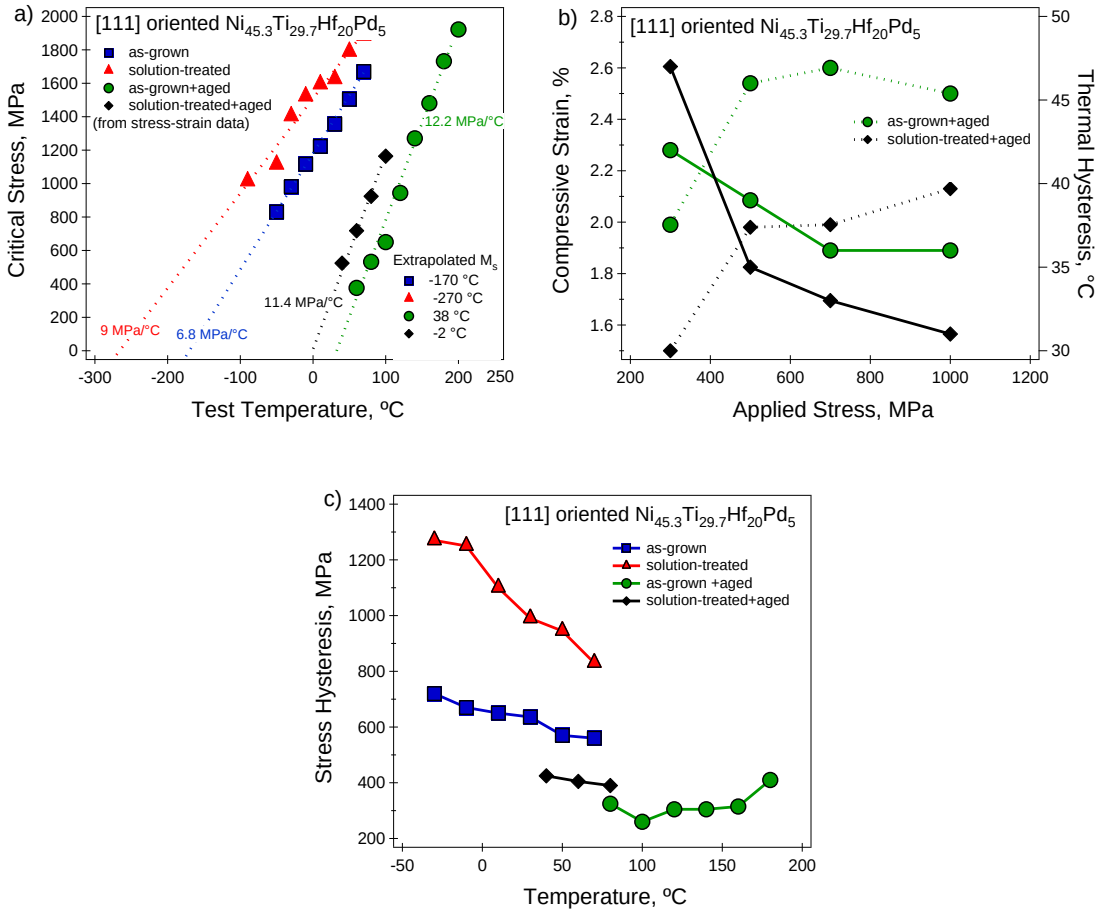

Figure 5.14: a) Transformation stress vs. temperature, b) temperature hysteresis (solid lines) & transformation strain (dotted lines) vs. compressive stress, and c) mechanical hysteresis as a function of temperature for [111]-oriented $Ni_{45.3}Ti_{29.7}Hf_{20}Pd_5$ shape memory alloys of various conditions

Figure 5.14b summarizes the transformation strains and the temperature hystereses as a function of stress, extracted from the strain-temperature responses shown in Figure 5.5a and Figure 11. The temperature hysteresis was graphically measured at the mid-point of the transformation strains between the cooling and heating curves. In the as-grown+aged sample, the temperature hysteresis decreased initially with stress up to 700 MPa and then saturated. The overall derease in hysteresis was relatively minor, only a 6 ^{o}C change between 300 and 1000 MPa.The temperature hysteresis of the solution-treated+aged material decreased abruptly from 47 ^{o}C to 37 ^{o}C as the stress increased from 300 MPa to 500 MPa and continued to decrease at a much slower rate to 28 ^{o}C at 1000 MPa. The initial decrease was attributed to a reduction in the number of active variants with stress and consequently, less variant interacion and friction, resulting in less hysteresis.

Transformation strains extracted from the thermal cycling experiments (Figure 5.11) were plotted as a function of applied stress in Figure 5.14b. The strain values started at 2 % at 300 MPa and peaked at 2.6% % at 700 MPa in the as-grown+aged sample and ranged from 1.55 % to 2.15 % in the solution-treated+aged sample at 300 MPa and 1000 MPa, respectively.

The difference in the transformation strains could be attributed to the ease with which the materials are capable of detwinning. It is known that if there are strong internal stresses (e.g. due to coherent precipitates or very fine-grained microstructure, etc), the detwinning process can be restricted. Since the precipitates were smaller and interparticle distances were shorter in the solution-treated+aged sample compared with the as-

grown+aged sample, detwinning might be reduced resulting in a smaller transformation strain as also reported for$Ti_{49.625}$-$Ni_{50.375}$ (at.%) single crystals [80].

Figure 5.14c shows the mechanical hystereses extracted from the superelastic stress-strain curves (Figures 5.1, 5.6a, 5.12 and 5.13) of the as-grown, solution-treated, as-grown+aged, and solution-treated+aged $Ni_{45.3}Ti_{29.7}Hf_{20}Pd_5$ single crystals. The stress hysteresis was calculated at the mid-point of the plateau strains between the forward and reverse transformations when the samples were loaded to 6 % strain in the as-grown and solution-treated materials and at 3 % strain in the as-grown+aged and solution-treated+aged materials. The [111] oriented $Ni_{45.3}Ti_{29.7}Hf_{20}Pd_5$ single crystalline alloys had mechanical hystereses of 1270 MPa and 720 MPa at -30 ^oC in the solution-treated and in the as-grown conditions, respectively. These values are relatively high compared to NiTi and NiTi-based alloys.For example, the mechanical hysteresis is 200-300 MPa in binary NiTi alloys [67] and 400-500 MPa in NiTiNb alloys [17]. However, a hysteresis as high as 1000 MPa has been reported in a recently published study on NbTi/NiTi nano-composites[19]. In the as-grown+aged material, the stress hysteresis values were between 300-380 MPa in the temperature range of 80-200 ^oC, and 400-365 MPa in the solution-treated+aged material at 40-80 ^oC. These values are much less than the unaged materials and more in line with typical nitinol materials.

For both the as-grown and the solution-treated materials, the stress hysteresis decreased with increasing test temperature. The decrease in the hysteresis could be rationalized by considering a possible increase in mobility of the martensite variants with temperature. Due to increased mobility of the variants, the movement of the phase front would be easier, occurring with less friction during the stress induced martensite

transformation, resulting in a decreasing hysteresis. In the as-grown+aged material, the stress hysteresis was essentially constant over a wide range in test temperature and then started increasing at the highest test temperature (160 ^{o}C). This increase in hysteresis at 160 ^{o}C is attributed to plastic deformation, as evidenced from the irreversible strain in the SE curve.

The stress hysteresis of the as-grown material was less than the solution-treated material (720 versus 1270 MPa at -30 ^{o}C), but both values are quite high compared to typical NiTi alloys [34, 35]. The high hysteresis has its source in part in the relatively high stress required for the forward austenite to martensite transformation in these materials. Comparatively, both materials have nearly the same stress requirement for the reverse martensite to austenite transformation, but the martensite start stress in the solution-treated alloy is nearly 50 % greater, resulting in about a 50% larger hysteresis. The high martensite start stresses may be due to high test temperatures compared to the transformation temperatures of the materials, since more stress is needed to initiate the transformation as the test temperature increases above A_f. While it was not possible to measure the transformation temperatures in these materials by a thermal analysis technique, the extrapolated M_s temperatures were -170 and -270 for the as-grown and solution treated materials, respectively, which is quite low. The requirement for significant unloading and therefore large hysteresis before the reverse transformation occurs is then microstructure/internal stress driven. The as-grown material contains a high density of very fine nanometer sized precipitates with probably overlapping stress fields. The internal stress would actually help promote martensite formation so that a large amount of unloading is required to get a point where the reverse martensite to

austenite transformation can occur. The solution-treated material, however, is essentially precipitate free but actually has a larger hysteresis. It is possible that in this material a preponderance of anti-site defects or clustering of point defects (since of all material conditions, this one would have a matrix composition farthest from stoichiometry) creates and even larger internal stress requiring an even larger unloading requirement for the reverse transformation to start. However, without a technique like neutron diffraction to corroborate the internal stress state, this is purely conjecture.

$Ni_{45.3}Ti_{29.7}Hf_{20}Pd_5$ has natural advantages of higher strength and moderate temperature capability, which could make the material suitable for high strength/force actuator applications, compared to conventional near-equiatomic NiTi alloys. Additionally, the material exhibits a large stress hysteresis around room temperature and may be valuable in high damping applications. The high strength can also provide advantages to $Ni_{45.3}Ti_{29.7}Hf_{20}Pd_5$ in saving on weight and portability of compact systems in places where the volume is important. The ability to govern the shape memory properties, including transformation temperatures, via microstructural control is a benefit of $Ni_{45.3}Ti_{29.7}Hf_{20}Pd_5$ alloys since this control can be achieved by simple heat treatments without requiring extra processes such as cold rolling, extrusion, or other thermo-mechanical treatments.

5.6. Summary and conclusions

The shape memory behavior under constant stress and superelastic properties of the [111] oriented $Ni_{45.3}Ti_{29.7}Hf_{20}Pd_5$ alloys were investigated through mechanical tests. Microstructural features were studied by TEM and consequently, following conclusions can be deducted;

1. The solution-treated single crystalline alloy showed full recovery of 6 % applied strain with 4.2 % transformation strain at - 30 ^{o}C. The superelastic window was at least 100 ^{o}C, between -30 ^{o}C and 70 ^{o}C. At 70 ^{o}C the yield strength was greater than 2500 MPa.

2. The solution-treated single crystalline alloy demonstrates a very large mechanical hysteresis of 1270 MPa at -30 ^{o}C, resulting in a maximum damping capacity of 44 J.cm^{-3}. Although, the stress hysteresis is essentially independent of transformation strain, it is highly dependent on test temperature, and diminished with increasing temperature to 815 MPa at 70 ^{o}C.

3. Perfect shape memory behavior at 1000 MPa and near-perfect shape memory effect with with 2.2 % transformation strain under an ultra high stress level of 1500 MPa was observed in [111]-oriented single crystals aged at 550 ^{o}C for 3 hours beside fully recoverable superelastic responses to stresses as high as 1.8 GPa

4. A decrease in transformation strain was observed in the material aged at 600 ^{o}C for 3 hours compared to the material aged at 550 ^{o}C for 3 hours.

5. Aging was very effective in decreasing the stress hysteresis from ≈1200 MPa (solution-treated sample) to ≈400 MPa (550 ^{o}C-3h) and 250 MPa (600 ^{o}C-3h).
6. The [111]-oriented single crystalline alloy has a high work output energy density of 33 J.cm^{-3} in the 550 ^{o}C-3h aged condition, which was measured for the thermally induced transformation. It was also observed that the work output decreased as the aging temperature increased to 600 ^{o}C, similar to the absorbed energy.
7. The as-grown single crystal showed fully reversible superelasticity with a large SE window from at least -30 ^{o}C to 70 ^{o}C. The maximum transformation strain was 4.4 % at – 30 ^{o}C with a mechanical hysteresis of 720 MPa. The elastic moduli of the austenite and martensite phases were 48-59 GPa and 87-97 GPa, respectively.

8. Manipulating the microstructure through simple thermal treatment was an effective way to control the shape memory behavior of the $Ni_{45.3}Ti_{29.7}Hf_{20}Pd_5$ alloy. Aging of the as-grown single crystals at 550 ^{o}C for 3 hours produced precipitates of ≈20-30 nm in size with interparticle distances of about twice the particle size. Aging solution-treated (1050 ^{o}C for 4 hours) single crystals at 550 ^{o}C for 3 hours produced smaller precipitates, ≈ 15-20 nm, with interparticle distances of about the same dimension.

9. The aged (550 ^{o}C for 3 hours) $Ni_{45.3}Ti_{29.7}Hf_{20}Pd_5$ single crystals (as-grown+aged or solution-treated+aged) exhibited recoverable shape memory strains of at least 2 % at stress levels as high as 1000 MPa in the thermal cycling experiments. High

temperature superelasticity was observed in the as-grown+aged material over a wide range of temperatures from 80 ^{o}C to 180 ^{o}C and at stress levels as high as 2 GPa. The combination of high strength, moderate temperature capability, and stable superelastic or shape memory behavior make the aged $Ni_{45.3}Ti_{29.7}Hf_{20}Pd_5$ alloys promising for industrial applications where that combination of properties is desired.

10. Shape memory properties of the $Ni_{45.3}Ti_{29.7}Hf_{20}Pd_5$ alloys (e.g. transformation temperatures) can easily be manipulated over a very wide range by microstructural control. M_s temperatures in the absence of stress can be adjusted between $\approx$-270 ^{o}C and 38 ^{o}C, while the Clausius-Clapeyron slopes were in the range of 6.8-12.2 MPa/^{o}C.

6. ORIENTATION DEPENDENCE OF THE SHAPE MEMORY PROPERTIES OF $Ni_{45.3}Ti_{29.7}Hf_{20}Pd_5$ ALLOYS

6.1. Introduction

It should be noted that most of the practical applications require processing of SMAs that might result in texture formation. Thus, it is important to investigate the single crystal properties of SMAs since their shape memory properties are highly orientation dependent and highly textured polycrystalline materials will mimic the behavior of single crystals with dominant orientation [38].

Several studies have been conducted on the orientation dependence of mechanical properties in NiTi single crystals [38-41]. Reports on the single crystal $Ni_{50.8}Ti_{49.2}$ (at. %) alloy under compressive loads revealed that [111] and [112] orientations have multiple correspondant variant pairs (CVPs) activated during stress induced martensite transformation resulting in high hardening [41] in SIM transformation regions. Due to this high hardening, they quickly reach the critical stress for slip, easily limiting their transformation strains and superelastic temperature window [41, 42]. In contrast to [111] and [112] orientations, only a single CVP is activated along the [148] orientation leading to a transformation strain that approaches to theoretically calculated values. In [001] and [-117] oriented $Ni_{50.3}Ti_{49.7}$ (at. %) and $Ni_{51}Ti_{49}$ (at. %) single crystals, the critical stress for slip is relatively high compared to other orientations, which is attributed to the zero Schmid factor for {001}<001> and {011}<001> dislocation systems [42, 139]. Hence, the slip systems are unfavorable in the [001] orientation and plastic deformation is hindered [41, 42, 139], providing a good opportunity to observe shape memory behavior without the complications from dislocation formation. In addition to orientation

dependence, other aspects of NiTi single crystals such as aging effects on shape memory responses [42], cyclic deformation behavior [115], and tension-compression asymmetry [39] have been investigated.

In the previous chapters, Pd addition to $Ni_{50.3}Ti_{29.7}Hf_{20}$ (at. %) alloys were investigated in polycrystalline and [111]-oriented single crystalline forms. In [111]-oriented $Ni_{45.3}Ti_{29.7}Hf_{20}Pd_5$ single crystals, superelastic properties in the temperature range of -30 ^{o}C to 70 ^{o}C were revealed using solution-treated material in compression. It was shown that the solutionized single crystal had 4.2 % reversible strain, extremely high critical and yield stress levels (> 2000 MPa), and high damping capacity (44 J.cm^{-3}) due to a high stress hysteresis (> 1200 MPa). Subsequently, the effects of aging temperature and aging time were investigated for [111] oriented crystals in compression. It was found that aging was an effective method to tailor transformation strains, transformation temperatures, and stress and temperature hysteresis. Aging of the $Ni_{45.3}Ti_{29.7}Hf_{20}Pd_5$ single crystals resulted in precipitation where precipitate size and spacing depend on aging time and temperature.

6.2. Orientation dependence of shape memory properties in aged $Ni_{45.3}Ti_{29.7}Hf_{20}Pd_5$ single crystals

In this section, the orientation dependence of the shape memory properties of $Ni_{45.3}Ti_{29.7}Hf_{20}Pd_5$ single crystals along the [111], [011] and [-117] orientations with two selected aging conditions were investigated. The single crystals were aged at 550 ^{o}C for 3 hours (550 ^{o}C-3h) or aged at 600 ^{o}C for 48 hours (600 ^{o}C-48h) to generate two distinct precipitate structures in order to determine the effect of microstructure on shape memory properties of single crystals as a function of orientation.

Laue back-scatter diffraction patterns were used to determine the orientation of the single crystal samples. Compression specimens, with a 16 mm^2 cross section and a 8 mm length, were cut by electro discharge machining from the single crystal ingots so that their loading axes were along either the [111], [011] or [-117] directions. The machined single crystal specimens were solutionized at 1050 ^oC for 4 hours in sealed quartz tubes followed by water quenching. After the solution treatment, single crystals were aged at 550 ^oC for 3 hours or at 600 ^oC for 48 hours in air and were quenched in water.

It was previously reported [10] that aging of $Ni_{45.3}Ti_{29.7}Hf_{20}Pd_5$ single crystals resulted in precipitation of a spindle-shaped phase with the same face-centered orthorhombic lattice structure as that observed in ternary NiTiHf alloys by Han et al. [13] and later described in more detail by Yang et al. [14] and Santamarta et al. [15]. These precipitates are oblate spindle shaped with a habit plane of $(100)_P$ // $(001)_{B2}$ and a long axis of $[001]_P$ // $[-110]_{B2}$ resulting in six orientationally different variants [13] as schematized in Figure 6.1a.

Figure 6.1a depicts the orientation relationships between the compression axes of single crystals and the six variants of the precipitates. For example if the $[001]_{B2}$ direction is selected as the compression axis, two variants (V1 and V2) of the precipitates are perpendicular to the $[001]_{B2}$ direction while the long axis of the other four variants (V3-6) is 45° away from the $[001]_{B2}$ direction. On the other hand, if the $[110]_{B2}$ direction is selected, the long axis of the four variants (V3-6) is located at 60° from the $[110]_{B2}$ direction while V1 and V2 are perpendicular and parallel to the $[110]_{B2}$ direction,

respectively. When the compression axis is the $[111]_{B2}$ direction, the long axis of three variants (V2, V4 and V6) is located at 35.3° from the $[111]_{B2}$ direction while the other three variants (V1, V3 and V5) are perpendicular to the $[111]_{B2}$ direction.

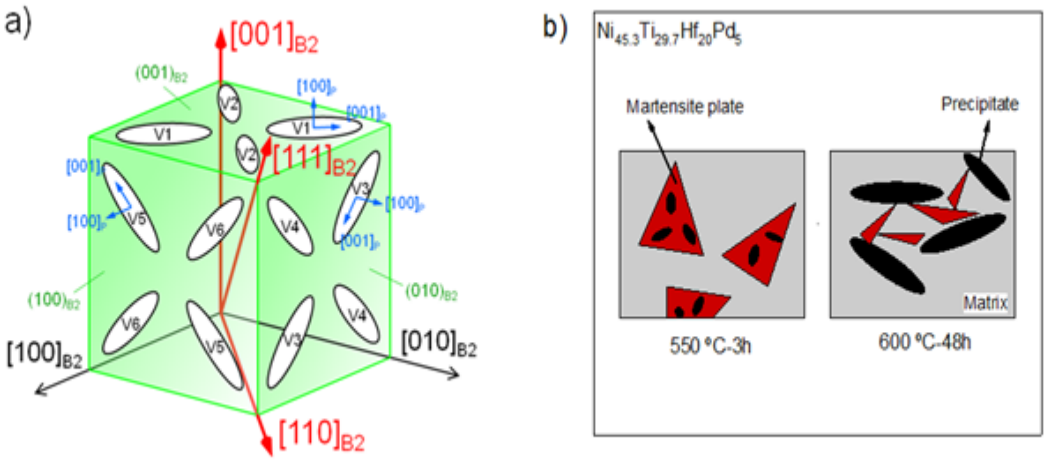

Figure 6.1: a) Three-dimensional distribution of the precipitates with six variants denoted as V1, V2, V3, V4, V5 and V6. The bold arrows indicate the compression axes selected in this study. b) Schematic microstructures for the aged $Ni_{45.3}Ti_{29.7}Hf_{20}Pd_5$ alloys.

It should be noted that the above-mentioned difference in the precipitate orientation does not affect the orientation dependence of the transformation strain considerably. It has been reported that the orientation dependence of the transformation strain is caused due to the selection of martensite variants depending on the resolved shear stress on the most favorable martensite variants under stress [41]. Since the resolved shear stress factor is not affected by the orientation of the precipitates, it is

considered that the transformation strain is not affected by the precipitate orientation significantly but mainly governed by the orientation of the external stress axis.

In $Ni_{45.3}Ti_{29.7}Hf_{20}Pd_5$ alloys, the microstructures and consequently, the main shape memory properties such as transformation temperatures, transformation strains and stress, and temperature hysteresis are effected by aging [138]. In particular, maximum strengthening was achieved by very fine (10-20 nm), coherent and homogeneously distributed precipitates through aging at 550 ^{o}C for 3 hours [10]. After aging at 600 ^{o}C for 48 hours, the precipitates coarsened in size to 200 nm and 20 nm along the long and short axes, respectively, and the interparticle distance increased to 80 nm [107]. In the 550 ^{o}C-3h condition, large martensite variants contained the fine precipitates while the martensite plates were constrained between the precipitates after aging at 600 ^{o}C for 48hours [107].

In the 550 ^{o}C-3h aged $Ni_{45.3}Ti_{29.7}Hf_{20}Pd_5$ alloy, since the precipitates were small and interparticle distance was short, the growing martensite plates bypassed and eneveloped the precipitates resulting in large martensite plates with embedded precipitates (Figure 6.1b). This is similar to observations in ternary NiTiHf and NiTiZr alloys [15] and CuAlMn SMAs with fine precipitates [133]. In the case of the $Ni_{45.3}Ti_{29.7}Hf_{20}Pd_5$ alloy, the energy required to complete the transformation was increased due to the process of bypassing and encapsulating the precipitates, as will be discussed below. Consequently, the elastic energy of the alloy was also increased during transformation [11, 120, 129, 134].

On the other hand, the precipitates were large enough in the 600 ^{o}C-48h condition, that martensite formation was constrained and formed between precipitates [12] instead of bypassing or envloping the precipitates (Figure 6.1b). In this condition, the main factor that determined the size of the martensite plates during transformationwas the interparticle distance.

Constant stress thermal cycling responses of the $Ni_{45.3}Ti_{29.7}Hf_{20}Pd_5$ single crytals oriented along [111], [011] and [-117] directions are shown in Figure 6.2 after aging at 550 ^{o}C for 3 hours while results for materials aged at 600 ^{o}C for 48 hours are shown in Figure 6.3. Applied compressive stress was varied from 100 MPa to 1000 MPa and the strain-temperature responses under stress levels of 300 MPa, 700 MPa and 1000 MPa are shown in Figures 6.2 and 6.3. Compressive stress was applied at temperatures above A_f and then, the sample was cooled down below M_f and heated back above A_f while under constant stress. It is clear from Figures 6.2 and 6.3 that reversible strains and TTs increased with stress in all orientations for both aging conditions. The distance between the cooling and heating lines at M_s is used to calculate the reversible strain after subtracting off the residual/irrecoverable strain and TTs were determined by the tangent method. Reversible strains for samples aged at 550 ^{o}C for 3 hours were 1.6 %, 0.8 % and 0.4 % under 300 MPa and 2.2 %, 2.7 % and 0.7 % under 1000 MPa, while M_s was 106 ^{o}C, 146 ^{o}C and 58 ^{o}C under 1000 MPa for [111], [011] and [-117] orientations, respectively. For samples aged at 600 ^{o}C for 48 hours, reversible strains were 1.6 %, 1.6 % and 0.6 % under 300 MPa and approximately 2.3 %, 2 % and 0.9 % under 1000 MPa while M_s was 176 ^{o}C, 198 ^{o}C and 130 ^{o}C under 1000 MPa for [111], [011] and [-117] orientations, respectively. It is clear that TTs can be altered by simple aging treatments

for $Ni_{45.3}Ti_{29.7}Hf_{20}Pd_5$ single crystals and this ability can provide advantages to engineering of NiTiHfPd SMAs for possible high temperature applications.

For samples aged at 550 ^{o}C for 3 hours and tested along the [111] and [-117] orientations, minimal or no irrecoverable strains were observed at stresses as high as 1000 MPa, while residual strain was observed at all stress levels along the [011] orientation, approaching 0.4 % at 1000 MPa. In the 600 ^{o}C-48h condition, residual strains were again observed at nearly every stress level reaching 1.9 % at 1000 MPa along the [011] direction. In constrast, no residual strain was observed along the [111] orientation up to 700 MPa and no plastic strain was observed along the [-117] direction up to 1000 MPa compressive stress. This indicates that the [-117] and [111] orientations have higher strength against plastic deformation compared to the [011] direction in $Ni_{45.3}Ti_{29.7}Hf_{20}Pd_5$ single crystals, regardless of aging condition. Also, compared to near equiatomic NiTi single crystalline alloys, $Ni_{45.3}Ti_{29.7}Hf_{20}Pd_5$ alloys have superior strength since it is known that $Ni_{50.1}Ti_{49.9}$ alloys produce irrecoverable strains even at stress levels of 160 and 175 MPa in thermal cycling experiments in [111] and [123] orientations, respectively [11].

It is clear that larger plastic strains were observed during thermal cycling in the [011] orientation at all stress levels and in the [111] orientation at 1000 MPa for samples aged at 600 ^{o}C for 48 hours compared to aging at 550 ^{o}C for 3 hours. This difference in strength between samples of similar orientation can be attributed to differences in the microstructure. In the 600 ^{o}C-48h aged condition, the material is weaker due to larger and presumably semi-coherent or incoherent precipitates with a larger interparticle distance [107]. Thus, the microstructure is much less resistant to dislocation motion.

After aging at 550 ^{o}C for 3 hours, the material is stronger due to the precipitation hardening effect of finer coherent precipitates [138], which significantly reduces the mobility and eventually generation of dislocations in the structure.

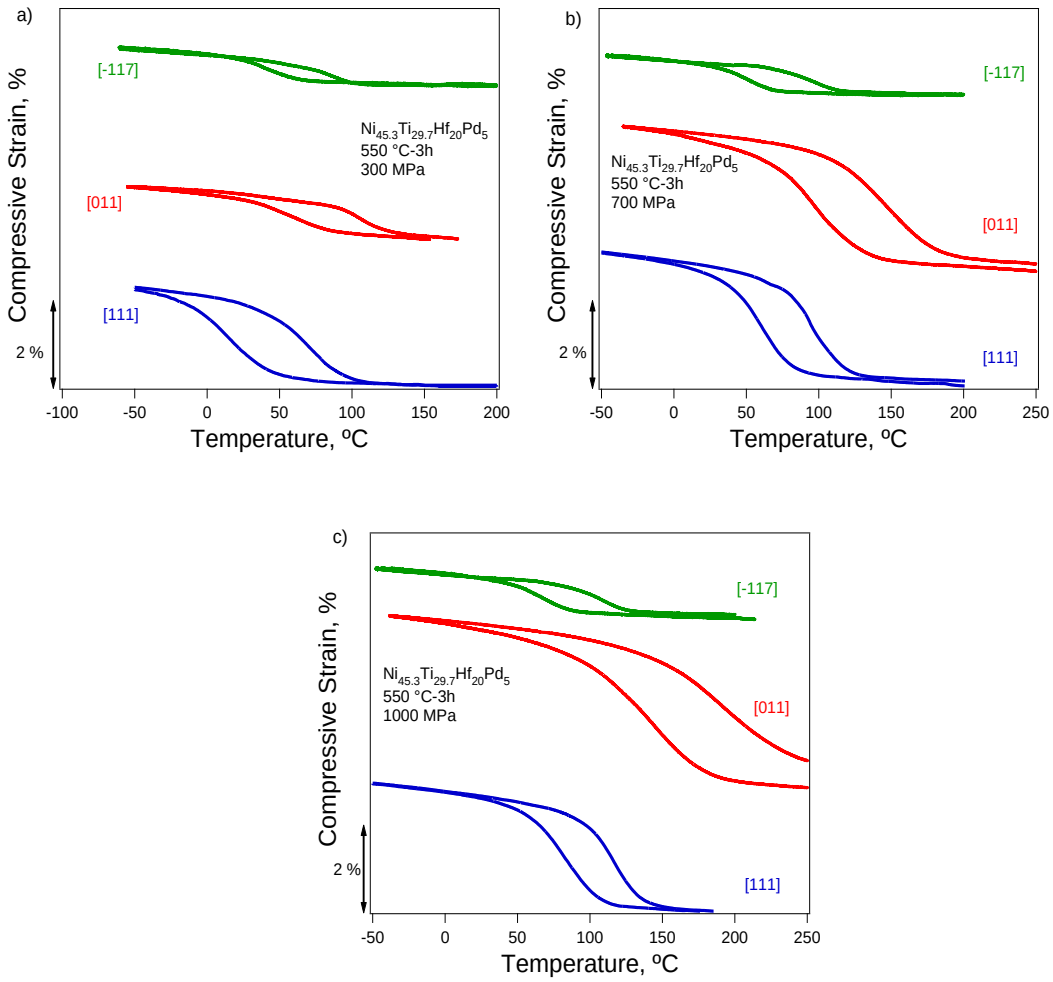

Figure 6.2: Shape memory behavior of $Ni_{45.3}Ti_{29.7}Hf_{20}Pd_5$ single crystals under compressive stresses of a) 300 MPa, b) 700 MPa and c) 1000 MPa after aging at 550 ^{o}C for 3 hours.

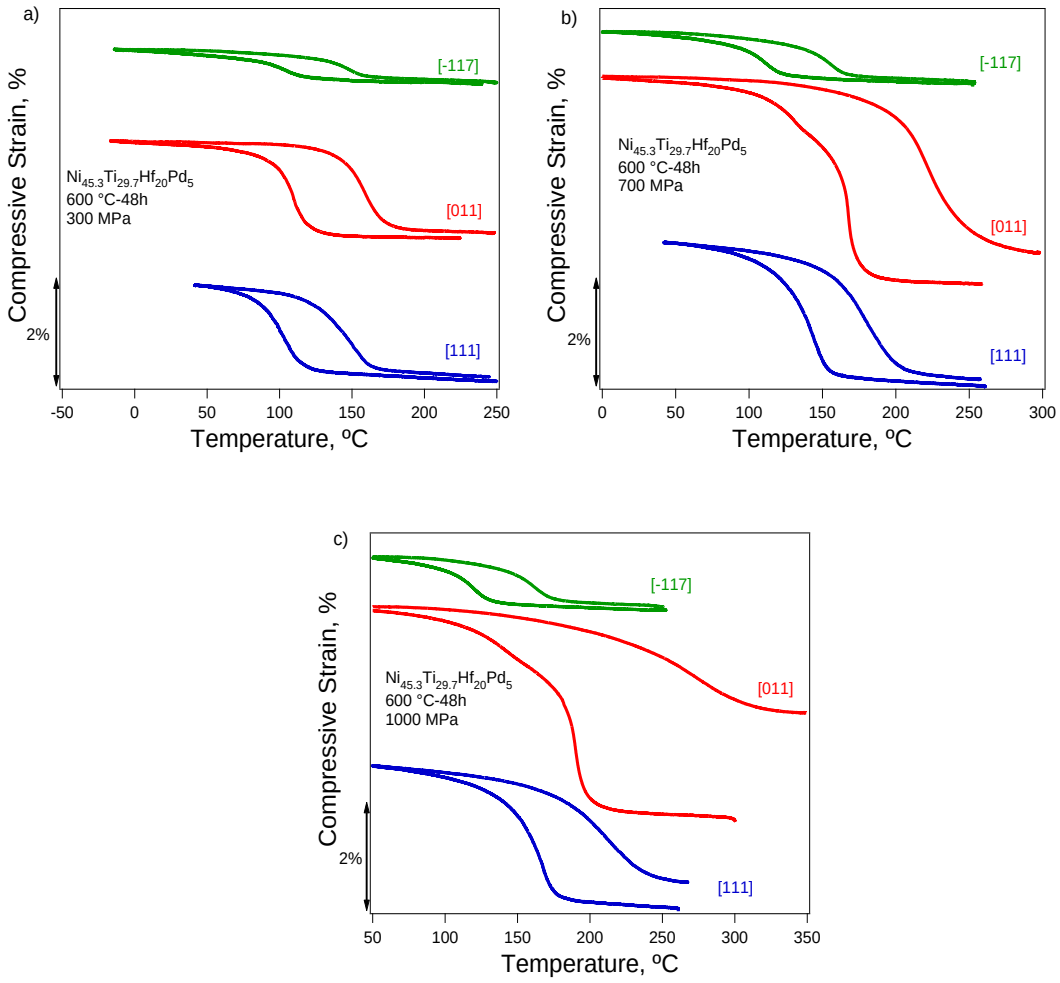

Figure 6.3: Shape memory behavior of $Ni_{45.3}Ti_{29.7}Hf_{20}Pd_5$ single crystals under compressive stresses of a) 300 MPa, b) 700 MPa, and c) 1000 MPa after aging at 600 ^{o}C for 48 hours.

Figures 6.4 and 6.5 show the isothermal stress-strain responses of [111], [011] and [-117] oriented $Ni_{45.3}Ti_{29.7}Hf_{20}Pd_5$ single crystals at selected test temperatures near or above A_f. Samples were loaded to 4 % in [111] and [011] orientations and 2 % in the [-117] direction after aging at 550 ^{o}C for 3 hours, while they were loaded to 3 % in the [111] and [011] orientations and 2.5 % in the [-117] direction after aging at 600 ^{o}C for 48 hours.

Under these conditions, near-perfect superelastic responses (resulting in little or no residual strain after unloading) were obtained in all orientations for both aging conditions. High hardening was observed in the transformation regions of all orientations. Hardening stems from the fact that additional energy is needed to grow the favored martensite variants due to the interaction between the growing martensite plates and precipitates, variant-variant interaction, and/or detwinning of martensite. $Ni_{45.3}Ti_{29.7}Hf_{20}Pd_5$ alloys have $(001)_{B19'}$ compound twins [92] as commonly observed in Ni-rich NiTiHf alloys [48, 53, 54]. Thin compound twins in the $Ni_{45.3}Ti_{29.7}Hf_{20}Pd_5$ alloy may make the growth of martensite variants and detwinning more difficult. Thus, the required energy to complete the stress induced martensite transformation increases, which would need to be supplied by an increasing external force during the transformation process. In contrast, it was also revealed that when the martensite is Type-II, as in a $Ni_{45.3}Ti_{39.7}Hf_{10}Pd_5$ (at.%) alloy, plateau-like behavior was observed instead of high-hardening behavior in the transformation region (see Chapter 4).

It should be noted that the [111] orientation had a higher degree of hardening during transformation than the [011] orientation in both aging conditions (e.g. at 60 ^{o}C in Figure 6.4a or at 140 ^{o}C in Figure 6.5a). The increased hardening along the [111] orientation can possibly be linked to the activation of a greater number of CVPs along the [111] orientation than [011] orientation. Those CVPs may interact with each other and the precipitates during transformation and consequently may result in a higher stress-strain slope in the transformation region [41]. In addition to higher hardening, the [111] orientation has a larger stress hysteresis compared to the [011] orientation, which supports the idea that the [111] orientation has more CVPs. Due to greater interaction

amongst those CVPs in the [111] crystals, larger dissipation of energy and consequently stress hysteresis may be observed due to higher friction, compared to the [011] orientation.

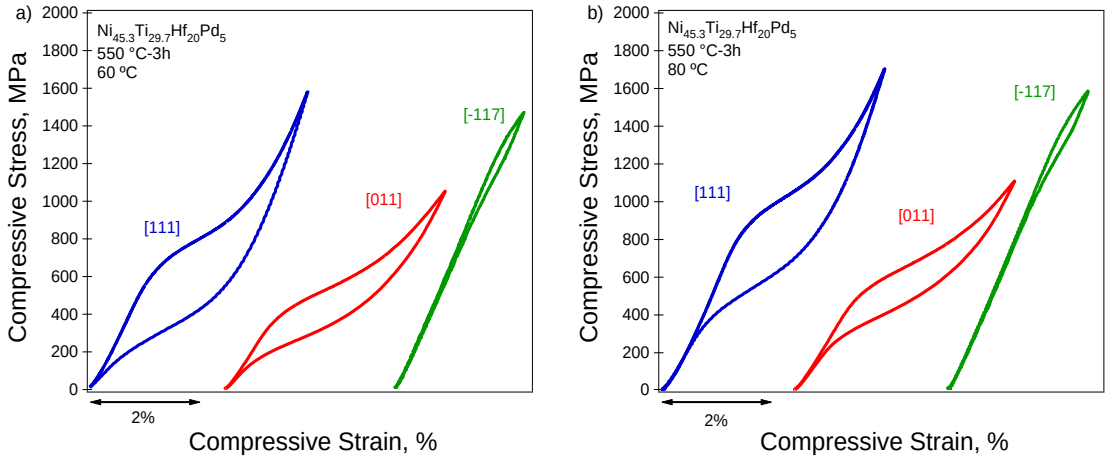

Figure 6.4: Superelastic responses of $Ni_{45.3}Ti_{39.7}Hf_{20}Pd_5$ single crystals at test temperatures of a) 60 ^{o}C, and b) 80 ^{o}C after aging at 550 ^{o}C for 3 hours.

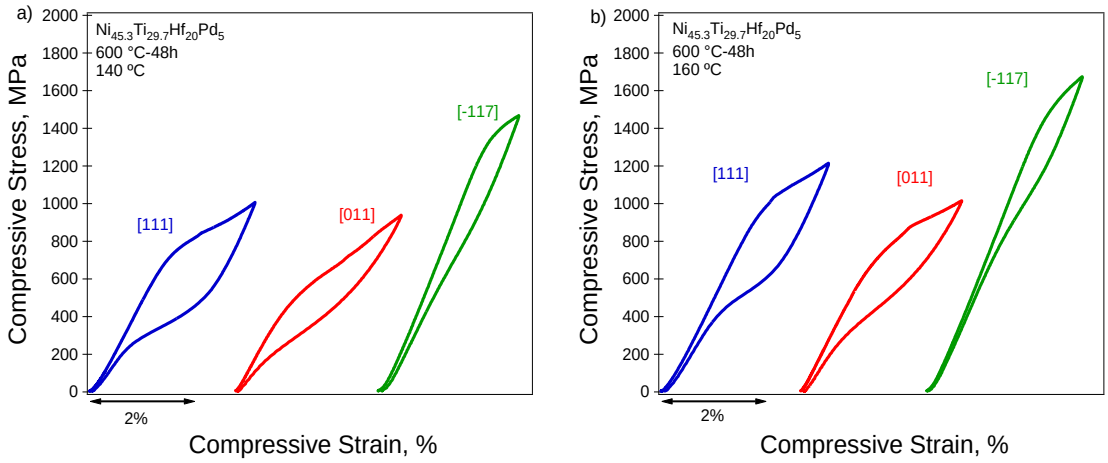

Figure 6.5: Superelastic responses of $Ni_{45.3}Ti_{39.7}Hf_{20}Pd_5$ single crystals at test temperatures of a) 60 ^{o}C, and b) 80 ^{o}C after aging at 600 ^{o}C for 48 hours.

The critical stress for the onset of the martensite transformation, σ_{cr}, was 650 MPa, 390 MPa and 1340 MPa at 60 ^{o}C along the [111], [011] and [-117] orientations, respectively, after aging at 550 ^{o}C for 3 hours. Values for σ_{cr} of 750 MPa, 540 MPa and 1375 MPa were measured at 140 ^{o}C along the [111], [011] and [-117] orientations, respectively, after aging at 600 ^{o}C for 48 hours. Hence, we can conclude that at a given temperature $\sigma_{cr}^{-117} > \sigma_{cr}^{111} > \sigma_{cr}^{011}$, which is expected when the Clausius-Clapeyron relationship is considered [75].

The M_s temperatures of the aged single crystals were extracted from the thermal cycling data in Figures 6.2 and 6.3 as a function of applied compressive stress and are shown in Figure 6.6a. The C-C slopes were 11.1 MPa/^{o}C, 8.2 MPa/^{o}C, and 27.6 MPa/^{o}C for the samples oriented along the [111], [011], and [-117], respectively after aging at 550 ^{o}C for 3 hours. After aging at 600 ^{o}C for 48 hours, slopes of 12.5 MPa/^{o}C, 9.3 MPa/^{o}C and 42.2 MPa/^{o}C were obtained along the [111], [011] and [-117] orientations, respectively. It is apparent that the C-C slope along the [-117] orientation is relatively high compared to [111] and [011] orientations for both aging conditions.

Since the ΔH and T_o are orientation independent, low transformation strain results in a high C-C slope. It should also be noted that M_s under zero stress is orientation independent as shown in Figure 6.6a. Thus, the temperature difference between M_s and the selected test temperature is same for all orientations. Consequently, high slope/low strain orientations (e.g. [-117] yield high critical transformation stress at the same test temperature.

Previous work indicated that the C-C slopes of $Ni_{51.5}Ti_{48.5}$ were 9.3 MPa/^{o}C and 7.5 MPa/^{o}C for [111] and [110] orientations, respectively, for crystals aged at 550 ^{o}C for 1.5 hours [42]. Also, the C-C slope for [001], which is only 12^{o} from the [-117] orientation, was 7.5 MPa/^{o}C for $Ni_{51.5}Ti_{48.5}$ single crystals with the same aging condition [42]. Similarly, the C-C slope for a $Ni_{50.3}Ti_{29.7}Hf_{20}$ (at %) single crystal aged at 550 ^{o}C for 3 hours was 11.58 MPa/^{o}C (in compression) along the [678] orientation, which is close to the [111] direction [118].

C-C curves were extrapolated from the $Ni_{45.3}Ti_{39.7}Hf_{20}Pd_5$ [111], [011] and [-117] orientations to obtain the predicted M_s temperature under zero stress. It was found that the stress-free M_s was approximately 10-15 ^{o}C after aging at 550 ^{o}C for 3 hours and it was around 100-105 ^{o}C after aging at 600 ^{o}C for 48 hours. It is clear that transformation temperatures increased after high temperature and longer time aging due to the formation of larger precipitates. It should be noted that these stress-free values for M_s were independent of orientation as expected.

Figure 6.6b shows the reversible strain data extracted from the constant stress strain-temperature responses of the $Ni_{45.3}Ti_{39.7}Hf_{20}Pd_5$ single crystals shown in Figures 6.2 and 6.3. Reversible strains of the samples were 0.3 %, 0.1 % and 0.1 % under 100 MPa and they were 2.2 %, 2.7 % and 0.7 % under 1000 MPa for [111], [011] and [-117] directions, respectively after aging at 550 ^{o}C for 3 hours. After aging at 600 ^{o}C for 48 hours, reversible strains of 0.4 %, 0.2 % and 0.2 % under 100 MPa and 2.3 %, 2 % and 0.9 % were obtained under 1000 MPa for [111], [011] and [-117] directions, respectively. It is clear that reversible strains increased initially and then saturated with applied stress

in almost all orientations for both aging conditions and the saturation was followed by a decrease in [011] oriented crystals aged at 600 ^{o}C for 48 hours.

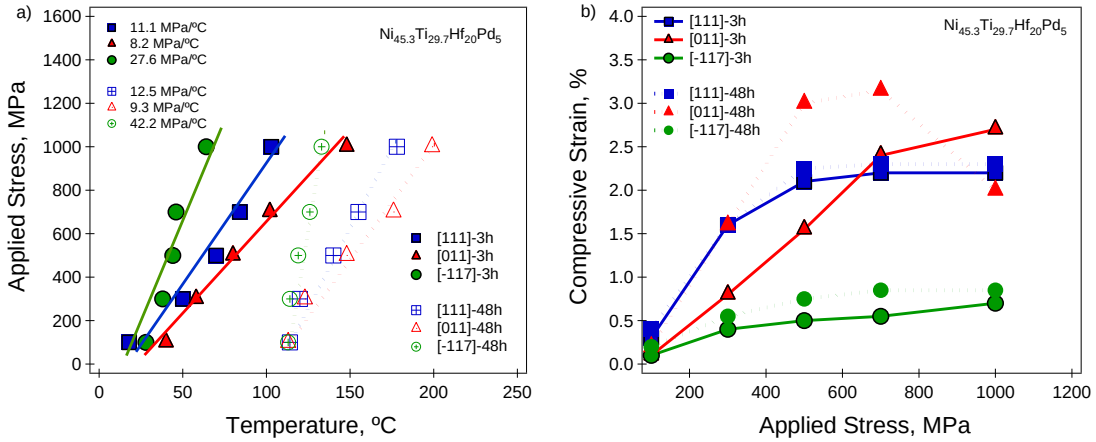

Figure 6.6: The change in a) M_s and b) reversible strain with applied stress for $Ni_{45.3}Ti_{39.7}Hf_{20}Pd_5$ single crystals along the [111], [011] and [-117] orientations aged for 3h at 550 ^{o}C and 48h at 600 ^{o}C.

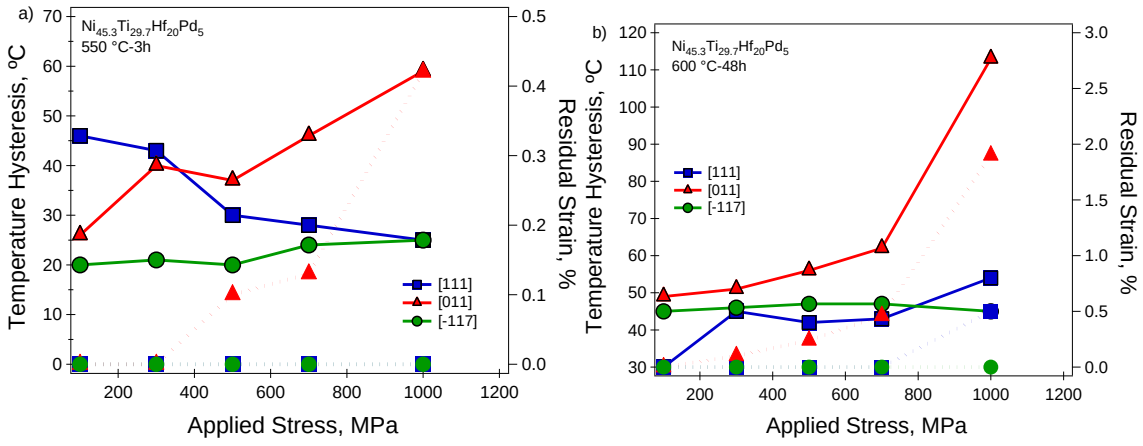

Figure 6.7: The change in thermal hysteresis (solid lines) and residual strain (dotted lines) with applied stress for $Ni_{45.3}Ti_{39.7}Hf_{20}Pd_5$ single crystals along the [111], [011] and [-117] orientations after a) 550 ^{o}C-3h and b) 600 ^{o}C-48h aging.

The reversible strains measured in compression from isothermal stress-strain (superelastic) experiments (Figures 6.4 and 6.5) on $Ni_{45.3}Ti_{39.7}Hf_{20}Pd_5$ were 2.2 %, 2.3 % and 0.3 % at 60 ^oC and they were 2 %, 2 % and 0.4 % at 80 C^o for [111], [011] and [-117] directions, respectively, after aging at 550 ^oC for 3 hours. After aging at 600 ^oC for 48 hours, superelastic reversible strains of 1.5 %, 1.2 % and 0.6 % at 140 ^oC and 1.2 %, 1.1 % and 0.5 % were obtained at 160 ^oC for [111], [011] and [-117] directions, respectively.

In comparison, the compressive superelastic strains in $Ni_{50.8}Ti_{49.2}$ (at.%) were 2.3 %, 3.2 % and 3.5 % for peak-aged (1.5 h at 673 K) and were 3 %, 3.6 % and 4.3 % for over-aged (15h at 773 K) single crystals along the [111], [110] and [100] orientations, respectively [39]. In $Ni_{51.5}Ti_{48.5}$ (at. %) single crystals, the transformation strains in compression from superelastic experiments were 1.2 %, 4.2 % and 3.9 % for solutionized (2h at 1273 K) and 3 %, 3.7 % and 3.3 % for aged (1.5 h at 823 K) single crystals along [111], [110] and [001] orientations, respectively [42].

Even though the binary NiTi and $Ni_{45.3}Ti_{39.7}Hf_{20}Pd_5$ shape memory alloys have the same crystal structures for the parent (B2) and martensite phases (B19'), they have different transformation strains along the same/similar crystallographic orientations in compression. But not only is the magnitude of the strains different for similar orientations but the orientation dependence of the transformation strains is different. In $Ni_{50.8}Ti_{49.2}$ alloys, the highest transformation strains occur along the [100] orientations while the [111] orientation has the lowest strain. In $Ni_{51.5}Ti_{48.5}$, the [011] orientation has the highest transformation strain, while the lowest strain also occurs in the [111] orientation. In contrast, the $Ni_{45.3}Ti_{39.7}Hf_{20}Pd_5$ alloy exhibits the smallest reversible strain along the [-117] (near [001]) and similar values along the [011] and [111] orientations.

These differences in transformation strains between the binary NiTi alloys and $Ni_{45.3}Ti_{39.7}Hf_{20}Pd_5$ can be attributed to the differences in *i)* lattice parameters, *ii)* precipitate characteristics, especially volume fraction, and *iii)* active twinning systems.

The transformation strains in SMAs are strongly lattice parameter dependent [2], since SMAs are strained by shearing the lattice structures of the transforming phases. When the reversible volumetric shear that depends on lattice parameters is high, transformation strain is expected to be high, neglecting plastic deformation by slip since plastic deformation may limit the reversibility of the shearing. Thus, lattice parameters (e.g. c/a ratio in B19' lattice structure) of the transforming phases will affect the magnitude of the transformation shear strains in SMAs.

Other reasons for the difference in transformation strains between the $Ni_{45.3}Ti_{39.7}Hf_{20}Pd_5$ and binary NiTi single crystal alloys can be attributed to precipitate characteristics (coherency,and volume fraction), and the density and type of twins. It has been reported that the volume fraction of precipitates is around 3.6 % in $Ni_{50.7}Ti_{49.3}$ after aging at 673 K for 1.5 h and 5 % in $Ni_{50.8}Ti_{49.2}$ after aging at 823 K for 1.5 h while the volume fraction of precipitates increased to 16-20 % in $Ni_{51.5}Ti_{48.5}$ after aging at 823 K for 1.5 h [25, 42]. The average area fraction of precipitates has been reported to be 18.2 % for a $Ni_{50.3}Ti_{29.7}Hf_{20}$ and 31 % in a $Ni_{51}Ti_{29}Hf_{20}$ alloy [140]. Thus, the volume fraction of precipitates in the $Ni_{45.3}Ti_{39.7}Hf_{20}Pd_5$ alloy is probably higher than the binary NiTi alloys, which means that there is less material to transform so the transformation strains will be proportionally smaller. Additionally, the residual stress around the precipitates can affect the transformation strain by activating CVPs other than the ones favored by the

applied stress. The increased number of CVPs may limit the transformation strain in $Ni_{45.3}Ti_{39.7}Hf_{20}Pd_5$ alloys as in $Ni_{50.8}Ti_{49.2}$ single crystals [41].

It should be noted that differences in lattice parameters and precipitate characteristics can only explain the differences in magnitude between transformation strains along the same orientations in $Ni_{45.3}Ti_{39.7}Hf_{20}Pd_5$ and NiTi alloys. There is also a difference in the orientation dependence of the transformation strains between the binary and quaternary alloys. The smallest transformation strain is observed along [111] orientation in the binary NiTi alloys and [-117] (near [001]) orientation in $Ni_{45.3}Ti_{29.7}Hf_{20}Pd_5$ alloys. Moreover, $Ni_{45.3}Ti_{29.7}Hf_{20}Pd_5$ showed relatively high reversible strain along the [111] orientation. This difference in behavior could be attributed to a difference in active twinning types in the martensite phase of the alloys. Transformation strains depend on the active twinning mode that dictates the CVP formation and detwinning properties [141].

It is well known that Type I and Type II are the most common twinning modes observed in binary NiTi alloys [41]. Conversely, initial results suggest that $(001)_{B19'}$ compound [92, 142] twins, similar to Ni-rich NiTiHf alloys [48, 53, 54], are active in $Ni_{45.3}Ti_{29.7}Hf_{20}Pd_5$ alloys depending on aging condition. It is known that compound twins generate lower transformation strain compared to a Type II twinning process [42]. Furthermore, the growth of CVPs in the $Ni_{45.3}Ti_{29.7}Hf_{20}Pd_5$ alloy could be more difficult due to frictional effects associated with the thin compound twins. Compound twins do not detwin easily, resulting in high hardening due to an increased stress required to complete the transformation [92, 143]. In turn, the high work hardening limits the amount of

detwinning that can occur prior to the onset of plastic deformation. Thus, a large detwinning strain is not expected in NiTiHfPd alloys.

Temperature hysteresis was determined graphically from Figures 6.2 and 6.3 at the mid-point of the transformation strain between the cooling and heating curves for all orientations and is summarized in Figure 6.7 for both aging conditions. In addition, the irrecoverable strains as a function of applied stress are also included in Figures 6.7a and b as a function of stress for the two aging conditions. Temperature hystereses of the 550 ^{o}C-3 h aged single crystals were 43 ^{o}C, 40 ^{o}C, and 21 ^{o}C under 300 MPa and 25 ^{o}C, 60 ^{o}C, and 25 ^{o}C under 1000 MPa along the [111], [011], and [-117] orientations, respectively. Along the [111] orientation, the temperature hysteresis decreased abruptly from 46 ^{o}C to 30 ^{o}C when the applied stress was increased from 100 MPa to 500 MPa and continued to decrease more slowly to 1000 MPa where a minimum hysteresis of 25 ^{o}C was observed in this orientation. In constrast, the hysteresis for [011] crystals increased with stress, consistent with an increase in plastic deformation. Finally, for [-117] crystals, the hysteresis was almost independent of stress.

After aging at 600 ^{o}C for 48 hours, temperature hystereses of the single crystals were 45 ^{o}C, 51 ^{o}C, and 46 ^{o}C under 300 MPa and 54 ^{o}C, 113 ^{o}C, and 45 ^{o}C under 1000 MPa along the [111], [011], and [-117] orientations, respectively. Similar to the 550 ^{o}C-3h condition, when stress was increased, temperature hysteresis increased in the [011] orientation due to greater plastic deformation, while it was almost constant in the [111] orientation prior to the any significant plastic deformation and then increased at higher stresses. Finally, the hysteresis was essentially constant for [-117] crystals over the entire range of stresses investigated, consistent with the lack of plasticity along this orientation.

The initial decrease in hysteresis with stress for [111] samples aged at 550 ^{o}C for 3 hours could be related to a decrease in the number of martensite variants formed with stress in this orientation. With fewer martensite variants present with stress, the interaction between the martensite variants would be less, resulting in a smaller hysteresis.

The temperature hysteresis for both the 550 ^{o}C-3h and 600 ^{o}C-48h aged samples along the [011] orientation increased gradually with stress up to approximately 500-700 MPa and then increased more rapidly with further increase in stress. For the former condition, it was 26 ^{o}C, 37 ^{o}C, 46 ^{o}C and 60 ^{o}C at 100 MPa, 500 MPa, 700 MPa and 1000 MPa, respectively. While in the later condition, it was 48 ^{o}C, 56 ^{o}C, 61 ^{o}C and 113 ^{o}C at 100 MPa, 500 MPa, 700 MPa, and 1000 MPa, respectively. In both cases, the increase in hysteresis with stress is directly attributed to accumulated plastic strain as the stress increased (as shown in Figure 6.7).

In the [-117] orientation, the temperature hysteresis was almost constant with applied stress in both aging conditions. It was 20 ^{o}C, 20 ^{o}C and 25 ^{o}C at 100 MPa, 500 MPa and 1000 MPa, respectively, after aging at 550 ^{o}C for 3 hours while it was 45 ^{o}C, 47 ^{o}C and 45 ^{o}C at 100 MPa, 500 MPa and 1000 MPa, respectively, after aging at 600 ^{o}C for 48 hours. This is consistent with the fact that irrecoverable strain was almost negligible for all applied stress levels for both aging conditions, so that little energy was disspated due to defect (e.g. dislocation) generation.

It is clear that the trend in the thermal hysteresis for [111] and [-117] oriented crystals was different compared to the [011] orientation. The hysteresis decreased with

stress in the [111] orientation after aging at 550 ^{o}C for 3 hours, while it was almost constant along the [-117] orientation for both aging conditions. However, for both aging conditions the thermal hysteresis increased with stress in the [011] orientation starting from 100 MPa. This difference correlates with the significant degree of plastic deformation associated with thermal cycling of [011] crystals compared to [111] and [-117]. In the [011] orientation, as applied stress increased, energy dissipation by dislocation generation also increased resulting in a widening thermal hysteresis with stress.

Work output is another important property of SMAs in the design of functional devices such as solid state actuators. In this case, work output can be calculated by multiplying the applied stress by the corresponding reversible strain from the isobaric thermal cycling experiments. Figure 6.8 shows the work output values as a function of stress for various orientations and aging conditions for single crystal $Ni_{45.3}Ti_{29.7}Hf_{20}Pd_5$.

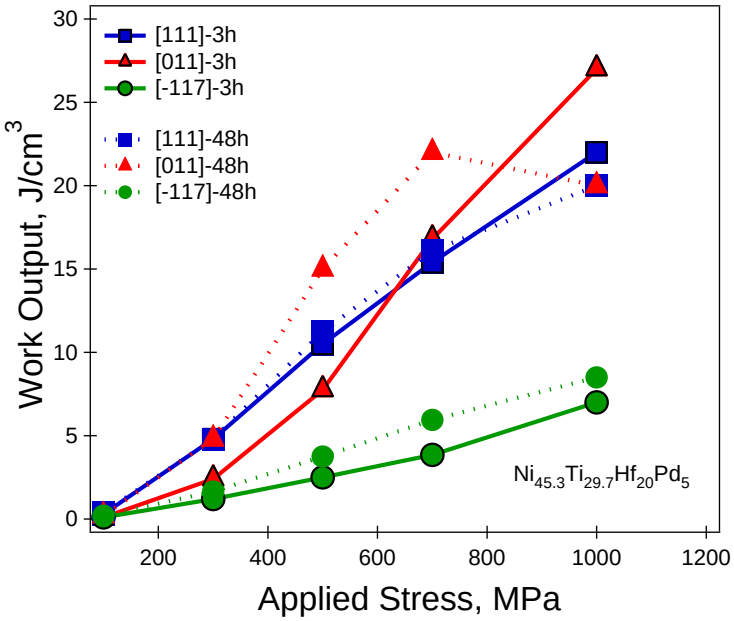

Figure 6.8: Work output as a function of orientation, aging treatment (550 ^{o}C-3 h and 600 ^{o}C-48 h), and applied stress for $Ni_{45.3}Ti_{39.7}Hf_{20}Pd_5$ single crystals.

Work output for the 550 ^{o}C-3 h aged samples increased with applied stress and reached maximum values of 22 J/cm^3, 27 J/cm^3, and 7 J/cm^3 at 1000 MPa along the [111], [011] and [-117] orientations, respectively. In the 600 ^{o}C-48 h aged condition, the maximum work output was 20 J/cm^3 and 8.5 J/cm^3 under 1000 MPa along [111] and [-117] orientations, respectively. In the [011] direction, the work output reached a maximum of 22 J/cm^3 at 700 MPa and then decreased to 20 J/cm^3 at a stress of 1000 MPa due to decreased reversible strain, as shown in Figure 6.6b.

It is clear that in $Ni_{45.3}Ti_{39.7}Hf_{20}Pd_5$ single crystals, work output values are strong functions of loading orientation and aging condition. [111] and [011] orientations have comparable work output values while the [-117] has lower work output values due to poorer reversible strains for both aging conditions. Aging at 600 ^{o}C for 48 hours results in

higher work output values due to higher reversible strains compared to aging at 550 ^{o}C for 3 hours for all orientations, based on the thermal cycling experiments shown in Figures 6.2 and 6.3. In comparison, binary NiTi alloys can generate work output values exceeding 20 J.cm^{-3} [144] and the work output for [111] oriented NiTiHf single crystals can be as high as 30 J.cm^{-3} [118].

Fundamental knowledge of the orientation dependence of shape memory properties is very important to predicting the behavior of textured polycrystalline materials. It is known that a strong <111> texture occurs during the drawing of NiTi alloys [38]. Thus, this type of texture would strongly benefit $Ni_{45.3}Ti_{39.7}Hf_{20}Pd_5$ alloys. The [011] and [111] orientations exhibit the highest reversible strains. But while [011] has the lowest strength amongst the studied orientations, [111] is one of the strongest orientations. Thus, a strong [111] texture would seem to optimize both the trasnformation strain and strength (minimize residual strain) of the alloy.

6.3. Summary and conclusions

Effects of crystal orientation on the shape memory properties of $Ni_{45.3}Ti_{29.7}Hf_{20}Pd_5$ (at %) alloys were investigated in aged conditions. In summary;

1. Shape memory responses of $Ni_{45.3}Ti_{29.7}Hf_{20}Pd_5$ single crystals were determined at stresses ranging from 100 to 1000 MPa in the [111], [011] and [-117] orientations. The maximum reversible strains were 2.2 %, 2.7 % and 0.7 % along the [111], [011] and [-117] orientations, respectively after aging at 550 ^{o}C for 3 hours. In the 600 ^{o}C-48h aging, the maximum reversible

strains were 2.3 %, 3.2 % and 0.9 % along the [111], [011] and [-117] orientations, respectively. The [-117] and [111] orientations were stronger compared to the [011] orientation in compression after aging at 550 ^{o}C for 3 hours and aging at 600 ^{o}C for 48 hours.

2. Fully reversible superelastic responses were possible with a larger than 2.2 %, 2.3 % and 0.3 % reversible strains along [111], [011] and [-117] orientations, respectively, at a test temperature of 60 ^{o}C after aging at 550 ^{o}C for 3 hours. After aging at 600 ^{o}C for 48 hours, reversible strains of 1.5 %, 1.2 % and 0.6 % were measured for the [111], [011] and [-117] orientations, respectively, at 140 ^{o}C. No irreversible strain was observed even when deformed to 1500 MPa in the [111] and [-117] orientations after both aging conditions.

3. It was observed that the C-C relations were strong functions of orientation and aging condition. The C-C slopes were 11.1 MPa/^{o}C, 8.2 MPa/^{o}C, and 27.6 MPa/^{o}C for the samples oriented along the [111], [011], and [-117], respectively, after aging at 550 ^{o}C for 3 hours. After aging at 600 ^{o}C for 48 hours, the slopes were 12.5 MPa/^{o}C, 9.3 MPa/^{o}C and 42.2 MPa/^{o}C along the [111], [011] and [-117] orientations, respectively.

4. Thermal hysteresis was also a strong function of orientation in the $Ni_{45.3}Ti_{29.7}Hf_{20}Pd_5$ single crystals. The thermal hysteresis was constant or

decreased along the [111] orientation, while it increased in the [011] orientation, and was essentially constant along the [-117] orientation for both aging conditions. Overall, the thermal hysteresis increased with the amount of irrecoverable strain for both aging conditions. Temperature hystereses of the 550 ^{o}C-3 h aged single crystals were 25 ^{o}C, 60 ^{o}C and 25 ^{o}C under 1000 MPa along the [111], [011] and [-117] orientations, respectively. After aging at 600 ^{o}C for 48 hours, temperature hystereses were 54 ^{o}C, 113 ^{o}C and 45 ^{o}C under 1000 MPa along the [111], [011] and [-117] orientations, respectively.

5. The work output values were also strong functions of orientation. Maximum work output values of 22 J/cm^3, 27 J/cm^3, 7 J/cm^3 were observed along [111], [011] and [-117] loading orientations, respectively, after aging at 550 ^{o}C for 3 hours. For samples aged at 600 ^{o}C for 48 hours, maximum work output values of 20 J/cm^3, 22 J/cm^3, 8.5 J/cm^3 were observed along [111], [011] and [-117] loading orientations, respectively.

6. The material aged at 600 ^{o}C for 48 hours is weaker due to larger, widely spaced, and presumably semi-coherent or incoherent precipitates. After aging at 550 ^{o}C for 3 hours, the material is stronger due to the formation of finer coherent precipitates, which do not allow energy dissipation by defect generation in contrast to the previous case as evidenced from load-biased thermal cycling experiments.

7. The difference in the crucial shape memory properties (e.g. transformation strain) compared to binary NiTi alloys could be stemmed from the difference in the twinning types. Intial results showed that $(001)_{B19'}$ compound twins were active in $Ni_{45.3}Ti_{29.7}Hf_{20}Pd_5$ alloys depending on aging condition while the most common twinning types were Type I and Type II in NiTi alloys.

7. MICROSTRUCTURE-PROPERTY-THERMODYNAMIC RELATIONS IN $Ni_{45.3}Ti_{29.7}Hf_{20}Pd_5$ SHAPE MEMORY ALLOYS

7.1. Introduction

SMAs display shape memory effect and superelasticity owing to thermoelastic solid to solid phase transformation [2]. In this chapter, the main aim is to reveal relationships between microstructure (e.g. precipitate size (d) and interparticle distances, λ) and martensitic transformations in high strength $Ni_{45.3}Ti_{29.7}Hf_{20}Pd_5$ polycrystalline and single crystal SMAs by using thermodynamical principles.

7.1.1. Transformation temperatures of martensitic transformation

Based on the general formula for the forward transformation (equation 1) and the free energy curves in Figure 1.1 in Chapter 1, the necessary conditions for the forward and back transformations are [25]

$$-\Delta G_{ch}^{p-m}+\Delta G_{el}^{p-m}+\Delta G_{irr}^{p-m}=0 \quad (5)$$

$$-\Delta G_{ch}^{m-p}-\Delta G_{el}^{m-p}+\Delta G_{irr}^{m-p}=0 \quad (6)$$

ΔG_{el}^{p-m} is the stored elastic energy during the forward transformation and it is released completely upon back transformation from martensite to austenite. Hence, the elastic energy storage is a mechanically reversible process [24]. The amount of the stored elastic energy should be equal to the released energy upon back transformation if there is no plastic relaxation due to dislocation generation/plastic deformation after a full transformation cycle [26, 27].

The irreversible energy ΔG_{irr}^{p-m} can be assumed as a combination of mainly frictional energy that is required to move phase front (between transforming phases), friction between internal twins in martensite and plastic relaxation energy due to dislocation generation. Both of the abovementioned mechanisms result in dissipation of energy and consequently, hysteresis in SMAs

The total elastic strain energy storage during the martensitic transformation (ΔG_{el}) is contributed by the elastic energies for nucleation (ΔG_{el}^{n}) and propagation (ΔG_{el}^{p}) of martensite [145]. Based on the equations (5) and (6), the TTs can be formulated as following [25];

$$M_s = T_o - \frac{\Delta G_{el}{}^{n}}{|\Delta S|} - \frac{\Delta G_{irr}}{|\Delta S|} \tag{7}$$

$$M_f = T_o - (\frac{\Delta G_{el}{}^{p}}{|\Delta S|} + \frac{\Delta G_{el}^{n}}{|\Delta S|}) - \frac{\Delta G_{irr}}{|\Delta S|} \tag{8}$$

Similar relations for A_s and A_f temperatures can be determined to be [25];

$$A_s = T_o - (\frac{\Delta G_{el}{}^{p}}{|\Delta S|} + \frac{\Delta G_{el}^{n}}{|\Delta S|}) + \frac{\Delta G_{irr}}{|\Delta S|} \tag{9}$$

$$A_f = T_o - \frac{\Delta G_{el}{}^{n}}{|\Delta S|} + \frac{\Delta G_{irr}}{|\Delta S|} \tag{10}$$

ΔS can be expressed as $|\Delta S| = \frac{\Delta\sigma}{\Delta T}.\varepsilon_{tr}$ [1] where $\frac{\Delta\sigma}{\Delta T}$ is the C-C slope and ε_{tr} is the maximum transformation strain which depends on aging condition and loading orientation.

T_o is generally expressed as [24, 146];

$$T_o = \frac{M_s + A_f}{2} \tag{11}$$

T_o is only chemical composition dependent. If there are constraints (e.g. multiple interfaces, precipitates, grain boundaries etc.) to transformational shape change, transformation temperatures are lowered and equation 11 may not give correct T_o values in those cases. Thus, T_o could be higher than $\frac{M_s + A_f}{2}$ [129] and even very close to A_f temperature [147] in the presence of constraints in microstructure. On the other hand, if there is internal stress in a microstructure, TTs could be elevated and in such a case, T_o could be lower than theoretically calculated value. Thus, several approaches will be used in the calculation of T_o throughout our analysis and results will be presented based on each approach in the chapter. As a first approach (A1), T_o will be calculated by equation 11 for all materials. Then, as a second approach (A2), T_o will be assumed to be equal to A_f for each material. Finally, the extruded material will be assumed to be a base material and due to the decreasing (e.g. small precipitates) and the increasing (e.g. internal stress) effects on TTs, the T_o of the extruded material (calculated by equation 11) will be assumed to be the T_o of all the aged alloys. The non-chemical free energies of the aged

materials will be calculated relative to the extruded material. This method will be abbreviated as A3.

7.1.2. Non-chemical energy terms related to martensitic transformation

In the thermoelastic martensitic transformations, the TTs temperatures are affected by the stored and released elastic strain energy as well as the irreversible energy as discussed previously. Thus, the whole phase transformation can be influenced by a change in elastic energy and irreversible (combination of frictional and plastic relaxation) contribution in equations (5) and (6).

The elastic energy due to propagation of martensite can be formulated as,

$$\left|\Delta G_{el}^{p}\right| = (M_s - M_f)\left|\Delta S\right| \tag{12}$$

where ΔS is the change in entropy upon phase transformation. On the other hand, the elastic energy (necessary driving force at M_s) for nucleation can be expressed as,

$$\left|\Delta G_{el}^{n}\right| = (T_o.\Delta S) - (M_s + A_f)\frac{\left|\Delta S\right|}{2} \tag{13}$$

In addition to the elastic strain energies, it could be useful to derive an expression for the irreversible energy from the above derived equations before starting the analysis. By combining the equations (13) and (16), the irreversible energy can be expressed as;

$$\Delta G_{irr} = \frac{A_f - M_s}{2}.\left|\Delta S\right| \tag{14}$$

7.2. Effects of microstructures on the transformation temperatures

The precipitate characteristics of the polycrystalline $Ni_{45.3}Ti_{29.7}Hf_{20}Pd_5$ alloys were presented in Chapter 3 through TEM observations conducted on as-extruded and aged samples at RT. The as-extruded specimen was expected to have tiny precipitates due to slow cooling process after homogenization. The 400 ^{o}C-3 hours aged specimens consist of a single B2 austenite phase without any visible precipitates with the conventional TEM, however it was assumed that the 400 ^{o}C-3h specimen had very small precipitates in size, that can only be detected by HRTEM. On the other hand, spindle-shaped precipitates were clearly observed in the 550 ^{o}C-3 hours and 650 ^{o}C-3 hours aged specimens. Fine precipitates with sizes of approximately 20-30 nm in length with interparticle distance of about 10-30 nm were formed after 550 ^{o}C-3 hours aging.

As the aging temperature increased to 650 ^{o}C, the precipitates were quite large when compared with the 550 ^{o}C-3 hours specimen, with a length that varies from about 80 nm to 300 nm and width of about 50 nm. The interparticle distance varied from 15 nm to 150 nm in the 650 ^{o}C-3h specimen.

Figure 7.1 shows the changes in the stress-free TTs (determined from the DSC results) with aging temperature after aging for 3 hours. An initial decrease in TTs with aging temperature was observed reaching a minimum at about 400 °C. Between 400 to 600 °C the TTs increased with increasing aging temperature, reaching a maximum at about 600 °C, decreasing once again with any further increased in aging temperature. For 3 hours aging time, A_f reached a maximum of 150 ^{o}C following aging at 600 ^{o}C.

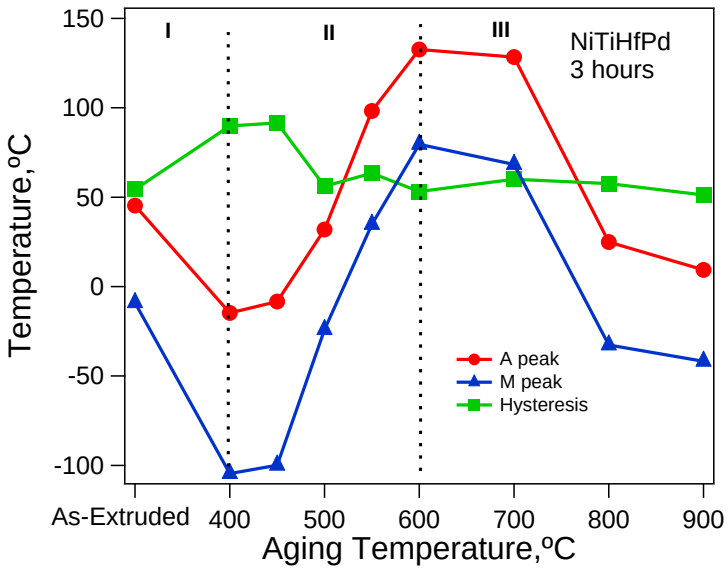

Figure 7.1: Regions in the change in TTs and thermal hysteresis in $Ni_{45.3}Ti_{29.7}Hf_{20}Pd_5$ polycrystalline alloys after various aging treatments

A possible change in the non-chemical free energy terms (elastic end irreversible energies) based on initial microstructures are thought to be responsible in the change of TTs in the following manner;

The initial drop in TTs was attributed to the formation of precipitates with very small size and very short interparticle distances. Thus, the resistance for martensite nucleation increases and formation of martensite required more energy change, which in turn required further undercooling ($\Delta T = T_o - M_s$) in the course of the forward transformation [55].

Based on thermoydnamics, following factors can be liable for the change of TTs in $Ni_{45.3}Ti_{29.7}Hf_{20}Pd_5$;

i) Elastic energy for nucleation is high due to small interparticle distance for the aging temperature up to 400 ^{o}C 3 hours in region I. When the precipitate size (d <10nm) and λ distances were small (high precipitate density,), the elastic energy for nucleation of martensite (ΔG_{el}^{n}) will be high and it will decrease the M_s temperature in spite of increased volume fraction of precipitates based on equation (13). In region II, the lower ΔG_{el}^{n} due to larger interparticle distances after aging at higher temperatures might help increase the TTs.

ii) In addition to the non-chemical energy terms, there is also ***an effect of chemical composition*** (ΔT_{comp}) on the martensitic transformation temperatures. In general, TTs are increased with aging in NiTi-based alloys due to an increase in the volume fraction of the Ni-rich precipitates, resulting in a change in composition of the remaining matrix material (e.g. Ni depletion in matrix). It is well known that TTs are highly composition dependent in NiTi based SMAs [2]. Hence, a decrease in the Ni content upon aging will result Ni depletion from the matrix and it will increase the M_s temperature by ΔT_{comp} depending on an increase or decrease in the Ni content.

In region I, the effect of the chemical composition was presumably suppressed by the effects of non-chemical energies and consequently, the TTs decreased. However, the chemical composition change can be quite dominant in the increased TTs in region II in addition to the abovementioned decrease in ΔG_{el}^{n} and ΔG_{irr} energies.

In region III, the second drop in TTs can be attributed to a reduction in precipitate volume fraction as the aging temperature increased and either approached or surpassed the precipitate solvus temperature. Once again resulting in a Ni-rich matrix and thus, decrease in TTs based on the equation that will be stated in later paragraphs.

iii) A***n increase in the*** ΔG_{irr} ***term*** was observed in region I as shown in Figure 7.1. The increase in the thermal hysteresis is a representation of an increase in irreversible energy term since hysteresis is an irreversible dissipation process. The increase in the ΔG_{irr} term decreased the M_s temperature in 400 ^{o}C-3h sample based on equation 7.

iv) Another factor in tailoring of the TTs can be ***local internal stress (*** $\Delta\sigma_{in}$***)*** originated from the mismatch between lattice parameters of the matrix and the formed precipitates in the materials. It is known that the TTs increase if there is internal stress in the microstructure since the formed internal stress acts as an external stress favoring martensitic transformations in SMAs [4]. The effect of the internal stress on M_s temperature can be expressed a change by ΔT_{int}.

In region I, the precipitates were small in size due to low aging temperature. Hence, the internal stress was not high enough to surpass the effects of non-chemical energies on TTs as mentioned earlier.

Dissimilarly; the precipitates became more coherent after aging temperatures of 400 ^{o}C resulting high internal stresses in the materials in region II. The formed internal stresses helped in favoring the martensite plates as external stress did and consequently, M_s increased.

After aging temperature of 600 ^{o}C in region III, the materials were already over-aged resulting non-coherent precipitates that relaxed surrounding internal stress fields. The relaxed internal stress was not as effective in increasing TTs in region III as it was in region II.

Figure 7.2 shows the change in non-chemical energies calculated by the abovementioned three approaches as a function of aging temperature in $Ni_{45.3}Ti_{29.7}Hf_{20}Pd_5$ alloys. In a and b, the elastic strain energies decreased while the friction energy slightly increased compared to the as-received case after aging at 400 ^{o}C. As the aging temperature increased to 550 ^{o}C, all the non-chemical energies abruptly increased while the decrease continued once the materials was over-aged at 650 ^{o}C.

In Figure 7.2c, when the material is aged at 400 ^{o}C, the elastic strain energies increased slightly while the friction energy was almost constant compared to the as-received case. As the aging temperature increased to 550 ^{o}C, the nucleation energy started to decrease while the propagation and friction energies increased. After aging at 650 ^{o}C, the friction energy was almost constant as the nucleation and propagation energies decreased.

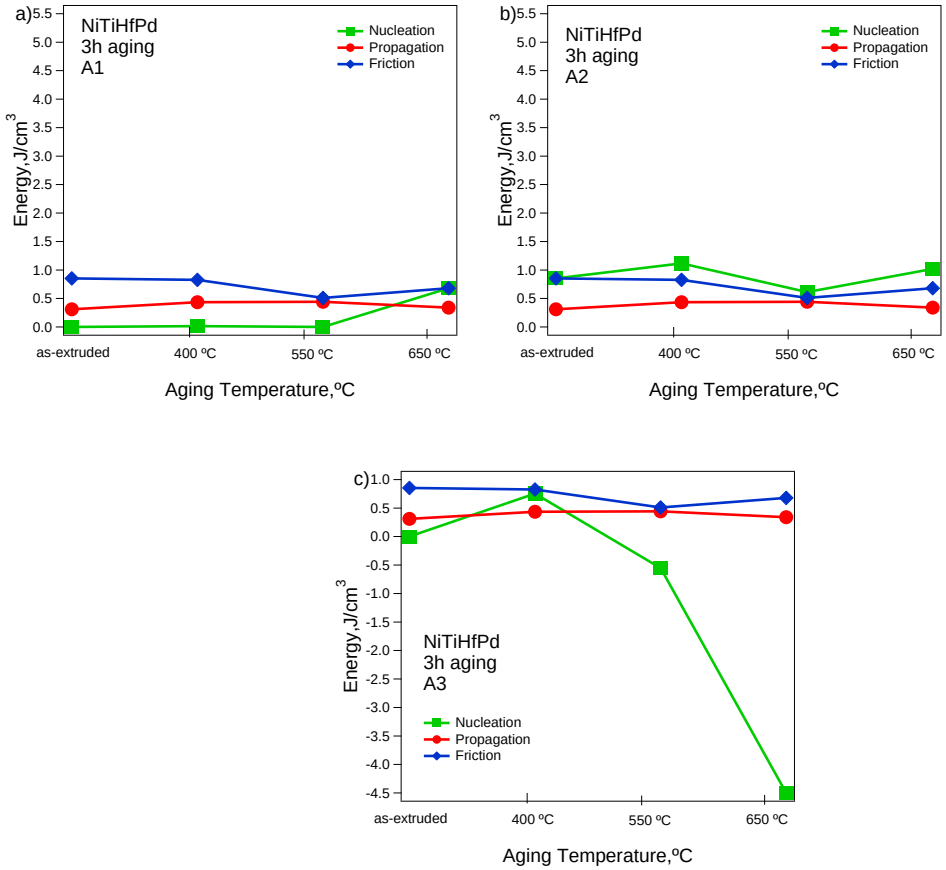

Figure 7.2: Non-chemical energies calculated by the methods of a) A1, b) A2 and c) A3 as a function of aging in $Ni_{45.3}Ti_{29.7}Hf_{20}Pd_5$ alloys

By considering all the above mentioned factors, a change in M_s temperature might be formulated as;

$$\Delta M_s = T_o - \frac{\Delta G_{el}{}^{n}}{|\Delta S|} - \frac{\Delta G_{irr}}{|\Delta S|} + \Delta T_{comp} + \Delta T_{\text{int}} \qquad (15)$$

Since the ΔG_{el}^{n} and composition effect are two computing mechanisms in the TTs change, we can combine two effects such that;

$$\Delta M_s = T_o + (\Delta T_{comp} - \frac{\Delta G_{el}{}^{n}}{|\Delta S|}) - \frac{\Delta G_{irr}}{|\Delta S|} + \Delta T_{\text{int}} \qquad (16)$$

7.3. Effects of aging and high stress on the non-chemical energies in transformation behavior

Constant-stress thermal cycling results of the as-extruded and heat treated $Ni_{45.3}Ti_{29.7}Hf_{20}Pd_5$ polycrystalline specimens under selected compressive stress levels ranging from 100 MPa to 1000 MPa are depicted in Figure 7.3. Specimens were loaded to selected stress levels at temperatures above A_f and then were thermally cycled under the selected constant stress. It is evident from Figure 7.3 that the TTs increased with stress.

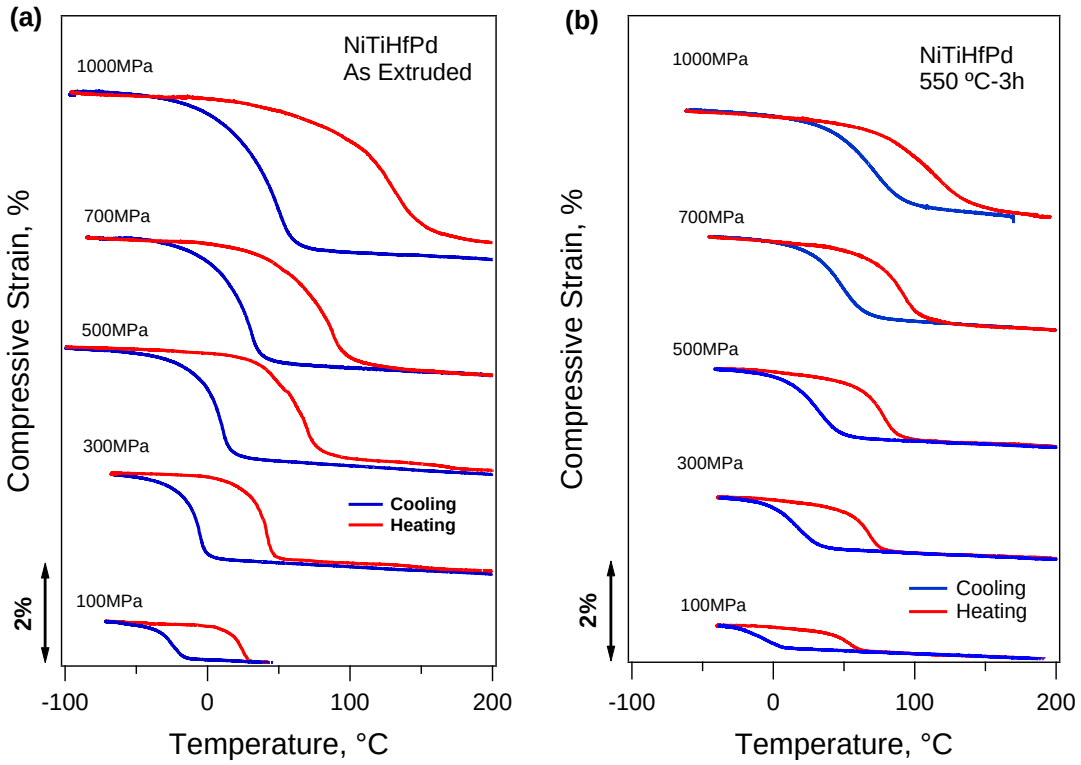

Figure 7.3: Constant-stress thermal cycling results for the $Ni_{45.3}Ti_{29.7}Hf_{20}Pd_5$ alloy a) as-extruded, b) aged at 550 ^{o}C for 3 hours [148]

Figure 7.4 shows the schematic representations of thermal cycling curves of the as-extruded and 550 ^{o}C-3h aged specimens at 100 MPa and 1000 MPa. In the as-extruded specimen, M_s and A_s were -16 ^{o}C and 15 ^{o}C under 100 MPa, and 60 ^{o}C and 102 ^{o}C under 1000 MPa, respectively. At both stress levels, A_s was higher than M_s in the as-extruded condition. In other words, the transformations were "Class I" [136] at 100 MPa and 1000 MPa ($M_s<A_s$). For the 550 ^{o}C-3h aged specimen, M_s was 13 ^{o}C and A_s was 38 ^{o}C under 100 MPa. Thus, it was also a "Class I" transformation. However, an anomaly was observed for the 550 ^{o}C-3hours aged specimen at 1000 MPa, compared to the previous cases, since M_s was 93 ^{o}C and A_s was 80 ^{o}C. It is clear that M_s was lower than A_s under 100 MPa while M_s was higher than A_s ("Class II" ($M_s>A_s$) [136]) under 1000 MPa for the aged sample. M_s and A_s for the as-extruded and 550 ^{o}C-3hours aged samples are given as a function of applied stress in Table 3.

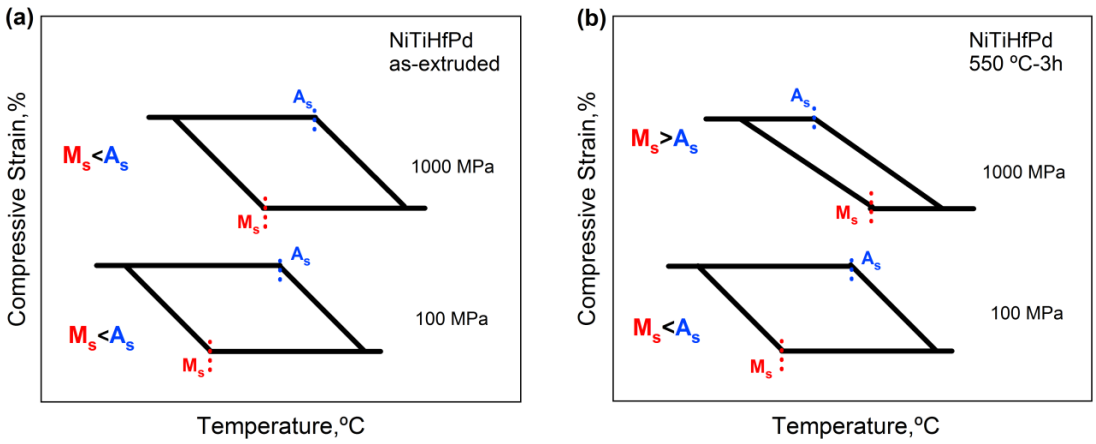

Figure 7.4: Schematic representation of the change in M_s and A_f temperatures with stress in a) as-extruded and b) 550 ^{o}C-3h aged material as a function of applied stress in constant-stress thermal cycling experiments [92].

The change from Class I to II transformation behavior with stress in the 550 ^{o}C-3 hours aged specimen can be attributed to the higher elastic energy storage during thermal cycling at the high stress of 1000 MPa compared to lower stress levels. The higher elastic energy storage might be a result of various factors including;

i) a change in twinning properties and lattice parameters

The $Ni_{45.3}Ti_{29.7}Hf_{20}Pd_5$ polycrystalline alloy undergoes a B2 to B19' phase transformation under zero stress. However, at stresses as high as 1000 MPa, the lattice parameters of the parent and martensitic phases may alter that will affect the compatibility of the transforming phases and twinning properties. Thus, elastic energy storage might increase during thermal cycling at 1000 MPa compared to thermal cycling at lower stresses (e.g. 100 MPa [27]. However, it is clear that for the as-extruded sample, the applied stress did not result in high elastic energy storage since $M_s<A_s$ for all applied stress levels. Thus, either applied stress did not increase the stored elastic energy or stored elastic energy relaxed after transformation due to plastic deformation in the as extruded sample.

ii) a possible habit plane distortion by extereme high stress

In NiTi shape memory alloys, it was reported that the habit plane between martensite and austenite distorts during detwinning process resulting in additional elastic energy storage [149]. It was also observed that the habit plane was distorted locally in a stress-induced martensite transformation in CuNiAl shape memory alloys [150] since the martensite was formed on the habit plane during transformation. Similiarly, in the

$Ni_{45.3}Ti_{29.7}Hf_{20}Pd_5$ polycrystalline alloys, the habit plane could be distorted during formation due to applied high stress and/or during propagation due to formed high back stress. This distortion in the habit plane may cause an increase in the elastic energy particularly at high stress levels and may change the transformation type as the stress increases in constant stress thermal cycling experiments if there is no elastic energy relaxation.

iii) increased detwinnig by extreme high stress

Transformation strain is obtained mainly by CVP formation and detwinning strain in SMAs [151]. Detwining can be explained as the growth of one variant at the expense of other CVPs in the microstructure [151]. Hence, it increases as a function of stress since the growth of one CVP variant in the expense of others requires further energy. In the $Ni_{45.3}Ti_{29.7}Hf_{20}Pd_5$ polycrystalline alloys, the applicable stress is exteremly high (e.g. >700 MPa) in constant stress thermal cycling experiments. Thus, this high stress may increase the detwining strain and result in further elastic energy storage at high stress levels. On the other hand, if the material is precipitation strengthened as in 550 ^{o}C-3h case, the internal stresses around precipitates could try to inhibit the detwining process and this may contribute the additional elastic energy storage in aged materials compared to not aged or over-aged materials.

Table 3: Change in M_s and A_s temperatures with applied stress in thermal cycling experiments of the as-extruded and 550 ^{o}C-3h aged specimen [92].

Stress	As-extruded		550 ^{o}C-3h	
	$M_s^{100\ MPa}$ (^{o}C)	$A_s^{100\ MPa}$ (^{o}C)	$M_s^{1000\ MPa}$ (^{o}C)	$A_s^{1000\ MPa}$ (^{o}C)
100 MPa	-16	15	13	38
300 MPa	-1	32	32	55
500 MPa	23	45	50	70
700 MPa	37	60	65	76
1000 MPa	**60**	**102**	**93**	**80**

iv) increased material strength and back stress

When the responses of the as-extruded and aged samples under 100 MPa (or DSC responses, Figure 3.3) were compared, it was clear that A_s was higher than M_s in both cases, indicating that precipitate formation did not solely result in high elastic energy storage. Since the 550 ^{o}C-3 hours aged material was precipitation hardened with nano size coherent particles upon aging, propagation of formed martensite was more difficult and consequently, elastic energy storage during the martensitic transformation were higher [129, 130] compared to the as-extruded sample (neglecting the effect of transformation strains since they were close). On the other hand, increased back stress due to martensite-particle interaction could make the motion of phase front more difficult and this may contribute the accumulation of elastic energy during propagation of

martensite. The increased back stress could be a result of both improved strength and application of high stress in $Ni_{45.3}Ti_{29.7}Hf_{20}Pd_5$ polycrystalline alloys. Although transformation type was the same for both cases, the difference between A_s and M_s decreased from 31 ^oC to 25 ^oC with aging. Thus, some increase in elastic storage or decrease in energy dissipation occured with aging.

When the sample was aged and then high stress was applied, the transformation type changed from "Class I" ($M_s<A_s$) to "Class II" ($M_s>A_s$) due to very high elastic energy storage [111]. Since the elastic energy helped back transformation and elastic energy relaxation by dislocation generation was not expected in the aged specimen, lower superheating was enough to initiate the back transformation. Lower superheating resulted in a relatively lower A_s during thermal cycling at 1000 MPa for the 550 ^oC-3 hours aged specimen as shown in Figure 7.3. The key point to note was the fact that stored elastic energy was not relaxed upon transformation due to high matrix strength in the aged sample while it was relaxed in the as extruded sample [26]. Thus, we can conclude that aging and applied high stress could increase the elastic storage energy and prevent its relaxation, which could lower A_s, decrease hysteresis, and change the transformation type.

The change in temperatures can be analyzed by the following thermodynamical assay. Recall that the M_s formula was expressed as equation 7 earlier.

Hence, when the friction to move the phase front is high in a material, meaning high irreversible/dissipation, M_s will be lowered according to the equation above. Similar to M_s, the equation for the A_s temperature was defined in equation 9.

In equation 9, ΔG_{el}^{p} was the accumulated elastic energy when the full martensite transformation is obtained (dictated by both nucleation and variant reorientation during growth). Thus, for a Class II transformation (M_s>A_s), the following equation can be written;

$$\Delta G_{el}{}^{p} - \Delta G_{el}{}^{n} > 2\Delta G_{irr} \qquad (17)$$

Equation 17 indicates that for a Class II transformation, ΔG_{el}^{p} should be large, $\Delta G_{el}{}^{n}$ and ΔG_{irr} should be small. ΔG_{el}^{p} can be increased if there is additional elastic energy creation during martensite reorientation and no relaxation due to defect generation, $\Delta G_{el}{}^{n}$ can be increased with decreased interparticle distance and increased shear modulus of the matrix. ΔG_{irr} depends on the compatibility of the transforming phases and the strength of the matrix. Thus, increased strength of the matrix could increase the stored elastic energy by increasing the elastic energy generated during forward transformation. The increased strength can also decrease the relaxation of elastic energy and the dissipation energy that could change the transformation class from I to II. In this study, precipitation formation was responsible for not only increasing the strength but may also alter the lattice parameters of the transforming phases, which could alter the compatibility and twinning properties of the martensite and thus the elastic energy and dissipation energy creation. However, precipitation hardening cannot change the transformation class alone in the studied alloys. High stress must be applied to increase the stored elastic energy by creating additional elastic energy due to variant reorientation and altering the elastic and dissipation energy terms due to change in lattice structures

and parameters of the transforming phases. A more detailed analysis regarding the non-chemical energies as a function of stress will be discussed in onward paragraphs.

Figure 7.5 shows the phase diagrams that were extracted from the constant stress thermal cycling experiments in the as-extruded and aged $Ni_{45.3}Ti_{29.7}Hf_{20}Pd_5$ polycrystalline alloys. The phase diagrams show the TTs under applied stress levels in addition to stress-free ones extracted from C-C curves.

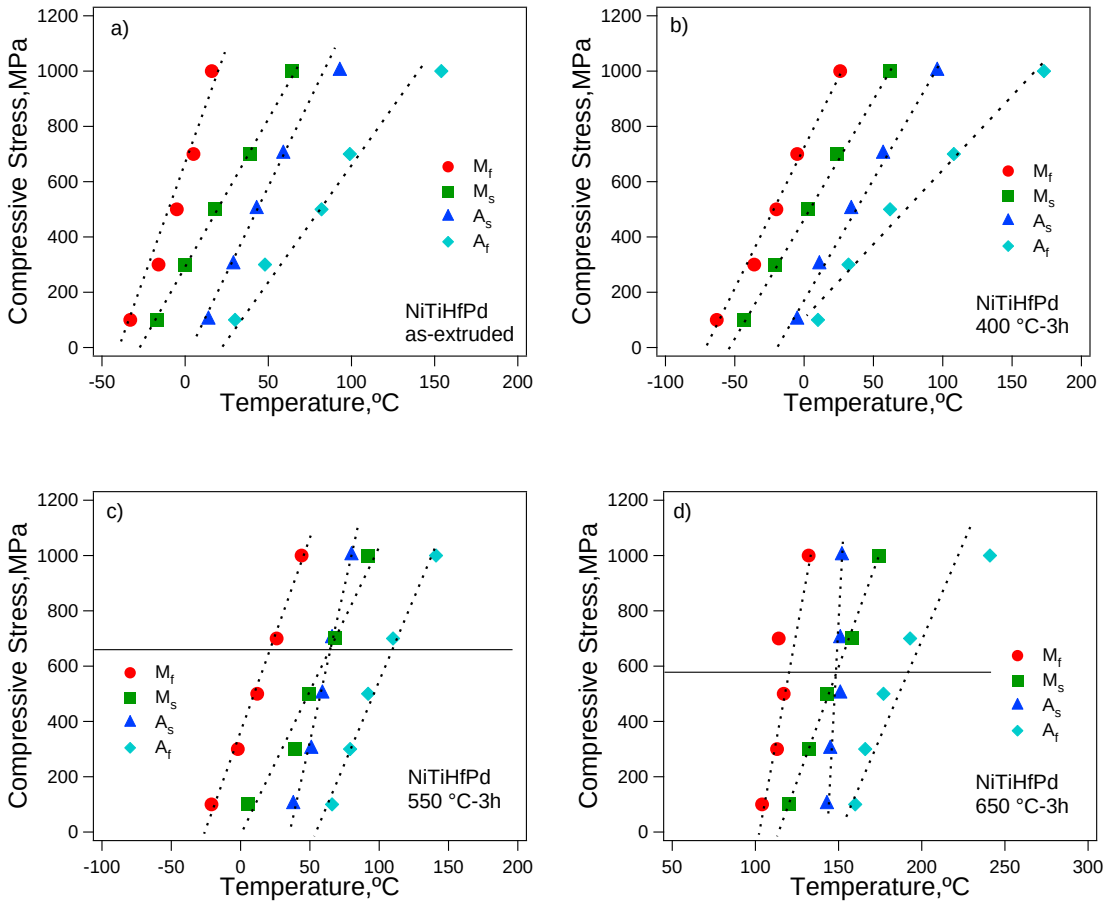

Figure 7.5: Experimentally observed phase diagrams for $Ni_{45.3}Ti_{29.7}Hf_{20}Pd_5$ polycrystalline alloys

As observed in Figure 7.5, the phase diagrams were clearly distinct from each other. In some diagrams, the curves for the TTs under load were linear (e.g. 550 ^{o}C-3h) while the others were not (e.g.650 ^{o}C-3h). It is clear that the difference in TTs (e.g. difference between A_f and M_s, ΔT_{Af-Ms} during the forward transformation increased with stress for all $Ni_{45.3}Ti_{29.7}Hf_{20}Pd_5$ specimens. However, the same increasing trend was not observed for the TTs difference during the back transformation in the 400 ^{o}C-3h and 650 ^{o}C-3h samples. The differences were almost constant up to a stress level that is 500 MPa and 700 MPa for the earlier and later materials, respectively. Then, the difference between M_s and A_f is increased suddenly. In contrast, the ΔT_{Af-Ms} decreased initially followed by staying almost constant with stress in the material aged at 550 ^{o}C for 3 hours. These differences on the change of TTs with stress will be discussed based on the non-chemical energy contributions in $Ni_{45.3}Ti_{29.7}Hf_{20}Pd_5$ alloys.

The phase diagrams of studied alloys were shown Figure 7.5. In the 550 ^{o}C-3h sample, the ΔT_{Af-Ms} was almost constant with increased stress up to 1000 MPa. However, the difference between A_f and M_s suddenly increased after 500 MPa in the 400 ^{o}C-3h and after 700 MPa for the 650 ^{o}C-3h phase diagrams. There could be two main deductions of the observed behaviors based on thermodynamic relations.

i) According to the equation (14), the difference between A_f and M_s was directly related to the irreversible energy, ΔG_{irr}. The increased ΔT_{Af-Ms} showed an increase in the irreversible energy based on the equation. This deduction can also be proved by the experimental data previously reported in [92]. As the applied stress increases to 500 MPa, a plastic deformation was observed in line with the unclosed curves (irrecoverable

strains) in the constant stress thermal cycling loops. The observed irrecoverable strain was a direct result of a dissipation in the material and consequently an increase in the ΔG_{irr} .

ii) ΔT_{Af-Ms} was also closely related to the elastic energy for nucleation of martensite, ΔG_{el}^{n} . It is clear that the increased ΔT_{Af-Ms} after 500 MPa in the 400 ^{o}C-3h and after 700 MPa for the 650 ^{o}C-3h specimens was observed after starting of plastic deformations in the constant stress thermal cycling experiments [92]. Upon plastic deformation in the materials, dislocations were generated that can make the nucleation of martensite easier in the materials since dislocations could act like nucleation sites for the martensite [152]. In the dislocated samples (e.g. 400 ^{o}C-3h and 650 ^{o}C-3h), the nucleation of the martensite will be easier causing a decrease in ΔG_{el}^{n} and measurable differences between A_f and M_s temperatures as observed in phase diagrams.

In contrast to easier nucleation by plastic deformation, the propagation of the phase fronts will be more difficult due to the pinning effects of dislocations compared to non-dislocated samples (e.g. 550 ^{o}C-3h). Consequently, ΔG_{el}^{p} increased as the applied stress increased, which helped the total elastic energy increase.

It was also clear that M_s temperature was lower than A_s after a certain stress level in the 550 ^{o}C-3h and 650 ^{o}C-3h samples as lined in the phase diagrams. This shows that the transformation type changed after this stress levels from class I to class II due to elastic energy accumulated as the stress increased in the constant stress thermal cycling experiments.

On the other hand, the change in reversible (ΔG_{el}^{n} and ΔG_{el}^{p}) and irreversible (ΔG_{irr}) energies can be discussed qualitatively as shown in following graphs. Figure 7.6 shows the non-chemical free energies calculated by the approach 1. Figure 7.6a and 7.6b show the change in ΔG_{el}^{n}, ΔG_{el}^{p} and ΔG_{irr} energies with stress for the $Ni_{45.3}Ti_{29.7}Hf_{20}Pd_5$ alloys in as-extruded and aged at 400 ^{o}C for 3 hours, respectively and Figure 7.6c and 7.6d show the related energy changes for the materials aged at 550 ^{o}C and at 650 ^{o}C for 3 hours, respectively.

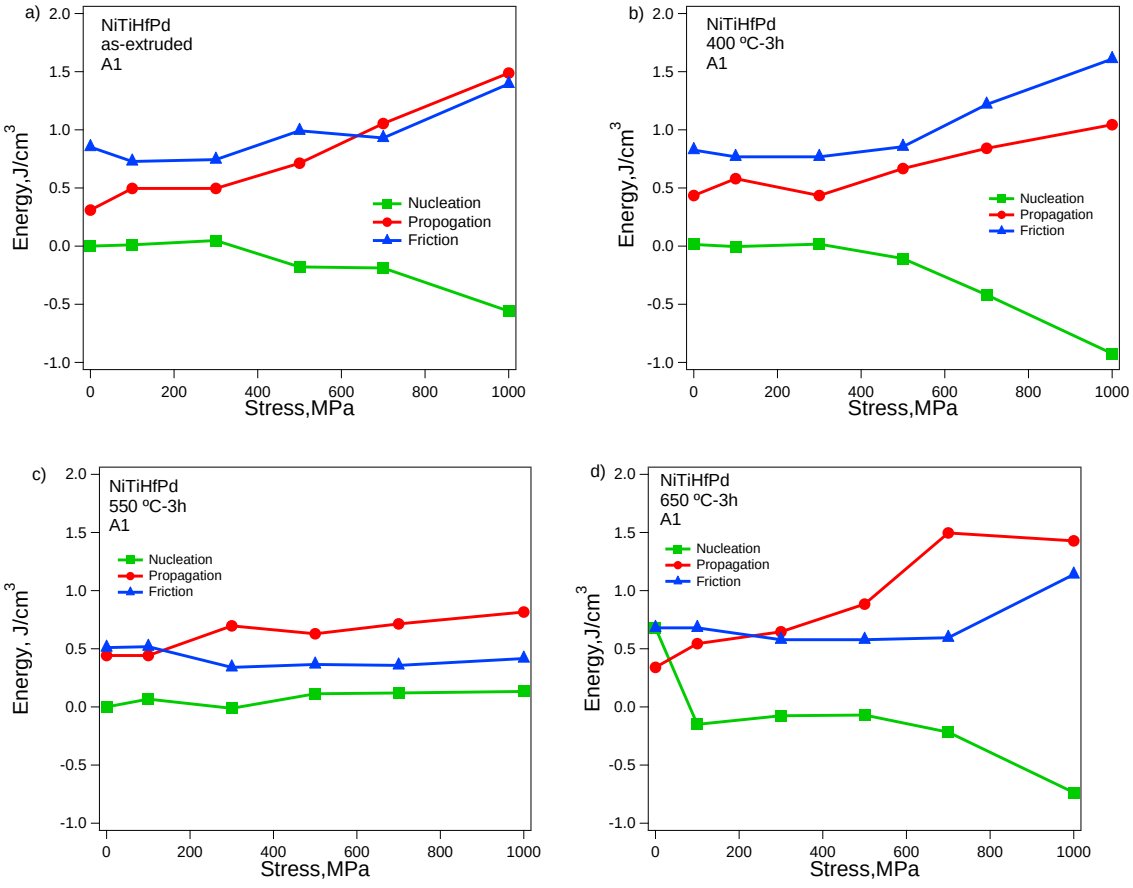

Figure 7.6: Dependence of the reversible (ΔG_{el}^{n} and ΔG_{el}^{p}) and irreversible (ΔG_{irr}) free energies (calculated by approach 1) on the applied stress during constant stress thermal

cycling experiments in a) as-extruded, b) 400 ^{o}C-3h, c) 550 ^{o}C-3h and 650 ^{o}C-3h $Ni_{45.3}Ti_{29.7}Hf_{20}Pd_5$ shape memory alloys

The elastic energy for nucleation in the as-extruded sample was 0 J/cm^3 under zero stress and slightly decreased to -0.55 J/cm^3 as the stress increased to1000 MPa. The elastic energy for propagation was 0.31 J/cm^3 in stress-free condition as it increased to 1.48 J/cm^3 under 1000 MPa. The friction energy was determined to be 0.85 J/cm^3 under zero MPa and stayed close up to 700 MPa. It increased to 1.4 J/cm^3 as the stress was 1000 MPa.

The elastic energy for nucleation in the specimen aged at 400 ^{o}C for 3 hours was 0.01 J/cm^3 under zero stress; however, as the applied stress increased, ΔG_{el}^{n} decreased to -0.003 J/cm^3 under 1000 MPa. The elastic energy for propagation was 0.43 J/cm^3 in stress-free condition as it increased to 1 J/cm^3 under 1000 MPa. The friction energy was determined to be 0.82 J/cm^3 under zero MPa and stayed almost constant up to 500 MPa. After 500 MPa, an abrupt increase was observed in ΔG_{irr}, which was 1.21 and 1.6 J/cm^3 under 700 and 1000 MPa, respectively.

Figure 7.6c showed the change in reversible and irreversible energies in $Ni_{45.3}Ti_{29.7}Hf_{20}Pd_5$ aged at 550 ^{o}C for 3 hours. The elastic energy for nucleation in the specimen aged at 550 ^{o}C for 3 hours was 0 J/cm^3 under zero stress; however, as the applied stress increased to 1000 MPa, ΔG_{el}^{n} increased to 0.06 J/cm^3. The elastic energy for propagation was 0.44 J/cm^3 in stress-free condition as it increased to 0.81 J/cm^3 under

1000 MPa. The friction energy was determined to be 0.51 J/cm^3 under zero MPa and 0.41 J/cm^3 at 1000 MPa. The irreversible energy in the 550 ^{o}C-3h material decreased initial as the stress reached to 300 MPa and was almost constant up to 1000 MPa, which is fairly consistent with the temperature hysteresis result reported previously [92]. Since there was no increase in the irreversible energy term, the temperature hysteresis was almost constant in the 550 ^{o}C-3h sample.

The elastic energy for nucleation in the specimen aged at 650 ^{o}C for 3 hours was 0.68 J/cm^3 under zero stress and decreased to -0.15 J/cm^3 as the stress increased to1000 MPa. The elastic energy for propagation was 0.34 J/cm^3 in stress-free condition as it increased to 1.42 J/cm^3 under 1000 MPa. The friction energy was determined to be 0.68 J/cm^3 under zero MPa and stayed almost constant up to 700 MPa. It increased to 1.14 J/cm^3 when the stress was as high as 1000 MPa.

Figure 7.7 shows the non-chemical free energies calculated by the approach 2. Figure 7.7a and 7.7b show the change in $\Delta G_{el}^{n}, \Delta G_{el}^{p}$ and ΔG_{irr} energies with stress for the $Ni_{45.3}Ti_{29.7}Hf_{20}Pd_5$ alloys in as-received and aged at 400 ^{o}C for 3 hours, respectively and Figure 7.7c and 7.7d show the related energy changes for the materials aged at 550 ^{o}C and at 650 ^{o}C for 3 hours, respectively.

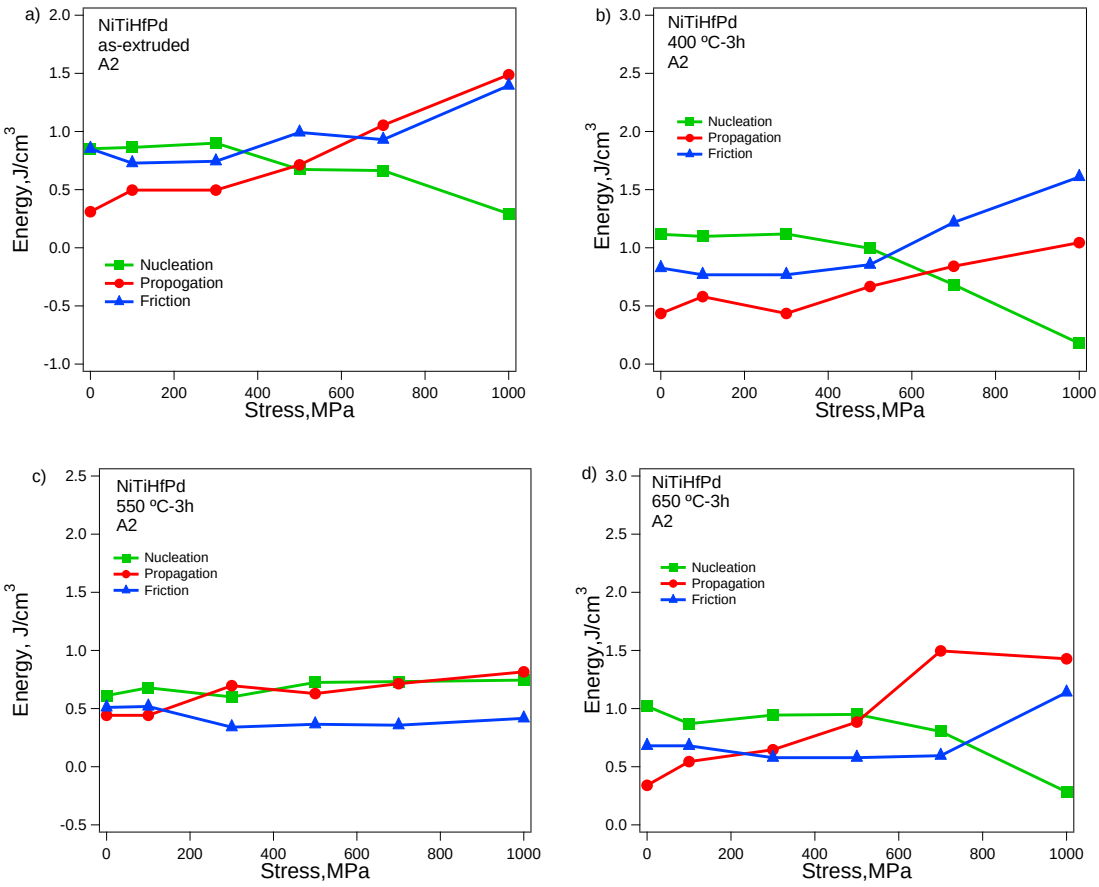

Figure 7.7: Dependence of the reversible (ΔG_{el}^{n} and ΔG_{el}^{p}) and irreversible (ΔG_{irr}) free energies (calculated by approach 2) on the applied stress during constant stress thermal cycling experiments in a) as-extruded, b) 400 ^{o}C-3h, c) 550 ^{o}C-3h and 650 ^{o}C-3h $Ni_{45.3}Ti_{29.7}Hf_{20}Pd_5$ shape memory alloys

The elastic energy for nucleation in the as-extruded sample was 0.85 J/cm^3 under zero and slightly decreased to 0.29 J/cm^3 as the stress increased to1000 MPa. The elastic energy for propagation was 0.31 J/cm^3 in stress-free condition as it increased to 1.48 J/cm^3 under 1000 MPa. The friction energy was determined to be 0.85 J/cm^3 under zero MPa and stayed close up to 700 MPa. It increased to 1.4 J/cm^3 as the stress was 1000 MPa.

The elastic energy for nucleation in the specimen aged at 400 ^{o}C for 3 hours was 1.11 J/cm^3 under zero stress; however, as the applied stress increased, 1000 MPa, ΔG_{el}^{n} decreased to 0.17 J/cm^3, which was the energy under 1000 MPa. The elastic energy for propagation was 0.43 J/cm^3 in stress-free condition as it increased to 1 J/cm^3 under 1000 MPa. The friction energy was determined to be 0.82 J/cm^3 under zero MPa and stayed almost constant up to 500 MPa. After 500 MPa, an abrupt increase was observed in ΔG_{irr}, which was 1.21 and 1.6 J/cm^3 under 700 and 1000 MPa, respectively.

Figure 7.7c showed the change in reversible and irreversible energies in $Ni_{45.3}Ti_{29.7}Hf_{20}Pd_5$ aged at 550 ^{o}C for 3 hours. The elastic energy for nucleation in the specimen aged at 550 ^{o}C for 3 hours was 0.61 J/cm^3 under zero stress; however, as the applied stress increased, 1000 MPa, ΔG_{el}^{n} increased to 0.74 J/cm^3, which was the energy under 1000 MPa. The elastic energy for propagation was 0.44 J/cm^3 in stress-free condition as it increased to 0.81 J/cm^3 under 1000 MPa. The friction energy was determined to be 0.51 J/cm^3 under zero MPa and 0.41 J/cm^3 at 1000 MPa.

The elastic energy for nucleation in the specimen aged at 650 ^{o}C for 3 hours was 1.02 J/cm^3 under zero stress and decreased to 0.28 J/cm^3 as the stress increased to1000 MPa. The elastic energy for propagation was 0.34J/cm^3 in stress-free condition as it increased to 1.42 J/cm^3 under 1000 MPa. The friction energy was determined to be 0.68 J/cm^3 under zero MPa and stayed almost constant up to 700 MPa. It increased to 1.14 J/cm^3 as the stress was 1000 MPa.

Figure 7.8 shows the non-chemical free energies calculated by the approach 3. Figure 7.8a and 7.8b show the change in $\Delta G_{el}^{n}, \Delta G_{el}^{p}$ and ΔG_{irr} energies with stress for the $Ni_{45.3}Ti_{29.7}Hf_{20}Pd_5$ alloys in as-received and aged at 400 ^{o}C for 3 hours, respectively and Figure 7.8c and 7.8d show the related energy changes for the materials aged at 550 ^{o}C and at 650 ^{o}C for 3 hours, respectively.

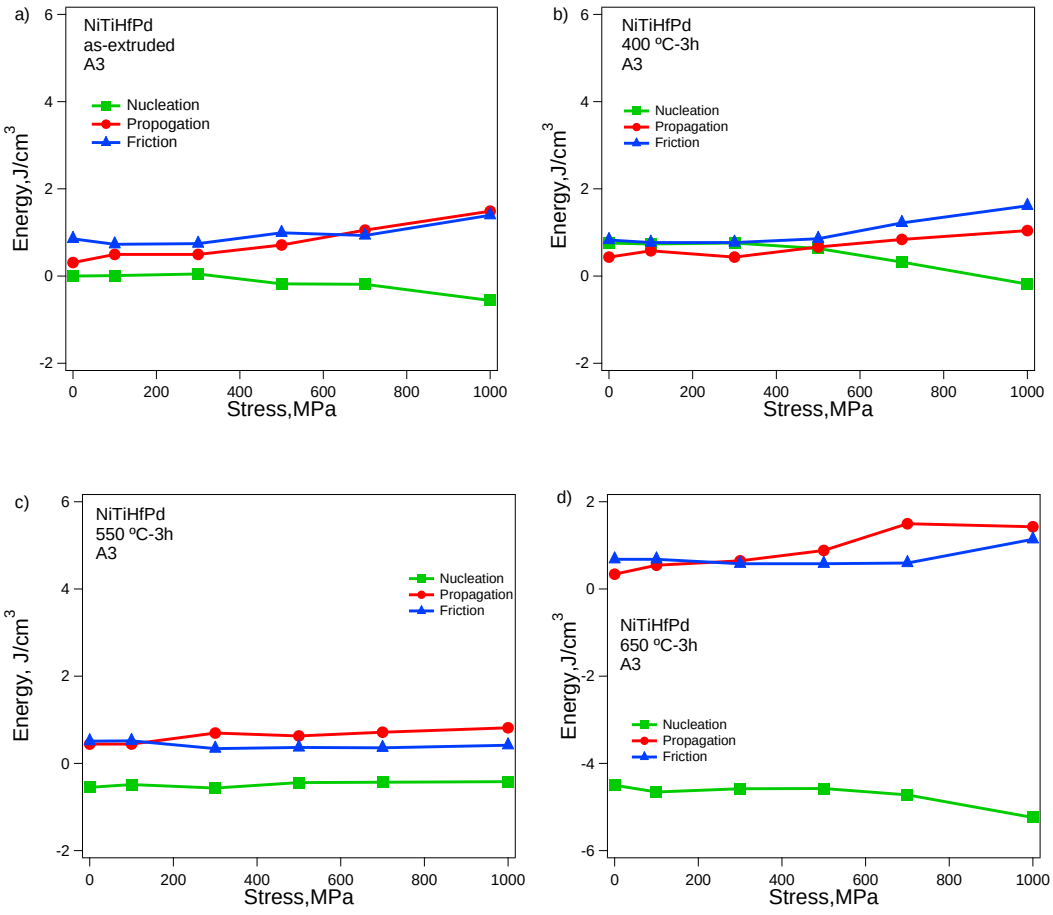

Figure 7.8: Dependence of the reversible (ΔG_{el}^{n} and ΔG_{el}^{p}) and irreversible (ΔG_{irr}) free energies (calculated by approach 3) on the applied stress during constant stress thermal cycling experiments in a) as-extruded, b) 400 ^{o}C-3h, c) 550 ^{o}C-3h and 650 ^{o}C-3h $Ni_{45.3}Ti_{29.7}Hf_{20}Pd_5$ shape memory alloys

The elastic energy for nucleation in the as-extruded sample was 0 J/cm^3 under zero and slightly decreased to -0.55 J/cm^3 as the stress increased to1000 MPa. The elastic energy for propagation was 0.31 J/cm^3 in stress-free condition as it increased to 1.48 J/cm^3 under 1000 MPa. The friction energy was determined to be 0.85 J/cm^3 under zero MPa and stayed close up to 700 MPa. It increased to 1.4 J/cm^3 as the stress was 1000 MPa.

The elastic energy for nucleation in the specimen aged at 400 ^{o}C for 3 hours was 0.75 J/cm^3 under zero stress; however, as the applied stress increased, 1000 MPa, ΔG_{el}^{n} decreased to -0.18 J/cm^3, which was the energy under 1000 MPa. The elastic energy for propagation was 0.43 J/cm^3 in stress-free condition as it increased to 1.04 J/cm^3 under 1000 MPa. The friction energy was determined to be 0.82 J/cm^3 under zero MPa and stayed almost constant up to 500 MPa. After 500 MPa, an abrupt increase was observed in ΔG_{irr}, which was 1.21 and 1.6 J/cm^3 under 700 and 1000 MPa, respectively.

The elastic energy for nucleation in the specimen aged at 550 ^{o}C for 3 hours was --0.55 J/cm^3 under zero stress and increased to 0.41 J/cm^3 as the stress increased to1000 MPa. The elastic energy for propagation was 0.44 J/cm^3 in stress-free condition as it increased to 0.81 J/cm^3 under 1000 MPa. The friction energy was determined to be 0.51 J/cm^3 under zero MPa and stayed almost constant up to 700 MPa. It decreased to 0.41 J/cm^3 as the stress was 1000 MPa.

Figure 7.7d showed the change in reversible and irreversible energies in $Ni_{45.3}Ti_{29.7}Hf_{20}Pd_5$ aged at 650 ^{o}C for 3 hours. The elastic energy for nucleation in the specimen aged at 550 ^{o}C for 3 hours was -4.5 J/cm^3 under zero stress; however, as the

applied stress increased, 1000 MPa, ΔG_{el}^{n} increased to 5.24 J/cm^3, which was the energy under 1000 MPa. The elastic energy for propagation was 0.34 J/cm^3 in stress-free condition as it increased to 1.42 J/cm^3 under 1000 MPa. The friction energy was determined to be 0.68 J/cm^3 under zero MPa and 1.4 J/cm^3 at 1000 MPa.

It is clear that the elastic energy for propagation increased with the applied stress in the all specimens. This means that the elastic energy increased with the applied stress in $Ni_{45.3}Ti_{29.7}Hf_{20}Pd_5$ SMAs in constant stress thermal cycling experiments if there was no relaxation of the stored energy by dislocation generation. Different than propagation energy, friction energy stayed almost constant up to certain stress level in the 400 ^{o}C-3h and 650 ^{o}C-3h samples. After a certain level, friction energy abruptly increased meaning there was energy dissipation in the material. This dissipation of energy can be explained by the dislocation generation in the materials which was also evident from the unclosed curves in the constant stress thermal cycling experiments [92].

In contrast to the as-extruded and 400 ^{o}C-3h sample, there was no increase in the friction energy with stress in the 550 ^{o}C-3h sample, which was in good agreement with the decreased/constant thermal hysteresis data [92]. In all the phase diagrams except 550 ^{o}C-3h, nucleation energy stayed almost constant up to certain stress level and decreased as the friction energy increased. This observation was in good agreement with the data on Cu-Al-Ni shape memory alloys previously reported [153]. This reverse behavior can be linked to a possible relaxation of the stored energy by dislocation generation as the applied stress increases [153] and/or formation of nucleation sites after plastic

deformation as discussed in previous paragraphs. Due to nucleation sites, nucleation of martensite was easier and ΔG_{el}^{n} decreased.

7.4. Effects of microstructures on constant stress shape memory behaviors

In this section, initial microstructures of $Ni_{45.3}Ti_{29.7}Hf_{20}Pd_5$ single crystals will be utilized in discussion on the relationships between experimentally observed shape memory behaviors via thermodynamic principles. Based on our previous experimental results, we know that the single crystals aged at 600 ^{o}C for various times (e.g. 3h, 48h and 72h) have more distinctive microstructures due to more homogeneous distribution of precipitates owing to lack of grain boundaries [2]. In polycrystalline materials, the precipitates may form inside grains and along grain boundaries and this may result a heterogeneous distribution of precipitates in addition to internal stress [154], which may affect a detailed shape memory response analysis negatively.

Figure 5.8 showed the shape memory responses of the [111] oriented $Ni_{45.3}Ti_{29.7}Hf_{20}Pd_5$ alloys aged at 600 ^{o}C for 3, 48 and 72 hours previously. The revealed precipitation characteristics with aging time are shown in Figure 7.9. The specimen aged for 3 hours showed very fine and homogeneously distributed precipitates (Figure 7.9a) with a length of ~50 nm along the long axis and 8 nm along the short axis. The average interparticle distance between precipitates was measured to be $\lambda \approx 35nm$.

In Figures 7.9b and 7.9c, “p” refers to precipitates and “m” refers to martensites. After aging for 48 hours, the precipitates were coarsened in size to 200 nm and 20 nm along the long and short axes, respectively, and interparticle distance was increased to

$\lambda \approx 80nm$ as depicted in Figure 7.9b. After 72 hours of aging, no further increase in precipitate size and interparticle distance was observed. It should also be noted that, for 48 hours and 72 hours aged specimens, the precipitate distribution was also homogeneous. Martensitic plates were not observed in the sample aged for 3 hours since this sample has an M_s lower than the room temperature. Martensitic plates were found to be confined by the surrounding precipitates in the both samples aged for 48 hours and 72 hours with the ones to be slightly larger in the 72 hours case.

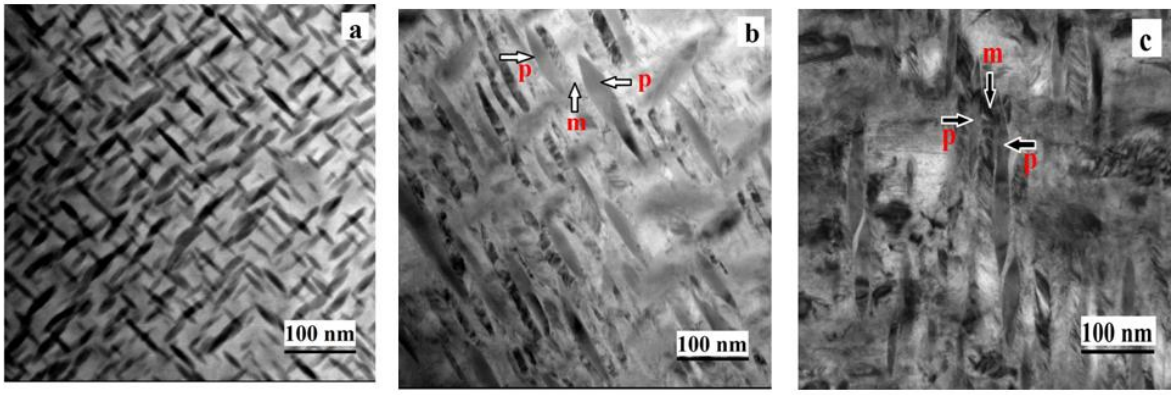

Figure 7.9: TEM images for the aged $Ni_{45.3}Ti_{29.7}Hf_{20}Pd_5$ at 600 ^oC for a) 3 hours, b) 48 hours and c) 72 hours

The thermal cycling responses of the 3 hours aged sample are very different compared to those aged for 48 and 72 hours (see Figure 5.8 in chapter 5). A schematic representation of phase transformations under stress for idealized cases and the current responses of 3 and 48 hours aged samples are depicted in Figure 7.10a and Figure 7.10b, respectively.

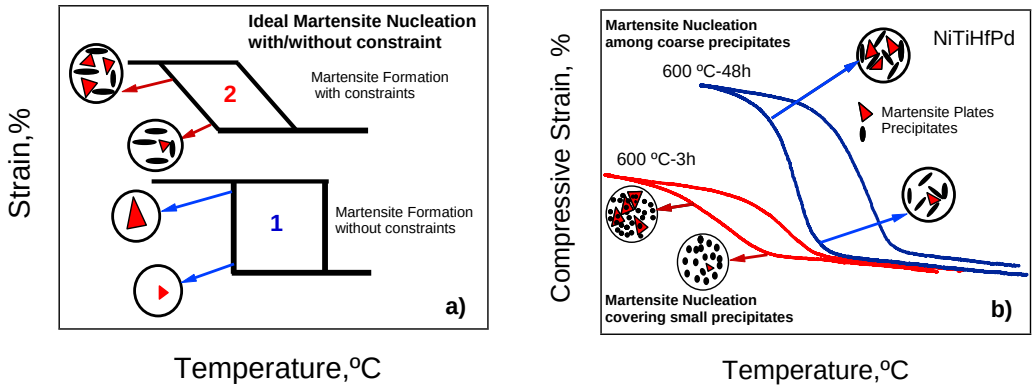

Figure 7.10: Schematic representation of martensite nucleation in single crystals during cooling in temperature cycling experiments for a) Ideal case with/without constraint. b) Actual test results for specimens aged at 600 ^{o}C for 3 hours and 600 ^{o}C for 48 hours.

In the absence of precipitates (and neglecting the inherent elastic energy storage of the material), martensite can form in an obstacle free environment, annotated as case 1 in Figure 7.10a. In this case, a single martensite variant would nucleate and grow rapidly without facing any resistance. If there are obstacles in the microstructure (e.g. grain boundaries, precipitates, dislocations, or other crystallographic defects,) additional energy is required to overcome these obstacles. The additional energy can be supplied by further undercooling, which would increase the chemical energy difference between phases. Thus, the transformation will not be as rapid as case 1, but would be more gradual, as represented by case 2. The reason for deviation from the ideal case is due to increased elastic energy storage [129]. The stored elastic energy is affected by martensite morphology and precipitation characteristics [11, 55] and will increase with increased resistance to the progression of the phase transformation [120, 129]. In the case of the

$Ni_{45.3}Ti_{29.7}Hf_{20}Pd_5$ alloy, the increased resistance can be attributed to the additional constraints arising from the small coherent precipitates (high precipitate density) against interface motion. Thus, the slope of the transformation strain – temperature curve (TST slope) decreases as the elastic energy storage increases in the material due to increased constraints in the microstructure. When the precipitates become larger and incoherent, the stored elastic energy may be relaxed due to dislocations acquired from incoherent precipitate boundaries [11]. In such a case, the TST slope will become steeper due to easier propagation of the transformation, resulting in lower elastic energy storage. Thus, as the resistance to the transformation-induced shape change increases, elastic energy storage increases, and the slopes of the TST curves decrease, as illustrated in case 2.

In Figure 7.10b, the actual thermal cycling response of the specimens aged for 3 and 48 hours at 300 MPa are shown. The response after 3 hours aging resembles the ideal case 2, while the response after 48 hours is similar to ideal case 1. The difference in these responses could be attributed to the effects of precipitates on the martensite morphology and elastic energy storage [11, 129]. When the precipitates are small and interparticle distance is short enough, the growing martensite plates will try to bypass and surround nearby precipitates resulting in larger martensite plates with embedded precipitates as it has been previously observed in CuAlMn SMAs [133]. However, if the precipitates are large enough, the martensite plates will not be able to bypass the precipitates but instead will tend to form in the channels between precipitates (as in Figures 7.10b and 7.10c).

The process of trying to bypass and encapsulate precipitates in the microstructure makes the growth of martensite slower and harder. This process increases the energy required to complete the transformation, which will need to be supplied by further

undercooling [55] and stored as elastic energy in the material [11, 120, 129, 134]. In thermal cycling experiments, the elastic energy storage could be observed as gradual increase/decrease in transformation strain with temperature as in the case of 3 hours aged specimen. Moreover, the additional undercooling is responsible for the lower TTs in the 3 hours aging case, compared to the 48 and 72 hours aged samples.

Higher elastic energy storage and lower TTs in 3 hours aging case can also be elucidated by the thermodynamical description of martensitic transformation. It was mentioned that the total elastic strain energy storage during the martensitic transformation (ΔG_{el}) is comprised of both the elastic energies for nucleation (ΔG_{el}^{n}) and propagation (ΔG_{el}^{p}) of martensite [145] earlier. The elastic energy due to propagation of martensite was previously formulated as,

$$\left|\Delta G_{el}^{p}\right| = (M_s - M_f)\left|\Delta S\right|$$

Due to smaller interparticle distances ($\lambda < 10-15nm$) in the 3 hours aged specimen (Figure 7.9), the nucleation of martensite will require more elastic energy than the 48 and 72 hours aged specimens.

In addition to the nucleation energy, the elastic energy for propagation of nucleated martensite is also larger in the 3 hours aged specimen according to the equation (12). This fact can clearly be seen by the difference between M_f and M_s is much higher due to gradual TST curve (Figure 7.10b) when it is compared with the 48 and 72 hours aged cases. Thus the combined contributions of ΔG_{el}^{n} and ΔG_{el}^{p} will result in higher elastic strain energy storage in the 3 hours aged sample than the 48 and 72 hours aged

samples. It should be recalled that the T_o depends on only chemical composition of the matrix. Since the chemical composition is most likely saturated after 72 hours of aging at 600 ^oC, T_o of the 72h aged $Ni_{45.3}Ti_{29.7}Hf_{20}Pd_5$ single crystals will be taken as a base value calculated by equation 17 and will be assumed to be same for also 3h and 48h aged materials.

The reversible and irreversible energies can be expressed as in the following table and plot;

Table 4: The reversible (ΔG_{el}^{n} and ΔG_{el}^{p}) and irreversible (ΔG_{irr}) free energies in $Ni_{45.3}Ti_{29.7}Hf_{20}Pd_5$ single crystals aged at 600 ^oC for 3, 48 and 72 hours at 300 MPa

Aging Time/Energy	ΔG_{el}^{n} (J/cm^3)	ΔG_{el}^{p} (J/ cm^3)	ΔG_{irr} (J/ cm^3)
3h	1.44	1.55	0.38
48h	0.54	0.96	0.75
72h	-0.5	2.16	0.76

Higher elastic energy storage for nucleation is responsible for the low TTs in the 3 hours aged specimen. Recall that the M_s was previously expressed in equation 16;

In the equation 16, ΔG_{irr} term represents the friction work that is required to move phase front and consequently, M_s depends mostly on elastic energy for nucleation, ΔG_{el}^{n} and friction work, ΔG_{irr} .

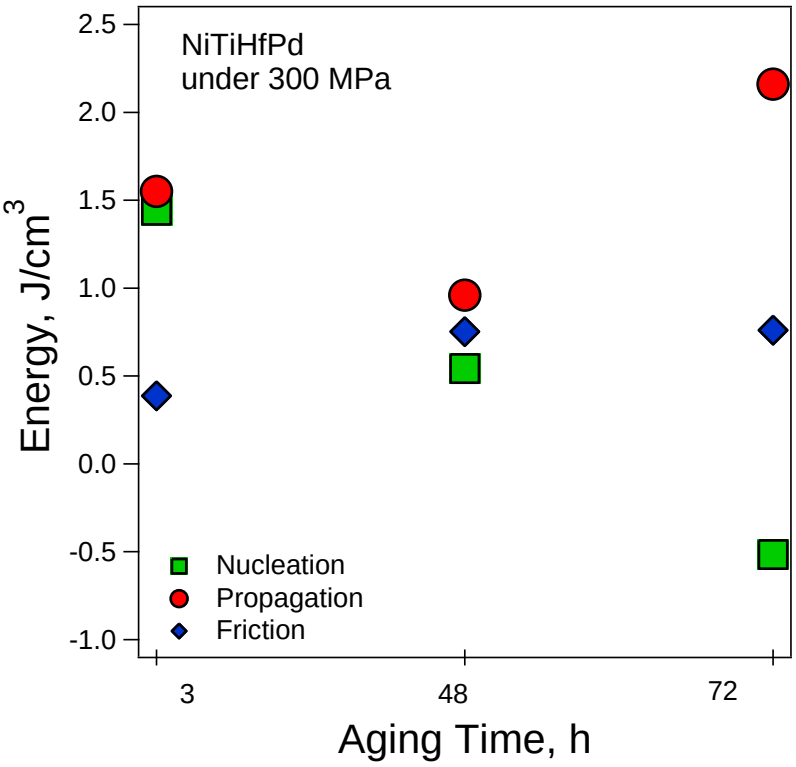

Figure 7.11: Non-chemical energy changes as a function of aging time in $Ni_{45.3}Ti_{29.7}Hf_{20}Pd_5$ single crystals

It is clear that due to fine coherent precipitates and smaller interparticle distances in 3 hours aging case, ΔG_{irr} and ΔG_{el}^{n} will be larger compared to those of the 48 and 72 hours aging cases as discussed above. Consequently, M_s will be lower after 3 hours aging according to equation (7).

When the precipitates are larger in size, as in the case of the 48 and 72 hours aged samples (Figures 7.10b and 7.10c), martensite plates form between precipitates [155]. In this case, interparticle distances become the main factor that determines the size of the martensite plates as tranformation takes place. The larger precipitatation size and interparticle spacing also enable easier nucleation of martensite plates favored by the

strain fields surrounding the precipitates, as shown in Figure 7.10b and 7.10c. As the aging time increased to 48 and 72h, the elastic energy for nucleation at 300 MPa decreases to 0.54 and -0.51 J/cm^3, respectively. The increased interpaticle distance also resulted in easier propagation of the formed martensite. The elastic energy for propagation at 300 MPa was 1.55, 0.96 and 2.16 J/cm^3 for the aging time of 3, 48 and 72 h, respectively.

Figure 7.12 shows the change in the non-chemical free energies $\Delta G_{el}^{n}, \Delta G_{el}^{p}$ and ΔG_{irr} with stress for the $Ni_{45.3}Ti_{29.7}Hf_{20}Pd_5$ single crystals aged at 600 ^{o}C for 3, 48 and 72 hours.

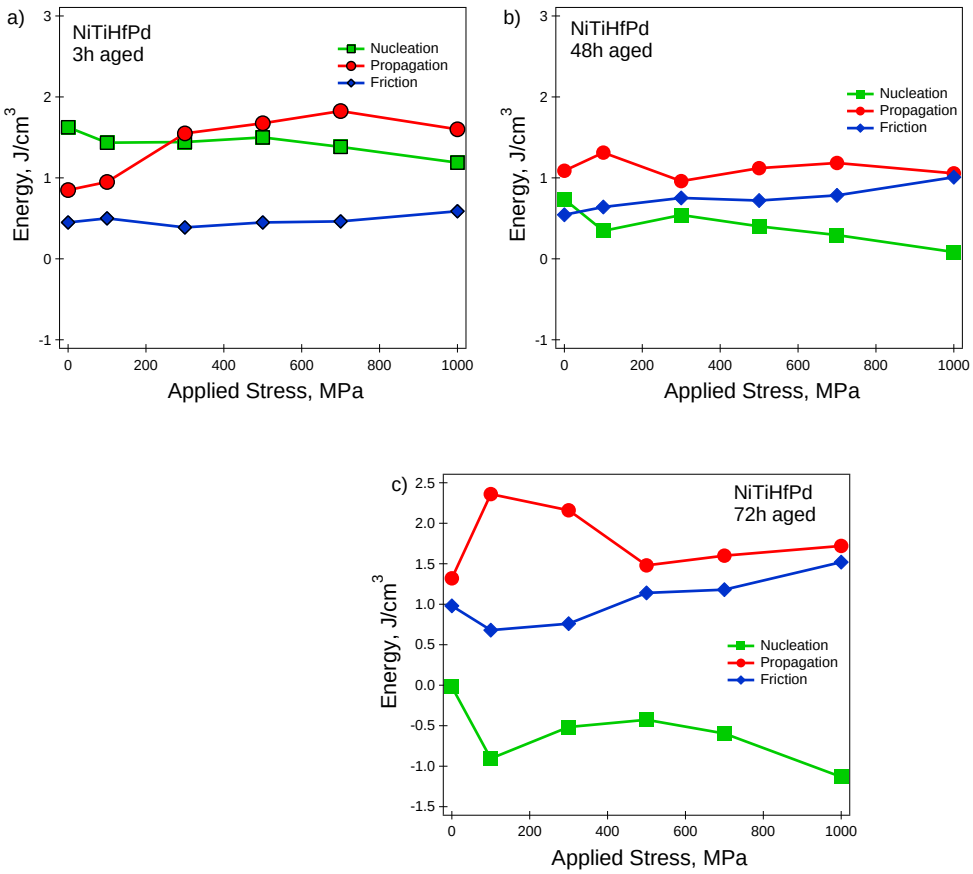

Figure 7.12: Dependence of the reversible (ΔG_{el}^{n} and ΔG_{el}^{p}) and irreversible (ΔG_{irr}) free energies on the applied stress during constant stress thermal cycling experiments in a) 3h aged, b) 48h aged, c) 72h aged $Ni_{45.3}Ti_{29.7}Hf_{20}Pd_5$ single crystals

The elastic energy for nucleation in the 3h aged sample was 1.62 J/cm^3 under zero and decreased to 1.18 J/cm^3 as the stress increased to1000 MPa. The elastic energy for propagation was 0.85 J/cm^3 in stress-free condition as it increased to 1.6 J/cm^3 under 1000 MPa. The friction energy was determined to be 0.45 J/cm^3 under zero MPa and stayed close up to 700 MPa. It increased to 0.58 J/cm^3 as the stress was 1000 MPa.

The elastic energy for nucleation in the specimen aged for 48 hours was 0.73 J/cm^3 under zero stress; however, as the applied stress increased, 1000 MPa, ΔG_{el}^{n}

decreased to 0.08 J/cm^3, which was the energy under 1000 MPa. The elastic energy for propagation was 1.08 J/cm^3 in stress-free condition as it slightly decreased to 1.05 J/cm^3 under 1000 MPa. The friction energy was determined to be 0.54 J/cm^3 under zero MPa and 1 J/cm^3 at 1000 MPa.

The elastic energy for nucleation in the specimen aged for 72 hours was -0.02 J/cm^3 under zero stress and decreased to -1.13 J/cm^3 as the stress increased to1000 MPa. The elastic energy for propagation was 1.32 J/cm^3 in stress-free condition as it increased to 1.72 J/cm^3 under 1000 MPa. The friction energy was determined to be 0.98 J/cm^3 under zero MPa and increased to 1.52 J/cm^3 as the stress was increased to 1000 MPa.

7.5. Comparison of the approaches

In the sections above, three approaches/methods were used in calculating the non-chemical energies to explain the functional properties of $Ni_{45.3}Ti_{29.7}Hf_{20}Pd_5$ shape memory alloys. In this part, the approaches will be compared.

Three different methods examined were as follows;

A1) T_o was assumed to be equal to equation of $T_o = \frac{M_s + A_f}{2}$ for all materials (extruded and aged).

A2) T_o was assumed to be equal to A_f for each material.

A3) The extruded material was assumed to be a base material and the T_o (calculated by equation 11) of the extruded material was assumed to be valid for the all the aged conditions..

The first approach could be appropriate if there was a material without precipitates or internal stress, which might affect the TTs and consequently T_o temperatures. If there are internal stress and constarints (limiting the mobility of transformation) in a material, the analysis will not give the correct tendency in a possible comparison between materials due to unknown effects. Thus, the first approach does not look suitable for the comparison between the extruded and aged $Ni_{45.3}Ti_{29.7}Hf_{20}Pd_5$ alloys.

The second approach has the same tendency with the approach one. The only difference is the value of the T_o temperature is higher and closer to A_f temperature when compared to A1. Thus, this method might be proper for a material with an ideal microstructure that has no precipitates .

The third approach looks the most promising method in explaining the non-chemical energy terms for the current $Ni_{45.3}Ti_{29.7}Hf_{20}Pd_5$ shape memory alloys. In this method, the extruded material was assumed to have an ideal microstructure without any factors affecting the TTs and T_o. Then, the energies for the aged materials were examined relative to the extruded base material and the comparison were undertaken. Because, it was mentioned that if there are constarints in the microstructure (e.g. small precipitates, grain boundary etc.), the TTs could be decreased. On the other hand, the TTs might be increased if there is internal stress due to mismatch of precipitates and matrix. Since these effects are not known quantatively for each material, the exact T_o values are non known. Thus, approach 3 could be useful comparison of aged materials.

7.6. Summary and conclusions

Based on the thermodynamical analysis, the following conclusions can be drawn for the Chapter 7;

1. Precipitate characteristics (precipitate size and interparticle distance) were found to be very effective to tailor the elastic energies for nucleation, propagation with dissipation energy and these energies affect the TTs in $Ni_{45.3}Ti_{29.7}Hf_{20}Pd_5$ alloys.

2. Aging and extreme high stress capabilities resulted in a change in transformation type from Class I to II as the stress increased (e.g. 700-1000 MPa) in constant stress thermal cycling experiments in $Ni_{45.3}Ti_{29.7}Hf_{20}Pd_5$ alloys. The observed change was a result of increased elastic energy storage as a function of stress.

3. Stress-temperature phase diagrams were strong functions of non-chemical elastic energies in $Ni_{45.3}Ti_{29.7}Hf_{20}Pd_5$ alloys. The elastic energy for propagation increased with applied stress in constant stress thermal cycling experiments while the nucleation energy decreased with stress for all aging conditions in polycrystalline and single crystals. The dissipation energy were constant initially in general and increased as the plastic deformation increased.

4. The precipitate characteristics were very effective in shape memory behavior of $Ni_{45.3}Ti_{29.7}Hf_{20}Pd_5$ single crystals owing to non-chemical free energy change. The nucleation energy decreased with aging time while the friction energy

increased by aging time. The propagation energy decreased after aging for 48 hours followed by an increase upon aging for 72h due to higher entropy value.

5. Three methods were used in calculating the non-chemical free energy terms and comparisons were made between the methods. For the $Ni_{45.3}Ti_{29.7}Hf_{20}Pd_5$ alloys, the third method that allows for the relative calculation and comparison were suggested to be the most proper approach.

8. GENERAL CONCLUSIONS AND FUTURE WORKS

$Ni_{45.3}Ti_{29.7}Hf_{20}Pd_5$, $Ni_{45.3}Ti_{34.7}Hf_{15}Pd_5$ and $Ni_{45.3}Ti_{39.7}Hf_{10}Pd_5$ polycrystalline and $Ni_{45.3}Ti_{29.7}Hf_{20}Pd_5$ single crystalline shape memory alloys were characterized using various experimental techniques including DSC, XRD, TEM, constant stress thermal cycling, and isothermal stress cycling tests. Effects of homogenization and heat treatments were also investigated. Thermodynamic analyses were performed to understand the experimental results. Based on the results, following conclusions can be arrived;

1. In $Ni_{45.3}Ti_{29.7}Hf_{20}Pd_5$ alloys, precipitates with sizes about 20-30 nm in length and interparticle distance of approximately 10-30 nm were formed after 550 ^{o}C-3 hours aging. The length of the precipitates varied from 80 nm to 300 nm with a width of about 50 nm and interparticle distances of 15 nm to 150 nm as the aging temperature was increased to 650 ^{o}C. Controlling aging temperature and time helped adjusting TTs between –100 ^{o}C and 100 ^{o}C. $(001)_{B19'}$ compound twins were observed in all samples regardless of thermal treatment.

2. $Ni_{45.3}Ti_{29.7}Hf_{20}Pd_5$ alloy exhibits a fairly high damping capacity (30-34 J.cm^{-3}) and a very high work output (30-35 J.cm^{-3}) capability at temperatures between 0 and 100 ^{o}C, especially in the as-extruded condition. On the other hand, an aged material at 550 ^{o}C for 3 hours showed very promising superelastic cyclic responses at high temperatures (160 ^{o}C) under high stress levels of 1600 MPa without any visible irrecoverable strains even after 5000 cycles.

3. The internal twins formed in $Ni_{45.3}Ti_{39.7}Hf_{10}Pd_5$ under stress free transformation in the large martensite plates were <011> type II twins, which are commonly observed in NiTi binary alloys. The difference between the evolutions of the thermal hystereses of NiTiPd-10Hf and NiTiPd-15Hf (and NiTiPd-20Hf) with the applied stress was linked to the difference in twinning types. A progressively increasing hysteresis with the applied stress in the load-biased thermal cycling tests was observed in the compound twinned NiTiPd-15Hfand NiTiPd-20Hf alloys in contrast to type-II twinned NiTiPd-10Hf alloy.

4. The $Ni_{45.3}Ti_{39.7}Hf_{10}Pd_5$ alloy exhibited near perfect shape memory response with 4.6 % transformation strain at 500 MPa. A near perfect superelastic response was observed at 90 ^{o}C with nearly complete recovery of 7 % applied strain, including ~4.3 % transformation strain at a stress level of 1250 MPa in $Ni_{45.3}Ti_{39.7}Hf_{10}Pd_{5.}$ A notable superelastic response was observed at 90 ^{o}C with nearly complete recovery of 5 % applied strain, including over 3 % transformation strain in $Ni_{45.3}Ti_{34.7}Hf_{15}Pd_5$ and $Ni_{45.3}Ti_{34.7}Hf_{15}Pd_5$ alloys while the high hardening limited the superelasticity in $Ni_{45.3}Ti_{29.7}Hf_{20}Pd_5$. As the Hf content was increased (replacing Ti), the transformation strain was decreased and the volume of crystal structures was expanded.

5. The $Ni_{45.3}Ti_{39.7}Hf_{10}Pd_5$ alloy exhibited 1.6 % two-way shape memory strain after a simple training procedure consisting of thermomechanical cycling at up to 700 MPa. The $Ni_{45.3}Ti_{34.7}Hf_{15}Pd_5$ and $Ni_{45.3}Ti_{29.7}Hf_{20}Pd_5$ alloys exhibited

two-way shape memory strains of 0.6 % and 0.8 %, respectively, after simple training.

6. The solution-treated single crystalline alloy showed full recovery of 6 % applied strain with 4.2 % transformation strain at - 30 ^{o}C along [111] orientation . The superelastic window was at least 100 ^{o}C, between -30 ^{o}C and 70 ^{o}C. At 70 ^{o}C the yield strength was greater than 2500 MPa. Perfect shape memory behavior at 1000 MPa and near-perfect shape memory effect with with 2.2 % transformation strain under an ultra high stress level of 1500 MPa was observed in [111]-oriented single crystals aged at 550 ^{o}C for 3 hours beside fully recoverable superelastic responses to stresses as high as 1.8 GPa, due to the combination of precipitation hardening and natural high strength.

7. The solution-treated single crystalline alloy demonstrates a very large mechanical hysteresis of 1270 MPa at -30 ^{o}C, resulting in a maximum damping capacity of 44 J.cm^{-3}. Although, the stress hysteresis is essentially independent of transformation strain, it is highly dependent on test temperature, and diminished with increasing temperature to 815 MPa at 70 ^{o}C.

8. Manipulating the microstructure through simple thermal treatment was an effective way to control the shape memory behavior of the [111] oriented $Ni_{45.3}Ti_{29.7}Hf_{20}Pd_5$ alloy. Aging of the as-grown single crystals at 550 ^{o}C for 3 hours produced precipitates of $\approx$20-30 nm in size with interparticle distances of about twice the particle size. Aging solution-treated (1050 ^{o}C for 4 hours)

single crystals at 550 ^{o}C for 3 hours produced smaller precipitates, ≈15-20 nm, with interparticle distances of about the same dimension.

9. Shape memory responses of $Ni_{45.3}Ti_{29.7}Hf_{20}Pd_5$ single crystals were determined at stresses ranging from 100 to 1000 MPa in the [111], [011] and [-117] orientations. The maximum reversible strains were 2.2 %, 2.7 % and 0.7 % along the [111], [011] and [-117] orientations, respectively after aging at 550 ^{o}C for 3 hours. In the 600 ^{o}C-48h aging, the maximum reversible strains were 2.3 %, 3.2 % and 0.9 % along the [111], [011] and [-117] orientations, respectively. The [-117] and [111] orientations were stronger compared to the [011] orientation in compression after aging at 550 ^{o}C for 3 hours and aging at 600 ^{o}C for 48 hours.

10. Fully reversible superelastic responses were possible with a larger than 2.2 %, 2.3 % and 0.3 % reversible strains along [111], [011] and [-117] orientations, respectively, at a test temperature of 60 ^{o}C after aging at 550 ^{o}C for 3 hours. After aging at 600 ^{o}C for 48 hours, reversible strains of 1.5 %, 1.2 % and 0.6 % were measured for the [111], [011] and [-117] orientations, respectively, at 140 ^{o}C. No irreversible strain was observed even when deformed to 1500 MPa in the [111] and [-117] orientations after both aging conditions.

11. The work output values were also strong functions of orientation. Maximum work output values of 22 J/cm^3, 27 J/cm^3, 7 J/cm^3 were observed along [111], [011] and [-117] loading orientations, respectively, after aging at 550 ^{o}C for 3 hours. For samples aged at 600 ^{o}C for 48 hours, maximum work output values of 20 J/cm^3, 22 J/cm^3, 8.5 J/cm^3 were observed along [111], [011] and [-117] loading orientations, respectively.

12. The difference in the shape memory properties (e.g. transformation strain) compared to binary NiTi alloys could be stemmed from the difference in the twinning types. Intial results showed that $(001)_{B19'}$ compound twins were active in $Ni_{45.3}Ti_{29.7}Hf_{20}Pd_5$ alloys depending on aging condition while the most common twinning types were Type I and Type II in NiTi alloys.

13. Precipitate characteristics (precipitate size and interparticle distance) were found to be effective on the elastic energies for nucleation, propagation with dissipation energy and these energies affect the TTs in $Ni_{45.3}Ti_{29.7}Hf_{20}Pd_5$ alloys. Aging and extreme high stress capabilities resulted in a change in transformation type from Class I to II as the stress increased (e.g. 700-1000 MPa) in constant stress thermal cycling experiments in $Ni_{45.3}Ti_{29.7}Hf_{20}Pd_5$ alloys. The observed change was a result of increased elastic energy storage as a function of stress.

14. Stress-temperature phase diagrams were strong functions of non-chemical elastic energies in $Ni_{45.3}Ti_{29.7}Hf_{20}Pd_5$ alloys. The elastic energy for

propagation increased with applied stress in constant stress thermal cycling experiments while the nucleation energy decreased with stress for all aging conditions in polycrystalline and single crystals. The dissipation energy were constant initially in general and increased as the plastic deformation increased.

In the current study, the effects of precipitation, orientation and composition on the shape memory behavior of high strength NiTiHfPd alloys was investigated. In the light of the observed results, possible future studies on these types of alloy systems could be to;

1. Investigate stress generation capabilities of NiTiHfPd polycrystalline and single crystalline alloys and compare them to NiTi alloys.

2. Characterize the fatigue properties of NiTiHfPd alloys by conducting isobaric thermal cycling and isothermal stress cycling experiments.

3. Investigate possible effects of chemical composition on the shape memory properties of NiTiHfPd high strength shape memory single crystal alloys.

4. Reveal the effects of stress-assisted aging on the shape memory properties (e.g. TTs. Transformation strain, TWSME) in NiTiHfPd alloy systems.

REFERENCES

[1] K.Otsuka CMW. Shape Memory Materials. Cambridge,UK: Cambridge University Press, 1998.

[2] Otsuka K, Ren X. Physical metallurgy of Ti-Ni-based shape memory alloys. Prog. Mater. Sci. 2005;50:511.

[3] Ma J, Karaman I, Noebe RD. High temperature shape memory alloys. Int. Mater. Rev. 2010;55:257.

[4] Frick CP, Ortega AM, Tyber J, Maksound AEM, Maier HJ, Liu Y, Gall K. Thermal processing of polycrystalline NiTi shape memory alloys. Materials Science and Engineering: A 2005;405:34.

[5] Padula S, II, Qiu S, Gaydosh D, Noebe R, Bigelow G, Garg A, Vaidyanathan R. Effect of Upper-Cycle Temperature on the Load-Biased, Strain-Temperature Response of NiTi. Metallurgical and Materials Transactions A 2012;43:4610.

[6] Gall K, Sehitoglu H, Chumlyakov YI, Zuev YL, Karaman I. The role of coherent precipitates in martensitic transformations in single crystal and polycrystalline Ti-50.8at%Ni. Scripta Materialia 1998;39:699.

[7] Liu Y, Blanc M, Tan G, Kim JI, Miyazaki S. Effect of ageing on the transformation behaviour of Ti-49.5 at.% Ni. Materials Science and Engineering: A 2006;438-440:617.

[8] Khalil-Allafi J, Dlouhy A, Eggeler G. Ni4Ti3-precipitation during aging of NiTi shape memory alloys and its influence on martensitic phase transformations. Acta Materialia 2002;50:4255.

[9] Gall K, Sehitoglu H, Chumlyakov YI, Kireeva IV, Maier HJ. The influence of aging on critical transformation stress levels and martensite start temperatures in NiTi: Part I - Aged microstructure and micro-mechanical modeling. J. Eng. Mater. Technol.-Trans. ASME 1999;121:19.

[10] Zarinejad M, Liu Y, Tong YX. Transformation temperature changes due to second phase precipitation in NiTi-based shape memory alloys. Intermetallics 2009;17:914.

[11] Hamilton RF, Sehitoglu H, Chumlyakov Y, Maier HJ. Stress dependence of the hysteresis in single crystal NiTi alloys. Acta Materialia 2004;52:3383.

[12] Nemat-Nasser S, Guo W-G. Superelastic and cyclic response of NiTi SMA at various strain rates and temperatures. Mechanics of Materials;38:463.

[13] Ronald N, Tiffany B, Santo P. NiTi-Based High-Temperature Shape-Memory Alloys. Advanced Structural Materials. CRC Press, 2006. p.145.

[14] Grummon D. Thin-film shape-memory materials for high-temperature applications. JOM Journal of the Minerals, Metals and Materials Society 2003;55:24.

[15] Bigelow G, Padula S, Garg A, Gaydosh D, Noebe R. Characterization of Ternary NiTiPd High-Temperature Shape-Memory Alloys under Load-Biased Thermal Cycling. Metallurgical and Materials Transactions A 2010;41:3065.

[16] Karaca HE, Saghaian SM, Ded G, Tobe H, Basaran B, Maier HJ, Noebe RD, Chumlyakov YI. Effects of nanoprecipitation on the shape memory and material properties of an Ni-rich NiTiHf high temperature shape memory alloy. Acta Materialia 2013;61:7422.

[17] Takagi T, Sutou Y, Kainuma R, Yamauchi K, Ishida K. Effect of prestrain on martensitic transformation in a Ti46.4Ni47.6Nb6.0 superelastic alloy and its application to medical stents. Journal of Biomedical Materials Research Part B: Applied Biomaterials 2006;76B:179.

[18] Tanaka Y, Himuro Y, Kainuma R, Sutou Y, Omori T, Ishida K. Ferrous Polycrystalline Shape-Memory Alloy Showing Huge Superelasticity. Science 2010;327:1488.

[19] Hao SJ, Cui LS, Wang YD, Jiang DQ, Yu C, Jiang J, Brown DE, Ren Y. The ultrahigh mechanical energy-absorption capability evidenced in a high-strength NbTi/NiTi nanocomposite. Applied Physics Letters 2011;99:024102.
[20] Ma J, Karaman I. Expanding the Repertoire of Shape Memory Alloys. Science 2010;327:1468.
[21] Fosdick R, Ketema Y, Jang-Horng Y. Vibration damping through the use of materials with memory. International Journal of Solids and Structures 1998;35:403.
[22] DesRoches R, Delemont M. Seismic retrofit of simply supported bridges using shape memory alloys. Engineering Structures 2002;24:325.
[23] Meng XL, Cai W, Zheng YF, Tong YX, Zhao LC, Zhou LM. Stress-induced martensitic transformation behavior of a Ti–Ni–Hf high temperature shape memory alloy. Mater. Lett. 2002;55:111.
[24] Wollants P, Roos JR, Delaey L. Thermally- and stress-induced thermoelastic martensitic transformations in the reference frame of equilibrium thermodynamics. Progress in Materials Science 1993;37:227.
[25] Panchenko E, Chumlyakov Y, Kireeva I, Ovsyannikov A, Sehitoglu H, Karaman I, Maier Y. Effect of disperse Ti_3Ni_4; particles on the martensitic transformations in titanium nickelide single crystals. The Physics of Metals and Metallography 2008;106:577.
[26] Sehitoglu H, Efstathiou C, Maier HJ, Chumlyakov Y. Hysteresis and deformation mechanisms of transforming FeNiCoTi. Mechanics of Materials 2006;38:538.
[27] Sehitoglu H, Karaman I, Zhang XY, Chumlyakov Y, Maier HJ. Deformation of FeNiCoTi shape memory single crystals. Scripta Materialia 2001;44:779.
[28] Liu Y, McCormick PG. Transformation dependence of two-way shape memory behaviour in NiTi. Scripta Metallurgica 1988;22:1327.
[29] Perkins J, Sponholz R. Stress-Induced Martensitic Transformation Cycling and Two-Way Shape Memory Training in Cu-Zn-Al Alloys. Metallurgical and Materials Transactions A 1984;15:313.
[30] Liu Y, Liu Y, Van Humbeeck J. Two-way shape memory effect developed by martensite deformation in NiTi. Acta Materialia 1998;47:199.
[31] Liu Y, McCormick PG. Factors influencing the development of two-way shape memory in NiTi. Acta Metallurgica et Materialia 1990;38:1321.
[32] Otsuka K, Ren XB. Recent developments in the research of shape memory alloys. Intermetallics 1999;7:511.
[33] Machado LG, Savi MA. Medical applications of shape memory alloys. Brazilian Journal of Medical and Biological Research 2003;36:683.
[34] Hartl DJ, Lagoudas DC. Aerospace applications of shape memory alloys. Proceedings of the Institution of Mechanical Engineers, Part G: Journal of Aerospace Engineering 2007;221:535.
[35] Jan VH. Non-medical applications of shape memory alloys. Materials Science and Engineering: A 1999;273–275:134.
[36] Knowles KM, Smith DA. The crystallography of the martensitic transformation in equiatomic nickel-titanium. Acta Metallurgica 1981;29:101.
[37] Zheng YF, Huang BM, Zhang JX, Zhao LC. The microstructure and linear superelasticity of cold-drawn TiNi alloy. Materials Science and Engineering: A 2000;279:25.
[38] Gall K, Sehitoglu H, Anderson R, Karaman I, Chumlyakov YI, Kireeva IV. On the mechanical behavior of single crystal NiTi shape memory alloys and related polycrystalline phenomenon. Materials Science and Engineering A 2001;317:85.

[39] Gall K, Sehitoglu H, Chumlyakov YI, Kireeva IV. Tension-compression asymmetry of the stress-strain response in aged single crystal and polycrystalline NiTi. Acta Materialia 1999;47:1203.
[40] Gall K, Sehitoglu H, Chumlyakov YI, Kireeva IV. Pseudoelastic cyclic stress-strain response of over-aged single crystal Ti-50.8at%Ni. Scripta Materialia 1998;40:7.
[41] Sehitoglu H, Karaman I, Anderson R, Zhang X, Gall K, Maier HJ, Chumlyakov Y. Compressive response of NiTi single crystals. Acta Materialia 2000;48:3311.
[42] Sehitoglu H, Jun J, Zhang X, Karaman I, Chumlyakov Y, Maier HJ, Gall K. Shape memory and pseudoelastic behavior of 51.5%Ni-Ti single crystals in solutionized and overaged state. Acta Materialia 2001;49:3609.
[43] Firstov GS, Van Humbeeck J, Koval YN. High temperature shape memory alloys problems and prospects. Journal of Intelligent Material Systems and Structures 2006;17:1041.
[44] Zarinejad M, Liu Y, Tong Y. Transformation temperature changes due to second phase precipitation in NiTi-based shape memory alloys. Intermetallics 2009;17:914.
[45] Firstov GS, Van Humbeeck J, Koval YN. Comparison of high temperature shape memory behaviour for ZrCu-based, Ti-Ni-Zr and Ti-Ni-Hf alloys. Scripta Materialia 2004;50:243.
[46] Meng XL, Cai W, Zheng YF, Tong YX, Zhao LC, Zhou LM. Stress-induced martensitic transformation behavior of a Ti-Ni-Hf high temperature shape memory alloy. Materials Letters 2002;55:111.
[47] Kim HY, Jinguu T, Nam T-h, Miyazaki S. Cold workability and shape memory properties of novel Ti–Ni–Hf–Nb high-temperature shape memory alloys. Scripta Materialia 2011;65:846.
[48] Meng XL, Cai W, Fu YD, Zhang JX, Zhao LC. Martensite structure in Ti–Ni–Hf–Cu quaternary alloy ribbons containing (Ti,Hf)2Ni precipitates. Acta Materialia 2010;58:3751.
[49] Meng XL, Cai W, Lau KT, Zhao LC, Zhou LM. Phase transformation and microstructure of quaternary TiNiHfCu high temperature shape memory alloys. Intermetallics 2005;13:197.
[50] Liang XL, Chen Y, Shen HM, Zhang ZF, Li W, Wang YN. Thermal cycling stability and two-way shape memory effect of Ni-Cu-Ti-Hf alloys. Solid State Commun. 2001;119:381.
[51] H.E. Karaca E.Acar, G.S. Ded, S. M. Saghaian, B. Basaran, H.Tobe, M.Kok, H. J. Maier, R. D. Noebe, YI Chumlyakov. Compression response of Ni45.3Ti29.7Hf20Cu5 high temperature shape memory alloys Materials Science and Engineering A 2014;submitted.
[52] Hsieh SF, Wu SK. Martensitic transformation of quaternary Ti50.5-XNi49.5ZrX/2HfX/2 (X=0-20 at.%) shape memory alloys. Materials Characterization 2000;45:143.
[53] Zheng YF, Cai W, Zhang JX, Wang YQ, Zhao LC, Ye HQ. High-resolution electron microscopy study on the substructure of Ti-Ni-Hf B19′ Martensite. Mater. Lett. 1998;36:142.
[54] Han XD, Zou WH, Wang R, Zhang Z, Yang DZ. Structure and substructure of martensite in a Ti36.5Ni48.5Hf15 high temperature shape memory alloy. Acta Materialia 1996;44:3711.
[55] E Hornbogen. The effect of variables on martensitic transformation temperatures. Acta Metallurgica 1985;33:595.
[56] Gao Y, Zhou N, Yang F, Cui Y, Kovarik L, Hatcher N, Noebe R, Mills MJ, Wang Y. P-phase precipitation and its effect on martensitic transformation in (Ni,Pt)Ti shape memory alloys. Acta Materialia 2012;60:1514.
[57] Sasaki T, Hornbuckle BC, Noebe R, Bigelow G, Weaver M, Thompson G. Effect of Aging on Microstructure and Shape Memory Properties of a Ni-48Ti-25Pd (At. Pct) Alloy. Metallurgical and Materials Transactions A 2013;44:1388.
[58] Meng XL, Cai W, Chen F, Zhao LC. Effect of aging on martensitic transformation and microstructure in Ni-rich TiNiHf shape memory alloy. Scripta Materialia 2006;54:1599.

[59] Sehitoglu H. Compressive response of NiTi single crystals, by H. Sehitoglu, I. Karaman, R. Anderson, X. Zhang, K. Gall, H.J. Maier and Y. Chumlyakov, originally published in Acta Materialia, Volume 48(13), pp. 3311-3326, 2000. Acta Materialia 2001;49:747.
[60] Miyazaki S, Igo Y, Otsuka K. Effect of thermal cycling on the transformation temperatures of Ti ・ Ni alloys. Acta Metallurgica 1986;34:2045.
[61] Barooah P, Rey N. Closed-loop control of a shape memory alloy actuation system for variable area fan nozzle: SPIE, 2002.
[62] Smart materails for high speed adaptive inlet nozzle design. NASA, 2004.
[63] Noebe R, Gaydosh D, II SP, Garg A, Biles T, Nathal M. Properties and potential of two (Ni,Pt)Ti alloys for use as high-temperature actuator materials: SPIE, 2005.
[64] Lin H, He J, Chen K, Liao H, Lin K. Wear characteristics of TiNi shape memory alloys. Metallurgical and Materials Transactions A 1997;28:1871.
[65] C. DellaCorte, S.V. Pepper, R. Noebe, D.R. Hull, and G. Glennon “Intermetallic Nickel-Titanium Alloys for Oil-Lubricated Bearing Applications,” NASA TM-2009-215646 (2009).
[66] C. DellaCorte, R.D. Noebe, M.K. Stanford, and S.A. Padula, "Resilient and Corrosion-Proof Rolling Element Bearings Made From Superealstic Ni-Ti Alloys for Aerospace Mechanism Applications", NASA/TM-2011-217105, (September 2011).
[67] Miyazaki S, Imai T, Igo Y, Otsuka K. Effect of cyclic deformation on the pseudoelasticity characteristics of Ti-Ni alloys. Metallurgical and Materials Transactions A 1986;17:115.
[68] Miyazaki S, Mizukoshi K, Ueki T, Sakuma T, Liu Y. Fatigue life of Ti–50 at.% Ni and Ti–40Ni–10Cu (at.%) shape memory alloy wires. Materials Science and Engineering: A 1999;273–275:658.
[69] Melton KN, Mercier O. Fatigue of NITI thermoelastic martensites. Acta Metallurgica 1979;27:137.
[70] Treppmann D, Hornbogen E. On the Influence of Thermomechanical Treatments on Shape Memory Alloys. J. Phys. IV France 1997;07:C5.
[71] Besseghini S, Villa E, Tuissi A. Ni ・ Ti ・ Hf shape memory alloy: effect of aging and thermal cycling. Materials Science and Engineering: A 1999;273‑275:390.
[72] Xie Z, Liu Y, Van Humbeeck J. Microstructure of NiTi shape memory alloy due to tension–compression cyclic deformation. Acta Materialia 1998;46:1989.
[73] Efstathiou C, Sehitoglu H, Wagoner Johnson AJ, Hamilton RF, Maier HJ, Chumlyakov Y. Large reduction in critical stress in Co–Ni–Al upon repeated transformation. Scripta Materialia 2004;51:979.
[74] Ma J, Karaman I, Maier HJ, Chumlyakov YI. Superelastic cycling and room temperature recovery of Ti74Nb26 shape memory alloy. Acta Materialia 2010;58:2216.
[75] Kumar PK, Lagoudas DC. Introduction to Shape Memory Alloys. Shape Memory Alloys. Springer US, 2008. p.1.
[76] Jost N, Hornbogen E. Influence of prior plastic deformation on the thermal-martensitic-transformation in an Fe-Ni-Al alloy. Journal of Materials Science Letters 1987;6:491.
[77] Andrade MS, Osthues RM, Arruda GJ. The influence of thermal cycling on the transition temperatures of a Fe-Mn-Si shape memory alloy. Materials Science and Engineering: A 1999;273–275:512.
[78] Chumlyakov Y, Panchenko E, Kireeva I, Efimenko S, Aksenov V, Sehitoglu H. Dependence of shape memory effect and superelasticity on the number of variants of dispersed particles in titanium-nickel single crystals. Doklady Physics 2002;47:510.
[79] Nishida M, Wayman CM, Chiba A. Electron microscopy studies of the martensitic transformation in an aged Ti-51at%Ni shape memory alloy. Metallography 1988;21:275.

[80] Sehitoglu H, Hamilton R, Canadinc D, Zhang X, Gall K, Karaman I, Chumlyakov Y, Maier H. Detwinning in NiTi alloys. Metallurgical and Materials Transactions A 2003;34:5.
[81] K. Yamauchi, I. Ohkata, K. Tsuchiya, S. Miyazaki, Shape Memory and Superelastic Alloys: Technologies and Applications, first ed., Woodhead Publishing, Cambridge, 2011
[82] Van Humbeeck J. Non-medical applications of shape memory alloys. Materials Science and Engineering: A 1999;273–275:134.
[83] Zhang CS, Zhao LC, Duerig TW, Wayman CM. Effects of deformation on the transformation hysteresis and shape memory effect in a Ni47Ti44Nb9 alloy. Scripta Metallurgica et Materialia 1990;24:1807.
[84] El Feninat F, Laroche G, Fiset M, Mantovani D. Shape Memory Materials for Biomedical Applications. Advanced Engineering Materials 2002;4:91.
[85] Bigelow GS, Garg A, Padula Ii SA, Gaydosh DJ, Noebe RD. Load-biased shape-memory and superelastic properties of a precipitation strengthened high-temperature Ni50.3Ti29.7Hf20 alloy. Scripta Materialia 2011;64:725.
[86] T.H.Nam, T.Saburi, Y.Nakata and K.Shimizu, Mater. Trans. JIM, 31 (1991) 1050
[87] T. Todoroki and H.Tamura, Mater. Trans. JIM, 50 (1986) 546
[88] T. H.Nam, T. Sabburi and K.Shimizu, Mater. Trans. JIM, 31 (1990) 959
[89] K.N.Melton, J.Simpson and T.W.Duerig, Proc. MRS Int. Conf. on Martennsitic Trans. (ICOMAT-86), Nara, Japan, (1986) p.105
[90] T.Saburi, Proc. MRS Int. Mtg. on Adv. Mats., Tokyo, Vol. 9 (Shape Memory Mater.) 91989) p.77
[91] Hsieh SF, Wu SK. Lattice parameters of martensite in Ti50.5-xNi49.5Zrx/2Hfx/2 quaternary shape memory alloys. Journal of Alloys and Compounds 2000;312:288.
[92] Karaca HE, Acar E, Ded GS, Basaran B, Tobe H, Noebe RD, Bigelow G, Chumlyakov YI. Shape memory behavior of high strength NiTiHfPd polycrystalline alloys. Acta Materialia 2013;61:5036.
[93] Zhongjie Pu H-KT, Kuang-Hsi Wu. An innovative system of high temperature shape memory alloys. SPIE, vol. 289. Orlando, FL, 1994. p.2189.
[94] Sehitoglu H, Hamilton R, Maier HJ, Chumlyakov Y. Hysteresis in NiTi alloys. J. Phys. IV France 2004;115:3.
[95] Cui J, Chu YS, Famodu OO, Furuya Y, Hattrick-Simpers J, James RD, Ludwig A, Thienhaus S, Wuttig M, Zhang Z, Takeuchi I. Combinatorial search of thermoelastic shape-memory alloys with extremely small hysteresis width. Nat Mater 2006;5:286.
[96] Delville R, Kasinathan S, Zhang ZY, Van Humbeeck J, James RD, Schryvers D. Transmission electron microscopy study of phase compatibility in low hysteresis shape memory alloys. Philos. Mag. 2010;90:177.
[97] James RD, Hane KF. Martensitic transformations and shape-memory materials. Acta Materialia 2000;48:197.
[98] Zarnetta R, Takahashi R, Young ML, Savan A, Furuya Y, Thienhaus S, Maass B, Rahim M, Frenzel J, Brunken H, Chu YS, Srivastava V, James RD, Takeuchi I, Eggeler G, Ludwig A. Identification of Quaternary Shape Memory Alloys with Near-Zero Thermal Hysteresis and Unprecedented Functional Stability. Adv. Funct. Mater. 2010;20:1917.
[99] Zhang ZY, James RD, Muller S. Energy barriers and hysteresis in martensitic phase transformations. Acta Materialia 2009;57:4332.
[100] Bhattacharya K, Conti S, Zanzotto G, Zimmer J. Crystal symmetry and the reversibility of martensitic transformations. Nature 2004;428:55.
[101] Lexcellent C, Blanc P, Creton N. Two ways for predicting the hysteresis minimisation for shape memory alloys. Materials Science and Engineering: A 2008;481-482:334.

[102] Bhattacharya K. Comparison of the geometrically nonlinear and linear theories of martensitic transformation. Continuum Mechanics and Thermodynamics 1993;5:205.
[103] Hane KF, Shield TW. Microstructure in the cubic to monoclinic transition in titanium-nickel shape memory alloys. Acta Materialia 1999;47:2603.
[104] Dalle F, Perrin E, Vermaut P, Masse M, Portier R. Interface mobility in Ni49.8Ti42.2Hf8 shape memory alloy. Acta Materialia 2002;50:3557.
[105] Liu Y, Xie Z, Van Humbeeck J, Delaey L. Deformation of shape memory alloys associated with twinned domain re-configurations. Materials Science and Engineering: A 1999;273–275:679.
[106] Stebner AP, Vogel SC, Noebe RD, Sisneros TA, Clausen B, Brown DW, Garg A, Brinson LC. Micromechanical quantification of elastic, twinning, and slip strain partitioning exhibited by polycrystalline, monoclinic nickel–titanium during large uniaxial deformations measured via in-situ neutron diffraction. Journal of the Mechanics and Physics of Solids 2013;61:2302.
[107] Acar E, Karaca HE, Basaran B, Yang F, Mills MJ, Noebe RD, Chumlyakov YI. Role of aging time on the microstructure and shape memory properties of NiTiHfPd single crystals. Materials Science and Engineering: A 2013;573:161.
[108] Contardo L, Guénin G. Training and two way memory effect in Cu・Zn・Al alloy. Acta Metallurgica et Materialia 1990;38:1267.
[109] Nagasawa A, Enami K, Ishino Y, Abe Y, Nenno S. Reversible shape memory effect. Scripta Metallurgica 1974;8:1055.
[110] Benafan O, Padula SA, II, Noebe RD, Sisneros TA, Vaidyanathan R. Role of B19[prime] martensite deformation in stabilizing two-way shape memory behavior in NiTi. Journal of Applied Physics 2012;112:093510.
[111] Tong HC, Wayman CM. Characteristic temperatures and other properties of thermoelastic martensites. Acta Metallurgica 1974;22:887.
[112] Karaca HE, Saghaian SM, Basaran B, Bigelow GS, Noebe RD, Chumlyakov YI. Compressive response of nickel-rich NiTiHf high-temperature shape memory single crystals along the [1 1 1] orientation. Scripta Materialia 2011;65:577.
[113] Takei F, Miura T, Miyazaki S, Kimura S, Otsuka K, Suzuki Y. Stress-induced martensitic transformation in a Ti-Ni single crystal. Scripta Metallurgica 1983;17:987.
[114] Miyazaki S, Kimura S, Takei F, Miura T, Otsuka K, Suzuki Y. Shape memory effect and pseudoelasticity in a Ti---Ni single crystal. Scripta Metallurgica 1983;17:1057.
[115] Sehitoglu H, Anderson R, Karaman I, Gall K, Chumlyakov Y. Cyclic deformation behavior of single crystal NiTi. Materials Science and Engineering A 2001;314:67.
[116] Gall K, Tyber J, Brice V, Frick CP, Maier HJ, Morgan N. Tensile deformation of NiTi wires. Journal of Biomedical Materials Research Part A 2005;75A:810.
[117] Dadda J, Maier HJ, Karaman I, Karaca HE, Chumlyakov YI. Pseudoelasticity at elevated temperatures in [0 0 1] oriented Co49Ni21Ga30 single crystals under compression. Scripta Materialia 2006;55:663.
[118] Karaca HE, Saghaian SM, Basaran B, Bigelow GS, Noebe RD, Chumlyakov YI. Compressive response of nickel-rich NiTiHf high-temperature shape memory single crystals along the [1 1 1] orientation. Scripta Materialia 2011;65:577.
[119] Kireeva IV, Chumlyakov YI, Zakharova EG, Karaman I. Shape memory effect and superelasticity in single-phase nickel titanium single crystals. J. Phys. IV 2004;115:175.
[120] Olson GB, Cohen M. Thermoelastic behavior in martensitic transformations. Scripta Metallurgica 1975;9:1247.
[121] Ortín J, Planes A. Thermodynamic analysis of thermal measurements in thermoelastic martensitic transformations. Acta Metallurgica 1988;36:1873.

[122] Roitburd AL, Kurdjumov GV. The nature of martensitic transformations. Materials Science and Engineering 1979;39:141.
[123] Karaca HE, Acar E, Basaran B, Noebe RD, Chumlyakov YI. Superelastic response and damping capacity of ultrahigh-strength [111]-oriented NiTiHfPd single crystals. Scripta Materialia 2012;67:447.
[124] Han XD, Wang R, Zhang Z, Yang DZ. A new precipitate phase in a TiNiHf high temperature shape memory alloy. Acta Materialia 1998;46:273.
[125] S. Padula, G. Bigelow, R. Noebe, and D. Gyadosh, and A. Garg, SMST 2006: Proceedings of the International Conference on Shape Memory and Superelastic Technologies, ASM International, Metals Park, OH., (2008), pp. 787-802.
[126] Karaman I, Karaca H, Luo Z, Maier H. The effect of severe marforming on shape memory characteristics of a Ti-rich NiTi alloy processed using equal channel angular extrusion. Metallurgical and Materials Transactions A 2003;34:2527.
[127] Gall K, Sehitoglu H, Chumlyakov YI, Kireeva IV, Maier HJ. The Influence of Aging on Critical Transformation Stress Levels and Martensite Start Temperatures in NiTi: Part II---Discussion of Experimental Results. Journal of Engineering Materials and Technology 1999;121:28.
[128] Ishida A, Sato M, Takei A, Nomura K, Miyazaki S. Effect of aging on shape memory behavior of Ti-51.3 At. pct ni thin films. Metallurgical and Materials Transactions A 1996;27:3753.
[129] Salzbrenner RJ, Cohen M. On the thermodynamics of thermoelastic martensitic transformations. Acta Metallurgica 1979;27:739.
[130] Rösner H, Schloßmacher P, Shelyakov AV, Glezer AM. The influence of coherent ticu plate-like precipitates on the thermoelastic martensitic transformation in melt-spun Ti50Ni25Cu25 shape memory alloys. Acta Materialia 2001;49:1541.
[131] Adrian Mihai Sandu KT, Masayuki Tabuchi, Shinya Yamamoto, Yoshikazu Todaka and Minoru Umemoto. Microstructural Evolution during Isothermal Aging in Ni-Rich Ti-Zr-Ni Shape Memory Alloys. Materials Transactions 2007;48:432.
[132] Zheng YF, Zhao LC, Ye HQ. HREM Study on the Intervariant Structure of Ti-Ni-Hf B19′ Martensite. Scripta Materialia 1998;38:1249.
[133] Dutkiewicz J, Pons J, Cesari E. Effect of γ precipitates on the martensitic transformation in Cu・Al・Mn alloys. Materials Science and Engineering: A 1992;158:119.
[134] Pons J, Cesari E. γ Precipitates in β-CuZnAl: Influence on martensitic transformations. Thermochimica Acta 1989;145:237.
[135] Evirgen A, Karaman I, Noebe RD, Santamarta R, Pons J. Effect of precipitation on the microstructure and the shape memory response of the $Ni_{50.3}Ti_{29.7}Zr_{20}$ high temperature shape memory alloy. Scripta Materialia 2013;69:354.
[136] Dunne D, Wayman C. The effect of austenite ordering on the martensite transformation in Fe-Pt alloys near the composition Fe₃Pt: I. Morphology and transformation characteristics. Metallurgical and Materials Transactions B 1973;4:137.
[137] Karaca HE, Acar E, Basaran B, Noebe RD, Chumlyakov YI. Superelastic response and damping capacity of ultrahigh-strength [111]-oriented NiTiHfPd single crystals. Scripta Materialia 2012;67:447.
[138] Karaca HE, Acar E, Basaran B, Noebe RD, Bigelow G, Garg A, Yang F, Mills MJ, Chumlyakov YI. Effects of aging on [111] oriented NiTiHfPd single crystals under compression. Scripta Materialia 2012;67:728.

[139] Panchenko E, Kireeva I, Chumlyakov Y, Aksenov V, Efimenko S, Karaman I, Sehitogly H. Features of thermoelastic martensitic transformations in [001] titanium-nickel single crystals. Doklady Physics 2003;48:34.
[140] Coughlin DR. Characterization of Stoichiometric and Aging Effects on NiTiHf High Temperature Shape Memory Alloys. Material Science and Engineering, vol. PhD: Ohio State University, 2013.
[141] Zhang X, Sehitoglu H. Crystallography of the B2 → R → B19′ phase transformations in NiTi. Materials Science and Engineering: A 2004;374:292.
[142] Santamarta R AR, Pons J, Eviregn A, Karaman I, Karaca HE, Noebe RD. TEM study of structural and microstructural characteristics of a preciptate phase i Ni-rich Ni-Ti-Hf and Ni-Ti-Zr shape memory alloys. Acta Materialia 2013;http://dx.doi.org/10.1016/j.actamat.2013.06.057.
[143] Acar E, Karaca HE, Tobe H, Noebe RD, Chumlyakov YI. Characterization of the shape memory properties of a Ni45.3Ti39.7Hf10Pd5 alloy. Journal of Alloys and Compounds 2013;578:297.
[144] R. Noebe DG, S. Padula, A. Garg, T. Biles, and M. Nathal. Properties and Potential of Two (Ni,Pt)Ti Alloys for Use as High-Temperature Actuator Materials. SPIE Conf., vol. 5761, 2005. p.364.
[145] Kockar B, Karaman I, Kim JI, Chumlyakov YI, Sharp J, Yu CJ. Thermomechanical cyclic response of an ultrafine-grained NiTi shape memory alloy. Acta Materialia 2008;56:3630.
[146] Wayman CM, Tong HC. On the equilibrium temperature in thermoelastic martensitic transformations. Scripta Metallurgica 1977;11:341.
[147] Smith JF, Jiang Q, Lčk R, Predel B. Cp and fractal phase transformation in the shape memory alloy Ni ・ 52Ti. Materials Science and Engineering: A 1991;149:111.
[148] Dead GS. Characterization of Ni-rich NiTiHf-based shape memory alloys. Mechanical Engineering, vol. Master of Science. Lexington: University of Kentucky, 2010.
[149] Gall K, Sehitoglu H, Anderson R, Karaman I, Chumlyakov YI, Kireeva IV. On the mechanical behavior of single crystal NiTi shape memory alloys and related polycrystalline phenomenon. Materials Science and Engineering: A 2001;317:85.
[150] Sun Q-P, Xu TT, Zhang X. On Deformation of A-M Interface in Single Crystal Shape Memory Alloys and Some Related Issues. Journal of Engineering Materials and Technology 1999;121:38.
[151] Sehitoglu H, Hamilton R, Canadinc D, Zhang XY, Gall K, Karaman I, Chumlyakov Y, Maier HJ. Detwinning in NiTi alloys. Metall and Mat Trans A 2003;34:5.
[152] Olson GB, Cohen M. A mechanism for the strain-induced nucleation of martensitic transformations. Journal of the Less Common Metals 1972;28:107.
[153] Daróczi L, Palánki Z, Szabó S, Beke DL. Stress dependence of non-chemical free energy contributions in Cu–Al–Ni shape memory alloy. Materials Science and Engineering: A 2004;378:274.
[154] Fan G, Zhou Y, Chen W, Yang S, Ren X, Otsuka K. Precipitation kinetics of Ti3Ni4 in polycrystalline Ni-rich TiNi alloys and its relation to abnormal multi-stage transformation behavior. Materials Science and Engineering: A 2006;438–440:622.
[155] Pons J, Cesari E. Martensitic transformation cycling in a β CuZnAl alloy containing γ-precipitates. Acta Metallurgica et Materialia 1993;41:2547.

VITA

Emre Acar

Emre Acar was graduated from Gazi University as a Mechanical Engineer in 2006 followed by a Master degree in the Division of Engineering at Brown University in 2010. In the summer of the same year, he started his PhD study in the Department of Mechanical Engineering at the University of Kentucky, under the guidance of Prof. Haluk E. Karaca. During the PhD study at the University of Kentucky, he focused on the investigation of the shape memory properties of high strength NiTiHfPd alloys. His research interests include also process-microstructure-mechanical properties relationships in metallic materials and mechanics of advanced metallic materials.